# Progress in multi-scale modeling of soot particle aggregation in laminar sooting flames

Liu, Fengshan; Yon, Jérôme; Morán, José; Kelesidis, Georgios; Escudero, Felipe; Fuentes, Andrés

**DOI**
10.1016/j.pecs.2025.101234

**Publication date**
2025

**Document Version**
Final published version

**Published in**
Progress in Energy and Combustion Science

Progress in Energy and Combustion Science 110 (2025) 101234

Contents lists available at ScienceDirect

Progress in Energy and Combustion Science

journal homepage: www.elsevier.com/locate/pecs

Review article

# Progress in multi-scale modeling of soot particle aggregation in laminar sooting flames

Fengshan Liu [a,*], Jérôme Yon [b], José Morán [c,d], Georgios A. Kelesidis [e], Felipe Escudero [f], Andrés Fuentes [f]

[a] National Research Council Canada, 1200 Montreal Road, Ottawa, ON K1A 0R6, Canada
[b] INSA Rouen Normandie, Univ Rouen Normandie, CNRS, Normandie Univ, CORIA UMR 6614, F-76000 Rouen, France
[c] Department of Mechanical Engineering, University of Minnesota, Minneapolis, MN 55455, USA
[d] Department of Mechanical Engineering, University of Ottawa, 161 Louis Pasteur, Ottawa, K1N 6N5, Canada
[e] Faculty of Aerospace Engineering, Delft University of Technology, Delft, 2629 HS, The Netherlands
[f] Departamento de Industrias, Universidad Técnica Federico Santa María, Av. España 1680, Valparaíso, Chile

## ARTICLE INFO

*Keywords:*
Fractal agglomerates
Soot formation
Particle dynamics
Discrete element methods
Population balance modeling

## ABSTRACT

The toxicity, climate impact, as well as the physical and chemical properties of ultra-fine soot particles emitted from combustion systems are strongly dependent on their size and morphology. Research attention has been paid in the last three decades to developing more accurate and capable methods to model soot particle coagulation in the presence of inception, surface growth, and oxidation, to predict particle size distribution as well as the detailed aggregate morphology of soot. While soot particle concentrations in hydrocarbon flames are primarily governed by soot kinetics, the morphology of soot particles is controlled by both soot kinetics and particle dynamics. Flame-generated soot particles are fractal aggregates formed by polydisperse and nearly spherical primary particles with a certain degree of overlapping. The properties of fractal aggregates, nanoparticle coagulation, and soot formation chemistry all play important roles in soot formation. This article reviews all these aspects but the focus is on recent progress in macro- and meso-scale modeling of soot particle aggregation in laminar sooting flames to avoid the complexities of turbulence. The reviewed macro-scale methods based on the population balance equation include the commonly used sectional methods and methods of moments. The main features of three recently developed state-of-the-art meso-scale methods, namely the event-driven Discrete Element Method, Monte Carlo Aggregation Code, and detailed stochastic population balance model are reviewed. To highlight the complexities of modeling the particle size distribution and detailed particle morphology without and with surface growth, numerical simulations of three test cases were conducted using the event-driven Discrete Element Method, the Monte Carlo Aggregation Code, and the two macro-scale methods. A detailed analysis of the results was presented to understand how different treatments of particle coagulation and surface growth in the two meso-scale methods affect the predicted particle size and morphology. The remaining challenges in modeling detailed soot particle morphology are outlined.

**Contents**



* Corresponding author.
*E-mail addresses:* fengshan.liu@nrc-cnrc.gc.ca (F. Liu), jerome.yon@insa-rouen.fr (J. Yon), jose.moran@uottawa.ca (J. Morán), g.kelesidis@tudelft.nl (G.A. Kelesidis), felipe.escudero@usm.cl (F. Escudero), andres.fuentes@usm.cl (A. Fuentes).

https://doi.org/10.1016/j.pecs.2025.101234
Received 30 May 2024; Received in revised form 9 April 2025; Accepted 28 April 2025
Available online 11 June 2025

## 1. Introduction

### 1.1. Background

Renewable energy has been increasingly adopted in recent years to slow down the increase in atmospheric carbon dioxide concentrations. However, combustion will likely remain the dominant source of the world's energy demand in the foreseeable future. More than 85% of the world's power generation and transportation are currently based on combustion [1]. The main objections against combustion of fossil fuels are the unavoidable emissions of combustion-generated pollutants, such as carbon dioxide, soot, and $NO_x$. Ultrafine soot particles are formed as a particulate byproduct during hydrocarbon combustion and biomass burning under locally fuel-rich conditions. Soot formation and emissions have many profound impacts on economic activities and society, such as power generation, energy utilization, health, and climate. Fig. 1 shows the main sources of anthropogenic soot and carbon black, the detailed morphology of a soot aggregate, and the positive (enhancing heat release and flame visibility, and being valuable nanomaterials) and negative (health and atmospheric pollution) impacts. Incomplete oxidation of soot particles in combustion devices, fires, and biomass burning leads to soot emissions that are detrimental to human health [2] and a major contributor to climate change. It has been suggested that soot, which is also called black carbon in aerosol and atmospheric sciences, is one of the largest climate forcers [3,4].

Although the emission of soot from combustion systems into the atmosphere is unwanted, soot formation is highly desirable in some applications, as shown in the lower left box of Fig. 1. The presence of soot greatly enhances radiative heat transfer from flame to load in furnaces and boilers, as well as improving flame visibility, which is an important safety consideration in certain situations. Produced annually at 11 megatons from hydrocarbons, carbon black (CB) is the largest flame-synthesized nanomaterial by quantity and value [5]. CB is formed through mechanisms similar to soot, however, it occurs under different

## Nomenclature

| | |
|---|---|
| $D$ | Diffusion coefficient, $m^2\ s^{-1}$ |
| $A$ | Hamaker constant, J |
| $a_a$ | Particle projected area, $m^2$ |
| $A_{\text{free}}$ | Available surface area, $m^2$ |
| $A_N$ | Number-based pair-correlation function |
| $A_V$ | Volume-based pair-correlation function |
| $A_v$ | Avogadro constant, $6.02214 \times 10^{23}\ mol^{-1}$ |
| $C_{\text{mass}}$ | Mass of a carbon atom, kg |
| $C_c$ | Cunningham slip factor |
| $C_{ov}$ | Overlapping coefficient |
| $C_{s-H}$ | Saturated soot surface sites |
| $C_s^{\bullet}$ | Dehydrogenated soot surface sites |
| $D$ | Diameter, m |
| $D_f$ | Fractal dimension |
| $D_{32}$ | Sauter mean diameter, m |
| $D_{\text{p,geo}}$ | Geometric mean diameter of primary particles, m |
| $D_c$ | Collision diameter, m |
| $D_{fp}$ | Population-based fractal dimension |
| $D_g$ | Gyration diameter, m |
| $D_m$ | Mobility diameter, m |
| $D_p$ | Primary particle diameter, m |
| $D_v$ | Volume equivalent diameter, m |
| $f$ | Filling factor, drag constant |
| $f_v$ | Soot volume fraction, ppm |
| $f_{agg}$ | Aerodynamic force, N |
| $f_e$ | Electric force, N |
| $K_n$ | Knudsen number |
| $k_B$ | Boltzmann constant, $1.380649 \times 10^{-23}\ m^2\ kg\ s^{-2}\ K^{-1}$ |
| $k_{fp}$ | Population-based fractal pre-factor |
| $m$ | Particle mass (kg), moment of particle number density function |
| $n$ | Number of elementary charges, number concentration ($\#/m^3$) |
| $N_p$ | Number of primary spheres in the aggregate, # |
| $n_p$ | Particle number density, $\#\ m^{-3}$ |
| $n_{pp}$ | Primary particle number density, $\#\ m^{-3}$ |
| $p$ | Pressure, Pa |
| $r$ | Radial distance, collision radius, center-to-center distance, m |
| $R_{\text{max}}$ | Half of the maximum distance between primary particles in an agglomerate, m |
| $R_g$ | Gyration radius, m |
| $R_m$ | Mobility radius, m |
| $R_p$ | Primary particle radius, m |
| $R_u$ | Universal gas constant, $8.3145\ J\ mol^{-1}\ K^{-1}$ |
| $T$ | Temperature, K |
| $t$ | Time, s |
| $u$ | Velocity, $m\ s^{-1}$ |
| $V$ | Volume, $m^3$ |
| $V_p$ | Primary particle volume, $m^3$ |
| $W$ | Potential energy, J |
| $w$ | Lennard-Jones inter-atomic potential, J |
| $x$ | Position, m |
| $Z_e$ | Electric mobility |
| $E$ | Electric field, N/C |
| $e$ | Elementary charge, $1.60217663 \cdot 10^{-19}$ C |
| $E_0$ | Binding energy, J |
| $E_{\text{barr}}$ | Long-range repulsive energy, J |
| $E_{\text{stick}}$ | Nondimensional potential energy |
| $F_{\text{B}}$ | Stochastic force, N |
| $F_{\text{ext}}$ | External force, N |
| $R_{\text{sinter}}$ | Sintering rate, 1/s |

### Greek symbols

| | |
|---|---|
| $\alpha$ | Scanning exponent, scaling exponent |
| $\alpha_s$ | Steric factor |
| $\beta$ | Stretching exponent |
| $\beta_{\text{c}}$ | Collision coefficient |
| $\chi$ | Particles' shape factor |
| $\chi_R$ | Radiant fraction |
| $\Delta t$ | Time step, s |
| $\epsilon$ | Potential well, J |
| $\eta$ | Dynamic viscosity ($kg\ m^{-1}\ s^{-1}$), particle number density function ($\#\ m^{-3}$) |
| $\eta_s$ | Sticking probability |
| $\gamma_{\text{coll}}$ | Collision efficiency |
| $\lambda$ | Degree of homogeneity |
| $\lambda_g$ | Mean free-path of gas molecules, m |
| $\lambda_p$ | Particle resistance distance, m |
| $\mu$ | Collisional reduced mass (kg), fluid viscosity ($kg\ m^{-1}\ s^{-1}$) |
| $\rho_{\text{eff}}$ | Effective density, $kg\ m^{-3}$ |
| $\rho_p$ | Particle bulk density, $kg\ m^{-3}$ |
| $\sigma$ | Characteristic distance for Lennard-Jones potential, m |
| $\sigma_{\text{p,geo}}$ | Geometric standard deviation |
| $\tau$ | Relaxation time, s |
| $\tau_s$ | Characteristic coalescence time, s |
| $\varphi$ | Packing factor |
| $\xi$ | Characteristic length scale of the agglomerate, m |

### Subscripts

| | |
|---|---|
| $agg$ | Aggregate |
| $pp$ | Primary particle |
| $s$ | Soot |

### Acronyms

| | |
|---|---|
| AAE | Ångstrom absorption exponent |
| AFM | Atomic force microscopy |
| APM | Aerosol particle mass analyzer |
| BCCA | Ballistic cluster-cluster aggregation |
| BLCA | Ballistic-limited cluster aggregation |
| BSU | Basic structure unit |
| CAHM | Carbon addition hydrogen migration |
| CB | Carbon black |
| CHRCR | Clustering of hydrocarbons by radical-chain reactions |
| CPMA | Centrifugal particle mass analyzer |
| DDA | Discrete dipole approximation |

| | |
|---|---|
| DEM | Discrete element method |
| DLCA | Diffusion-limited cluster aggregation |
| DMA | Differential mobility analyzer |
| DPBM | Detailed population balance model |
| DQMOM | Direct quadrature method of moments |
| DSPB | Detailed stochastic population balance |
| EDEM | Event-driven discrete element method |
| HAB | Height above burner |
| HACA | Hydrogen abstraction acetylene (carbon) addition |
| HMOM | Hybrid method of moments |
| HRTEM | High resolution transmission electron microscope |
| LD | Langevin dynamics |
| LES | Large-eddy simulation |
| LN | Log-normal |
| MAC | Mass absorption cross-section |
| MC | Monte Carlo |
| MCAC | Monte Carlo aggregation code |
| MD | Molecular dynamics |
| MOM | Method of moments |
| MOMIC | Method of moments with interpolative closure |
| MPBM | Monodisperse population balance model |
| MSC | Mass scattering cross-section |
| NDF | Number density function |
| PAH | Polycyclic aromatic hydrocarbon |
| PBE | Population balance equation |
| PM | Particulate matter |
| PN | Particle number |
| PPSD | Primary particle size distribution |
| PSD | Particle size distribution |
| RANS | Reynolds-averaged Navier–Stokes |
| RF | Radiative forcing |
| RLCA | Reaction-limited cluster aggregation |
| RMD | Reactive molecular dynamics |
| SM | Sectional method or model |
| SMPS | Scanning mobility particle sizer |
| SPSD | Self-preserving size distribution |
| SSKM | Sectional soot kinetics model |
| TEM | Transmission electron microscope |
| vdW | Van der Waals |

thermal and chemical conditions, involving the pyrolysis and decomposition of hydrocarbons [5,6]. Another difference between soot and CB formation is the particle concentration, which affects the particle coagulation regimes and rates and ultimately the particle size and morphology [7]. Methane pyrolysis has recently been proposed as a promising method to produce zero-emission hydrogen [8]. However, it is critical to produce high quality CB as a value-added product to make this process economically viable [9]. Developing modeling capabilities to predict the size distributions of both primary particles and aggregates, and detailed morphology of soot particles during the evolution of soot production, are indispensable for assessing the effects of soot emissions on health, air quality, and climate [2,3,10,11]. Furthermore, such modeling capabilities are essential for accurate quantification of soot via optical diagnostic techniques [12–14], for the fine-tuning of operational conditions within combustion devices to achieve more efficient and cleaner combustion, and for optimizing the operation parameters of CB reactors to produce specific grades of CB [7]. To this end, it is paramount to gain detailed understanding of all the processes involved in soot formation.

Significant research effort has been devoted to soot research in the last few decades to gain a fundamental understanding of the physical and chemical mechanisms governing the formation, growth, particle dynamics, and oxidation of soot in flames and reactors [21–28]. Despite the considerable progress in soot formation mechanisms, the soot inception process describing the transition from gas-phase precursor species to condensed phase particles remains poorly understood [27,29]. Once incipient soot particles are formed, they subsequently undergo concurrent coalescence, agglomeration, aggregation, surface growth, oxidation, and oxidation-induced fragmentation. It is useful to point out at this point that the terminology used throughout this review to describe particle dynamics and interactions, follows the recent work of Michelsen et al. [30]. In particular, the definitions of important terms frequently used throughout this review are given here:

- Inception: the process of transition from gaseous precursor species to condensed phase particle.
- Incipient particles: the products of inception.
- Coalescence: merging of two or more particles into one. It generally refers to spherical particles of miscible substances. For soot, coalescence is generally only relevant to incipient liquid-like particles of less than about 10 nm.
- Critical coalescence diameter: referring to the critical soot particle diameter above which soot particles are considered solid and can no longer undergo coalescence.
- Primary particles: the constituent building blocks of agglomerates and aggregates.
- Coagulation: referring to different processes that join two or more particles together, including coalescence, agglomeration, and aggregation.
- Agglomerates: referring to a group of particles loosely held together, i.e., physically bound particles.
- Agglomeration: referring to the process leading to agglomerates.
- Aggregates: referring to a group of particles firmly bound together, i.e., chemically bonded particles.
- Aggregation: referring to the process leading to aggregates.

It has been known that soot inception plays the bottleneck role in the overall soot formation process, whereas soot surface growth and aggregation play the dominant role in the sizes of both primary particles [31,32] and aggregates [33,34]. Conversely, the morphology of soot particles affects soot surface growth and oxidation by altering the available particle surface area for surface reactions. Therefore, there exists an intimate coupling between soot particle dynamics and soot kinetics. The pioneering studies of CB by Medalia and Heckman [35] and flame-generated soot by Dobbins and Megaridis [36,37], established that CB and soot particles are complex fractal-like aggregates formed by nearly spherical and polydisperse primary particles. Such complex morphology of soot and CB particles has profound implications to their physical, chemical, and optical properties and cannot be represented by a simple equivalent sphere. Indeed, a soot or CB fractal aggregate has a fairly open structure with a much higher surface area than its volume-equivalent sphere representation. A schematic illustrating the different interactions with gas molecules and photons between a fractal aggregate and its volume-equivalent sphere is shown in Fig. 2. The lower panel of Fig. 2 lists several areas that are directly affected by the particle morphology.

Traditionally, the soot volume fractions in flames and soot mass concentrations in the exhaust of combustion systems are the quantities of interest. To further reduce particulate matter (PM) emissions from the transportation section, the particle number (PN) emissions (for particles larger than 23 nm) have been regulated in Europe and China since 2013 and 2020, respectively, initially for emissions from passenger cars and later for light-duty vehicles. Regulations on PN emissions have led to

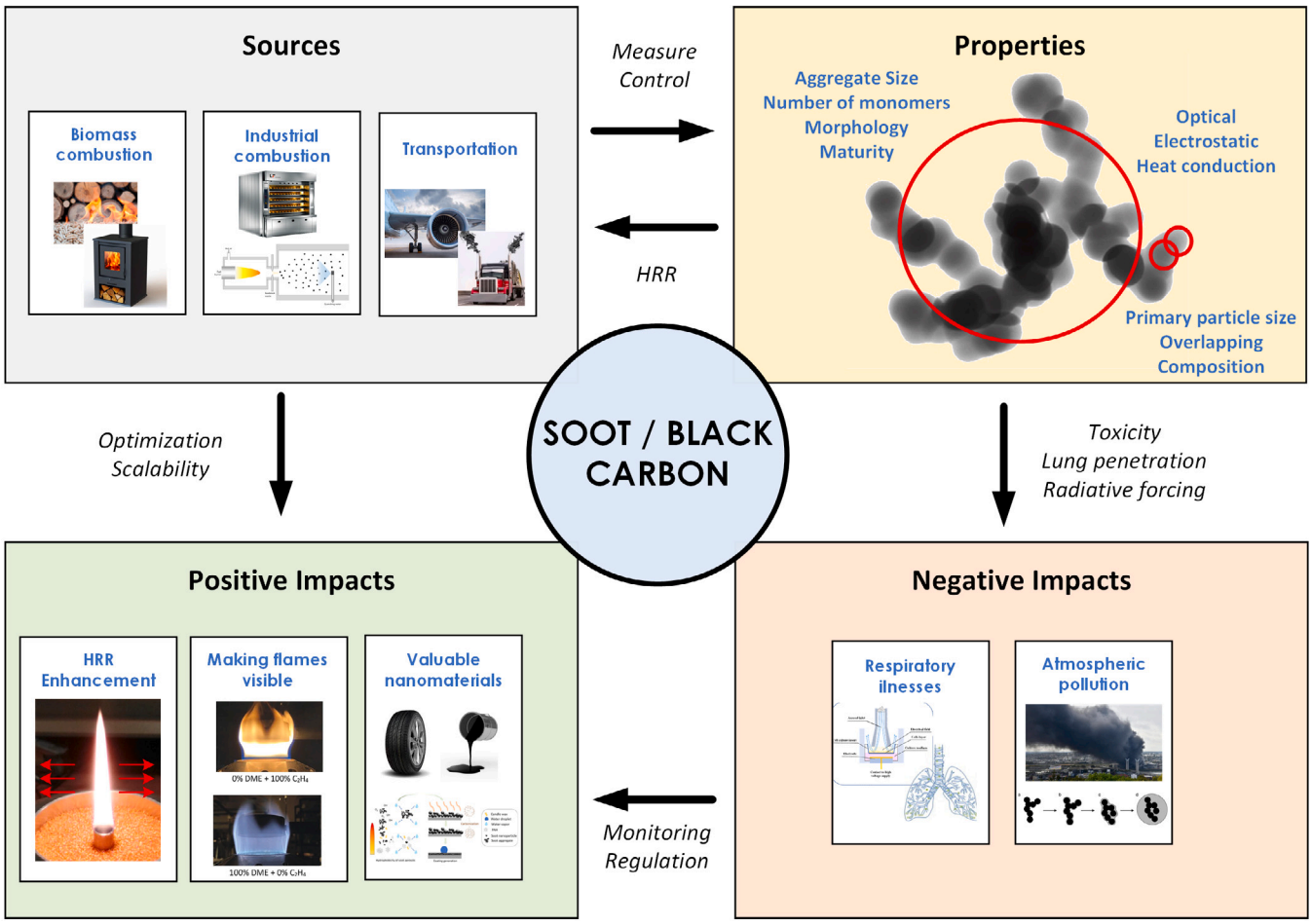


**Fig. 1.** Main sources of anthropogenic soot and carbon black, soot particle morphology and properties, and their positive and negative impacts. HRR represents heat release rate. *Source:* Adapted from different sources from the literature including flame synthesis of nanomaterials [15,16], changing flame visibility [17], toxicology [18], atmospheric pollution [19], biomass and industrial combustion [20].

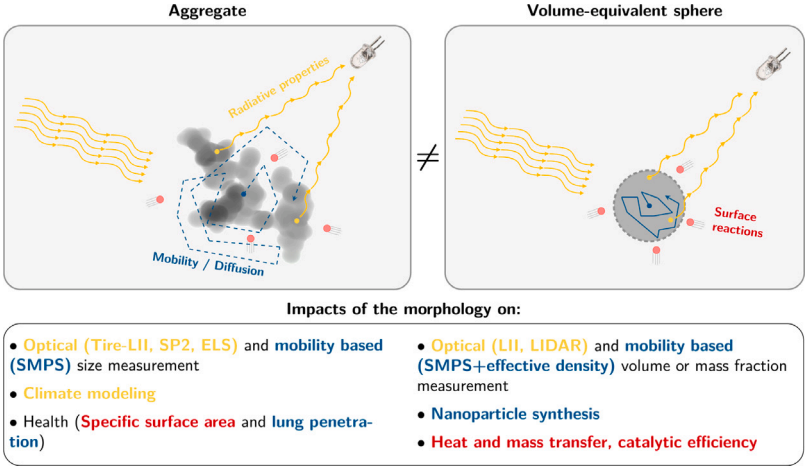


**Fig. 2.** Schematic illustrating the interactions of a soot aggregate and its volume-equivalent spherical particle with gas molecules (red dots) and photons (yellow waves). The blue curves indicate the particle mean free path (trajectories of the particle center of mass) related to its mobility/diffusion and the longer dashed blue lines than the shorter solid blue lines imply that the fractal aggregate has a higher mobility than its spherical counterpart. Correctly predicting the detailed soot particle morphology has significant impact on different applications listed in the lower panel, color-coded according to the figure. Tire-LII stands for time-resolved laser-induced incandescence, SP2 for single particle soot photometer, ELS for elastic light scattering, and SMPS for scanning mobility particle sizer.

increased attention on ultrafine particles (diameters below 100 nm), as these particles typically dominate PN emissions despite contributing only marginally to total particle mass. This shift in focus contrasts with earlier regulations that primarily targeted particulate mass, overlooking the possible high number concentration and small sizes of emitted particulate matter, and their potential impact on human health. The regulations on PN emissions indicate that more attention is paid to ultrafine particles below 100 nm, since they dominate PN emissions but

contribute only slightly to particle mass. Increasing research attention has been paid to developing modeling capabilities in the last two decades to predict the soot particle size and morphology due to their important impact on the properties of soot, such as toxicity, mobility diameter, collision diameter, surface area, and absorption and scattering cross sections. The increasingly more stringent emission standards further motivate the development of more accurate and more capable models to predict not only soot volume fraction, but also the size, morphology, and number density in flames and combustion devices.

As mentioned above, soot size and its morphology are governed by kinetics and particle dynamics. While the former deals with chemistry of soot formation, namely soot inception and surface reactions with gaseous species for surface growth and oxidation, the latter concerns all the particle interactions affecting the size and morphology of soot particles. The evolution of polydisperse size distributions of both primary particles and aggregate of soot particles is described by the integro-differential Smoluchowski equation, which is commonly known as the population balance equation (PBE) [38–40]. The history and derivations of PBE have been reviewed by Rigopoulos [39] and Solsvik and Jakobsen [40]. PBE has been generalized to take into account various physical and chemical processes that affect particle size distribution (PSD), such as inception, surface growth, oxidation, coalescence, agglomeration, and fragmentation. In addition, the PBE has been widely used to model particle dynamics in many fields of science and engineering, including but not limited to crystallization, carbon black synthesis, flame synthesis of nanoparticles, soot, atmospheric aerosol, and separation. It is important to point out that PBE is a macroscopic equation used to describe the evolution of size distribution of a system containing a large number of polydispersed particles. Therefore, population balance modeling typically does not deal with the evolution of individual particles and consequently cannot be used to predict the morphology of individual particles. On the contrary, population balance modeling relies on assumptions of certain aspects of particle morphology to predict soot aggregate size distribution. For example, it is necessary to assume the soot aggregate fractal dimension to calculate the collision rate between soot particles [41–43].

In the context of modeling soot formation in flames, PBE has often been coupled with soot kinetic models through the method of moments (MOM) [39,44–46] or sectional methods (SM) [42,43,47–49]. In MOM, the PBE is reformulated into a small number (typically about 5 to 10) of transport equations of the moments of the PSD required to determine the physical quantities of interest, such as soot particle number density and volume fraction, or to evaluate the rates of various physical and chemical processes involved in soot formation and particle dynamics, such as soot particle collision, inception, and surface growth. The main advantage of MOM is its high computational efficiency since only few transport equations of moments are to be solved to deal with soot particle dynamics. However, MOM requires a closure to relate the higher-order to lower-order moments, and are in general unable to provide the PSD, except in situations where the PSD can be assumed to follow a specific mathematical expression. Nonetheless, recent approaches have partially overcome this limitation by integrating moment methods with reconstructive techniques that approximate the full PSD. For example, Salenbauch et al. [50] used superimposed kernel density functions, Ferraro et al. [51] applied a similar strategy in turbulent conditions, and Wu et al. [52] employed joint moment projection and maximum entropy reconstruction to capture bimodal distributions in diesel engines. In essence, the goal of the MOM is to predict the moments of PSD in flames without explicitly tracking the PSD, since the moments are often the physical quantities of interest. In this context, Frenklach [53] formulated governing equations for moments of the discrete soot size distribution, with Frenklach and Harris [54] later applying these to pure coagulation and combined nucleation, coagulation, and growth cases. Their MOM with polynomial interpolation closure (MOMIC) led to modeling soot under various conditions, including premixed flames at low and high pressures and the transition from coalescent to aggregation growth [55–59]. Alternative closures, such as QMOM [60] and DQMOM [61,62], were later introduced. Mueller et al. [63] combined MOMIC and DQMOM in an Hybrid MOM (HMOM), adding a delta function for small incipient particles. For a more detailed overview, the reader is referred to the review of Rigopoulos [64] and Section 4 of this work.

In sectional methods, the entire range of particle mass or volume relevant to the particle system of interest is divided into a number of discrete bins or sections. Then, transport equations of particle number density in each section are solved to provide the discrete PSD. Two main approaches have been employed for implementing sectional methods in soot modeling. In the first, the soot particle population is treated separately from the gas-phase chemistry, with incipient particles introduced via PAH collisions, and the coupling to the gas phase occurring primarily through these nucleation steps. For example, Colket and Hall [65] applied such a strategy to laminar premixed flames, incorporating inception, surface growth, and particle coalescence. Smooke et al. [66] further refined this approach to model laminar coflow diffusion flames. Park and Rogak [67] then mitigated the substantial numerical diffusion inherent in fixed-sectional methods [68], and integrated these models into general kinetic packages such as Chemkin [47]. In the second approach, soot is represented as a series of pseudo-gas species integrated directly within the chemical kinetic mechanism. Richter et al. [69] extended the concept of PAH-based soot growth to include “bins” of species spanning from large PAHs (up to 3200 amu) to soot-like molecules (treated as pseudo-gas species, starting from 3201 amu). D’Anna and Kent subsequently employed this representation to develop skeletal soot production mechanisms that accounted for inception, surface growth, coagulation, and oxidation [70], and they demonstrated successful applications to both non-premixed [71] and premixed [72] flames. Sirignano et al. [73] built upon this integrated framework to include dehydrogenation pathways to capture soot graphitization, and $O_2$-induced fragmentation. These fully coupled sectional approaches have also been applied to unsteady counterflow flames [74], turbulent flames [75], and implemented within the OpenSMOKE++ simulation environment [76]. The sectional methods (SMs) are in general significantly more computationally demanding than MOM. In addition, the fixed sectional method suffers substantial numerical diffusion [68]. To take into account the fractal-like structure of soot aggregates, quasi-bivariate MOM and SM, which consider polydisperse aggregate size but monodisperse primary particle size, have often been employed to model soot particle dynamics in sooting flames. Although these macroscopic quasi-bivariate methods are able to predict the aggregate size distribution and the mean primary particle size, they cannot derive the primary particle size distribution, the degree of primary particle overlapping, or the aggregate fractal dimension. Therefore, they are unable to predict the detailed morphology of soot particles.

Based on transmission electron microscope (TEM) images, it has been established that both soot and CB particles form fractal-like aggregates. These aggregates consist of polydisperse and nearly spherical primary particles that exhibit a certain degree of overlap and necking [37,77]. These morphological features have been found to be the result of complex interactions between soot kinetics and soot dynamics. Simulation using detailed particle models has shown that the high sphericity of primary particles is due to the simultaneous aggregation with incipient soot and surface growth [31,32], whereas the overlap/neck between neighboring primary particles in soot aggregates is attributed to particle coagulation in the presence of surface growth [31,33,34,78]. The morphological details of soot particles have significant impact on their optical and physical properties, as well as the specific surface area of soot particles. Detailed morphology of soot particles is required to accurately predict their radiative properties [79–81] and other physical properties, such as heat conduction rate and drag [82–84]. The complex morphology of soot particles poses

challenges in accurately modeling particle dynamics and resolving morphological details. This complexity is characterized by polydispersity in the size of both primary particles and their aggregates, overlap among neighboring primary particles, and variations in the number of spheres in contact (coordination number) or the presence of necking at the contact regions between primary particles. To accurately predict the detailed morphology of individual soot particles, a comprehensive understanding is necessary. This includes the mechanisms controlling soot particle agglomeration/aggregation in the presence of inception, surface growth, oxidation, and oxidation-induced particle fragmentation. These processes vary across different flow and aggregation regimes, which are characterized by factors such as Knudsen numbers, residence time, and soot particle concentration. Additionally, it is necessary to employ a detailed particle model that explicitly tracks the evolution of individual particles. Physics-based particle models track the motion, coagulation, and mass transfer with gas-phase species (surface growth and oxidation) of individual particles, including both primary particles and agglomerates/aggregates, by commonly solving the Langevin equations. These particle models are known as discrete element methods (DEMs) and include the extensively studied diffusion-limited, ballistic-limited, and reaction-limited cluster-cluster aggregation (DLCA, BLCA, RLCA) [85–87]. Meso-scale methods typically resolve physical domains on the order of few hundreds of nanometers and track particles ranging from the constituent primary particles of several nanometers to fairly large aggregates consisting of a few hundreds of primary particles. Meso-scale particle methods, however, do not describe the soot inception process, i.e., the transition from gaseous precursor species to condensed phase particles, and rely on a soot inception model to provide the incipient soot particles, or assume a known size distribution of primary particles to initiate the particle dynamics. Although soot inception has often been modeled as a result of collision among assumed PAH (polycyclic aromatic hydrocarbons) precursor species, molecular dynamics (MD) simulations are able to describe the details of soot inception, e.g. [88], a topic that is beyond the scope of this review. This review concerns mainly the meso- and macro-scale particle dynamics methods.

Two types of method have been developed to numerically generate soot aggregates to study their optical and physical properties: tunable algorithms and physics-based particle models. Tunable algorithms include the early cluster-particle aggregation and cluster-cluster aggregation algorithms of monodisperse spherical primary particles including FLAGE [82,89], and more recently developed FracVAL [90] algorithm for polydisperse primary particles. These methods were developed to generate fractal aggregates of specified parameters, i.e., primary particle diameter, number of primary particles, fractal dimension, and fractal prefactor, regardless of the mechanisms leading to such agglomerates. These methods only generate fractal aggregates formed by either monodisperse or polydisperse spherical primary particles in point-contact. Realistic aspects of soot particles observed in TEM images, namely primary particle overlapping and necking, can be added to the numerically generated fractal aggregates in a post-processing manner [79,83,91,92]. Physics-based particle models include the EDEM (Event Driven Discrete Element Method) [33,93,94], the DEM-based Monte Carlo model termed MCAC (Monte Carlo aggregation code) [95,96], and the detailed population balance model (DPBM) [97–99]. These physics-based methods are capable of generating realistic soot aggregates formed by polydisperse primary particles with certain degree of overlapping without making assumptions with regard to the morphology of soot aggregates.

### 1.2. Aims and scope

Considerable effort has been devoted to develop increasingly more capable and accurate methods to predict particle size distribution and detailed particle morphology at both macro- and meso-scales over the last three decades. Several recent reviews have appeared to summarize the progress in different aspects of particle dynamics modeling. Singh et al. [100] discussed the numerical methods for solving the PBE with a focus on the finite volume method, Monte Carlo (MC) method, and the sectional method. Rigopoulos [39] discussed the strengths and weaknesses of two methodologies for dealing with polydisperse particles in reacting flows. One method involves the Lagrangian tracking of individual particles, while the other employs a statistical description of a particle system in the form of a PBE, which describes the evolution of the particle size distribution function. Although the focus was on the development and application of PBE-based methods, these are used for modeling reacting flows involving particles, such as soot, flame synthesis of nanoparticles, droplet combustion, and coal flames. An in-depth discussion was devoted to the development and solution methods of PBE as well as various closure issues in modeling particle dynamics in turbulent flows. More recently, Rigopoulos [64] reviewed the progress and challenges in modeling soot aerosol dynamics in turbulent flows. The review discussed available soot kinetic models, different methods to deal with soot aerosol dynamics, such as Monte Carlo methods, method of moments, and discretization methods, and the closure problem of soot modeling in turbulent flows. In particular, the focus of Rigopoulos [64] was placed on closure of various terms arisen from turbulence-soot interactions in Reynolds-averaged Navier–Stokes (RANS) modeling or sub-grid modeling in large-eddy simulation (LES). Turbulence affects soot through both soot kinetics (inception, surface growth, and oxidation) and aerosol dynamics. Endres et al. [101] provided a comprehensive review of models describing the contact forces between nanoparticles within the context of discrete element modeling of aggregation, agglomeration, and film formation. However, the review of Endres et al. did not focus on specific aerosol applications. Li et al. [102] discussed soot models of different length scales. The authors considered the one- and two-equation soot models as macro-scale, PBE-based soot models as meso-scale, and DEM and molecular dynamics (MD) based soot models as microscale. Additionally, dedicated reviews involving reactive MD for combustion systems can be found elsewhere [103]. It is worth pointing out that the multi-scale modeling of soot aggregation to be discussed in the present review differs significantly from the review of Li et al. [102] in terms of both contents and classification of methods. The focus of our review is on soot particle dynamics modeling and we regard PBE based methods, namely MOM and sectional methods, DEM, and MD as macro-scale, meso-scale, and microscope methods, respectively, as illustrated in Fig. 3. This classification of particle methods of different scales is consistent with Buesser and Pratsinis [104], who reviewed multiscale tools for the design of aerosol reactors and processes for the synthesis of nanomaterials. Methods of multiscale consist of macro-scale, meso-scale, molecular dynamics, and quantum mechanics models that span 10 and 15 orders of magnitude in length and time, respectively. Buesser and Pratsinis [104] discussed the inter-dependence of these multiscale methods and emphasized the dominant role of coagulation in nanoparticle growth due to high particle number concentration in such aerosol processes. Eggersdorfer and Pratsinis [105] provided an excellent overview of applications, characterization, and formation of agglomerates and aggregates formed by spherical primary particles. The focus of the review of Eggersdorfer and Pratsinis [105] was on collision between fractal-like agglomerates and the important role of sintering on aggregate formation for non-soot nanoparticles, though the effect of surface growth on soot aggregation was also briefly discussed. More recently, Boje and Kraft reviewed stochastic population balance methods developed in the last two decades for detailed modeling of aerosol particles produced in flames [99]. This type of methods, also termed detailed population balance modeling approach or high-dimension particle models, is able to predict the complex shape of particles, such as fractal aggregates formed by polydisperse primary particles with overlapping, by introducing detailed particle type space models to track the compositions, size, and the relative positions of primary particles. The focus of the review of Boje and Kraft [99] was

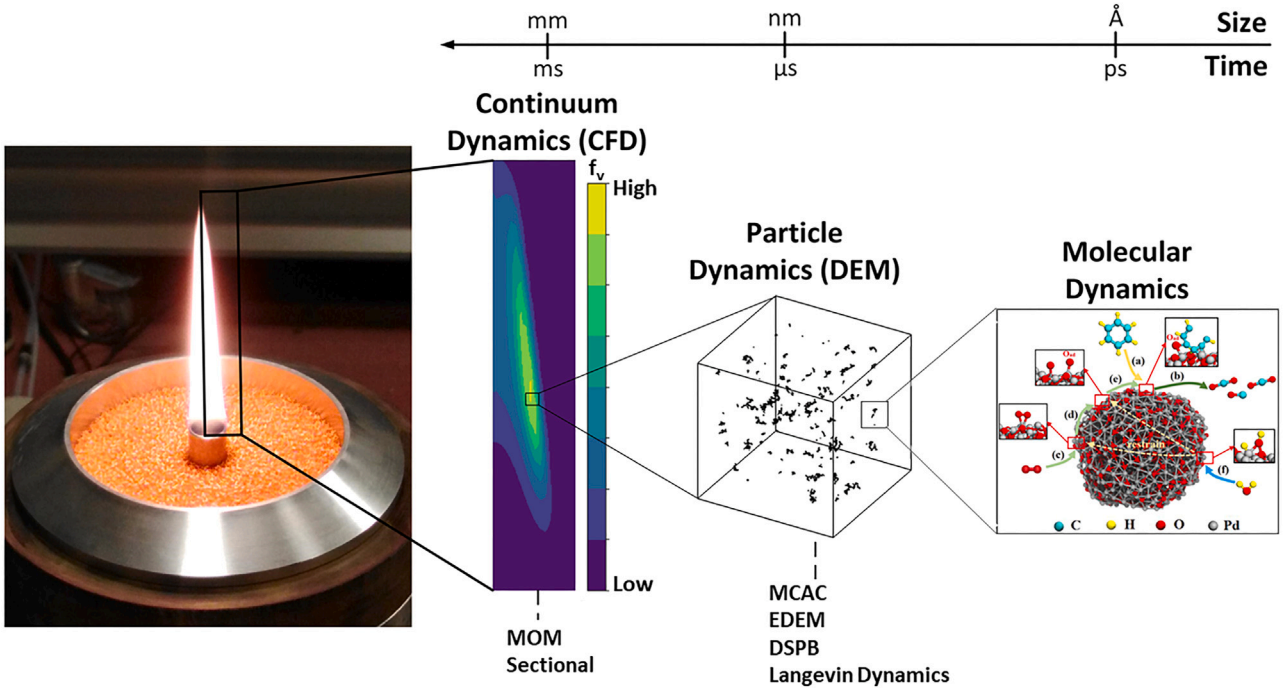


**Fig. 3.** Multi-scale simulations of soot particle formation in flames. The laminar coflow diffusion flame is modeled using macro-scale methods (left part) for solving gas-phase conservation equations. The PBE (population balance equation) has often been solved using MOM or the sectional method. The solution domain of macro-scale modeling is on the order of the actual flame size. Meso-scale methods, namely MCAC (Monte Carlo aggregation code), EDEM (event-driven discrete element method), DSPB (detailed stochastic population balance) models, and Langevin dynamics (middle part), are used to investigate the coagulational behavior and detailed morphology of individual soot particles. The solution domain of meso-scale simulations is on the order of few to few tens of nm. MD simulations are used to study certain particle properties at the molecular level. MD can resolve individual atoms in a system of the order of a few nm (right part). The length and time scales of multi-scale simulations are shown at the top of the plot.
*Source:* Molecular Dynamics figure is reproduced from [106].

the development, implementation, and application of detailed stochastic particle modeling. These recent reviews focused on different aspects of particle dynamics. However, none of the above-mentioned reviews provided a broad overview of soot particle dynamics and an in-depth view of recent progress in discrete element methods applied to soot particle agglomeration in the presence of surface growth.

In this article, we intend to provide a detailed review of recent progress in modeling soot aggregation in laminar sooting flames. The review covers both macroscopic and meso-scale approaches of particle dynamics, and the focus is placed on the recent development of discrete element modeling of fractal agglomerates and its applications to model detailed morphology of individual soot particles in the presence of surface growth under conditions relevant to laminar sooting flames.

## 2. Morphology and properties of fractal aggregates

As explained in the introduction, the main challenge in multi-scale modeling of soot is to take into account its complex morphology, which affects its physical, chemical and optical properties. As illustrated in Fig. 2, the mobility of a fractal cluster is indeed very different from that of its volume-equivalent spherical counterpart, which has, as an example, an impact on aggregation and therefore on size. Similarly, the specific surface area of the fractal object is significantly higher than the spherical particle, strongly affecting surface-based processes, such as surface growth.

In this regard, meso-scale methods have provided detailed descriptions of the soot fractal-like morphology, facilitating the monitoring of soot emissions, as well as the characterization of the soot climate and health effects. For example, the soot agglomerate morphology derived by DEM can assist the robust monitoring of soot emissions. Also, a DEM-derived power law for the effective density of soot, $\rho_{\text{eff}}$, was recently interfaced with scanning mobility particle sizer (SMPS) measurements to assist the accurate monitoring of the soot volume fraction, $f_v$, in flame reactors and combustion engines. The soot $f_v$ is a key property for combustion models as it is essential to close the soot mass balance [107,108]. Such models are often benchmarked with soot $f_v$ data obtained by SMPS assuming spheres. Neglecting the aggregate and agglomerate structure of soot results in an overestimation of the true soot $f_v$ obtained directly by aerosol particle mass analyzer (APM) by up to a factor of 4 [109]. So, the DEM-derived power law for soot $\rho_{\text{eff}}$ enabled the accurate monitoring of soot $f_v$ by SMPS, assisting combustion models to close their mass balance [109]. Oversimplifications regarding the morphology of soot are made often by toxicologists to determine its lung deposition. In particular, computational algorithms, such as the multi-path particle dosimetry model [110], are used to estimate the mass of soot nanoparticles deposited at different regions of the respiratory system using the bulk density $\rho_b$ instead of $\rho_{\text{eff}}$. The inhaled doses estimated that way are used in in-vitro cell studies to determine various health effects of soot nanoparticles. However, neglecting the realistic soot agglomerate structure and $\rho_{\text{eff}}$ overestimates its lung deposited mass by a factor of about two [111]. Therefore, accounting for the ramified structure of soot is essential to determine accurately its impact on public health. The morphology of soot nanoparticles affects also their optical properties that are essential to estimate their direct climate impact. The light scattering and absorption by soot agglomerates are quantified by their mass scattering (MSC) and absorption (MAC) cross-sections. These are the equivalent cross-sections of spheres exhibiting the same light scattering and absorption with the soot agglomerates normalized by their mass. The soot light scattering and absorption can be estimated by interfacing agglomerates simulated by EDEM or MCAC with discrete dipole approximation (DDA) [112]. The soot optical properties derived by DEM-DDA accounting for its realistic structure are in excellent agreement with light scattering and absorption measurements of soot from premixed, diffusion flames and combustion engines [113]. Most importantly, the global distribution of the direct radiative forcing (RF) induced by soot agglomerates was

obtained by interfacing a climate model with the MAC derived by DEM-DDA. That way, it was shown that accounting for the realistic soot morphology increases its direct RF globally by 25–50%, explaining nicely the satellite observations [114]. For these reasons, this section aims to describe the morphology of soot aggregates and define the main size and morphological parameters involved in different physical processes.

The advent of electron microscope in the 1930s was seminal for the study of aerosols. In the 1950s, some studies proposed to quantify the shape of observed particles by introducing shape factors and the projected surface area or perimeter length [115,116]. Up to now, transmission electron microscope (TEM) image analysis remains the most direct way to determine the primary particle diameter of soot ($D_p$), and significant progress has been achieved to improve the exploitation of TEM images for more efficient and accurate recognition and reconstruction of primary particle size distribution and aggregate morphology [36,117–119]. It is also the most direct way to determine the degree of overlapping between adjacent primary spheres as quantified by the overlapping coefficient [92]. Nevertheless, the access to other 3D quantities has to take into account the fact that the aggregate projection on TEM images is two-dimensional. Therefore, some 3D-2D conversion correlations have been developed [37,120,121]. For example, Köylü et al. have determined a relationship between 2D and 3D radii of gyration for DLCA aggregates [122]. The radius of gyration is defined as the radius of a sphere with the same inertia as the particle under consideration. It is particularly important for the interaction between light and particles in the Rayleigh regime [123]. It can be calculated as the square root of the average of summation over all primary spheres of the squared distance between their center and the aggregate center of mass. For numerically generated aggregates, this can be done in 3D with the knowledge of the positions of primary spheres in 3D space. For real (2D) TEM images, this can be done by identifying the positions of the primary spheres in the projected image. Köylü observed that the 3D radius of gyration was 1.24 times that of the 2D one, regardless of the aggregate size characterized by the number of primary particles.

Although 3D reconstruction of electron tomography has been employed to investigate detailed morphology of flame-generated soot particles [124–127], this process is significantly more time-consuming than the conventional TEM image analysis and therefore has rarely been used.

### 2.1. Fractal scaling law and population based fractal parameters

On the basis of established correlations relating the aggregate projected area to the number of primary spheres in the aggregate $N_p$ and those relating the 2D gyration radius or the maximum projected length to the 3D gyration radius $R_g$ [128], a widely accepted power-law called the fractal scaling law has been empirically established [37]:

$$N_p = k_{fp}\left(\frac{2R_g}{D_p}\right)^{D_{fp}}, \tag{1}$$

where $D_p$ is the primary sphere diameter. This scaling law is extremely useful since it relates the particle mass to its size and parametrizes key morphological parameters (see Fig. 4). The origin of this power-law stems from the quasi self-similar process of agglomeration. Correspondingly, two parameters $k_{fp}$ and $D_{fp}$, called respectively the fractal prefactor and fractal dimension, began to appear in the literature. The values of those parameters for soot are between 1 and 3 for $k_{fp}$ and between 1.6 and 2 for $D_{fp}$. By nature, $D_{fp}$ is related to the particle structural compactness since $D_{fp} = 1$ refers to a line shape whereas $D_{fp} = 3$ corresponds to spheres. On the other hand, $k_{fp}$ , among others, is related to a local compactness. The overlapping between primary spheres, the presence of necking at the contact region, and the coordination number (the average number of connection between neighboring primary particles) can affect these parameters. Nevertheless, because the fractal law is based on $R_g$, $k_{fp}$ also depends on the particle size [129], anisotropy [130], and even the fractal dimension itself [131]. The determination of $k_{fp}$ and $D_{fp}$ for a population of particles consists in simply fitting $N_p$ as a function of $2R_g/D_p$ on log–log scale by an affine function. As such, $D_{fp}$ equals to the slope of the plot and $k_{fp}$ is related to the intercept. It is noticed that each data point on this plot represents a particular aggregate, thus, a large number of aggregates are required to obtain statistically meaningful $D_{fp}$ and $k_{fp}$. Therefore, the resultant $D_{fp}$ is statistical and represents the population-based fractal dimension (as implied by the subscript $p$ in $D_{fp}$). Experimentally determined fractal parameters using TEM image analysis and light scattering methods are population-based. The analysis of TEM images commonly relies on the correlation given in Eq. (2), originally proposed by Medalia [116], between the number of primary particles in the aggregate and the ratio of the projected area ($A_a$) of the aggregate and the cross section area of primary particle ($A_p$):

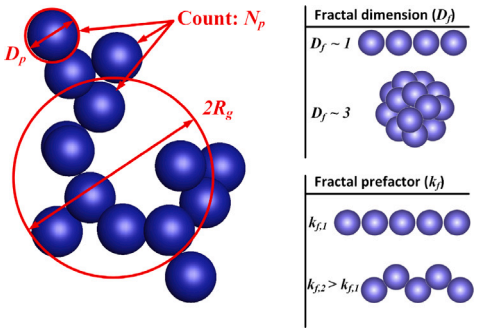


**Fig. 4.** The properties of a soot aggregate in the fractal-law.

$$N_p = k_\alpha\left(\frac{A_a}{A_p}\right)^{\alpha}, \tag{2}$$

where $\alpha$ and $k_\alpha$ are empirical constants. These population-based approaches do not allow to describe adequately the morphology of individual particles, which may become necessary to better evaluate the morphology, specific surface area, radiative properties, or any other properties of individual particles. Autocorrelation of binarized images or the application of box-counting methods [132] can provide morphological information of individual particles. Nevertheless, with the exception of rare studies that have analyzed the 3D morphological properties of soot reconstructed by electron microscopy tomography [133], the analysis has generally been performed on projected 2D images with some loss of information, particularly if the individual fractal dimension is greater than 2. For these reasons, it is necessary to develop modeling capabilities that are able to resolve the 3D morphology of individual particles from meso-scale modeling or to improve algorithms of tomographic reconstruction based on 3D TEM imaging. The importance of modeling the morphology of individual soot particles is further discussed at the beginning of Section 5.

### 2.2. Pair-correlation and individual particle fractal dimension

One of the most powerful methods to describe the morphology of an individual fractal-like aggregate is through the analysis of its pair-correlation function. The latter can be evaluated in two different ways, namely, (1) the number-based pair correlation $A_N(r)$, and (2) the volume-based pair correlation $A_V(r)$. $A_N(r)$ represents the probability of finding a given number of primary particles at a given distance $r$ from the center of any primary particle belonging to an aggregate [82,131,134]. Similarly, $A_V(r)$ indicates the probability of finding material from any point belonging to the aggregate. $A_N(r)$ has been commonly used in different disciplines, such as physics, chemistry, and material science, to describe the geometry of molecules, crystals, and polymers. However, $A_N(r)$ may not be well suited for certain nanoparticles, such

as those generated in flames, because we cannot neglect the primary particle volume. We also focus on $A_V(r)$ since it is more adapted to the description of aggregates whose primary particles are not in point-contact, making the definition of the number of primary particles less obvious than for agglomerates formed by point-contact primary particles, i.e., without overlapping. Moreover, the volume approach can easily account for primary particle polydispersity [90]. The zeroth moment of the isotropic pair correlation function $A_V(r)$ is directly related to the total volume of the aggregate $V_{\text{agg}}$ as:

$$A_V(r) = V_{\text{agg}} \frac{dV_{\text{agg}}}{4\pi r^2 dr}, \qquad \int_{r=0}^{\infty} A_V(r) 4\pi r^2 \, dr = V_{\text{agg}}^2. \tag{3}$$

The ratio of the fourth and second moments gives the squared radius of gyration of the aggregate, which is used in the fractal law shown in Eq. (1). $A_V(r)$ is also directly related to the radiative properties of agglomerates since the angular distribution of scattered light by a particle is proportional to the Fourier transform of $A_V(r)$ [135]. Moreover, it also plays an important role in physical phenomena involving interactions (or coupling) between primary particles. For example, the van der Waals (vdW) interaction forces between agglomerates can be modeled based on the pair-correlation function [136,137]. The pair-correlation function has also been used to determine the hydrodynamic interactions of primary particles in the continuum flow regime (Stokes) based on the Kirkwood-Riseman theory [138,139].

For idealized large fractal agglomerates, when the pair-correlation is averaged over many orientations of the agglomerate, one can find the following scaling-law $A_V(r) \propto r^{D_{fi}-3}$, where $D_{fi}$ is the fractal dimension of the individual agglomerate studied. This scaling-law is only observed for intermediate scales between $r \gg R_p$ (referred to as small scale) and $r \ll 2R_{\max}$ (referred to as the large scale) where $R_{\max}$ is the half of the maximum distance between primary particles in an agglomerate. A more general model for the volume-based pair correlation function was recently proposed for fractal agglomerates by considering primary particle polydispersity as well as cutoff functions at the referred small and large scales [129],

$$A_V(r) = A_{\text{pp}}(r) + A_{\text{agg}}(r) \tag{4a}$$

$$A_{\text{pp}}(r) = \sum_{i=1}^{N_p} V_{p,i} \left(1 + \frac{r}{4R_{p,i}}\right) \left(1 - \frac{r}{2R_{p,i}}\right)^2, \qquad r \in [0, 2R_{p,i}] \tag{4b}$$

$$A_{\text{agg}}(r) = \frac{\varphi D_{fi}}{3} \left(\frac{r}{R_v}\right)^{D_{fi}-3} \left[\exp\left(-(r/\xi_{\max})^{\beta}\right) + \exp\left(-(r/\xi)^{\beta}\right)\right], \qquad r > 0 \tag{4c}$$

where the subscripts pp and agg refers to primary particle and aggregate, $R_{p,i}$ and $V_{p,i}$ are respectively the $i$th primary particle radius and volume, $R_v$ is the volume equivalent primary sphere radius, $\xi$ and $\xi_{\max}$ are characteristic lengths of the agglomerate, $\beta$ is the stretching exponent, and $\varphi$ is the packing factor which quantifies the local compactness. The greater the stretching exponent $\beta$, the greater the decrease in the pair correlation function for a given radius. This means that the probability of finding material falls rapidly towards zero at that radius, as does a sphere. The more anisotropic the particle, the less the decrease in pair correlation, corresponding to lower values of $\beta$. Heinson et al. [130] have shown a correlation between this parameter and the aggregate anisotropy defined as the ratio between the largest and smaller eigenvalues of the particle's inertia matrix. They also found a correlation with the population based fractal prefactor $k_{fp}$. For a given aggregate size $R_g$, primary particle $D_p$ and fractal dimension $D_{fp}$, a larger $k_{fp}$ corresponds to a more massive aggregate (larger $N_p$). This means that locally, the number of spheres increases, for example by increasing the average number of primary spheres in contact, which is linked to a higher packing factor $\varphi$. We note here that some previous studies have preferred the parameter $f = 1/\varphi$ referred to as the filling factor [139]. The packing factor, which directly acts on the pair correlation function amplitude in the fractal domain, indicates the compactness of primary particles, i.e., how close primary particles are and the level of overlapping between them. Based on the proposed model, $k_{fp}$ can be determined after calculating the aggregate volume and radius of gyration, which shows that $k_{fp}$ also depends on the size parameter, making it less relevant from a physical point of view. Fig. 5 shows a graphical representation of this model and its different parameters.

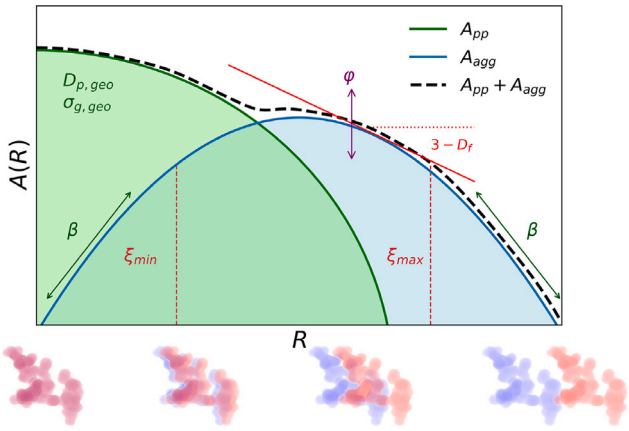


**Fig. 5.** Properties of the volume-based pair-correlation function. *Source:* Adapted from [129].

The model given by Eqs. ((4)a-c) is valid for all radial distances $r > 0$ and can be used to model aggregates of any size down to an isolated primary particle where $A_{\text{agg}} = 0$ and $A(r) = A_{\text{pp}}$. Thereby, quantities $\varphi$, $D_{fi}$, $\xi_{\max}$, $R_{pv}$ and $\beta$ can be fitted to the numerical computation of volume-based pair correlation function of numerically generated aggregates, providing detailed and relevant morphological information [34].

### 2.3. Mobility-based description

As explained in the previous sections, the fractal dimension of agglomerates (based either on population or determined for individual particles) is one of the most important parameters to characterize structural compactness. Complementarily, the local compactness can be evaluated by the packing factor $\varphi$ or less directly by the fractal prefactor $k_f$. These descriptors are purely geometrical. Most of the time, they are derived from TEM image analysis or by light scattering experiments. Nevertheless, attempts have been made to express similar information based on mobility-based experiments. Indeed, a reference non-optical method to characterize aerosols is to make use of their electrical mobility diameter $D_m$. When exposed to an electric force, the charged particles quickly reach a terminal velocity in the surrounding gas. That terminal velocity is obtained when an equilibrium between the electric force $f_e = neE$ and the aerodynamic force $f_{agg} = \frac{3\pi\eta D_m}{C_c(D_m)} V_{rel}$ is reached and, therefore, for a given electric field, that terminal velocity depends on the particle size. In these expressions, $n$ is the number of elementary charges, $e$ the charge of a single particle, $E$ the external electric field, $\eta$ the dynamic viscosity, $C_c$ the Cunningham slip correction factor, and $V_{rel}$ the relative velocity. Thus, only particles having a specific size can reach the outlet of the column of a Differential Mobility Analyzer (DMA) after having been exposed to a given electric field. This specific size is defined by the particle's electrical mobility, $Z_e$, which is defined as the ratio of the terminal velocity and the corresponding electric field,

$$Z_e = \frac{neC_c(D_m)}{3\pi\eta D_m}. \tag{5}$$

In this expression, the particle is supposed to carry $n$ elementary charges $e$, to move in a fluid of dynamic viscosity $\eta$. It is characterized

by its mobility diameter $D_m$, and $C_c$ is the Cunningham slip factor that has been established in order to consider the change of flow regime for spheres. Therefore, if the particle is spherical, $D_m$ corresponds to the geometric diameter. If the particle is not spherical, the mobility diameter becomes difficult to interpret. It is important to notice that mobility diameter, contrary to the gyration radius, depends on the flow regime. Also, the electrical mobility $Z_e$ is found to be proportional to the particle diffusion coefficient $D$ since $Z_e = \frac{ne}{k_B T} D$ with $k_B$ the Boltzmann constant and $T$ the temperature.

#### 2.3.1. Flow regime and its impact on particle mobility

The interactions between aerosol particles and the molecules of surrounding gas, such as heat, mass, and momentum transfer, depend on the flow regime. The flow regime is characterized by the flow Knudsen number defined as the ratio of the mean-free-path of gas molecules $\lambda_g$ to the particle mobility radius $R_m$, $K_{n_f} = \lambda_g / R_m$ [140].

The mobility of a particle is related to its drag in the flow and hence depends on the flow regime. For $K_{n_f} > 10$, which is termed free-molecular regime, gas molecules move ballistically and nearly collisionlessly (between gas molecules) and the collision rate between gas molecules and the particle is the controlling factor determining the particle drag force. For $K_{n_f} < 0.01$, the momentum exchange between the particle and the surrounding gas molecules takes place in the continuum regime where the drag experienced by the particle is controlled by the gas viscosity. In the transition regime of intermediate flow Knudsen numbers, characterized by $0.1 < K_{n_f} < 10$, there are collisions among gas molecules and between gas molecules and the particle; the particle drag in these flow regimes depends on the flow Knudsen number and is determined by both the gas viscosity and the collision rate between gas molecules and the particle. For a given particle, the flow regime can vary with the temperature and pressure of the gaseous medium through their strong impact on the mean-free-path of the gas molecules. The mobility diameter of DLCA fractal agglomerates formed by monodisperse primary particles in different flow regimes has been reviewed by Sorensen [140].

#### 2.3.2. Mobility of fractal aggregates

When particles are not spherical, the dynamic shape factor can be used (if known) to interpret the mobility diameter. Indeed, the shape factor $\chi$ of a particle is defined as the ratio of the drag force on the particle divided by the drag force on the particle's volume equivalent sphere [141]. For soot aggregates, this parameter increases quite linearly with the mobility diameter to reach $\chi \approx 2$ for $D_m = 200$ nm [142], meaning that the actual aerodynamic force can be up to twice that of the equivalent sphere due to the larger surface exposed by the aggregate to the surrounding gas. Unfortunately, there is no theoretical approach to provide an analytical expression of the shape factor. For complex morphologies, this practical function has to be determined empirically or based on numerical simulations of drag forces.

Another way to express the morphological deviation from a sphere is to determine the particle's effective density defined as the particle mass $m$ divided by the volume of a sphere having the same mobility diameter, $\rho_{\text{eff}} = 6m/\pi D_m^3$. It is noted that unless otherwise explicitly indicated, all the primary particles are assumed to have the same physical and chemical properties throughout this review. The particle effective density can be measured by coupling a DMA and a mass spectrometer, such as a centrifugal particle mass analyzer (CPMA) or an APM. For spherical particles, such a measurement corresponds to the bulk density of particle material and is therefore independent of the particle diameter. For fractal aggregates, experiments establish a power-law decrease of $\rho_{\text{eff}}$ as a function of $D_m$ [143] taking the form $\rho_{\text{eff}} \propto D_m^{\alpha-3}$, where $\alpha$ is called scanning exponent. As for the shape factor, there is no theoretical approach enabling an analytical expression of the scaling exponent. The empirical observation of this power law suggests that mobility diameter, similar to the gyration radius, evolves in a power-law of the number of primary spheres. The same conclusion has been reached by Sorensen [140], who provided a review focusing on the link between the mobility diameter of a DLCA fractal agglomerate, i.e., for $D_{fp} = 1.78$ and $k_{fp} = 1.3$, and its number of primary spheres or the corresponding gyration radius. Sorensen concluded that in the continuum flow regime characterized by small Knudsen numbers ($K_n \ll 0.1$), the mobility diameter can be expressed as

$$D_m = D_p N_p^{0.46}, \quad N_p < 100 \tag{6a}$$

$$D_m = 0.65 D_p N_p^{0.56}, \quad N_p > 100, \tag{6b}$$

whereas in free-molecular regime (large Knudsen numbers, $K_n \gg 10$),

$$D_m = D_p N_p^{0.46}, \quad \text{for all } N_p \tag{7}$$

and in the slip regime (intermediate Knudsen numbers, $0.1 \le K_n \le 10$),

$$D_m = D_p N_p^{0.46}, \quad N_p < 100 \tag{8a}$$

$$D_m = D_p \times 10^{\left(-1.02 K_n^{0.043} + 0.92\right)} N_p^{0.51 K_n^{0.043}}, \quad N_p > 100. \tag{8b}$$

It is important to notice that the Knudsen number $K_n$ is based on the aggregate mobility diameter $K_n(D_m) = 2\lambda_g / D_m$ ($\lambda_g$ refers to the mean free-path of the surrounding gas molecules). A more detailed description of flow regimes is given in Section 2.3.1. It is also often considered in the literature that the mobility diameter in the free-molecular and transition flow regimes is related to the particle projected area $a_a$ [144–146],

$$D_m = 2\left(\frac{a_a}{\pi}\right)^{1/2}. \tag{9}$$

The projected area can be estimated based on Monte Carlo sampling and averaged over 5 random orientations of each aggregate/agglomerate [147]. The $D_m$ of EDEM-derived aggregates and agglomerates obtained using Eq. (9) can be related to their volume-area equivalent number, $N_{va}$, and diameter $D_{va}$ or the Sauter mean diameter, $D_{32}$, of the soot primary particles by [94] (note the slight change of $N_p$ exponent as compared to Eq. (7)):

$$D_m = D_{va} N_{va}^{0.45}. \tag{10}$$

For agglomerates containing monodisperse primary particles in point-contact, $N_{va} = N_p$ and $D_{va} = D_p$. Eq. (10) was derived by fitting the $D_m$ of EDEM-derived aggregates and agglomerates [94]. It should be noted that Eq. (10) is similar to the power law proposed by Sorensen [140] (Eq. (7)) for agglomerates in the free molecular regime. However, Eq. (10) has been derived for aggregates and agglomerates in both the free molecular and transition regimes. In addition, unlike Eq. (7) that is valid for monodisperse soot primary particles, Eq. (10) has been derived for polydisperse ones [94]. So, the difference between Eqs. (7) and (10) is based on physics. Eq. (10) has been validated with measurements of soot nanoparticles produced in premixed [81], diffusion [94], and spray [148] flames. Eq. (10) is also in excellent agreement with data from agglomerates of inorganic nanoparticles [149], including silica [150], zirconia [147], gold [151], and silver [152] nanoparticles.

By comparing the effective density measurements of different kinds of fractal aggregate, Yon et al. [153] proposed a semi-empirical model of the effective density,

$$\rho_{\text{eff}} = \rho_p \left(\frac{C_c(D_p)}{C_c(D_m)}\right)^{\alpha} \left(\frac{D_m}{D_p}\right)^{\alpha-3}. \tag{11}$$

The authors observed that the scaling exponent $\alpha$ deviates further from $D_{fp}$ as the Knudsen number based on the primary particle $K_n(D_p) = 2\lambda_g / D_p$ increases. The scaling exponent can be estimated as:

$$\alpha = \frac{D_{fp}}{1.378}\left[\frac{1}{2} + \frac{1}{2}\text{erf}\left(\frac{K_n(D_p) + 4.454}{10.628}\right)\right]^{-1}. \tag{12}$$

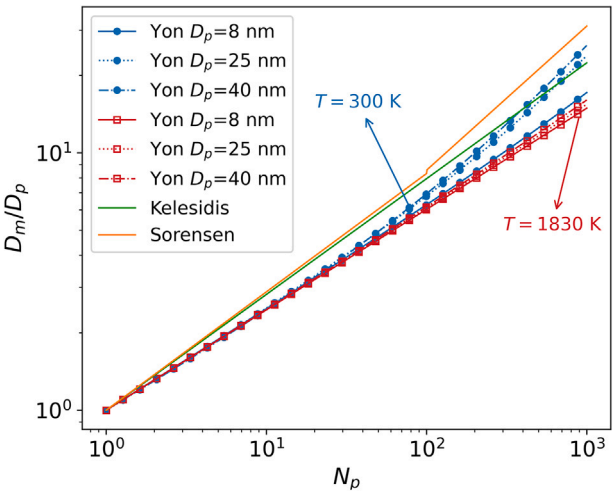


**Fig. 6.** Ratios of the mobility diameter to primary particle diameter as a function of $N_p$ from the models of Sorensen, Kelesidis et al. and Yon et al. The comparison is done at two temperatures (300 K in blue and 1830 K in red) for the model of Yon et al. and for different primary sphere diameters. The models of Sorensen and Kelesidis et al. are not temperature dependent..

From this last study [153], the mobility diameter of a fractal aggregate, and therefore its aerodynamic force, can be expressed as a function of the number of primary particles regardless of the flow regime and the primary sphere diameter,

$$D_m = D_p \frac{C_c(D_m)}{C_c(D_p)} N_p^{1/\alpha}. \tag{13}$$

Eqs. (12) and (13) derived from the semi-empirical Eq. (11) have been adjusted based on experimental measurements. The authors considered polydisperse primary particles by imposing the mean $D_p$ in Eqs. (11)–(13) to be the mass equivalent diameter ($\sqrt[3]{\overline{D_p^3}}$) [153]. This expression has been found in good accordance with Eq. (6) and (7) for asymptotic regimes and was implemented in MCAC [95]. Nevertheless, it is important to point out that the use of Eqs. (10) and (13) can produce different results. Indeed, Fig. 6 compares both models as well as Sorensen's expressions (Eq. (6)) by plotting the mobility diameter divided by the primary sphere diameter as a function of the number of primary spheres per aggregate. Because the model of Yon et al. depends on both the flow regime and $D_p$, we report the comparison for different typical values of temperature and $D_p$, including ambient temperature, as in the case of SMPS measurements for example, and also at a typical flame temperature of 1830 K. The model proposed by Yon et al. provides smaller ratios at flame temperatures. However, it converges towards Sorensen and Kelesidis et al. ratios at ambient temperatures, in particular for large $D_p$, i.e., in the transition flow regime.

The above discussion shows that converting a size distribution expressed in gyration diameter (a purely morphological parameter) into a distribution in mobility diameter (which, in addition to being shape-dependent, also depends on the flow regime) is not straightforward. Different relationships exist for different flow regimes, giving a different influence to certain parameters. For example, Bouaniche et al. [108] have shown that the agreement between their simulations and SMPS measurements can be excellent as a function of the diameter of the primary spheres considered for the conversion. It should also be considered that temperature plays an important role in the flow regime and that the latter is naturally different in flame compared to the temperature of the effluent transmitted to the granulometer which analyzes the mobility at room temperature.

Optical techniques based on light scattering are therefore preferred for a comparison of simulated soot particle size distribution with experiments because they are *in-situ* and depend only on the morphology of the particles. But it is true that the implementation of optical techniques is often much more difficult than the installation of a sampling probe and a commercial granulometer. A comparison with *ex-situ* measurements of the SMPS type are naturally possible but require a conversion based on laws that must be systematically explained as well as the quantities considered, such as $T$, $D_f$, $D_p$, $C_c(K_n)$.

### *2.4. Aggregate size distribution: self-preserving, log-normal, and linkage to particle kinetics*

Soot particles are generally less than 1 μm making sedimentation negligible. The size distribution, generally expressed in $dn/d\ln(D)$, where $n$ represents the number concentration and $D$ the considered diameter of the particle (can be gyration, mobility, aerodynamic or volume-equivalent sphere) is usually composed of two modes. The smaller one is related to nuclei (or isolated primary spheres) that quickly coalesce and coagulate to form the larger mode (accumulation mode). If the smaller one can be treated as spherical particles, the second one then corresponds to aggregates. In various flame conditions (e.g. premixed flames; [154,155]), nanoparticle inception may persist and take place concurrently with coagulation [156]. This results in bi-modal size distributions at small heights above the burner and residence times [156]. Still, these incipient nanoparticles coagulate fast with the larger soot aggregates [157]. Monte Carlo simulations suggest that these small nanoparticles do not affect significantly the morphology of the particles in the accumulation mode [158]. The distribution becomes unimodal when the concentration of nuclei or aggregates becomes negligible relative to the other. When both co-exist, the smaller mode is often neglected because its mass fraction is negligible as well as its contribution to light scattering or laser-induced incandescence signals. Based on experimental measurements relying on soot sampling (TEM or SMPS), it is found that both modes can be well modeled by a log-normal (LN) distribution. Therefore, the driving parameters of the probability density function are reduced to two parameters: the geometric mean diameter $D_{\text{geo}}$ and the geometric standard deviation $\sigma_{\text{geo}}$. Although the LN distribution has been commonly assumed, there is no theoretical explanation to support the log-normal nature of the size distribution for each mode. For this reason, some authors prefer to resort to the self-preserving size distribution (SPSD), which is actually supported by a theory well suited for coalescence and aggregation.

Indeed, the aggregation process is driven by what we call the inter-particle collision kernel $K(V_i, V_j)$ that defines the rate at which particles of volume $V_i$ and $V_j$ collide and stick to form a larger one. According to [159], it can be related to the product of the diffusion coefficient and the particle size. The larger a particle is, the smaller its mobility but larger its cross section. The collision kernel is thus a balance between mobility and cross section. Thus, it depends on the particle size, density, and flow regime. If for given fractal aggregates and a given flow regime, both the diffusion coefficient and particle size can be expressed as power-laws of the number of primary spheres, then the collision kernel can also be expressed as a power-law of the particle volume and therefore such aggregation can be seen as an auto-similar process described as:

$$K(\gamma V_i, \gamma V_j) = \gamma^{\lambda} K(V_i, V_j). \tag{14}$$

This self-similar approach is an idealized construction that is theoretically valid only for ideal fractal objects. Nevertheless, it is the basis for the analytical expression of the size distribution, as explained below. In this equation, $\lambda$ is called the degree of homogeneity. For $\lambda = 0$, the collision probability of two particles is not scale dependent. For example, whatever the volume of a particle, the probability to collide with a particle having twice its volume is the same. If $\lambda$ is larger than 1, the collision will be more efficient at larger scales whereas if it is smaller than 1, on the contrary, the collisions will be more efficient at smaller scales. From this point of view, it seems logical to state that a larger $\lambda$ leads to a broader size distribution. The dependence of $\lambda$

on the flow regime and on the fractal dimension has been investigated by different authors [159–161]. Based on a scaling analysis, Pierce et al. [162] proposed different expressions of the dependence of $\lambda$ on the fractal dimension for different regimes of aggregation. According to this study, $\lambda$ is found to be about 0.55 for ballistic aggregation, 0.22 and 0 in the continuum flow regime in the intermediate and diluted environment, respectively, and −0.14 and −0.36 in Epstein regime (free-molecular particle-gas interaction regime, $K_n \gg 10$) in the intermediate and diluted environment, respectively.

This auto-similar property of the kernels enables an analytic solution of the population balance equation. Recently, it has been shown that whatever the considered diameter, the SPSD can be expressed by a Generalized Gamma function [96]. We report here the generic expression of the probability density function expressed in log scale:

$$\frac{1}{n}\frac{dn}{d\ln(X)} = \frac{p}{a^d\,\Gamma(d/p)} X^d \exp\left[-\left(\frac{X}{a}\right)^p\right], \tag{15}$$

where $dn$ corresponds to the concentration of particles whose size parameter $x$ (namely either the number of primary spheres $N_p$, the volume equivalent diameter $D_v$, the gyration diameter $D_g$, or the mobility diameter $D_m$) falls in the range $[x, x+dx]$. $X = x/\tilde{x}$ is a normalized form of the size parameter with $\tilde{x}^p = \tilde{x^p}$ representing the moment at order $p$ of the selected size parameter. $p$ is a dimension parameter depending on $x$ equal to 1, 3, $D_f$ and $D_{fm}$ (also called scaling exponent and determined by effective density measurements) for $N_p$, $D_v$, $D_g$ and $D_m$, respectively. Parameters $a$ and $d$ are respectively defined by $a = (1-\lambda)^{-1/p}$ and $d = p(1-\lambda)$.

The kinetic exponent $z = (1-\lambda)^{-1}$ is a power-law time dependence of the particle growth by aggregation process valid after the establishment of the auto-similarity. The results provided by Wang and Sorensen [159] can be generalized to any size parameter:

$$\tilde{x} \propto t^{z/p}. \tag{16}$$

It indicates that aggregation is faster for ballistic aggregation and slower in Epstein flow regime (larger $z$). It is also slower for large $p$, meaning that the growth rate of the sphere equivalent volume diameter appears slower than the growth rate of the gyration diameter. Nevertheless, as shown by Eq. (15), when represented as a function of the normalized size parameter $X$, the size distribution has no apparent time dependency and adopts what is called a Self-Preserving nature.

From Eq. (15), one can derive (see S1 of the Supporting Material) the analytical expression of moments at order $q$ of the size parameter $x$, the geometric mean $x_{\text{geo}}$ and the geometric standard deviation $\sigma_{x,\text{geo}}$:

$$\tilde{x^q} = (\tilde{x})^q \frac{\Gamma(1-\lambda+q/p)}{(1-\lambda)^{q/p}\,\Gamma(1-\lambda)}, \tag{17a}$$

$$x_{\text{geo}} = a\tilde{x}\exp\left(\frac{1}{p}\Psi^0(1-\lambda)\right), \tag{17b}$$

$$\sigma_{x,\text{geo}} = \exp\left(\frac{1}{p}\sqrt{\Psi^1(1-\lambda)}\right), \tag{17c}$$

where $\Psi^n = \frac{d^{n+1}\ln(\Gamma(x))}{dx^{n+1}}$ is the derivative of order $n$ of the digamma function.

Based on Eq. (17c), it is interesting to notice that dispersion of the size distribution, usually quantified by the geometric standard deviation $\sigma_{x,\text{geo}}$, only depends on $\lambda$ and $p$. This explains, for example, why the gyration geometric standard deviation is larger than the mobility ones $\sigma_{g,\text{geo}} > \sigma_{m,\text{geo}}$.

Fig. 7 reports the log-normal and SPSD expressed in gyration diameter having the same $\tilde{D}_g$ and $\sigma_{g,\text{geo}}$ for different regimes of agglomeration. Whatever the considered regime, the decrease of distribution after the peak at large diameters is always steeper for the SPSD than LN. This is the expected result of the self-preserving distribution under given $\tilde{D}_g$ and $\sigma_{g,\text{geo}}$. On one hand, the SPSD becomes increasingly asymmetric with increasing $\lambda$. Specifically, as $\lambda$ increases, the SPSD increases more gradual towards the peak and then decreases more rapidly after the peak with increasing $D_g$. Regardless of the values of $D_f$ and $\lambda$, the SPSD always peaks at $D_g = \tilde{D}_g$. On the other hand, the LN distribution remains symmetric and always peaks at a $D_g < \tilde{D}_g$. These different features of the SPSD and LN distribution explain why the decrease of SPSD after the peak is always steeper than the LN distribution when the two distributions have the same $\tilde{D}_g$ and $\sigma_{g,\text{geo}}$. It is important to recall that the theory behind the SPSD only considers aggregation occurring at a fixed flow regime (constant $\lambda$). In reality, the flow regime and aggregation regime evolve with time due to the increase of the particle size [96], and the local thermodynamic conditions also evolve. Moreover, other phenomena, such as inception and surface growth, also affect the size distribution [163]. These concurrent complex processes on soot particle size distributions may explain why most of the measurements are better modeled by a log-normal size distribution [164] with a longer tail. As noticed in [123], this difference is of importance when considering the computation of high order moments, which are required for example when evaluating the light scattering cross section. In any case, there has been no consensus to date on the preference to be given to one model over the other. The lognormal law seems empirically to correspond better to granulometric measurements based on the mobility diameter, the difficulty of interpretation of which has been discussed earlier. The self-similar law has the advantage of being based on a theoretical aggregation model. However, this may not be sufficient when other mechanisms are simultaneously involved. An effort must be made to better determine which law should be used for given conditions.

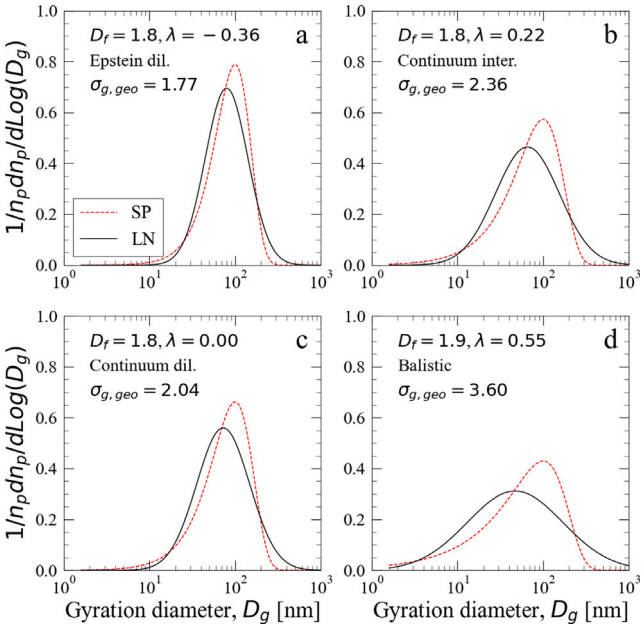


**Fig. 7.** Comparison of log-normal (black plain) and self-preserving (red dashed) probability density functions having the same geometric means and geometric standard deviations expressed as a function of the gyration diameter for different regimes of aggregation. For each plot, $\tilde{D}_g$ is fixed at 100 nm, $D_{g,geo}$ and $\sigma_{g,geo}$ are determined according to Eqs. (17b) and (17c) by considering $D_f$ and $\alpha$ identified in [162].

### 2.5. Anti-correlation of $D_{fp}$ and $k_{fp}$

The population based fractal dimension $D_{fp}$ and prefactor $k_{fp}$ have been found to be anti-correlated (see Fig. 8) as initially suggested by Sorensen and Roberts [165] who analyzed 24 ensembles of 3-dimensional DLCA simulations and obtained $D_{fp}$ and $k_{fp}$ from a log–log fit of Eq. (1). In this context, the power-law $k_{fp} = 4.46 D_{fp}^{-2.08}$ was proposed by Ehrl et al. [166], which is valid in the range of $D_{fp} \in [1.6, 3.0]$. This empirical power-law is found in reasonably

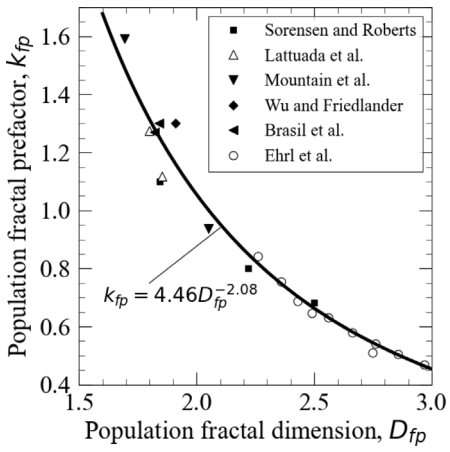


**Fig. 8.** Anticorrelation between the prefactor $k_{fp}$ and the fractal dimension $D_{fp}$. *Source:* Adapted from Ehrl et al. [166].

good agreement with the literature for agglomerates generated by DLCA [134,167–171], RLCA [134], diffusion-limited particle-cluster agglomerates [170] and more recently in the transition between BLCA and DLCA regimes [96].

## 3. Overview of soot particle growth

There are various physical and chemical processes associated with soot formation in hydrocarbon flames. The main processes include [21,23,30] (i) fuel pyrolysis and formation of radicals and intermediate hydrocarbon species, (ii) formation of benzene, (iii) formation and growth of PAHs, (iv) formation of incipient soot particles (soot inception), which then evolve into solid primary soot particles after they reach the critical coalescence diameter through coalescence and surface growth and carbonization/graphitization, (v) particle growth through simultaneous surface growth and coagulation and formation of fractal-like soot aggregates through aggregation of soot particles, and finally (vi) oxidation and oxidation-induced fragmentation of soot aggregates. Among these processes, formation of incipient soot particles, i.e., inception, marks the transition from gas-phase precursor species (PAHs and aliphatic-linked PAHs) to condensed phase particles or the birth of particles, and initiates the subsequent surface growth and particle dynamics. Given the focus of this review is the progress in the prediction of soot particle aggregation in the presence of surface growth (step v in the overall soot formation process), the aim of this section is to provide an overview of the physical and chemical processes involved in the early stage of evolution of incipient soot particles, namely coagulation and surface growth. Therefore, soot inception, soot oxidation, and oxidation-induced fragmentation will not be included in this section. Comprehensive reviews and some recent studies of these processes can be found in the literature. For soot inception, various mechanisms and models have been proposed and reviewed in the seminal monographs [22,23], and several excellent reviews [21,26–29]. For soot oxidation and oxidation-induced fragmentation, experimental measurements and models of soot oxidation [155,172–180] and oxidation-induced fragmentation [181–188] have also been extensively conducted in the literature.

Once incipient soot particles of about 1 to 3 nm in volume-equivalent diameter are formed, they undergo concurrent processes of coagulation, carbonization/graphitization, surface growth, and oxidation. Although soot oxidation also takes place in the early stage of soot formation, it plays a less important role compared to soot surface growth because soot formation takes place under locally fuel rich conditions. However, this by no means suggests that soot oxidation is not important or can be neglected. Carbonization/graphitization of soot particles also proceeds simultaneously with the transformation of chemical compositions both on the particle surface and the interior [189–191]. The evolution of soot maturity results in various changes in the physical and chemical properties as well as the internal nanostructure of soot as discussed in [14,189,190]. It is useful to recall that surface growth causes an increase in the amount of soot mass but does not change the particle number density. In contrast, coagulation, which refers to the collision and sticking or coalescence of particles, increases the volume of individual particles involved in coagulation, reduces the particle number density, but does not change the amount of soot mass. The literature on soot particle coagulation, coagulation efficiency, and surface growth are discussed in the following sub-sections.

### 3.1. Coalescence

Soot particle coalescence has long been believed to play an important role in the early stage of soot formation, e.g. [21,32]. Coalescence instantaneously enlarges the size of young soot particles through complete merging of two or more liquid-like incipient soot particles upon collision, reduces the particle number density and available surface area, causing a profound influence on soot surface growth and the predicted primary particle size [42,192–194]. The liquid-like nature of incipient soot particles are revealed from TEM and atomic force microscopy (AFM) images (see [29] and references cited therein). Due to the rapid evolution of incipient soot particles and the concurrent presence of many complex processes during soot formation in flames, it is very challenging to obtain direct experimental evidence of soot particle coalescence, though we recognize that the difference in coalescence between PAH clusters and incipient soot particles has not been made clear. Instead, the importance of coalescence has been assessed indirectly by comparing the predicted soot particle primary diameter distribution and/or particle number density against experimental data in laminar flames [42,193–195]. Smooke et al. [195] assumed that primary particles undergo either coalescence if their diameters are below the cut-off value of 25 nm or otherwise agglomeration when the diameters of colliding primary particles are larger than the cut-off value. Zhang et al. [42] employed a cut-off size-based soot particle coalescence model to investigate the influence of coalescence on the predicted average number of primary particles per aggregate, mean primary particle diameter, number density of primary particles ($n_{pp}$), as well as soot volume fraction using a detailed soot model and a cut-off soot diameter of 3 nm. They found that consideration of coalescence predicted larger $D_p$, but lower $N_p$, $n_{pp}$, and $f_v$ and the quantitative influence of particle coalescence is also strongly affected by the assumed particle coagulation efficiency. Veshkini et al. [192] proposed a collision-driven finite-rate sintering coalescence model based on the conservation of primary particle number density. The sintering rate is expressed as [192,196]

$$\frac{\partial n_i^p}{\partial t} = -\frac{3}{\tau_s}(N_p - N_p^{2/3})n_i^a \tag{18}$$

where $n_i^p$ and $n_i^a$ are the number density of primary particles and number density of aggregates of the $i$th section, respectively. The characteristic coalescence time $\tau_s$ is given as

$$\tau_s = A_s D_p^4 \, T \, \exp(E_s/T) \tag{19}$$

where the pre-exponential factor $A_s = 7.44 \times 10^8$ s/(K cm$^4$) and the activation energy $E_s = 3.31 \times 10^4$ K. This characteristic coalescence time implies that the sintering/coalescence can be neglected when the temperature decreases below 1500 K or the primary particle diameter increases above 40 nm [192]. Veshkini et al. also considered a cut-off coalescence model with a cut-off diameter of 20 nm. The coalescence models were implemented into the CoFlame code [43] to investigate the effects of coalescence modeling on the prediction of soot volume fraction and particle properties ($D_p$, $n_{pp}$, and $N_p$) in the Santoro flame (laminar coflow ethylene/air diffusion flame). They concluded that it

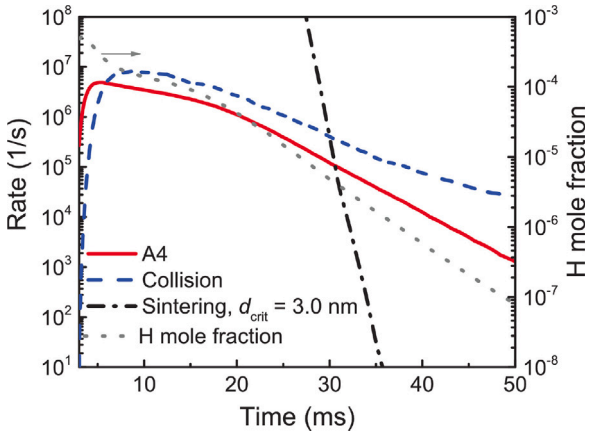


**Fig. 9.** Evolution of the rates of A4 production, collision, and sintering (left Y-axis) and mole fraction of H (right Y-axis) with residence time in the burner-stabilized ethylene premixed stagnation flame.
*Source:* Adapted from Hou et al. [98].

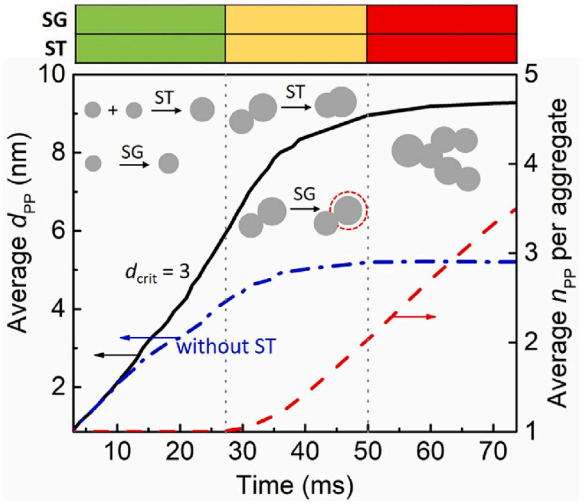


**Fig. 10.** Evolution of the computed average primary particle diameter (left Y-axis) and average number of primary particle per aggregate (right Y-axis). The table above indicates the rate of particle processes of surface growth (SG) and sintering (ST) by different colors (Green: fast; Yellow: slow; Red: almost stop) over three time periods.
*Source:* Adapted from Hou et al. [98].

is necessary to take into account soot particle coalescence to better predict the primary particle diameter and the primary particle number density against available experimental data.

In the detailed stochastic population balance (DSPB) model developed by Kraft and co-workers, sintering has been assumed to be an important process in the early stage of soot formation and the transition from coalescence/sintering to agglomeration/aggregation was modeled by using a finite-rate sintering model [98,194,197,198]. The sintering rate is given as [98,197]

$$R_{\text{sinter}} = 1/\tau_s = \left\{ A_s D_{i,j} \exp\left[\frac{E_s}{RT}\left(1 - \frac{d_{\text{crit}}}{D_{i,j}}\right)\right]\right\}^{-1} \tag{20}$$

where $A_s$ (in s/m) is the pre-exponential factor, $d_{i,j}$ is the smaller diameter of the two neighboring primary particles, $E_s$ is the activation energy, and $d_{\text{crit}}$ is the critical primary particle diameter below which primary particles are assumed to be liquid-like and will sinter instantaneously, i.e., undergoing coalescence. Therefore, coalescence is simply a special case in this sintering model. A similar sintering model has been adapted by D'Anna and co-workers in their kinetic sectional soot model [72,73]. Chen et al. [197] obtained the best fit sintering model parameters by reproducing the measured soot particle size distribution in a laminar premixed flame as: $A_s = 1.1 \times 10^{-14}$ s/m, $E_s = 799$ kJ/mol, and $d_{\text{crit}} = 1.58$ nm. The sintering model has recently been used by Hou et al. [98] and Botero et al. [194] to predict soot primary particle size distributions (PPSDs) in both premixed and diffusion flames. Sensitivity studies were also conducted to investigate the effect of sintering model parameters to the predicted soot primary particle size distributions. They found that the predicted primary particle size distributions are sensitive to the sintering model parameters. Using the DSPB method and the soot sintering model given in Eq. (20), Hou et al. [98] modeled the PPSD in the burner-stabilized premixed ethylene stagnation flame investigated experimentally by Wang et al. [199] (Flame A3 in [199], stagnation plate height 1.2 cm). The computed PPSDs were sensitive to the rate of production of A4, coagulation rate, and surface growth rate. They compared the rates of A4 production (the dimerization of A4 was the inception step), collision rate, sintering rate, and the mole fraction of H against the residence time shown in Fig. 9.

The rate of A4 production (the solid red line) is an indication of soot inception rate. The collision rate (the blue dashed line) represents the sum of the rates of all collision processes, i.e., inception (collisions between PAH molecules), condensation (collisions between PAH molecules and particles), and coagulation (collisions between particles). The sintering rate, represented by the dash-dotted line, is calculated from Eq. (20) with $D_{i,j}$ evaluated as the average diameter of all primary particles. The sintering rate displays a very steep decrease with residence time: before about 30 ms it is several orders of magnitudes higher than A4 production and collision; but after 30 ms, it becomes almost negligible. This behavior of the sintering rate reflects its strong sensitivity to the primary particle diameter due to its nearly exponential variation with $D_{i,j}$. The mole fraction of H atoms shown in Fig. 9 is an indication of the rate of soot surface growth due to the important role of H abstraction reactions in the HACA mechanism. The rates shown in Fig. 9 suggest that before 30 ms coalescence and sintering are the dominant processes. However, coagulation (aggregation) becomes dominant after 30 ms. The rapid decrease of the sintering rate also suggests that the transition from coalescence/sintering to agglomeration/aggregation occurs rapidly, i.e., over a very short time of the order of few milliseconds. Hou et al. [98] also analyzed the evolution of average primary particle diameter $D_p$ and number of primary particles per aggregate $N_p$. These results are shown in Fig. 10.

It can be seen from Fig. 10, the growth of primary particles can be divided into three stages from the variation rate marked by the vertical dashed lines. In the first stage (below 30 ms), primary particle growth is attributed to rapid coalescence/sintering and surface growth. Soot particles remain spherical at this stage because the average number of primary particle per aggregate remains at 1. In the second stage (30 to 50 ms), the variation rate of $D_p$ is much slower, suggesting that both sintering and surface growth rates are considerably lower than those in the first stage. In the last stage beyond 50 ms, the average primary particle diameter remains nearly constant, consistent with the negligible surface growth and sintering rates shown in Fig. 9. At this stage, coagulation (aggregation) is the dominant particle process and the average number of primary particle per aggregate increases linearly with time. In Fig. 10, the evolution of average primary particle diameter without coalescence/sintering (the blue dash-dotted line) is also plotted to show the relative importance of surface growth and sintering to the growth of primary particle diameter. Without coalescence/sintering, surface growth is the only mechanism for the growth of primary particles and the average diameter reached about 5 nm in the third stage. By contrast, when coalescence/sintering was taken into account, the average primary particle diameter in the third stage reached about 9.3 nm, nearly twice as large as that without coalescence/sintering and in better agreement with the experimental data.

In another recent numerical study, Sun et al. [196] extended the conservative finite-volume one-PBE (CFV-1PBE) sectional method to

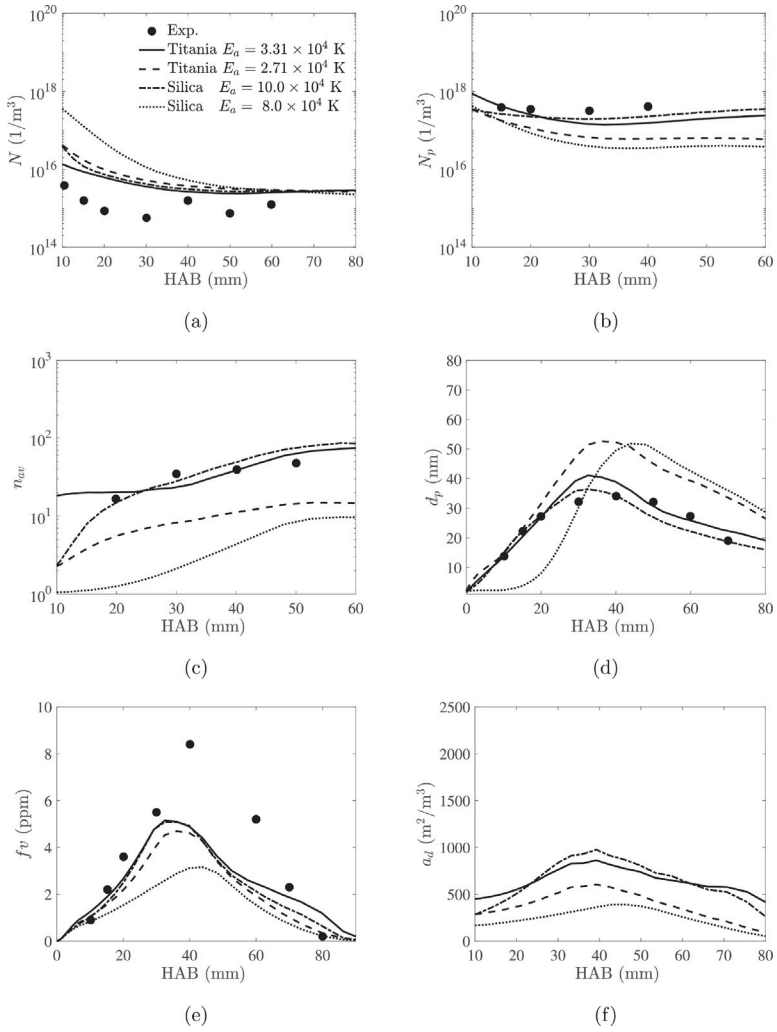


**Fig. 11.** Comparison of predicted soot properties using the CFV-2PBE model along the annular pathline containing maximum soot volume fraction with experimental data and the effects of different activation energies in the silica, Eq. (20), and titania model, Eq. (19). (a) Number density of aggregates, (b) number density of primary particles, (c) average number of primary particles per aggregate, (d) diameter of primary particles, (e) soot volume fraction, and (f) surface area density. Solid line: titania model with $E_a = 3.31 \times 10^4$ K; Dashed line: titania model with $E_a = 2.71 \times 10^4$ K; Dash-dot line: silica model with $d_{\text{crit}} = 5$ nm, $E_a = 8.0 \times 10^4$ K; Dotted line: silica model with $d_{\text{crit}} = 5$ nm, $E_a = 10.0 \times 10^4$ K. *Source:* Adapted from Sun et al. [196].

CFV-2PBE by solving an additional transport equation for the primary particle number density in each section. They investigated the importance of finite-rate sintering, which was called fusing in [196], of primary particles within aggregates in the Santoro laminar coflow ethylene/air diffusion flame using both the CFV-1PBE and CFV-2PBE sectional methods coupled with a detailed soot kinetic model. The results are highlighted in Fig. 11. Their results showed that coalescence/sintering significantly affect the predicted particle number density (primary particle and aggregate), soot volume fraction, and soot particle size (aggregate size distribution, primary particle size, average number of primary particles per aggregate) and the results are sensitive to the sintering models and the assumed activation energy. These findings are overall similar to those of Veshkini et al. [192].

Although the above-discussed studies are useful to illustrate the potential importance of coalescence/sintering to the prediction of various soot properties in laminar flames, the results and findings from these studies must be considered model specific. The main concern of the methodology for assessing the importance of coalescence/sintering lies in the uncertainties in other sub-models of the overall soot model, such as the PAH formation sub-mechanism of the gas-phase mechanism, the soot inception model, and the soot particle coagulation efficiency. Given the significant uncertainties in PAH formation sub-mechanism and soot inception model [26,27], the coalescence model may be considered as an additional tunable term in an overall soot model at the current stage of soot modeling.

To gain fundamental insights into the coalescence process of incipient soot particles, Hou et al. [193] have recently investigated the coalescence and sintering of PAH clusters of 3 to 6 nm over the temperature range of 300 to 750 K using MD. Later, Sharma et al. [191] also studied the coalescence/sintering of incipient soot particles of about 1 to 3.5 nm over the temperature range of 800 to 1800 K using reactive MD. Hou et al. [193] found that the sintering rate of two PAH clusters is strongly dependent on temperature. When the sintering temperature is higher than the melting temperature of the PAH clusters, reported to range between 250 and 575 K for clusters composed of 50 to 500 PAH molecules according to Chen et al. [200], the characteristic sintering time $\tau_s$ is about $10^{-2}$ ns. In contrast, when the sintering temperature is below the melting temperature, $\tau_s$ is much longer with $\tau_s > 5$ ns. The implications of these results are that PAH clusters sinter instantaneously at flame temperatures. Based on the results of reactive MD simulations, on the other hand, Sharma et al. concluded that the coalescence/sintering rate depends on temperature and the cluster structure and composition. Specifically, at relatively low temperatures of about 800 to 1000 K incipient soot particles coalesce instantly. At higher temperatures (1200 to 1600 K), incipient soot particles are less likely to coalesce due to the higher aromatic to aliphatic carbon ratios,

which correspond to more rigid particles. Larger particles consisting of more than 1300 C atoms (volume equivalent diameter about 2.5 nm) did not coalesce within the simulation time (up to 5 ns). The findings of Sharma et al. tend to support the conjecture that soot particles do not sinter [30,59], or that the characteristic sintering time increases very rapidly with increasing the primary particle size so that the transition from coalescence to agglomeration takes place nearly instantaneously. Nevertheless, the relevance of sintering to soot formation deserves further research and more discussion of sintering will be given in Section 7.

### 3.2. Collision and sticking probability

The coagulation rate of young soot ($D_p$ <~ 10 nm) is determined not only by their collision frequency, but also by their collision and sticking probability, simply because the coagulation rate is the product of collision frequency and sticking probability. While the theory of collision frequency has been well established, e.g. [38,201], the sticking probability of young soot is subject to large uncertainty and very different values varying over two-orders of magnitude have been assumed in both macro- and meso-scale modeling of soot particle dynamics, as discussed by Huo et al. [202]. The sticking probability strongly influences the prediction of soot particle size distributions in laminar sooting flames, e.g. [202–205]. In the context of soot particle dynamics, almost all the studies conducted to date have considered neutral or uncharged soot particles and implicitly assumed that the collision probability of either primary particles or aggregates is unity with perhaps the only exception of a recent study by Morán et al. [206], who investigated the collision and sticking of charged young soot particles and quantified both the collision and sticking probability. Collision occurs when the relative kinetic energy of the two colliding particles along the direction of collision is higher than the repulsive energy barrier. When collision occurs, there are two possible outcomes: the two particles either stick or rebound. The results of Morán et al. showed that collision is always successful for uncharged or oppositely charged soot particles. Their results of the sticking probability will be discussed later. The sticking probability is also termed coagulation probability, coagulation efficiency, or collision efficiency in the literature, e.g. [202,207–209]. To unify the different terminologies used in the literature to describe the probability of a successful sticking of two particles upon collision, the sticking probability is used throughout this review. Soot particles are assumed electrically uncharged in the following discussion.

The van der Waals attraction and Born repulsion are commonly regarded as the potentials explaining the sticking of particles upon collisions [202,206,207,209,210]. These studies are all based on the pair-wise Lennard-Jones potential between two atoms or molecules expressed as,

$$U_{ab} = 4\epsilon\left[\left(\frac{\sigma_{ab}}{r_{ab}}\right)^{12} - \left(\frac{\sigma_{ab}}{r_{ab}}\right)^{6}\right], \tag{21}$$

where $\epsilon$ is the potential well depth, $\sigma_{ab}$ is the finite distance between the two interacting objects at which the interaction potential is zero, and $r_{ab}$ is the center-to-center distance between the two objects. The interaction energy between two solid particles can be evaluated by integrating the Lennard-Jones potential over the entire volumes of the two particles [202,206,209],

$$\Phi(a_1, a_2) = q_1 q_2 \int_{V_1}\int_{V_2} U_{ab} dV_2 dV_1 \tag{22}$$

where $a_i$, $q_i$, and $V_i$ ($i$ = 1, 2) are respectively the radius, atom or molecule number density, and volume of particle $i$. The analytical expression for the double integration in Eq. (22) can be found in Hou et al. [209] and Huo et al. [202]. Caution should be taken as the separation distance between the two colliding particles was defined differently in these two studies. Soot particle collisions are complex and may not necessarily result in sticking upon collisions due to the thermal rebound effect, especially for incipient soot particles of a few nanometers in diameter at flame temperatures. D'Alessio et al. [207] measured low and strongly size-dependent sticking probabilities of soot particles with a diameter below 10 nm: it increases exponentially from about 0.002 at $D$ = 2 nm to nearly unity at about $D$ = 10 nm. The experimental results of D'Alessio et al. have later been used to formulate soot sticking probability models [208,211]. Subsequent experimental studies by D'Alessio and co-workers have also observed significantly small sticking probabilities for soot particles in the above mentioned size range, finding good agreement between simulations based on D'Alessio et al. [207] sticking probability model and experiments based on DMA and AFM [212,213]. Interestingly, Sirignano and D'Anna [204] have experimentally observed a degradation of coagulation of soot particles with diameter between 2–4 nm when temperature was increased from 300 K to 600 K in a tubular reactor. It is noticed that increasing temperature causes two competing effects. On one hand, with increasing temperature the kinetic energy of colliding particles is enhanced and so is the probability of the particle to escape the interaction potential well, leading to a lower sticking probability. On the other hand, increasing temperature also increases the collision frequency. The experimental results of Sirignano and D'Anna imply that temperature has a much stronger impact on the sticking probability than on the collision frequency for these very small particles, at least over the temperature range investigated. The recent study by Huo et al. [202], who showed that the coagulation rate (the product of collision frequency and sticking probability) decreases monotonically with increasing temperature for collisions of small particles, has confirmed this conjecture.

For Brownian coagulation the sticking probability of two colliding particles in the free-molecular regime is given as [207,210]:

$$\eta_s(a_1, a_2) = 1 - \left(1 + \frac{\Phi_0(a_1, a_2)}{k_B T}\right)\exp\left(-\frac{\Phi_0(a_1, a_2)}{k_B T}\right) \tag{23}$$

where $\Phi_0$ is the potential well depth, $k_B$ is the Boltzmann constant, and $T$ is the particle temperature. The potential well depth $\Phi_0$ is the minimum potential energy where $d\Phi(a_1, a_2)/dh_{12} = 0$ ($h_{12}$ is the distance between the two colliding particles). D'Alessio et al. [207] were the first to propose using Eq. (23) to model soot sticking probability based on the study of Narsimhan and Ruckenstein [210]. More recently, by assuming a mass density of 700 kg/m$^3$, C/H = 1.8, and uniform distributions of C and H atoms inside spherical soot particles, Hou et al. [209] reported the potential well depth of two colliding soot particles with diameters between 1 and 15 nm through detailed calculations considering all pair-wise interactions between C and H atoms, i.e., C–C, H-H, H-C, and C-H, within the two particles expressed as

$$\Phi = \Phi_{CC} + \Phi_{CH} + \Phi_{HC} + \Phi_{HH} \tag{24}$$

where the first and second subscript refer the atoms in the first and second particle, respectively. For example, $\Phi_{CH}$ is the interaction energy between C atoms in particle 1 and H atoms in particle 2. The resultant potential well depth $\Phi_0$ was fitted as a polynomial function of the reduced collision diameter $D_c = D_1 D_2/(D_1 + D_2)$, with $D_1$ and $D_2$ being the diameters of the two colliding particles, as

$$\begin{aligned}\Phi_0(D_c) = &-5.5373\times10^{-21} + 1.1394\times10^{-20} D_c \\ &+ 1.1244\times10^{-21} D_c^2 - 6.6891\times10^{-23} D_c^3\end{aligned} \tag{25}$$

where the unit of $\Phi_0$ and $D_c$ is J and nm, respectively. Using Eqs. (23) and (25), Hou et al. [209] obtained the sticking probability of small soot particles shown in Fig. 12. The collision efficiency (sticking probability) of soot decreases with decreasing particle sizes but increases with decreasing temperature. For example, at flame temperatures the collision efficiency decreases quickly from about unity to about 0.2 when the reduced collision diameter decreases from 7 nm to about 1 nm. Although the decreasing trend of $\eta_s$ with decreasing the reduced collision diameter is consistent with the experimental results of D'Alessio et al. [207], the rate and extent of decrease are much

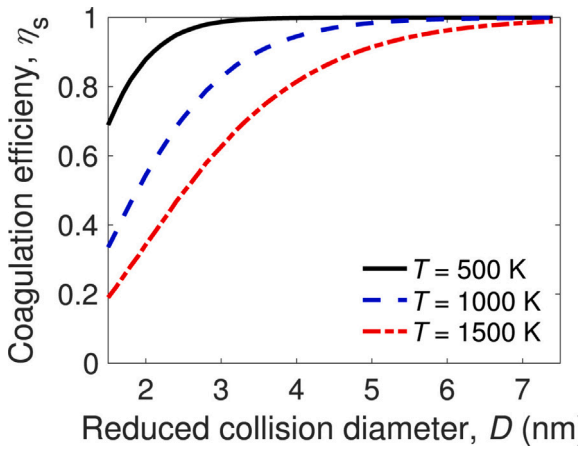


**Fig. 12.** Variation of sticking probability (coagulation efficiency) with the reduced collision diameter at $T$ = 500, 1000 and 1500 K.
*Source:* Adapted from Hou et al. [209].

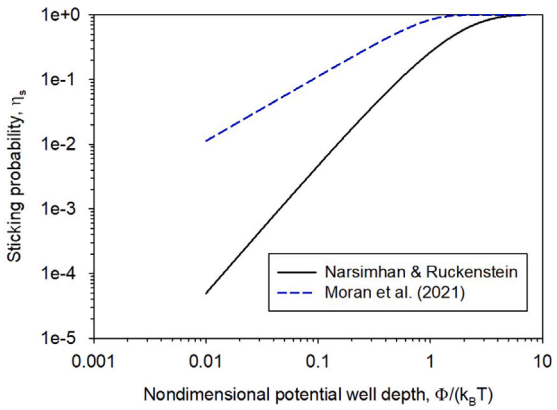


**Fig. 13.** The sticking probabilities calculated by the expressions of Narsimhan and Ruckenstein [210] and Morán et al. [206].

smaller than the experimental data. For example, at 2 nm and 1500 K the calculated $\eta_s$ by Hou et al. [209] is about 0.25, while the measured sticking probability by D'Alessio et al. [207] is about $2\times10^{-3}$. This large discrepancy in $\eta_s$ between the numerical results of Hou et al. and the experimental data of D'Alessio et al. was not explained in the study of Hou et al. [209]. Although the assumed mass density of incipient soot of 700 kg/m$^3$ is clearly too low, the sensitivity study of Hou et al. [209] suggests that the uncertainty in the assumed soot mass density or C/H ratio cannot explain the large discrepancy between their numerical results and the experimental data of D'Alessio et al. Hou et al. [209] also showed that accounting for the size dependent collision efficiency has a significant influence on the predicted soot particle mobility size distribution in a premixed flame.

Morán et al. [206] investigated the collision and sticking of charged soot particles by accounting for both the short-range Lennard-Jones potential and the long-range electrostatic potential. They derived a different expression for the sticking probability of two colliding particles from that obtained by Narsimhan and Ruckenstein [210] and used in previous studies [204,207,209]. The new sticking probability is written as

$$\eta_s(a_i, a_j) = \mathrm{erf}\left(E_{\mathrm{stick}}^{0.5}\right) - E_{\mathrm{stick}}^{0.5}\exp(-E_{\mathrm{stick}}) \tag{26}$$

where $E_{\mathrm{stick}} = (\left|\Phi_0(a_i, a_j)\right| + E_{\mathrm{barr}})/(k_B T)$ is the nondimensional potential energy and $E_{\mathrm{barr}}$ is the long-range repulsive energy associated with the charged particles. For uncharged soot particles considered here, $E_{\mathrm{barr}}$ vanishes and $E_{\mathrm{stick}}$ is simply the nondimensional potential well depth. The sticking probabilities calculated using Eqs. (23) and (26) as a function of the nondimensional potential well depth are compared in Fig. 13. It is clear from Fig. 13 that the expression of Morán et al. yields significantly higher $\eta_s$ and the relative difference between the two expressions increases with decreasing the nondimensional potential well depth. It is also noticed from Fig. 13 that the expression of Narsimhan and Ruckenstein can indeed return very low sticking probability down to around $10^{-3}$ if the nondimensional potential well depth can reach a level of $10^{-2}$, which corresponds to a shallow potential well. Using Eq. (26) and the same approach and Lennard-Jones potential parameters for C–C, H-H, and C-H interactions as those of Hou et al. [209] but more realistic soot mass density for calculating the potential between two soot particles, Morán et al. obtained similar size dependent $\eta_s$ at $T$ = 1700 K as that obtained by Hou et al. [209] at $T$ = 1500 K, the red-dashed curve shown in Fig. 12. It is noticed that Hou et al. [209] calculated $\eta_s$ using Eq. (23). Based on Fig. 13 and the similar size dependent $\eta_s$ results of Morán et al. and Hou et al. [209], we suspect that the significantly higher sticking probabilities calculated in these two studies may be attributed to how the potential energy was evaluated, which resulted in high nondimensional potential well depths, i.e., deep potential wells. Indeed, even for a small reduced collision diameter of $D_c$ = 2 nm, Eq. (25) returns a quite large nondimensional potential well depth of $\Phi_0/(k_B T)$ = 1.024 (at $T$ = 1500 K), which corresponds to $\eta_s$ = 0.264 from Eq. (23), confirming the above conjecture.

The sticking probability of two colliding spherical young soot particles has also been recently investigated by Huo et al. [202] using the Lennard-Jones potential and the sticking probability expression of Narsimhan and Ruckenstein given in Eq. (23). The critical difference between the study of Huo et al. [202] and that of Hou et al. [209] lies in how the interaction potential energy between the two colliding particles was calculated. While Hou et al. [209] obtained the potential energy between two particles by adding all pair-wise Lennard-Jones potentials between all the C and H atoms in the two particles given in Eq. (24) and estimated the number density of C and H atoms from assumed soot mass density and C/H ratio, Huo et al. [202] calculated the interaction potential energy of the two colliding particles considering three cases: carbon–carbon (C-C), benzene-benzene (A1-A1), and pyrene-pyrene (A4-A4) interaction to approximate the H/C ratio = 0, 1, and an intermediate value of 0.625, respectively. The corresponding Lennard-Jones potential parameters were given in [202]. In addition, Huo et al. [202] estimated the atom (C) or molecule (A1 and A4) number density using $q_i = 1/(\lambda V_{M,i})$ with $\lambda$ being a model parameter representing the molecule packing fraction and $V_{M,i}$ is the volume of a single atom (C) or molecule (A1 and A4). They calculated the sticking probability of equal-sized soot particles at $T$ = 1500 K and for three different values of $\lambda$ = 1.0, 1.25, and 2.0. Their results for $\lambda$ = 2.0, which led to the best agreement with the experimental data of D'Alessio et al. [207], are shown in Fig. 14. It is worth pointing out that although $\lambda$ = 2 led to the best agreement between their calculated sticking probabilities (coagulation efficiency) and the experimental data of D'Alessio et al., it resulted in significantly worse predicted soot particle size distribution in an ethylene burner-stabilized stagnation premixed flame and soot volume fraction in a laminar coflow methane diffusion flame than those assuming $\lambda$ = 1 and 1.25 (a lower $\lambda$ causes the sticking probability to increase more rapidly with increasing particle diameter $D$) compared to the experimental results.

It is interesting to notice that the sticking probability obtained by Huo et al. [202] displays similar behavior as the experimental data of D'Alessio et al. namely it decreases nearly exponentially with decreasing the particle diameter and reaches about 0.002 at $D$ = 2 nm, regardless of the pair of atom (C-C) or molecule (A1-A1 or A4-A4) considered. Based on the results shown in Figs. 12, 13, and 14 and the above discussion, it is reasonable to conclude that the sticking

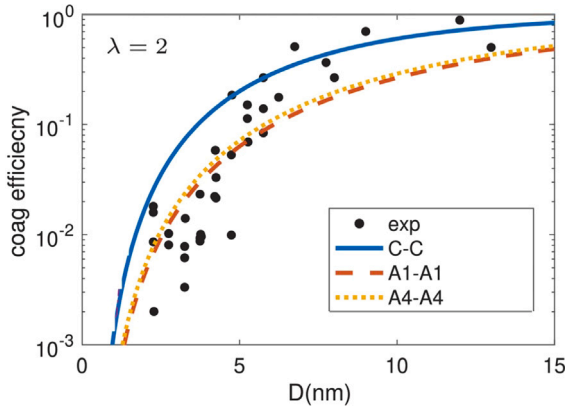


**Fig. 14.** The sticking probabilities of two equal-sized soot particles at $T$ = 1500 K calculated using the expression of Narsimhan and Ruckenstein [210] and the Lennard-Jones potential of C–C, A1-A1, and A4-A4.
*Source:* Modified from Huo et al. [202].

probability of young soot particles is sensitive to how the interaction potential energy between two colliding particles is calculated and Eq. (26) predicts significantly higher values than Eq. (23).

In another recent effort to quantitatively understand the sticking probability of incipient soot particles, Huo et al. [214] investigated the coagulation of two cross-linked PAH clusters about 2 nm over the temperature range of 1500 to 2000 K using reactive MD (RMD) simulations, which presumably can account for the potential interactions of the two PAH clusters accurately without making the assumptions of rigid sphere or uniform distributions of C and H atoms in the two colliding PAH clusters. Limited by the large computing times of RMD simulations and a large number of simulations for statistical significance, they did not vary the sizes of PAH clusters. Their results showed that the sticking probability decreases with increasing the temperature, consistent with their previous findings [209]. However, the sticking probability of 2 nm particle predicted by RMD is slightly higher than their earlier result reported in [209] at the same temperature, resulting in even larger discrepancies with the experimental data of D'Alessio et al. [207]. Clearly, more research is required to reconcile and understand the differences in the sticking probabilities of PAH clusters and incipient soot particles between theoretical calculations and measurements. It is also of interest to understand quantitatively how the sticking probability affects the soot particle size distributions in the early stage of growth in flames, though it is challenging to resolve this issue given the uncertainties in PAH formation and growth pathways and a lack of clear understanding of soot inception mechanism.

### 3.3. Aggregation

#### 3.3.1. Regimes of particle coagulation and its impact on particle–particle collision

The regimes of particle–particle collisions can be described by the diffusive Knudsen number defined as the ratio of the particle persistent distance $\lambda_p$, i.e., the particle's characteristic distance of momentum relaxation (also called mean free path in the literature), to the particle mobility radius $R_m$, $K_{n_D} = \lambda_p/R_m$ [162]. When $\lambda_p \gg R_m$, the particle will experience a ballistic motion, while in the limit $\lambda_p \ll R_m$, the particle experiences a diffusive motion. The regime of particle–particle interaction will define a different collision kernel and the dependence on the diffusive Knudsen number cannot be neglected. In this context, numerous studies have reported a correction for the collision kernels as a function of the diffusive Knudsen number starting with the Fuchs' flux-matching theory [215] to more recent ones based on theoretical [216–218] or numerical simulations [219–221].

#### 3.3.2. Aggregation dynamics

The dynamics of soot nanoparticles under the flame thermodynamic conditions determines their aggregation kinetics and particle morphology. The key parameter describing such dynamics is the particle–particle or diffusive Knudsen number discussed above. As particle grow through aggregation, their dynamics commonly evolves from ballistic ($K_{n,D} \gg 1$) to transition regime ($K_{n,D} \sim 1$). In this context, the continuum regime collision kernel ($\beta_{ij,\mathrm{C}}$) between particles $i$ and $j$ is,

$$\beta_{ij,\mathrm{C}} = 4\pi \frac{k_B T}{f_{ij}} R_{c,ij}, \qquad K_{n,D} \ll 1 \tag{27}$$

where $f_{ij} = f_i f_j/(f_i + f_j)$ is the reduced friction coefficient, and $R_{c,ij} = R_{c,i} + R_{c,j}$ is the combined collision or Smoluchowski radius. In this regime, the particles moves following diffusive trajectories and thus their collision kernel can be obtained from the diffusion equation. Eq. (27) is valid in the diffusive regime ($K_{n,D} \ll 1$) under dilute conditions ($f_v \ll 1000$ ppm) and neglecting external forces such as van der Waals or electrostatic. We note that the friction coefficient $f$ depends on the particle-gas or gas Knudsen number $K_n$ which is the ratio between the gas mean free path and a characteristic particle radius. As discussed in Section 2.3, dedicated works to determine $f$ for fractal-like aggregates for all $K_n$ numbers can be found in the literature [84,222]. Significant efforts have been made in previous works to accurately determine $R_{c,i}$ for fractal-like aggregates of different morphologies [223], including the aggregate rotation [221], and proposing simplified expressions to ease their implementation in population balance simulations [224]. Similarly, in the ballistic regime, the collision kernel $\beta_{ij,\mathrm{B}}$ is,

$$\beta_{ij,\mathrm{B}} = \sqrt{\frac{8k_B T}{\pi m_{ij}}} \mathrm{PA}_{ij}, \qquad K_{n,D} \gg 1 \tag{28}$$

where $m_{ij} = m_i m_j/(m_i + m_j)$ is the reduced mass, and $\mathrm{PA}_{ij}$ is the combined projected area for the colliding particles $i$ and $j$. In this regime, the particle move following ballistic trajectories and the collision kernel is obtained based on the kinetic theory of gases. Eq. (28) is valid in the ballistic particle–particle interaction regime $K_{n,D} \gg 1$, under diluted conditions ($f_v \ll 1000$ ppm), and neglecting external forces such as van der Waals or electrostatic. Extensions of Eqs. (27) and (28) to high concentration (numerical [225] and theoretical [226,227], numerical including hydrodynamic interactions [228]) and including external forces (numerical, van der Waals [229] and Coulomb [230]) are available in the literature. Accurate determination of $\mathrm{PA}_{ij}$ was initially achieved by Zurita-Gotor and Rosner [221] and more recently improved [223,224,231]. Equations for the transition regime, expressed as a function of the $K_{n,D}$, were initially developed by Fuchs [215] (flux matching approximation), Dahneke [232] (kinetic theory), and Sahni [216] (solving the Fokker–Planck equation). Transition regime collision kernels were initially incorporated in soot agglomeration modeling in 1998 by Kazakov and Frenklach [58] based on the harmonic mean approach originally proposed by Pratsinis [233] which exhibits a maximum deviation of 15.4% regarding Fuchs' approach in the transition regime. More recent works, have proposed more accurate expressions for $\beta_{ij}$ in the transition regime based on Langevin dynamics simulations [234,235].

#### 3.3.3. Rotation of aggregates and its importance to aggregation process

The rotation of aggregates, as the result of interaction with the surrounding gas or with other clusters, is commonly neglected in DEM and MC simulations of soot formation under flame conditions due to its believed low impact on inter-particle collision frequency and agglomerates' morphology. We remark that a random rotation of aggregates before collisions is allowed in the DSPB simulations [97]. In addition, Zurita-Gotor and Rosner [221] analytically accounted for agglomerates' rotation effect on their collision diameters in the transition particle–particle interaction regime. Langevin dynamics simulations of agglomeration have found up to 16% increase in effective collision

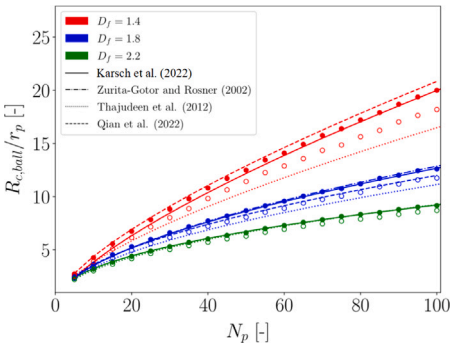


**Fig. 15.** Comparison of Karsch et al. [224] Langevin Dynamics simulations for the ballistic collision radius with existing models. Filled circles represent results obtained from computations that include cluster rotation whereas open circles indicate simulation results that account for translation only.
*Source:* Adapted from [224].

**Table 1**
Soot surface reactions that include the HACA mechanism for soot surface growth and oxidation [239] with reaction rate per-site given as $k = AT^b\exp(-E/RT)$. $\varphi_{OH}$ is the collision efficiency between soot particles and OH radicals.

| | Reaction | $A$ ($cm^3$/mol/s) | $b$ | $E$ (kcal/mol) |
|---|---|---|---|---|
| $R_1$ | $C_{s-H} + H \leftrightarrow C_s^\bullet + H_2$ | $4.2\times10^{13}$ | 0 | 13.0 |
| $R_2$ | $C_{s-H} + OH \leftrightarrow C_s^\bullet + H_2O$ | $1.0\times10^{10}$ | 0.734 | 1.43 |
| $R_3$ | $C_s^\bullet + H \rightarrow C_{s-H}$ | $2.0\times10^{13}$ | 0 | 0 |
| $R_4$ | $C_s^\bullet + C_2H_2 \rightarrow C_{s-H}$ | $8.0\times10^{7}$ | 1.56 | 3.8 |
| $R_5$ | $C_s^\bullet + O_2 \rightarrow 2CO + product$ | $2.2\times10^{12}$ | 0 | 7.5 |
| $R_6$ | $C_{s-H} + OH \rightarrow CO + products$ | $\varphi_{OH} = 0.13$ | | |

radius in the diffusive regime [224] (see Fig. 15). In addition, coarse-grained models for agglomerates' rotation friction coefficient in the transition particle-gas interaction regimes have been developed based on an extended Kirkwood–Riseman theory [236], that may allow considering aggregates' rotation. In addition, the inclusion of rotation may lead to agglomerates with lower fractal dimensions compared to those obtained when rotation is neglected [235,237].

### 3.4. Surface growth

Subsequent to soot inception under fuel-rich conditions, incipient soot particles grow in size and mass through concurrent heterogeneous surface reactions with some gaseous hydrocarbon species, PAH adsorption upon collision with certain PAH species, and coagulation upon collision with other soot particles. The relative importance of these processes varies with the particle size, particle number density, and the local flame conditions (temperature and concentrations of radicals, $C_2H_2$, and PAHs). At later stages of soot formation when soot particles are transported to locally fuel-lean regions of diffusion flames, soot oxidation and oxidation-induced fragmentation become dominant.

The hydrogen abstraction acetylene (carbon) addition (HACA) reaction sequence [238–240] has been accepted to be the dominant mechanism for soot particle surface growth through heterogeneous surface reactions with small hydrocarbon species, predominantly acetylene. The reactions involved in soot surface growth and oxidation are listed in Table 1 following the study by Appel et al. [239]. It is noticed that the first four reactions constitute the HACA mechanism for soot surface growth while the last two reactions ($R_5$ and $R_6$) are actually soot oxidation reactions by $O_2$ and OH and not part of the HACA mechanism.

The kinetics of surface reactions in the HACA mechanism of soot surface growth are described based on surface sites [238,239]. Surface sites refer to carbon atoms that can be saturated with hydrogen, $C_{s-H}$, or dehydrogenated, $C_s^\bullet$. Soot surface is assumed to be composed of unreactive aromatic basal planes and reactive free-edge, zig-zag, and armchair sites. Reactions $R_1$ and $R_2$ are the hydrogen abstraction process through which the saturated surface sites are activated by H and OH radicals to form surface radicals, $C_s^\bullet$, which can also be deactivated by combination with H radical through reaction $R_3$. Reaction $R_4$ is the acetylene addition step to the soot active surface sites through which soot particles gain mass. The rate of soot particle mass gain by reaction $R_4$ can be evaluated as [238],

$$\dot{S}_{sg} = 2C_{\text{mass}}k_4[C_2H_2]\frac{\alpha_s\chi_{C_s^\bullet}A_s n_p}{A_v} \tag{29}$$

where $C_{\text{mass}}$ is the mass of a carbon atom, $k_4$ is the reaction rate of $R_4$ on per site basis, $[C_2H_2]$ is the molar concentration of acetylene, $\chi_{C_s^\bullet}$ is the number of dehydrogenated sites per unit surface area, $A_s$ is the soot particle surface area available for reactions, $n_p$ is the particle number density ($m^{-3}$), $A_v$ is Avogadro number, and $\alpha_s$, the steric factor, is a parameter between 0 and 1 introduced to account for the probability of a $C_2H_2$ molecule to collide with the reactive edge planes [238]. Assuming $C_s^\bullet$ is in steady-state, $\chi_{C_s^\bullet}$ can be evaluated as [238],

$$\chi_{C_s^\bullet} = \frac{(k_1[H] + k_2[OH])\chi_{C_{s-H}}}{k_{-1}[H_2] + k_{-2}[H_2O] + k_3[H] + k_4[C_2H_2] + k_5[O_2]} \tag{30}$$

where $\chi_{C_{s-H}}$ is the number of sites per unit soot particle surface area and takes the value of $2.3\times10^{15}$ sites/$cm^2$ [238]. It should be noticed that this surface site number density was estimated based on a dimer of benzene and represents its upper limit on soot surface. This is the second rationality of introducing the steric factor $\alpha_s$. The third rationality to introduce $\alpha_s$ is to account for dehydrogenation or the decrease in soot surface reactivity as a result of soot chemical transformation, i.e., soot evolves from young soot with high H/C ratios to mature soot with low H/C ratios, which has often been termed soot aging in the literature.

Although the HACA mechanism described in detail by Appel et al. [239], along with the rate constants, has been extensively used to model soot surface growth through $C_2H_2$ addition, very different values or functional expressions of $\alpha_s$ have been assumed in different studies to achieve reasonable agreement with measured soot volume fractions. Different models of $\alpha_s$ as a function of temperature, soot particle size, or thermal age have been proposed and some of these models can be found in a recent review [241] and in [242]. An extended expression of Appel et al. [239] for $\alpha_s$ has been recently proposed by Kholghy and Kelesidis [243]. It is also worth noticing that Chen et al. suggested that the upper limit of $\alpha_s$ is 0.8 to about 0.9 based on a microscopic analysis of accessible surface of homogeneous coronene clusters to $C_2H_2$ molecules [244]. However, none of the proposed $\alpha_s$ values or models can perform equally well for different flame conditions. At the current stage of soot formation modeling using detailed soot models, $\alpha_s$ has to be treated as a tunable model parameter. This situation may be attributed to at least the following two factors. First, the mechanisms of soot mass growth are not fully understood. Second, there are significant uncertainties in the PAH formation and growth pathways leading to soot and the associated kinetic parameters. As a result, the value of $\alpha_s$ requires adjustment when the same soot model is coupled with a different gas-phase reaction mechanism that include PAH formation.

Several attempts have been made to improve the HACA mechanism documented in [239] for soot surface growth. Besides the attempts discussed in [241], Wang et al. extended H-abstraction reactions by three hydrocarbon radicals, namely $CH_3$, $C_2H$, and $C_3H_3$, in addition to H-abstraction by H and OH radicals [245]. This extended HACA mechanism has been recently used by Hoerlle and Pereira [246] to model soot formation in counterflow ethylene non-premixed flames. A very detailed model of PAH growth in soot particles has been developed by Celnik et al. [247]. However, this comprehensive PAH and soot growth model has not gained widespread use in sooting flame modeling, likely owing to its complexity. It is also noticed that more detailed soot surface reactions than the commonly used HACA mechanism of Appel et al. [239] given in Table 1 have been proposed and implemented

into sectional soot kinetics models (SSKMs) [69,72,73,211] discussed in Section 4. These models also emphasized the role of radicals in PAH growth and soot surface reactions.

In addition to the HACA mechanism, growth of soot particles through PAH adsorption is another important route for soot particles to gain mass. This growth mechanism is modeled as collision between soot particles and the soot precursor PAH species [42,43,198,248,249]. Hence, there is an important difference between the HACA mechanism and PAH adsorption for soot surface growth: $C_2H_2$ molecules can only be added to dehydrogenated or reactive sites in the HACA mechanism, but PAH adsorption is not subject to this limitation. The rate of soot particle mass growth through PAH adsorption can be written as,

$$\dot{S}_{sg,\mathrm{PAH}} = 2.2\eta_{\mathrm{PAH}} A_v [\mathrm{PAH}] \beta_{coll} n_p, \tag{31}$$

where the factor 2.2 is an enhancement factor [250], $\eta_{\mathrm{PAH}}$ is the adsorption probability, [PAH] is the PAH molar concentration, and $\beta_{coll}$ is the collision frequency between the PAH species and soot particles, which can be modeled using the free-molecular expression under typical flame conditions at atmospheric pressure [58,249,251,252],

$$\beta_{coll} = \sqrt{\frac{\pi k_B T}{2}} \left( \frac{1}{m_p} + \frac{1}{m_{\mathrm{PAH}}} \right)^{1/2} (D_{c,p} + D_{c,\mathrm{PAH}})^2, \tag{32}$$

where $m_p$, $D_{c,p}$, $m_{\mathrm{PAH}}$, and $D_{c,\mathrm{PAH}}$ are the mass and collision diameter of the soot particle and PAH molecule, respectively. In sooting flames at elevated pressures, it is necessary to employ the transition-regime collision frequency approximated as the harmonic mean between the free-molecular and continuum-regime expressions [58]. Following Frenklach and Wang [251], the PAH collision diameter is estimated as,

$$D_{c,\mathrm{PAH}} = d_A \sqrt{2 m_{\mathrm{PAH}}/3} \tag{33}$$

where $d_A = 1.395\sqrt{3}$ Å is the size of a single aromatic ring. For soot aggregates, different collision diameter models have been proposed [231]. However, the collision diameter of a soot aggregate has often been approximated as the gyration diameter, i.e., $D_{c,p} \approx D_g$ [211,249]. It is noticed that Eq. (31) can be easily generalized to account for adsorption of multiple PAHs on soot surface.

Similar to the sticking probability for soot inception (collision between PAH soot precursors) and for coalescence (collision between young soot particles), the adsorption probability $\eta_{\mathrm{PAH}}$ for the adsorption of PAHs on soot particle surface is also subject to uncertainty and very different values have been assumed in different soot models as discussed in a recent study by Zhou et al. [253]. Zhou et al. [253] investigated the adsorption probability (also called condensation efficiency in some literature) of benzene, naphthalene, pyrene, and coronene on quasi soot surface using reactive MD simulations. Their results showed that the adsorption probability of all the four aromatic species decreases with increasing temperature, especially for lighter molecules. These results are expected since with increasing temperature the molecules have a higher kinetic energy, which results in a higher probability for the molecules to escape the potential well. Based on their reactive MD simulation results, Zhou et al. proposed the following PAH adsorption probability model,

$$\eta_{\mathrm{PAH}} = \begin{cases} 1, & \text{for } \tilde{T} \le p\tilde{n}_c^q \\ \exp\left[ -\left( \dfrac{\tilde{T} - p\tilde{n}_c^q}{r\tilde{n}_c^s} \right)^2 \right], & \text{for } \tilde{T} > p\tilde{n}_c^q \end{cases} \tag{34}$$

where $\tilde{T} = T/1000$ is the scaled temperature ($T$ in K) and $\tilde{n}_c$ is the scaled number of carbon atoms in the PAH molecule relative to that of benzene, i.e., $\tilde{n}_c = n_C/6$. The four model parameters were reported by Zhou et al. [253] as $p = 0.2941$, $q = 0.5063$, $r = 0.6239$, and $s = 0.4528$. They applied their PAH adsorption probability model to the prediction of soot volume fraction evolution in a plug flow reactor containing a rich mixture of $C_2H_4/O_2/N_2$ (equivalence ratio 2.2) at three different temperatures from 1520 to 1705 K. The results showed that (1) this temperature and PAH size dependent PAH adsorption probability model led to good agreement between the prediction and experimental data, (2) the predicted soot volume fraction evolution is sensitive to the assumed constant value of $\eta_{\mathrm{PAH}}$, and (3) no assumed constant value of $\eta_{\mathrm{PAH}}$ can predict the soot volume fraction evolution well at all three temperatures.

Both HACA and PAH adsorption can be important pathways for soot surface growth. However, the relative importance of HACA and PAH adsorption to soot particle surface growth depends on several factors, such as the number density of surface sites on soot particle surface, which is related to the level of soot maturity, and the local flame conditions characterized by pressure, temperature, and concentrations of H and OH radicals, resonantly stabilized hydrocarbon radicals, acetylene, and PAHs. It is worth pointing out that the flame structure or the type of flame also strongly affects the relative importance of HACA and PAH adsorption to soot surface growth. For example, it has been well-known that in the laminar coflow ethylene/air diffusion flame at atmospheric pressure soot surface growth is primarily attributed to the HACA mechanism along the flame wing, where the temperatures and H radical concentrations are high, but to PAH adsorption in the flame centerline region, where the temperatures and H radical concentrations are low [254]. In contrast, the numerical study of Demarco et al. [255] has demonstrated that HACA plays a negligible role in soot surface growth in a laminar coflow inverse diffusion flame. It has also been shown that the relative importance of PAH adsorption to soot surface growth is more significantly enhanced with increasing pressure than the HACA mechanism [256,257]. In premixed flames, the relative importance of HACA and PAH adsorption to soot surface growth was found to depend on the equivalence ratio and the assumption of PAH adsorption reversibility [258].

A large number of numerical studies showed that the modeled soot volume fractions are generally significantly underpredicted in the centerline region of laminar coflow normal diffusion flames fueled with either gaseous hydrocarbons, e.g. [254], or vaporized liquid fuels [259,260], using available detailed soot models. This deficiency of the detailed soot modeling may be partially attributed to uncertainties in PAH formation sub-mechanisms [254,259], PAH sticking probability (also known as collision efficiency) [202,207,209,261], and inception models based purely on physical ground. The recently proposed carbon addition hydrogen migration (CAHM) mechanism [262] may potentially improve the prediction of soot concentration in the centerline region of laminar coflow normal diffusion flames, since the CAHM mechanism of soot surface growth does not require radicals to activate surface sites for acetylene addition. However, the importance of CAHM in soot modeling has not been adequately evaluated and is subject to ongoing debate [263]. Likewise, the recently proposed CHRCR mechanism [264] in PAH growth and soot inception has not been implemented in detailed soot modeling in hydrocarbon flames and its importance to soot inception and growth requires further evaluation [265]. It is also noticed that the reversibility of PAH adsorption on soot particles has drawn attention in recent years [258,266,267]. The reversibility of PAH adsorption on soot surface deserves further investigations and should be done in conjunction with PAH adsorption probability.

## 4. Macroscopic modeling of particle dynamics

In addition to solving the conservation equations of mass, momentum, energy and species mass fractions, a detailed macroscopic numerical simulation of sooting flames generally also requires the solution of the population balance equation (PBE) for soot particles. As mentioned previously, this approach generally does not allow prediction of detailed structure or morphology of individual soot aggregates. In fact, the starting point of macroscopic modeling of soot particle dynamics is to first assume the shape of soot particles. Once the particle shape is assumed, either spheres or fractal aggregates, the modeler will proceed with either the univariate or the bivariate formulation of the

PBE and a proper PBE solving method. When the soot particles are treated as fractal aggregates, some further assumptions, such as soot aggregates are formed by point-contact primary particles and have prescribed fractal properties (e.g. fractal dimension and fractal prefactor), have to be imposed to the PBE solver. The aim of macroscopic modeling of soot particle dynamics is to predict the particle number density, particle size, the mean primary particle diameter and the mean number of primary particle per aggregate if soot particles are assumed fractal aggregates.

Two types of macro-scale approach to couple the gas-phase conservation equations with the PBE for soot particles have been developed. The first type explicitly solves the PBE and takes into account the coupling between soot and gas-phase species involved in soot inception, surface growth, and oxidation to ensure the overall mass balance. Methods of the first type are schematically shown in Fig. 16. It is evident that the gas-phase (left box) and particle-phase (right box) are solved separately, though the two phases are coupled through inception (commonly modeled as collision of PAHs) and surface reactions (HACA and PAH adsorption for surface growth and soot oxidation by OH and $O_2$). Most macroscopic numerical studies of soot formation in laminar flames have been performed using this type of approach to model soot particle dynamics. On the other hand, the other type does not solve the PBE explicitly; instead, it incorporates the aerosol discrete sectional equations into the gas-phase reaction mechanism and express the rates of all the aerosol processes, such as soot inception, surface growth, and coagulation, in the same Arrhenius equation as elementary gas-phase reactions. This latter type of approach, called the sectional soot kinetics model (SSKM) below, was proposed by Howard and co-workers [69,268] and later further developed and applied by the CRECK modeling group [211,269], D'Anna and co-workers [72,73,270], and Gerlinger and co-workers [248,271–273]. The second type approach for incorporating particle dynamics into soot formation modeling is schematically illustrated in Fig. 17, which corresponds to the study of Saggese et al. [211] and should be treated as a specific implementation of the SSKM. Heavier PAHs and soot particles beyond the gaseous species resolved in the gas-phase reaction mechanisms are discretized into a number of bins in terms of either molar mass or the number of carbon atoms. Each bin can be considered pseudo species that are representative of a number of species whose carbon numbers fall in a relatively narrow range. To account for soot surface growth via $C_2H_2$ addition to radical sites through the HACA mechanism, each bin contains both a pseudo stable species and its radical counterpart as a result of hydrogen abstraction. In the example shown in Fig. 17, heavy PAHs and soot particles are discretized into 20 bins in terms of the number of carbon atoms ($N_c$). PAHs with carbon numbers between 20 and 40 are lumped into BIN1 and each next larger BIN covers about twice the carbon numbers. BIN1 to BIN4 represent lumped PAHs and their radicals (PAHs*). BIN5 to BIN12 represent spherical particles with volume-equivalent diameters ($D$) from 2.04 up to 10.14 nm. For larger particles beyond BIN12, they are considered as agglomerates of spherical particles with a diameter of 10.14 nm, i.e., spherical particles in BIN12, and the number of primary particles $N_p$ in each bin is also shown at the bottom row of Fig. 17. The main difference between the SSKMs and the first type of method is that the SSKMs do not solve the PBE explicitly and treat the particle-phase as pseudo species. Further details of SSKM will be discussed in Section 4.3. A discussion on the advantages and disadvantages of the PBE-based methods (the first type) and SSKMs will be given in Section 4.4.

This section discusses the use of both types of macroscopic methods to model soot particle dynamics, the typical solution methods of the PBE for modeling sooting flames using methods of the first type, advantages and disadvantages of the two types of method, and their limitations as compared to detailed discrete element methods.

### 4.1. Population balance equation

The distribution of aerosol particle sizes is described by the number density function (NDF). The NDF is defined as the expected number of particles, $\eta$, presenting certain properties of interest ($\boldsymbol{\zeta}$, called *internal coordinates* and constituting the *phase-space*) inside an infinitesimal control volume located at physical position $\boldsymbol{x} = (x_1, x_2, x_3)$ at time $t$. Here, it is assumed that the length scales of changes in the *continuous* phase are much larger than the *disperse* phase (solid particles for the case of soot). The PBE is a conservation statement that describes how the NDF ($\eta = \eta(\boldsymbol{x}, t; \boldsymbol{\zeta})$) evolves in physical-space, time, and phase-space. The general form of the PBE for soot particles can be written as [38,39]:

$$\frac{\partial \eta}{\partial t} + \frac{\partial}{\partial x_i}\left(u_i \eta\right) - \frac{\partial}{\partial x_i}\left(V_{T,i}\eta\right) - \frac{\partial}{\partial x_i}\left(\mathcal{D}\frac{\partial \eta}{\partial x_i}\right) = \dot{S}_{\boldsymbol{\zeta}}(\boldsymbol{\zeta}). \tag{35}$$

In Eq. (35), from left to right, the terms represent respectively the accumulation or temporal variation rate of NDF, the advection or drift terms in physical-space due to the fluid velocity ($\boldsymbol{u} = (u_1, u_2, u_3)$) and the thermophoretic effects, the diffusion of the NDF controlled by the diffusion coefficient $\mathcal{D}$, and finally the source term $\dot{S}_{\boldsymbol{\zeta}}(\boldsymbol{\zeta})$. Eq. (35) is written in Einstein's notation, i.e., repeated indices mean summation. The source term on the right-hand-side (RHS) of the equation comprises continuous and discontinuous changes on each of the internal coordinates selected for the particle description:

$$\dot{S}_{\boldsymbol{\zeta}}(\boldsymbol{\zeta}) = P - \frac{\partial}{\partial \zeta_i}\left(G_{\zeta_i}\eta\right). \tag{36}$$

In the context of soot modeling, $P$ accounts for discontinuous processes such as inception, aggregation or fragmentation, whereas $G_{\zeta_i}$ is a growth (or shrink) function representing the continuous rate of change of particle size in each particular internal coordinate $\zeta_i$. Note that on a fundamental level, all processes are discontinuous, but they can be treated as continuous if their length and time scales are much smaller than the changes on the particle. For soot formation in flames, surface growth via polycyclic aromatic hydrocarbon (PAH) adsorption and the HACA mechanism, and the surface shrinkage via oxidation by OH radicals and $O_2$ molecules can be treated as continuous processes.

The description of the NDF can be accomplished by using one (univariate), two (bivariate), or multiple (multivariate) internal coordinates, depending on the level of detail desired for the aggregate description and computational time restrictions. The univariate formulations use the mass or volume-equivalent diameter of the aggregate as the sole internal coordinate, which effectively considers soot aggregates as spherical particles. The simplest univariate formulation is to treat soot aggregates as locally monodisperse spherical particles as done in empirical two-equation soot models, such as in [274]. The univariate formulation allows access to the overall mean properties of the NDF, but provides no further details about the morphology of soot aggregates beyond the volume-equivalent diameter. To take into account the fractal-like structure of soot particles, at least two independent internal coordinates are required to predict the mean diameter of primary particles and the number of primary particles per aggregate. Different options for the two independent internal coordinates have been used: aggregate volume and surface area [45,275,276], aggregate volume and the number of primary particle [46,277], the number densities of aggregate and primary particle in each soot section [42,43,67].

### 4.2. Solution methods of PBE

The main issue for finding the solution of the PBE lies in the closure of the source terms $\dot{S}_{\boldsymbol{\zeta}}(\boldsymbol{\zeta})$. These terms account for particle–particle or particle-gas interactions in continuous or discontinuous fashion. Either way, they have to consider all the possible sizes of the particle population for each internal coordinate, resulting in infinite integrals (unclosed terms) that have to be evaluated. This has prompted the development of different methods to attain the source terms' closure and obtain an approximate solution of the PBE. Stochastic methods,

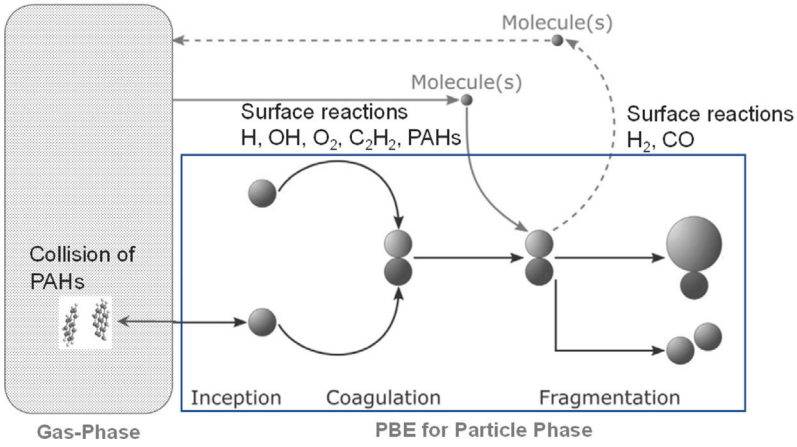


**Fig. 16.** Schematic of the relationship between the gas-phase (left box) and the particle phase (right box) in the first type methods for dealing with soot particle dynamics in modeling sooting flames. The two phases are coupled through soot inception and soot surface reactions involved in soot surface growth and oxidation.
*Source:* Modified from Boje and Kraft [99].

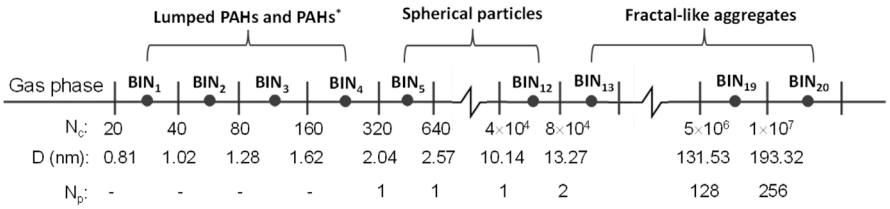


**Fig. 17.** Schematic illustrating how the heavier PAHs and soot particles are handled in the sectional soot kinetics model (SSKM). The PAH and particle mass space is divided into a number of bins in terms of the number of carbon atoms $N_c$. The corresponding volume-equivalent diameter $D$ and the number of primary particles per aggregate $N_p$ for each bin are also shown.

such as the direct simulation Monte Carlo (DSMC) algorithm [278–281], are the most accurate methods to reproduce the NDF. These kinds of method simulate each underlying soot event explicitly, with a probability of occurrence based on the rate of each soot process. However, these methods are extremely computationally expensive and, thus, suited only for 0D or 1D configurations of reactive systems, or in an uncoupled fashion with the flow field. Therefore, the two alternative methods that are less computationally expensive, namely the sectional methods and moment-based methods, have been extensively used for modeling particle dynamics in complex configurations. Fig. 18 shows a schematic of different selected PBE methods, discussed below, and their capabilities to reproduce the PSD of a bimodal distribution, characteristic of sooting zones where both inception and aggregation are present. Monte Carlo methods are able to reproduce accurately the actual PSD. With an adequate resolution of particle size, the sectional method can well capture the actual PSD, though numerical diffusion can be a concern [282,283]. The method of moments (MOM) can predict the mean particle size and the deviation with reasonable accuracy; however, it in general cannot predict the PSD unless the functional form of PSD were prescribed. The hybrid MOM, which was proposed by Mueller et al. [63], is able to capture the mean particle size for both the first mode (inception mode) and the second mode (aggregation mode). Boje and Kraft presented an overview of PBE solution methods in their recent review [99].

#### 4.2.1. Sectional methods

Sectional methods are macroscopic models that discretize the continuous particle size or mass space into a series of sections or bins, in which each section represents a relatively narrow range of particle sizes or masses. To effectively capture the entire size distribution of soot particles, these sections should be sufficiently fine and span a broad size range covering from the smallest to the largest particles in the system of interest. The design of the section spacing and span can leverage prior information about the PSD. This discretization transforms the particle size distribution into a set of transport equations for the particle number densities within each section, enabling an explicit and detailed tracking of PSD evolution. In soot modeling, two main approaches have been developed within the framework of sectional methods. The first treats soot particles separately from the gas phase, explicitly solving the population balance equation, a strategy widely used in the aerosol community. The second represents soot particles as pseudo-gas species with properties linked to their size and mass, integrating them into the kinetic mechanism governing flame chemistry. The following discussion focuses on the first approach, which directly solves the PBE, while details of the second approach, namely the sectional soot kinetic model (SSKM), will be discussed in Section 4.3.

The literature contains numerous studies and variations of sectional methods. In this review, we highlight only a selection of studies relevant to our focus, without attempting a comprehensive overview. For a more exhaustive review, readers are referred to [99]. In the context of explicitly solving the PBE, different variations of sectional methods have been developed based on whether the sections are fixed or moving, as well as on the number and type of internal coordinates used to describe the number density function (NDF). These developments have been greatly driven by the aerosol scientific community, and adopted to some extent by the combustion community. For example, Gelbard and Seinfeld [284] developed a univariate sectional method that accounted for coagulation, intraparticle reactions, inception of solid particles from the gas phase, and particle growth and shrinkage, with the objective of capturing the evolving size distribution, as well as the variation of chemical composition with particle size. Building on this, Xiong and Pratsinis [285] introduced a bivariate sectional method that accounted for simultaneous changes in particle volume and surface area, considering coagulation and sintering processes, implemented for gas phase powder production. Colket and Hall [65]

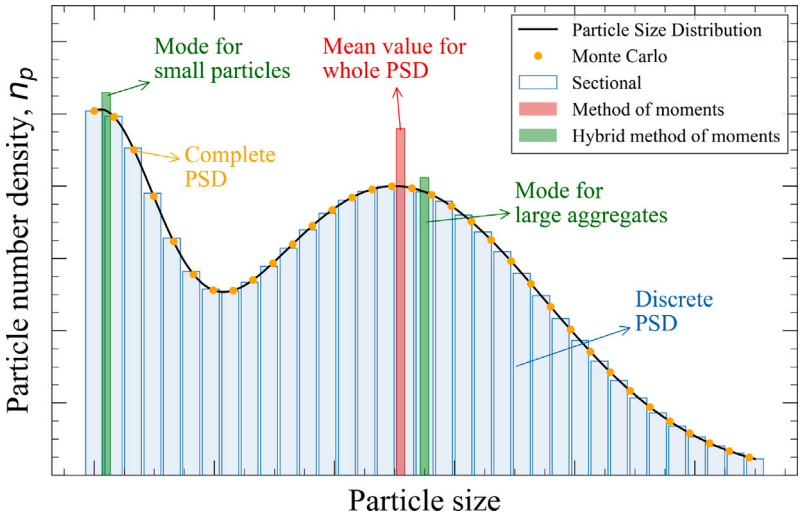


**Fig. 18.** Schematic of the capabilities of predicting the particle size distribution by different methods for solving the PBE.

also employed a fixed-sectional approach to model laminar premixed flames, accounting for inception, surface growth, and particle coalescence. Smooke et al. [66] extended these methods to laminar coflow diffusion flames. Nakaso et al. [286] further refined these methods to provide a more accurate representation of the smallest particles, finding qualitative agreement with experiments performed on titania particles. Although these formulations improved the fidelity of soot predictions, the computational demand grew substantially with the complexity of the description. To mitigate the computational cost, modified sectional methods were developed. For example, assuming a uniform particle size within each section reduces the number of integrals needed to evaluate coagulation and adsorption kernels, thereby decreasing computational expense [67,287,288]. Different internal coordinates have also been employed for the particle description: both volume- and surface-based sectional methods have been studied [275,276], and Park and Rogak [277] introduced a method that uses the number of primary particles as an internal variable to explicitly consider surface growth through the deposition of small clusters. They subsequently developed a bivariate fixed-sectional method using both aggregate number density and primary particle number density as internal coordinates, enabling a fractal representation of soot aggregates [67], and developed subroutines [47] that can be easily employed in kinetic packages such as Chemkin. This approach supported the development of the CoFlame code [42,43], a numerical tool that has been used in various studies for soot modeling in laminar coflow flames. Implementations in this code discretize the PSD into $N_S$ fixed mass sections and solve conservation equations for both aggregate number density ($n_p$) and primary particle number density ($n_{pp}$), capturing soot inception, surface growth, oxidation, and aggregation-induced redistribution of particles between sections. Subsequent improvements by Dworkin et al. [254], Veshkini et al. [242], and Saffaripour et al. [289,290] have enhanced predictions of soot volume fraction and particle size distributions in diverse flame configurations. Notably, adding comprehensive PAH growth pathways, thermal aging mechanisms, and reversible PAH adsorption models have further strengthened the predictive capabilities across both premixed and diffusion flames [242,266]. More recently, Kholghy et al. [189] enhanced this sectional method by incorporating the tracking of hydrogen atoms within each section alongside the number densities of primary particles and aggregates. This advancement enabled the calculation of a hydrogen-to-carbon (H/C) ratio for each section, providing a basis to quantify the degree of maturity of soot particles.

It is worth noting that, despite the computational cost of this method, it has been successfully applied even in turbulent flame conditions. For instance, Rodrigues et al. [48] utilized a soot sectional model in large-eddy simulations of turbulent non-premixed flames. Similarly, Sun and Rigopoulos [291] applied a sectional approach to turbulent flames, focusing on accurate moment conservation in the discretization of aggregation while employing the same gas-phase chemistry, soot kinetics, and aerosol dynamics models previously used for laminar coflow flames [196]. For a more comprehensive review of soot dynamics in turbulent flows, readers are directed to the work of Rigopoulos [64].

One of the problems of the fixed-sectional method, as mentioned before, is that it suffers from numerical instability and numerical diffusion, arising from the continuous surface growth term (second term at the left-hand-side of Eq. (35)) of the population balance equation [68]. Different efforts have been made to diminish this effect and improve the accuracy on the PSD predictions. One straightforward manner to avoid these problems is using a moving sectional method, where the representative sizes of the sections change depending on the surface growth rate [282]. However, this method is difficult to apply to spatially inhomogeneous systems. Another way to diminish numerical diffusion is through high resolution schemes, such as the one proposed by Qamar et al. [292], which is capable to resolve sharp peaks and shock discontinuities, or using coupling the fixed-sectional with stochastic methods [293]. More recently, efforts by Rigopoulos and colleagues have focused on reducing numerical diffusion in fixed-sectional methods through more sophisticated numerical techniques such as adaptative grid approaches [294] or using a composite grid [295].

To address the computational challenge of sectional methods, methods of moments have been developed and employed as an alternative approach to model sooting flames. By reducing the complexity of the problem to the calculation of a small set of moments, these methods can significantly reduce the computational cost, making them more suitable for modeling multidimensional sooting flames and for multivariate formulations. Alternatively, monodisperse population balance models (MPBMs) can be used to simulate particle dynamics minimizing the computational cost [296]. For example, a three-equation MPBM for the total number, area, and volume concentration was developed to describe the evolution of soot volume fraction, number concentration, mean mobility, and primary particle diameters during surface growth, oxidation, and coagulation in the free-molecular [243] and transition [297] regimes. This MPBM was interfaced with EDEM-derived power-laws [94] to account for the evolving soot morphology and found good agreement with experimental data from premixed flames. Nevertheless, the choice between sectional methods and methods of moments often depends on the specific requirements of the problem at hand, including the level of detail needed and the available computational resources.

#### 4.2.2. Methods of moments

Methods of moments (MOM) solve transport equations only for a set of few selected moments of the NDF. Usually, these are lower-order moments that represent physical properties of interest. For example, choosing the volume $V$ and surface $S$ as internal coordinates ($\boldsymbol{\zeta} = (V, S)$) to describe the soot particle morphology, the bivariate moment $m_{kl}$ of the NDF is defined as [45]:

$$m_{kl} = \int_0^\infty \int_0^\infty \eta(\boldsymbol{x}, t; V, S) V^k S^l dV dS. \tag{37}$$

With this definition, the PBE can be transformed into transport equations for the selected set of moments as:

$$\frac{\partial m_{kl}}{\partial t} + \frac{\partial}{\partial x_i}\left(\tilde{u}_i m_{kl}\right) - \frac{\partial}{\partial x_i}\left(\Gamma \frac{\partial m_{kl}}{\partial x_i}\right) = \int_0^\infty \int_0^\infty \dot{S}_{\boldsymbol{\zeta}}(\boldsymbol{\zeta}) V^k S^l dV dS, \tag{38}$$

where $\tilde{u}_i = u_i - V_{T,i}$. The RHS of Eq. (38) is the transformed source term $\tilde{S}_{\boldsymbol{\zeta}}(\boldsymbol{\zeta})$, which has to be closed. Based on the closure strategy, different MOMs have been developed.

Frenklach pioneered the development of moment-based methods applied to soot modeling, introducing governing equations for the moments of a discrete soot particle size distribution in [53]. Frenklach and Harris [54] later implemented these equations numerically, demonstrating the approach for pure coagulation as well as cases involving simultaneous nucleation, coagulation, and surface growth. They employed a polynomial interpolation closure known as MOMIC (Method of Moments with Interpolative Closure), which approximates unknown moments from tracked ones using logarithmic polynomial interpolation. Although MOMIC is efficient, its estimates for unsolved moments, especially those requiring extrapolation, can be inaccurate. An extensive discussion of this method and its application to model soot particle dynamics has been given by Wick et al. [298]. Subsequent work expanded the applicability of MOMIC-based methods. These approaches were used to model soot formation in premixed flames of various fuels [55], at both low [56] and high pressures [57,58], and even captured transitions from coalescent to aggregation growth in laminar premixed flames [59]. Beyond polynomial closures, new strategies emerged to improve accuracy and flexibility of these methods. The Quadrature Method of Moments (QMOM) [60] approximated the source terms by representing the NDF with a set of quadrature nodes and weights, yielding high accuracy for univariate NDFs. However, QMOM proved difficult to extend to multivariate NDFs. Variations such as brute-force QMOM [299], tensor-product QMOM [300–303], and conditional QMOM (CQMOM) [304] partially addressed multivariate challenges, though often with reduced accuracy. The extended QMOM (EQMOM) [305] introduced non-negative weight functions to allow more nodes without increasing the number of tracked moments, and the Direct Quadrature Method of Moments (DQMOM) [62,306] solved transport equations directly for quadrature weights and abscissas, facilitating straightforward multivariate applications. Zucca et al. [307] then coupled the DQMOM approach in its monovariate form to model soot formation in turbulent flames.

In parallel, simplified moment-based formulations also emerged. Assuming spherical, locally monodisperse particles and using mass as the only internal coordinate, Leung et al. [274] developed the classic two-equation model. This model, widely used in complex combustion simulations, has been frequently applied in literature as a simple yet effective tool for soot predictions. Mueller et al. [45] extended MOMIC to a bivariate formulation using volume and surface area as internal coordinates, and Blanquart et al. [308] further refined the approach to track hydrogen content alongside volume and surface. Linking the hydrogen-to-carbon ratio to soot absorption and maturity enabled a more detailed description of soot particles without increasing significantly the computational cost. To enhance the ability of moment methods to capture the distinctive behavior of small incipient soot particles, Mueller et al. [63] also combined MOMIC and DQMOM into the Hybrid Method of Moments (HMOM). HMOM introduces a delta function fixed at the smallest particle size, explicitly accounting for incipient particles and improving predictions of bimodal particle size distributions.

As knowledge of soot morphology advanced, it became evident that fractal-like aggregate structures cannot be fully captured by univariate moment methods alone. At least a quasi-bivariate formulation is required to represent the polydispersity and fractal nature of soot aggregates composed of locally monodisperse primary particles. Various combinations of internal coordinates have been proposed, including particle volume and surface area [45], total particle mass and primary particle number [58], and particle volume combined with primary particle number [46]. Incorporating fractal-like morphology significantly improves predictions, as demonstrated by Xing et al. [46], who found that bivariate moment methods yielded peak soot volume fractions nearly twice those predicted by univariate models in laminar coflow methane/ethanol diffusion flames at 2, 4, and 6 atm. This improvement comes from a more realistic representation of soot surface area and, consequently, its growth and oxidation behavior. Similar findings had also been made in earlier studies, e.g. by Morgan et al. [78]. Salenbauch et al. [50] introduced an EQMOM variant based on superimposed kernel density functions, splitting the entire NDF into sub-NDFs that collectively approximated a gamma distribution. This approach matched the accuracy of Monte Carlo simulations in fuel-rich premixed flames and could also predict particle oxidation. Ferraro et al. [51] subsequently applied this method, combined with LES/presumed probability density function flamelet/progress variable approaches, to model soot PSD in a turbulent Delft Adelaide Flame. Similarly, Wu et al. [52] developed a joint moment projection and maximum entropy reconstruction method to accurately reproduce soot PSDs, successfully simulating soot formation and oxidation in diesel engines and capturing the bimodal distribution arising from concurrent inception and surface growth.

For more detailed overviews of these methods, readers are referred to the reviews by Rigopoulos [64] and Boje and Kraft [99].

#### 4.2.3. Hybrid approaches

In an attempt to benefit from the advantages of sectional methods and MOM while overcome their disadvantages, various hybrid approaches have been developed. Bruns and Ezekoye [309] presented a hybrid sectional quadrature-based moment method. In their model, they discretize the NDF across multiple bins, representing the NDF within each bin using a limited set of Delta functions. They observed that the model delivered superior performance when leveraging coarser sections and a high-order quadrature within each section. Similarly, Laurent et al. [310,311] developed a two-size moment method, which uses a continuous function within each section to reconstruct the NDF and evaluate the particle fluxes between neighboring sections. Recently, Yang and Mueller [312] developed a multi-moment sectional method (MMSM) using polynomial or exponential functions within each section to reconstruct the NDF. Their findings revealed that the MMSM significantly improved the rate of convergence, showing an improvement factor of two when compared to the conventional sectional method. Then, Maldonado and Mueller [313] used this method in a volume-surface formulation coupled to a LES framework to simulate laboratory-scale turbulent non-premixed jet flame. Other approaches combining Monte Carlo and the sectional method have also been proposed, such as the hybrid stochastic/fixed-sectional method [293]. This method combines a fixed number of stochastic particles and discrete fixed-sections to manage agglomeration and inception source terms effectively.

#### 4.2.4. Application to agglomeration with surface growth

To simulate particle agglomeration with surface growth in the case study presented in Section 6, details of how methods of moments deal with agglomeration and surface growth are given here. The DQMOM was selected due to its more straightforward implementation for multivariate formulations [62]. For the test cases studied in Section 6,

a simplified PBE is dealt with since advection, thermophoresis, and diffusion are absent. The source term for surface growth is considered a continuous process, whereas agglomeration is considered a discontinuous one (see Eq. (36)). The DQMOM is formulated in terms of the internal coordinates volume $V$ and surface $S$ of the soot particle. Therefore, growth functions $G_V$ and $G_S$ describing the temporal rate of change for particle volume and surface due to surface growth are required. The specified mass growth rate $\dot{\omega}$ in kg/m$^3$/s is assumed to be deposited on the soot surface homogeneously, so we define a surface mass flux as $\varphi_m = \dot{\omega}/s_{\text{tot}}$, where $s_{\text{tot}}$ is the total specific surface of the aggregate in m$^2$/m$^3$. In a time step $\Delta t$, the mass of an aggregate will increase as:

$$\Delta m = \Delta V \rho_p = S \varphi_m \Delta t \Rightarrow \frac{\partial V}{\partial t} \equiv G_V = \frac{S\dot{\omega}}{\rho_p s_{\text{tot}}}. \tag{39}$$

Considering that in the context of the DQMOM, primary particles are assumed to be spherical and in point-contact, the surface growth function can be obtained using the chain rule as:

$$G_S \equiv \frac{\partial S}{\partial t} = \frac{\partial S}{\partial V}\frac{\partial V}{\partial t} = \frac{\partial S}{\partial V} G_V \Rightarrow G_S = \frac{2}{3}\frac{S^2}{V}\frac{\dot{\omega}}{\rho_p s_{\text{tot}}}. \tag{40}$$

To model the aggregation process, a collision kernel (denoted by $\beta$) is required. At this point, a fractal dimension and prefactor have to be selected to evaluate the collision kernel. Having the collision kernel for aggregation, and growth functions for surface growth, closure of the source terms in the context of DQMOM is direct [62,63,303]. These terms for the moment $kl$ for surface growth ($\dot{S}_{kl}^{\text{sg}}$) and aggregation ($\dot{S}_{kl}^{\text{agg}}$) can be written as:

$$\dot{S}_{kl}^{\text{sg}} = \frac{\dot{\omega}}{\rho_{\text{p}} s_{\text{tot}}} \sum_{i=1}^{N_\delta} w_i \left(k + \frac{2}{3} l\right) V_i^{k-1} S_i^{l+1} \tag{41}$$

$$\dot{S}_{kl}^{\text{agg}} = \frac{1}{2}\sum_{i=1}^{N_\delta}\sum_{j=1}^{N_\delta} \beta_{ij} w_i w_j \left[\left(V_i + V_j\right)^k \left(S_i + S_j\right)^l - V_i^k S_i^l - V_j^k S_j^l\right], \tag{42}$$

where $N_\delta$ is the number of delta functions used for the quadrature approximation and $w_i$ are the weights of these functions. Finally, selecting $N_\delta$ and a set of $3N_\delta$ moments is sufficient to evaluate the source terms.

### 4.3. Sectional soot kinetics models

As shown in Fig. 17, the sectional soot kinetics models (SSKMs) are inherently a sectional approach to incorporate the soot particle dynamics into an extended reaction mechanism, in which heavier PAHs (beyond those included in the base gas-phase reaction mechanism) and soot particles are considered as pseudo chemical species. The framework of SSKM was proposed by Howard and co-workers [69,268] and subsequently modified and improved by several groups [72,211,270,271,273]. It is well-known that PAHs undergo dehydrogenation in flames as they evolve from smaller aromatics with high H/C ratios to pericondensed aromatics with low H/C ratios [21,69]. Soot also undergoes dehydrogenation as they evolve from liquid-like particles at inception to graphitic mature aggregates. It is interesting to notice that dehydrogenation has been taken into account in all the SSKMs. Three similar but somewhat different approaches have been used to account for the dehydrogenation of PAH and soot particles. Richter et al. [69] assigned a single H/C ratio to each bin that decreases with increasing the carbon number (or the bin number). A similar approach was used by Gerlinger and co-workers [271,273]. Saggese et al. [211] considered three subclasses with different H/C ratios for heavier PAHs and spherical soot particles (BIN1 to BIN12 in Fig. 17) and two subclasses for fractal-like aggregates (BIN13 to BIN20 in Fig. 17). This H/C ratio model has also been adopted in a very recent study from the CRECK modeling group [314]. Finally, D'Anna and co-workers [72,270] utilized five bins to track the H/C ratio over the range of 0 to 1. Since radicals (either PAHs or BINs, denoted as PAH* and BIN*; PAH here refers to PAH species resolved in the gas-phase reaction mechanism), not their stable counterparts, are involved in reactions, such as surface growth reactions with $C_2H_2$, each BIN consists of both a stable lumped PAH or soot particle and its radical. All possible reactions involving BIN* with PAH (BIN*-PAH), BIN* with PAH radicals (BIN*-PAH*), and stable BINs with PAH radicals (BIN-PAH*) are included in the extended reaction mechanism and modeled in the same way as gas-phase reactions with details given later. In addition, reactions between stable PAHs, between PAH and BIN, and between stable BINs are also taken into account but modeled as a collision process. Similar to PAHs, stable BINs are activated by hydrogen abstraction with H and OH radicals [69,73] or with only H radicals [211,273,314].

It is important to point out that the H/C ratio in each bin is required in SSKMs to correctly calculate the stoichiometric coefficients of the pseudo reactions involving the pseudo species (bins) to ensure conservation of elements, namely C, H, and O [69,202,211,271,273,314]. To facilitate the discussion of SSKMs, the model of Saggese et al. [211] is used as an example. The classification of BINs and the pseudo reactions and rates are provided in Supporting Material (S3). The BINs defined in this model is also shown in Fig. 17. In this model, the reaction between two pyrene molecules is written as

$$\begin{aligned} C_{16}H_{10} + C_{16}H_{10} &\rightarrow C_{32}H_{20} \rightarrow 0.4\text{BIN}_1 + 0.6\text{BIN}_2 \\ &\rightarrow 0.1667\text{BIN}_{1,\text{A}} + 0.2333\text{BIN}_{1,\text{B}} \\ &+ 0.25\text{BIN}_{2,\text{A}} + 0.35\text{BIN}_{2,\text{B}} \end{aligned} \tag{43}$$

The stoichiometric coefficients of this reaction are derived first using linear interpolation for the number of C atoms in $C_{32}H_{20}$ and those of $BIN_1$ ($N_c$ = 20) and $BIN_2$ ($N_c$ = 40) and then for the number of H atoms from the H/C ratios in the sub-BINs in $BIN_1$ and $BIN_2$ given in Table S3.1.

In the SSKM of Saggese et al. [211], soot inception was modeled as reactions among all the stable and radical lumped PAHs ($BIN_1$ to $BIN_4$ in Table S3.2). In addition to HACA, soot surface growth was also attributed to reactions (i) between stable and radical BINs with resonantly stabilized radicals of hydrocarbon molecules (denoted as RR*), such as $C_3H_3$ and $C_5H_5$, (ii) between stable and radical $BIN_i$ with PAH* for $i \geq 5$, and (iii) between lumped PAHs ($BIN_i$ and $BIN^*_i$, $i \leq 5$) and particle radical BINs ($BIN^*_n$, $n \geq 5$). Oxidation of BINs by O and OH radicals and $O_2$ was taken into account. While $O_2$ was assumed to oxidize only radical BINs, O and OH can oxidize both stable and radical BINs. Coagulation of particles was modeled as follows. While collisions between primary particles ($BIN_5$ to $BIN_{12}$) and between a primary particle and an aggregate ($BIN_{13}$ and above) were assumed to result in coalescence, collisions between two aggregates led to aggregation.

Of particular interest in the context of this review is how particle dynamics is incorporated into the extended gas-phase reaction mechanism in SSKMs. For reactions involving radicals (PAH* and BIN*), the reaction rate was derived from that of a reference gas-phase reaction and consideration of structural similarity [69,70,202,211]. For example, the reaction given in Eq. (43) was taken as the reference gas-phase reaction for soot inception due to reaction between two stable BINs within the first four BINs. Its reaction rate (pre-exponential factor $A_{ref}$ and activation energy $E_{a,ref}$) is given in Table S3.2. The activation energy of reactions between BINs is assumed the same as that of the reference reaction. However, the pre-exponential factor is assumed to vary in proportion to the collision frequency because of the increase in collision diameter of lumped PAHs as

$$\frac{A}{A_{ref}} = \frac{C_f}{C_{f,ref}} \tag{44}$$

where the collision frequency is calculated from the gas kinetic theory as

$$C_f = \sigma^2 \sqrt{\frac{8\pi k_B T}{\mu}} \tag{45}$$

where $\mu$ is the reduced mass, $\sigma$ is the collision diameter. Saggese et al. [211] modeled the soot aggregate collision diameter as

$$\sigma = \sqrt{5/3} \times 2R_g = \sqrt{5/3} \times D_p \times (N_p/k_f)^{1/D_f} \tag{46}$$

Similar to other macro-scale methods, the fractal dimension $D_f$ and prefactor $k_f$ have to be assumed. It is noticed that the latter can be estimated from an anti-correlation between $D_f$ and $k_f$ discussed in Section 2.5. For surface growth by HACA, i.e., $C_2H_2$ + BIN*$_i$ → products, the pre-exponential factor is assumed to be related to that of the reference reaction given in Table S3.2 as

$$\frac{A}{A_{ref}} = 1 + \frac{\chi D^2 \times H/C}{d_{ref}^2} \tag{47}$$

where $D$ is the volume equivalent diameter of the BIN$_i$ for $i \leq 12$ or the primary particle diameter for aggregates ($i \geq 13$), which are formed by spherical particles in BIN$_{12}$ with $D_p$ = 10.14 nm in the SSKM of Saggese et al. [211], $d_{ref}$ = 1.91 nm. The parameter $\chi$ is either 1 for non-aggregate bins ($i \leq 12$) or the number of primary particles, $N_p$, for aggregate bins. For surface growth through addition of RR*, PAH*, and lumped PAH (BIN$_i$ and BIN*$_i$, $i \leq 4$), the reference kinetic parameters are modified by a size dependent sticking probability (collision efficiency) $\eta_s$ as

$$k = A_{ref} \times T^{0.5} \times \eta_s = A_{ref} \times T^{0.5} \times \frac{100 + \sigma^{6.5}}{10^5 + \sigma^{6.5}} \tag{48}$$

where the collision diameter $\sigma$ is in nm. Coalescence and aggregation have no energy barrier and the rate constants are determined in a similar manner to that of PAH adsorption to soot surface, i.e., the pre-exponential factor is multiplied by a size dependent sticking probability given as

$$\eta_s = \frac{100 + \sigma^{8.5}}{10^5 + \sigma^{8.5}} \tag{49}$$

It is noticed that this sticking probability for coalescence and aggregation is higher than that for surface growth given in Eq. (48). However, Saggese et al. [211] did not provide a justification for this choice.

It is somewhat surprising to notice that the rates of coalescence, aggregation, and PAH adsorption on soot surface in the SSKM of Saggese et al. [211] do not depend explicitly on the collision frequency. In other SSKMs, such as Huo et al. [202] and Eigentler and Gerlinger [273], the rate constants of collision-driven processes, namely inception, coalescence, aggregation, and PAH adsorption, are expressed explicitly in terms of the collision frequency. In a recent study, Nobili et al. [314] modified the coalescence and aggregation rate constants by multiplying the volume ratio of the two colliding entities and the number of carbon atoms, respectively. Overall, the rate constants in the SSKMs described by Blacha et al. [271] and Gerlinger [273] are formulated more explicitly in terms of particle related quantities, such as the collision frequency, soot surface area, primary particle diameter. Despite various differences in the division of bins, kinetic constants of pseudo reactions, and the sticking probability model among available SSKMs, these models provide an alternative to solving the PBE explicitly in modeling soot formation in flames.

### 4.4. Discussions of the two types of macro-scale method

Approaches of the first type for macro-scale modeling of soot formation incorporate explicitly soot kinetics into the PBE mainly using the methods of moments or sectional methods. They generally offer a more detailed representation of soot particle dynamics, especially when the PBE is solved using a discrete sectional method. Since the PBE describing the particle-phase processes is solved separately from the gas-phase chemistry frequently through operator splitting, even though the two phases are coupled as shown in Fig. 16, PBE-based methods offer great flexibility to solve the gas-phase governing equations and the PBE using different solvers and at different levels of accuracy when the simulation time is of a concern. Correspondingly, PBE-based methods can be more modular. The flexibility of using different solvers for the gas-phase and particle-phase allows researchers to develop advanced soot kinetic models (inception, surface growth, and oxidation) or better PBE solvers with minimum amount of work to implement the new model or solver into the existing code. On the other hand, solving the PBE using a different methodology from that of the gas-phase requires a careful model formulation to handle the coupling of the two phases to ensure the overall mass, element, and energy conservation. Implementing these methods often involves intricate code development and careful integration with existing solvers, and the computational costs can become significant if a high level of resolution in the particle size distribution is required. In addition, significant efforts are needed to add more advanced capabilities to PBE-based soot models, such as to predict H/C ratio in MOM [315] and the discrete sectional method [189].

In contrast, SSKMs, in which heavy PAHs and soot particles are represented as pseudo-gas species and integrated directly into the chemical mechanism, naturally achieve the coupling of soot kinetics, particle dynamics, and gas-phase reactions. By embedding soot-related physical and chemical processes directly into the standard chemical solver, the complexity of data exchange is reduced since both soot and gas species are treated together within the chemical mechanism, potentially simplifying the implementation and maintenance of the overall model. In fact, if the chemical mechanism contains these pseudo-species, it is straightforward to use it in codes developed for simulation of non-sooting flames without explicit particle dynamic solvers. In addition to tracking the H/C ratio with ease, it is also straightforward to incorporate more detailed soot inception and PAH and soot growth models, as well as dehydrogenation models of PAH and soot particle in SSKMs by adding appropriate pseudo reactions for these processes in the reaction mechanism [73,211]. It is noticed that adding more reactions to a SSKM only slightly increases the simulation time, which increases strongly with the number of pseudo species or bins. On the other hand, this approach can introduce substantially additional numerical stiffness into the system of equations, as it must simultaneously resolve the highly nonlinear and often stiff gas-phase kinetics along with the pseudo-species representing particle-related reactions and dynamics. The SSKM of Sirignano et al. [270] consists of 125 lumped stable species and 125 radicals, meaning that additionally 250 species transport equations must be solved simultaneously with those for gaseous species. Although the SSKM of Saggese et al. [211] employed a smaller number of pseudo lumped species of 100, it is still substantial. For these reasons, SSKMs have often been applied to 1D premixed and counterflow diffusion flames, especially when the primary particles are allowed to vary in the recent development of the SSKM [314]. This extended capability was achieved at the cost of a very large increase in the computational time as a result of using 465 lumped pseudo species.

In addition to being lack of flexibility and having to deal with a very large reaction mechanism, SSKMs suffer additional difficulties. First, the rate constants of reactions involving lumped PAHs and particles are estimated based on some empirically chosen reference gas-phase reactions based on structural similarity and some scaling relationships. Secondly, the thermochemical properties of the pseudo species, such as specific heat and enthalpy, are also estimated. Thirdly, SSKMs have commonly made some highly simplified assumptions of soot particle morphology. For examples, soot particles were assumed spherical in [69,202,270,271] or spherical for small particles and agglomerates formed by monodisperse primary particles of a prescribed diameter for larger particles [211]. A slightly more realistic soot particle morphology model was used by Eigentler and Gerlinger [273]. They assumed soot particles are spherical when their diameters are below 14 nm. Above this value, primary particles undergo aggregation and the primary particle diameters and the number of primary particles in two adjacent aggregate BINs satisfy

$$D_{p,i} = (2/\chi_{coag})^{1/3} D_{p,i-1} \tag{50}$$

$$N_{p,i} = \chi_{coag} N_{p,i-1} \tag{51}$$

where $\chi_{coag}$ is an adjustable parameter to describe coalescence ($\chi_{coag}$ = 1), agglomeration ($\chi_{coag}$ = 2), or anywhere between the two limits (1

$< \chi_{coag} < 2$). It is noticed that the particle volume in $BIN_i$ is twice that in $BIN_{i-1}$, consistent with the classification of BINs [273]. To overcome the limitation of the SSKM of Saggese et al. [211], Nobili et al. [314] recently proposed an improved SSKM in which each aggregate BIN is further classified into sub-bins of different primary particle diameters under the condition that the particle mass is kept constant. As mentioned earlier, this improved capability of predicting primary particle size is gained at the expense of significant increase in the computing time due to the use of 465 bins compared to 100 bins used by Saggese et al.

In summary, macroscopic modeling of soot formation using the first type of methods solves the PBE explicitly for the particle number density function or its moments, while the soot kinetics provide the various source terms describing soot inception, surface growth, and oxidation. In contrast, the second type of methods, namely SSKMs, treat heavy PAHs and soot particles as pseudo chemical species and solve their species transport equations together with those of gaseous species. While the former methods emphasize the particle nature of soot, the latter models treat soot as lumped species. This explains why the former methods can better resolve particle dynamics, particle size distribution, and mean primary particle size and the latter offers a convenient way to incorporate more detailed soot chemistry for inception, surface growth, dehydrogenation, and oxidation.

### 4.5. Limitations of macroscopic methods

The PBE-based macroscopic methods for modeling particle dynamics of fractal soot aggregates in sooting flames discussed above, using either MOMs or sectional methods, have commonly been developed as a quasi-bivariate model assuming polydisperse aggregates formed by locally monodisperse primary particles in point-contact. This practice aims to maintain a compromise between computational efficiency and capabilities since these methods are often used in coupled calculations with flow, gas-phase chemistry, and detailed soot kinetics. As a consequence, such PBE-based macroscopic methods are unable to resolve any details, such as primary particle size distribution, degree of primary particle overlap, and fractal parameters of soot particles beyond the distribution of aggregate size and mean primary particle size in the case of sectional methods, or quantities of interest related to low-order moments in the case of MOMs. On the contrary, these macroscopic methods rely on assumed soot aggregate fractal parameters to evaluate their collision frequency. Even with these limitations, it is preferred to use a quasi-bivariate particle morphology model over the sphere model to more accurately estimate the particle surface area. These limitations also exist in the SSKMs. In fact, it is even more difficult and more computationally expensive for a SSKM to predict the mean primary particle diameter.

### 4.6. Summary of macroscopic approaches

The macroscopic approaches discussed in this review have been implemented in a variety of computational frameworks designed for modeling reactive flows, with different capabilities and levels of complexity for soot predictions. These codes range from specialized solvers focused on fundamental flame studies to large-scale simulation environments suited for practical engineering applications. Their soot modeling strategies differ in terms of numerical formulations, coupling between gas-phase chemistry and particle dynamics, and the level of detail in soot formation and growth/oxidation processes. Table 2 provides a comparative summary of selected codes developed for soot formation modeling in a range of applications, from 0D, 1D, and 2D laminar flames to multi-dimensional turbulent engine combustion, with the features of soot formation modeling highlighted.

## 5. Meso-scale methods for modeling soot particle aggregation

Meso-scale methods track the dynamics of individual particles in the simulation volume and are able to provide their detailed morphological information. The reason for developing modeling capabilities of the morphology of individual soot particles is to not only understand the diversity in the morphology of individual soot particles during the evolution of soot maturity from the viewpoint of particle dynamics but also to better quantify the population-based soot morphology. The latter is required by macro-scale modeling using MOM, a sectional method, or any other macro-scale approaches. Such assumed values of $D_f$ and $k_f$ are typically based on DLCA agglomerates or TEM image analysis and subject to uncertainties, since it has been made clear that soot morphology evolves during the formation process and can have different $D_f$ and $k_f$ from those of DLCA and may vary with flame conditions. In addition, our intention is to make the reader aware of the importance of distinguishing the individual morphology of an aggregate from that deduced statistically on a population (classical method). Indeed, it has been recently shown that the two fractal dimensions can differ, with the individual fractal dimension being lower than the population dimension [129].

In this section, we will first introduce tunable algorithms, which are a class of methods to numerically generate fractal agglomerates with prescribed morphological parameters. Then the rest of this section is dedicated to some fundamental aspects and details related to available meso-scale methods for modeling particle agglomeration and aggregation. The focus is the three commonly used meso-scale approaches to model soot particle agglomeration in the presence of inception, surface growth, and oxidation, namely the event-driven DEM (EDEM), MCAC, and DSPB. Although the DSPB model has recently been reviewed by Boje and Kraft [99], it is useful to include this meso-scale model in the following discussion to better understand the similarities and differences among the three meso-scale approaches.

### 5.1. Tunable algorithms

Tunable algorithms generate individual fractal aggregates consisting of spherical primary particles by particle-cluster or cluster-cluster agglomeration. In these types of methods, the morphology of the growing agglomerate is constrained to respect prescribed fractal dimension and/or prefactor, rather than controlled by certain physical or chemical mechanisms, as implied in their name. Therefore, tunable algorithms are purely a tool to numerically generate agglomerates obeying certain prescribed properties. Aiming at fixing the fractal dimension, Thouy and Jullien [324] introduced the first tunable cluster-cluster agglomeration algorithm. Subsequently, several algorithms were developed [82,166,325–333]. Filippov et al. [82] introduced a method able to preserve both the fractal dimension and the prefactor. This method has been further improved for efficient generation of agglomerates formed by point-touch monodisperse [89] and polydisperse [89,90] primary particles. Tunable algorithms are widely used to study soot morphology [334,335] and particle-light interaction properties [336–339], they are a versatile tool allowing to generate agglomerates of different fractal dimensions that cannot be easily generated with DEM approaches (e.g. $D_f > 2$). Therefore, they are useful to generate fractal agglomerates of different morphology for the purpose of studying the effects of morphology on the physical and optical properties of fractal agglomerates. However, they cannot, in principle, be used to study the physics of soot formation or particle dynamics in flames because they do not take into account the physical or chemical processes involved. It should be emphasized that the particle morphology is imposed in these types of algorithms rather than naturally resulting from the particle dynamics. Also, the selection of the pair of fractal parameters (fractal dimension and prefactor) when varying one of these parameters is uncertain. In this context, the anti-correlations between fractal dimension and prefactor derived from DEM simulations can be

**Table 2**
Summary of codes used for modeling reactive flows and their implementation of soot modeling.

| Code | Description | Soot modeling | Ref. |
|---|---|---|---|
| NGA | LES/DNS solver for variable-density, low-Mach-number reactive flows. | Has been used for soot modeling using different method of moments based formulations in laminar and turbulent flows. | [316] |
| Flamemaster | A 0D reactors and 1D laminar flame solver featuring detailed gas-phase kinetics and flame structure analysis. | Integrates the method of moments to model soot formation and evolution. Supports detailed precursor (e.g., PAH) chemistry and is widely used for fundamental soot formation studies in laminar flames, and to generate tabulated flamelet libraries. | [317] |
| Cantera | An open-source platform for thermodynamics, transport, and detailed chemical kinetics simulations, including 0D reactors and 1D laminar flames. | Does not include a default soot model but allows user-defined coupling of soot formation and growth mechanisms via custom kinetics modules in Python or C++. Flexible for integrating PAH-based soot formation pathways. | [318] |
| CoFlame | A detailed kinetic modeling tool tailored for laminar non-premixed coflow flames. | Employs a fixed-sectional approach to model soot production. Incorporates detailed PAH chemistry to capture soot precursor kinetics, making it suitable for fundamental soot formation studies in laminar flames. | [43] |
| CRECK modeling group codes | Detailed kinetic modeling tools with comprehensive reaction mechanisms for complex fuels and pollutant formation. | Uses lumped PAH and soot precursors treated as pseudo-gas species, allowing soot evolution to be integrated directly with the chemical reaction network. Provides a flexible platform for both laminar and turbulent simulations. | [211] |
| Open SMOKE++ | An object-oriented framework for detailed kinetics simulations developed by the CRECK modeling group. | Has been coupled with methods of moments to predict soot production, and also integrating SSKMs. Integrates detailed gas-phase kinetics and PAH chemistry. | [76] |
| CHEMKIN-Pro | A commercial general-purpose kinetics simulation software used widely in industry and academia. | Offers built-in soot modeling capabilities, including sectional and method of moments approaches coupled with particle tracking, and supports detailed chemical mechanisms. Additionally, it has been used with SSKMs. | [319] |
| OpenFOAM | An open-source CFD toolbox employing finite volume methods for a broad range of fluid flow problems. | Soot modeling depends on user-implemented models and available extensions. Has been used with empirical, semi-empirical, and more detailed soot formulations (e.g., sectional or moment-based) integrated alongside turbulent combustion models. Also, it is the base for OpenSMOKE++. | [320] |
| S3D | A DNS code designed primarily for fundamental turbulent studies in reacting flows. | Incorporates Lagrangian particle tracking and detailed PAH chemistry. Has been used along with the method of moments for soot production. | [321] |
| AVBP | A LES solver for the compressible Navier–Stokes equations in laminar and turbulent reactive flows, capable of handling complex geometries and combustion systems. | It can simulate two-phase flows, including soot, using either Lagrangian or Eulerian frameworks, and has been applied with methods of moments, sectional methods, as well as simplified empirical and semi-empirical approaches. | [322] |
| KIVA | A CFD code widely used for internal combustion engine simulations. | Uses Lagrangian particle tracking for soot, and has been coupled with method of moments and simplified phenomenological approaches. | [323] |

used (see Section 2.5). Recently, Tomchuk et al. [340] explored the limits in fractal dimension and prefactor that can be generated with tunable algorithms. Tunable algorithms have been recently reviewed by Tomchuk [341]. To summarize,

- Tunable algorithms can generate aggregates with a fractal dimension commonly between 1.4 and 2.4.
- For a prescribed fractal dimension $D_f$, the corresponding fractal prefactor has to be chosen carefully. An anticorrelation between fractal dimension and prefactor can be used for this purpose, see Section 2.5.
- Cluster-cluster approach should be preferred over monomer-cluster. The latter should be limited to generate aggregates containing a relatively small number of monomers ($< 20$).
- Tunable algorithms are limited in terms of the physics of aggregation as they do not explicitly simulate the trajectories of particles controlled by the underlying physical processes and thus they cannot account for effects of temperature, particle chemical composition, surface reactions, and particle concentration on the particle morphology.

### 5.2. An overview of meso-scale methods

In this review paper we consider the following definition of DEM simulations: a discrete element method (DEM) is any of a family of numerical methods for computing the motion of a population of particles explicitly (Lagrangian). In DEM simulations, the interactions and contacts involving particles can be resolved individually. Unlike similar methods of molecular dynamics, DEM particles are modeled as coarse-grained objects consisting of a large number of atoms not simulated explicitly. Fig. 19 shows the properties related to simulation system and particles commonly found in DEM simulations. In the context of soot simulations, DEM approaches falling on this definition include velocity-resolved methods and Monte Carlo and DSPB models. Velocity-resolved methods, including Langevin Dynamics, event-driven DEM (EDEM), and MCAC, are briefly discussed below. Monte Carlo models are explained in the next section.

#### 5.2.1. Velocity-resolved methods

Velocity-resolved DEMs simulate detailed evolution of individual particle position and velocity as a function of the residence time based

on the conservation of momentum. Langevin dynamics [342] is one of the most widely used velocity-resolved DEMs. In this method, the dynamics of individual particles are simulated by solving the Langevin equation [342]

$$m\frac{d\vec{u}}{dt} = -f(\vec{u}-\vec{u}_f) + \vec{F}_B + \sum \vec{F}_{ext}, \tag{52}$$

which is a linear, first-order, inhomogeneous stochastic differential equation corresponding to the conservation of linear momentum for an individual particle of mass $m$, velocity $\vec{u}$ and acceleration $d\vec{u}/dt$. The particle dynamics is determined by the external forces $\sum \vec{F}_{ext}$ and the fluid-particle interaction forces, explained as follows. The particle-gas interaction is decomposed into two distinctive forces namely a systematic or Stokes drag $-f(\vec{u}-\vec{u}_f)$ ($\vec{u}_f$ is the surrounding fluid flow velocity and $f$ is the drag constant) and a stochastic force $\vec{F}_B$ resulting from remaining random collisions between the suspended particle and the gas molecules when the drag force is already considered. This force is commonly modeled as Gaussian noise and considered uncorrelated in time,

$$\langle F_B(t)\rangle = 0, \tag{53a}$$

$$\langle F_B(t)F_B(t')\rangle = 6fk_BT\delta(t-t'), \tag{53b}$$

where the brackets $\langle \dots \rangle$ indicate ensemble averages, $T$ is the surrounding gas temperature considered in thermal equilibrium with the particle, $t$ and $t'$ are two distinctive times, and $\delta(\cdot)$ is the Dirac's delta function. The Langevin equation is able to predict the transition from ballistic ($t \ll \tau$) to diffusive ($t \gg \tau$) motion of suspended particles. In this context, it has been used to determine inter-particle collision kernels in the transition regime of particle–particle interactions theoretically [218,343] or numerically without external forces [87,219,220,223,224,226,231,234,235] and considering external forces [229,230]. In particular, soot aggregation has been simulated based on the Langevin equation in Refs. [188,344,345]. Computational implementations of the Langevin equation are commonly done based on the first-order time step Ermak and Buckholz method [346]. However, there are many other methods including a fourth-order time step Runge–Kutta [347] and the Verlet algorithm [344]. A detailed tutorial about the computational implementation of the Langevin equation to simulate suspended particles such as soot is provided by Suresh and Gopalakrishnan [347].

Despite the robustness of Langevin dynamics, the simulation of dilute nanoparticle systems (such as those typically anticipated in laminar sooting flames) can be computationally expensive. And yet, for most of the particles, the trajectory can be easily decomposed in successions of broken lines corresponding to average free paths, at the end of which orientations can be considered random. This drastic simplification, while computationally convenient, ultimately corresponds to what was done for the first DEM-type simulations developed in the 80s and 90s, called diffusion, ballistic or reaction-limited aggregation codes [348]. It should be noted that, in these codes, the mean free path was generally fixed arbitrarily. Although these codes became popular for simulating aggregates with detailed morphology, they suffer from certain limitations including difficulties mentioned as follows. For instance, persistent distance or mean free path was generally aggregation regime dependent, and the codes were unable to evaluate residence times, and were not able to account for other phenomena, relevant to soot formation, such as nucleation or surface reactions taking place in addition to aggregation. This is why the EDEM, MCAC and DSPB codes, which will be discussed in more detail below, were developed.

Event-driven, velocity-resolved methods, such as EDEM [93] can offer good alternatives to standard Langevin dynamics in terms of improved computational time. Event-driven methods can describe the ballistic motion and collision between two particles or agglomerates assuming a hard sphere potential [349]. Based on the initial particle position and velocity, the collision time between two hard spheres can be estimated analytically [349]. So, unlike Langevin dynamics that rely on explicit forward integration schemes with a time step, in event-driven methods the time is propagated based on the smallest time required for two particles or agglomerates to collide [349]. After collision of two particles, the new velocity is estimated based on the momentum conservation [349]. That way, the ballistic motion and coagulation of monodisperse [93] or polydisperse [350] nanoparticles in the free molecular regime is derived from quasi first principles. In addition, event-driven methods have been extended to account for the diffusive motion of nanoparticles in the transition regime [93], as well as for their growth by reactions with gaseous molecules [33]. More details regarding EDEMs used for soot formation, as well as their thorough validation with theory and experimental data are provided in the following sections.

MCAC is similar to EDEM in the sense of tracking individual particles but relies on different methods for estimating the particle persistent distance and its corresponding time step, physical residence time and taking into account the surface growth of primary particles. The particle persistent distance was determined by discretizing the Langevin trajectories of individual particles into segments respecting the application of the random particle orientation rule after displacement [95]. The corresponding time step is deduced by respecting the temporal diffusive advance imposed by Eistein's diffusion equation. This approach ensures an accurate match between the particle trajectories predicted by Langevin dynamics and those predicted by MCAC. A probability for particle displacement is defined to respect a physical residence time for a population of polydisperse aggregates and/or monomers. The mobility diameter of the simulated aggregates, necessary to evaluate their persistent distance, is based on an empirical law described previously (Section 2.3.2) and based on effective density measurements, and taking the regime of primary particle-gas interaction into account [96] and thus resulting in a different approach as compared to other models in the literature. MCAC also allows surface growth to be taken into account [34]. The effect of soot maturity has also been incorporated in terms of particle composition which determines particle–particle van der Waals interactions [206]. Finally, oxidation-induced fragmentation has been implemented in MCAC, enabling it to be coupled with a macro-scale CFD code (CoFlame) to simulate the behavior of soot in a laminar coflow diffusion flame [163].

#### 5.2.2. Monte Carlo methods

Monte Carlo (MC) methods are very versatile but statistical in nature. For this reason, MC methods developed for modeling particle dynamics are often termed stochastic particle methods. Frenklach and co-workers developed a dynamic MC method to study soot particle aggregation with simultaneous surface growth and inception in premixed sooting flames [31,32,158]. In this dynamic MC method, a single particle to be studied, called the *collector*, is placed in the environment consisting of spherical incipient soot particles and gaseous surface-growth species. A primary particle, called the *candidate*, is then chosen and translated towards the collector along a randomly selected ballistic trajectory. Upon collision, the candidate and collector stick together without rearrangement. The collision coefficient $\beta_c$ was calculated using the Fuch's expression [201] with the gas properties evaluated at the local flame temperature. The elapsed time of a single collision (mean time between collisions) $\Delta t$ is defined as

$$\Delta t = 1/\left(\beta_c n_{pp}\right) \tag{54}$$

where $n_{pp}$ is the number density of primary particles. During the elapsed time surface growth can take place at the collector particle surface uniformly through the addition of the gaseous growth species [31,59].

Kraft and co-workers developed a stochastic particle algorithm to model the evolution of soot particle dynamics under concurrent particle inception, surface reactions, and coagulation [78,278] based on the direct simulation Monte Carlo (DSMC) algorithm developed by

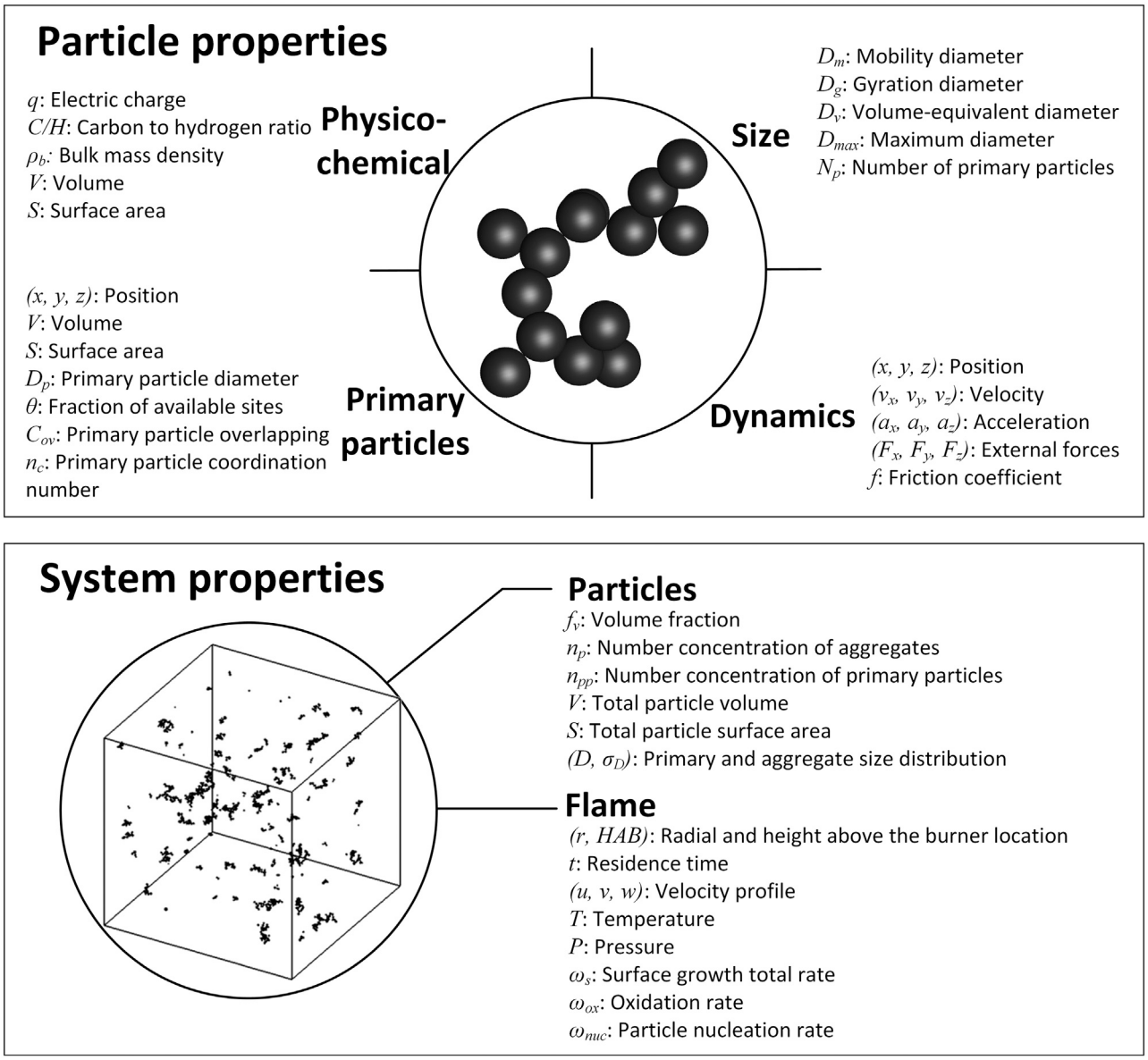


**Fig. 19.** The main internal degrees of freedom in DEM simulations related to the system and particle properties.

Gillespie [351]. Kraft and co-workers made various enhancements to improve the computational efficiency of the stochastic particle model over the DSMC method, such as the use of majorant kernels and fictitious jumps in the calculation of particle coagulation kernel [78,99] and the linear process deferment algorithm [99,280]. Instead of solving the PBE directly, the stochastic particle algorithm approximates the solution of PBE by mimicking the physics of particle dynamics through random generation of events, such as coagulation and surface growth, with the probability of an event being related to its rate. The stochastic particle algorithm, or detailed stochastic population balance (DSPB) model, of Kraft and co-workers was implemented using the waiting time or event-driven method. The DSPB model has been outlined and improved in the last two decades in a series of publications, e.g. [78, 97,205,252,278], and reviewed recently by Boje and Kraft [99]. In the DSPB model, soot particles are treated as fractal-like aggregates formed by overlapping primary particles and each primary particle is composed of a number of PAHs. The following six particle processes are taken into account in the DSPB model: particle inception, coagulation, surface growth, PAH adsorption (commonly termed condensation in the literature), sintering, and coalescence [97,205].

The distinct advantage of the stochastic particle model is that it permits a large number of internal variables of soot particles, including but not limited to the size and relative position of primary particles as well as the C/H ratio. As such, the detailed stochastic particle model is capable of providing comprehensive information of soot particles, such as fractal dimension, primary particle size distribution, degree of overlap between neighboring primary particles, and even the particle composition [197,205,352,353], namely PAHs in the case of soot, which can be related to soot maturity. The disadvantage of stochastic particle models, like other meso-scale methods, is their high computational cost. Consequently, meso-scale methods are typically used as post-processing to obtain detailed morphological and composition information of soot particles [163,205,353].

#### 5.2.3. DEM simulation

In DEM, the dynamics of coarse-grained individual particles are simulated explicitly. As shown in Fig. 19, these types of simulations involve different degrees of freedom related to particle and system properties to be explained as follows. In this context, a fairly large number of spherical primary particles (in the order of thousands)

are initially randomly placed in a domain box, avoiding overlapping between neighbors, and assigned an initial velocity. Particles could be initialized in overlapping positions but then an additional relaxation or energy minimization step, such as the steepest descent method, is needed along with repulsive interaction potentials to iteratively bring the particles apart by fixing a maximum displacement and avoiding numerical error due to infinitely large repulsion forces [354]. The latter method may be needed for simulating systems with extremely high volume fractions ($f_v > 10\%$) where algorithms to search free spaces avoiding overlapping may become too slow or may simply not work. As time evolves, the trajectories of individual particles are simulated considering periodic boundary conditions. Without loss of generality, let us consider a given axis $x$ spanning the range $x = [0, L]$, where $L$ is the length of the domain, a particle that exits the domain at the position $L$ will re-enter at the position $x = 0$ preserving its velocity. The periodic boundary conditions intend to emulate the suspension of particles into an infinitely large system and avoid any nonphysical effect due to the finite size of the domain. In this context, the simulation domain is commonly considered cubic which simplifies the treatment of the periodic boundary conditions. As discussed by Allen and Tildesley [355], in the context of similar Molecular Dynamics simulations, the treatment of periodic boundary conditions in a spherical domain may not be trivial. In addition, the size of the cubic domain $L$ is commonly determined based on a given volume fraction $f_v$, and the total volume of particles in the domain. For example, if a total of $N$ spherical particles, monodisperse in size with diameter $D_p$, are considered, then $L$ is given by Eq. (55a). On the other hand, when particles have a log-normal size distribution with geometric standard deviation $\sigma_{\mathrm{p,geo}}$ and geometric mean $D_{\mathrm{p,geo}}$ then $L$ is given by Eq. (55b) [334],

$$L = \left( \frac{N(\pi/6)D_p^3}{f_v} \right)^{1/3} \quad \text{for a monodisperse PPSD,} \tag{55a}$$

$$L = \left( \frac{N(\pi/6)D_{\mathrm{p,geo}}^3 \exp(9\ln^2[\sigma_{\mathrm{p,geo}}]/2)}{f_v} \right)^{1/3}$$

for a polydisperse PPSD. (55b)

#### 5.2.4. Coarse-graining the morphology of aggregates in DEM

One important question that arises in the context of DEM simulations of nanoparticle aggregates is how to coarse-graining their morphology, i.e., up to what level of detail we need to describe the aggregates to simulate their dynamics and transport phenomena. As shown in Fig. 20, we distinguish two models, the rigid-body and the so-called monomer-resolved models. In the rigid-body model, the aggregate consists of point-touching primary particles, the dynamics of the aggregates are described by a single velocity and position vectors, and they are displaced as rigid or non-deformable bodies. In the so-called monomer-resolved model, the movement of each individual primary particle belonging to the aggregate is simulated. In this model, each primary particle belonging to the aggregate has an independent velocity vector, and primary particles are held together by attractive interaction potentials. As discussed by Inci et al. [356], without including bonds limiting the sliding and rolling of monomers on the surface of neighbors this model will result in compact and sphere-like aggregates. The rigid-body model is commonly preferred in the literature for the following reasons: (1) simplicity as it requires much less number of interactions to be computed, it does not involve models for inter-monomers interaction potentials, as well as sliding and rolling criteria, (2) despite not being monomer-resolved, it can consider the inter-aggregate aerodynamic interaction through a properly adapted friction coefficient as discussed in Section 2.3, (3) computational efficiency and stability. Of course, resolving the dynamics of each primary particle belonging to an aggregate may be computationally expensive, especially at long residence times where large soot aggregates may be formed. In addition, the monomer-resolved model may become numerically unstable in the limit of infinitely large aggregates due to the propagation of stochastic forces within the aggregates.

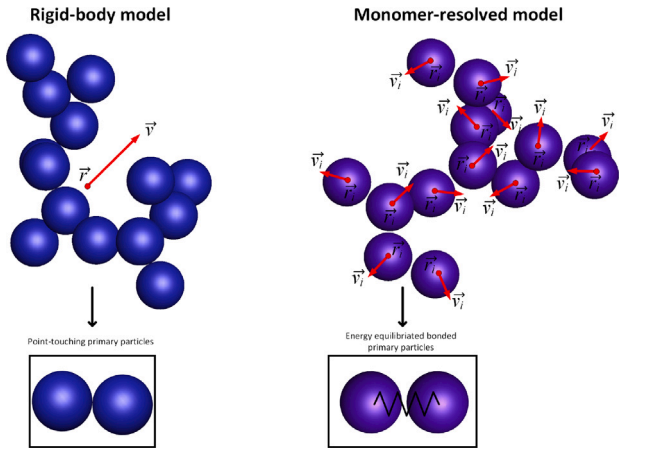


**Fig. 20.** Two models for coarse-graining the morphology of soot aggregates including the rigid-body where the aggregate dynamics are described by a single velocity and position vector and the aggregate is considered as a rigid body. The so-called monomer-resolved model simulates the dynamics of each individual primary particle.

#### 5.2.5. Particle–particle interaction potentials

Soot particle interaction forces $\vec{F}$ can be long-range (e.g., Coulomb) and short-range (e.g., van der Waals). These forces can be alternatively analyzed in terms of the potential energy $W$, which is related to $\vec{F}$ as $\vec{F} = -\vec{\nabla}W$, where $\vec{\nabla}$ is the gradient operator. The short-range interactions, notably van der Waals, may considerably enhance coagulation. Harris and Kennedy [250] estimated that an enhancement factor of about 2.2 leads to good agreement between simulated and measured soot particle size distribution. Such coagulation enhancement is especially important in the ballistically-limited, as compared to the diffusion-limited, particle collisions [229].

In the context of DEM simulations, the short-range particle interaction potentials can be modeled considering a Lennard-Jones interatomic potential $w(r)$, where $r$ is the center-center distance and $w(r)$ is the interaction energy between atoms,

$$w(r) = w_{\mathrm{rep}}(r) + w_{\mathrm{vdW}}(r) = 4\epsilon \left[ \left(\frac{\sigma}{r}\right)^{12} - \left(\frac{\sigma}{r}\right)^{6} \right] \tag{56}$$

where parameters $\epsilon$ and $\sigma$ correspond to the potential well and the characteristic distance where the inter-atomic potential is null, respectively. Both $\epsilon$ and $\sigma$ are dependent on the type of atoms and thus on the chemical composition of particles. This potential is composed of two components, namely $w_{\mathrm{rep}}(r)$ and $w_{\mathrm{vdW}}(r)$ corresponding to the repulsion due to the overlap of electron orbitals, and the van der Waals attractions, respectively. However, all-atom calculations are too computationally expensive, and thus coarse-grained models must be employed to determine these interaction potentials between macroscopic bodies. As described in the following section, such coarse-graining can be done at either the primary particle or the agglomerate level.

*Primary particle coarse-grained potentials*

Integrating Eq. (56) over the volume $V_1$ and $V_2$ of two spherical particles having $\rho$ atom number density and separated by a center-center distance $d$ leads to an attractive term $W_{\mathrm{vdW}}(d)$ originally derived by Hamaker [357], and an analogous repulsive term $W_{\mathrm{rep}}(d)$ proposed by Inci et al. [356],

$$\begin{aligned} W(d) &= W_{\mathrm{rep}}(d) + W_{\mathrm{vdW}}(d) \\ &= \rho^2 \int_{V_1}\int_{V_2} w_{\mathrm{rep}}(r) dV_2 dV_1 + \rho^2 \int_{V_1}\int_{V_2} w_{\mathrm{vdW}}(r) dV_2 dV_1 \end{aligned} \tag{57}$$

We note that $w(r)$ and $W(d)$ are different interaction energies. While the former corresponds to the interaction between a pair of atoms, the latter is the coarse-grained or integrated interaction between two macroscopic objects consisting of a large number of atoms. These

integrals have the following analytical solutions for the attractive ($W_{\mathrm{pp,vdW}}(d)$) and repulsive ($W_{\mathrm{pp,rep}}(d)$) components [357],

$$W_{\mathrm{pp,vdW}}(d) = -\frac{A}{12}\left[\frac{y}{x^2+xy+x}+\frac{y}{x^2+xy+x+y} + 2\ln\left(\frac{x^2+xy+x}{x^2+xy+x+y}\right)\right] \tag{58a}$$

$$W_{\mathrm{pp,rep}}(d) = \frac{1}{37800}A\left(\frac{\sigma}{2r_1}\right)^6\left(W_{r1}+W_{r2}+W_{r3}+W_{r4}\right) \tag{58b}$$

where the four components of the repulsive potential ($W_{r1}$, $W_{r2}$, $W_{r3}$, and $W_{r4}$) are given by,

$$\begin{cases} W_{r1} = \dfrac{2x^2+7y^2+9x+29y+9xy+7}{(1+2x+y)(1+x+y)^7} \\ W_{r2} = \dfrac{-2x^2-9x+20y+5xy-7}{(1+2x+y)(1+x)^7} \\ W_{r3} = \dfrac{-2x^2-7y^2+5x+20y-9xy}{(1+2x+y)(x+y)^7} \\ W_{r4} = \dfrac{2x^2-5x+15y-5xy}{(1+2x+y)x^7} \end{cases} \tag{59}$$

with $x = 0.5(d-r_1-r_2)/r_1$ and $y = r_2/r_1$, $r_1$ and $r_2$ are the primary particle radii, and $A$ is the Hamaker constant. Different experimental works such as D'Alessio et al. [207] have highlighted the importance of considering interaction potentials, notably, the Hamaker constant to better understand soot size distribution in flames. A few studies have considered this approach for DEM [231,345] and population balance simulations [209] of soot formation under flame conditions.

*Agglomerate coarse-grained potentials*

Determining the inter-particle interactions at the primary particle level may still be highly computationally expensive. In this context, an alternative method has recently been proposed by Morán et al. [137], where the vdW potential of fractal-like agglomerates with fractal dimensions $D_{f1}$ and $D_{f2}$ and volume-equivalent diameters $D_{v1}$ and $D_{v2}$ can be determined based on the following semi-analytical equation,

$$W_{\mathrm{agg,vdW}} = -\frac{(D_{v1}D_{v2})^3}{9x_d^6}A\left(\frac{(x_d/d)^6}{\left(1-(x_d/d)^{\overline{D_f}-\alpha}\right)\left(4-(x_d/d)^{\overline{D_f}-\alpha}\right)}\right), \qquad \overline{D_f} = \frac{2D_{f1}D_{f2}}{D_{f1}+D_{f2}} \tag{60}$$

where $x_d$ and $\alpha$ are fitted parameters accounting for a vdW characteristic distance between the agglomerates' center of mass, and their morphology, respectively [137].

### 5.3. Implementations of EDEM, MCAC, and DSPB

In this section, some essential aspects related to the implementation of the three commonly used meso-scale methods, i.e., EDEM, MCAC, and DSPB, are reviewed in terms of how to handle the initial incipient soot particles, particle motion and coagulation, and surface growth and oxidation. Moreover, Table 3 provides a detailed comparison of all relevant aspects affecting soot particle size and morphology implemented in EDEM, MCAC, and the DSPB model in terms of physical properties and models, some of which are discussed below.

#### 5.3.1. Initial incipient soot particles

*Event-driven DEM (EDEM)*

In event-driven discrete element modeling, the particle dynamics start with initially assumed incipient soot particles since soot inception is typically not coupled with DEM. In addition, the incipient soot particles are also regarded as soot primary particles in discrete element modeling. In EDEM, 1000 spherical, monodisperse soot primary particles having an initial diameter of $D_{p,o}$ = 2–3 nm, are randomly distributed in a cubic simulation cell [33]. Using 1000 particles in EDEM offers a good balance between computational efficiency and statistics. In particular, using more than 1000 particles does not alter soot dynamics. On the other, reducing the number of initial particles in the simulation box increases the statistical variability of the EDEM simulations. During the evolution of the particle system, the temperature $T$ can be held constant [33] or varied with residence time to be consistent with experimental measurements [163,361]. The pressure is held constant over time but can be varied from 1 to 10 bar to simulate soot particle aggregation at different pressures [360]. The pressure range used in EDEM is limited by the accuracy of the employed air mean free path in such conditions. In this regard, robust relations for the air mean free path derived by atomistic molecular dynamics at a wide range of pressures and temperatures [362] can be used in EDEM to improve its accuracy even beyond 10 bars. An initial soot diameter of 2 - 3 nm is typically chosen here as it is the smallest size identified in the inception peak of laminar premixed flames [155,363] and is a typical nucleus diameter used in soot modeling [364]. The initial number concentration is set based on the highest ones measured in flames at a height where inception has largely stopped [155]. The initial particle velocity is sampled randomly from the Maxwell–Boltzmann distribution based on the set $T$. So, the mean thermal velocity ($\bar{c}$) of each particle is given by [365]:

$$\bar{c} = \sqrt{\frac{8k_BT}{\pi m}}. \tag{61}$$

*Monte Carlo aggregation code (MCAC)*

Similar to the discrete element modeling described in the previous section, spherical primary particles having a critical coalescence diameter are initially introduced into the simulation box. In this context, primary particles are randomly placed in the simulation domain avoiding overlapping with neighbors. As listed in Table 4, most meso-scale simulations in the literature considered soot inception to have stopped at the beginning of the simulation. One exception is the recent study of Morán et al. [163], who considered a time-evolving soot inception rate $\dot{\omega}_{\mathrm{Incep}}$ obtained from macro-scale simulation of a laminar coflow diffusion flame using a detailed soot model. In this approach of accounting for soot inception, the number of monomers ($N_{pp}$) to be added into the simulation system is determined as,

$$\frac{dN_{pp}}{dt} = \frac{\dot{\omega}_{\mathrm{Incep}}}{m_{\mathrm{Incep}}} \tag{62}$$

where $m_{\mathrm{Incep}}$ is the mass of the incipient soot particles.

*Detailed stochastic population balance method*

The DSPB algorithm of Kraft and co-workers starts with the selection of a predefined maximum number of particles to be simulated $N_{\max}$ in the simulation volume. The simulated particle ensemble represents the real population of particles in the simulation volume. The size of the initial simulation volume is determined according to the following expression

$$V_{\mathrm{simu}} = \frac{N_{\max}}{n_{p,\max}} \tag{63}$$

where $n_{p,\max}$ is the maximum particle number density over the course of simulation for the problem being studied [97]. Due to particle aggregation, the number of particles in the simulation volume can decrease over time. To maintain a statistically significant number of simulated particles in the simulation volume, the particle ensemble is doubled when $N(t) < N_{\max}/2$ occurs. This is done by duplicating each particle and doubling the size of simulation volume [97]. Although it is possible to initiate the detailed stochastic population balance (DSPB) modeling by introducing a large number of primary particles in the simulation volume similar to MCAC and EDEM described above, DSPB modeling has typically been coupled with a kinetic Monte-Carlo aromatic site (KMC-ARS) model for growth of PAHs [247,370] and a PAH-based soot

**Table 3**
A detailed summary of the features used in EDEM, MCAC, and DSPB model.

| | EDEM | | | MCAC | | | DSPB | | |
|---|---|---|---|---|---|---|---|---|---|
| | Relation/Equation | Comment | Ref. | Relation/Equation | Comment | Ref. | Relation/Equation | Comment | Ref. |
| The smallest size ($D_c$) | 2–3 nm | Smallest particle diameter measured for soot and CB nanoparticles. | [94] | 8 nm | Considered as the minimum non-coalescing particles. | [34] | Not prescribed | Different sized PAHs are simulated using the kinetic Monte Carlo method. Two PAHs sticking together upon collisions form a primary particle. | [197, 198, 205] |
| Coalescence | Ø | Considered in the early development of EDEM. Coalescence results in an underestimation of the mean mobility size of soot by 25%, thus, it has not been considered since then. | [94] | Ø | Not considered ($D_c$ is supposed large enough) | [34] | ✓ | Considered as a special case of sintering, i.e., the characteristic sintering time is very small when a colliding particle diameter is less than the critical $d_p$ set to be about 1.58 nm. | [197, 205, 353] |
| Evaluation of aggregate gyration radius ($R_g$) | ✓ | Based on the radial density distribution of the discretized particle. | [93, 128] | ✓ | Based on the matrix of inertia of the discretized particle | [131] | ✓ | Based on an imposed $D_f$ = 1.8 in earlier version of DSPB, e.g. [198]. In the current version, $R_g$ is calculated based on its definition. | [97, 205] |
| Evaluation of aggregate mass ($m$) | $m = m_p N_p$ | Sum of the mass of the monomers. The real mass of overlapping primary particles is estimated using the Vorlume software, and has been validated with analytical relations for nanoparticle sintering. | [358, 359] | $m = m_p N_p$ | Sum of the mass of the monomers, with a correction considering the overlapping. Exact determination on post-treatment based on a discretization | [34] | $m = \sum_{i=1}^{N_p} m_i$ | Sum of the mass of monomers. The actual monomer mass was evaluated by removing the mass of the caps formed by overlap with its neighbors. | [205] |
| Evaluation of aggregate mobility diameter ($D_m$) | $D_m = 2\sqrt{\frac{a_a}{\pi}}$ | Based on the aggregate/agglomerate projected area, $a_a$. | [144–146] | $D_m = \frac{C_c(D_m)}{C_c(D_p)} D_p N_p^{\alpha/D_f}$ | Semi empirical relation based on effective density measurements. $D_f$ is *a-priori* fixed | [153] | $D_m = 2R_g(N_p^{-0.2} + 0.4)$ for $N_p > 3$, $D_m = 2R_g$ for $N_p \leq 3$ | The mobility diameter is closely related to the particle gyration diameter for $N_p > 3$ and assumed to be the same as the particle collision diameter for $N_p \leq 3$. | [205] |
| Consideration of change of flow regime | ✓ | Particles follow ballistic or diffusive trajectories based on their mean free path. | [93] | ✓ | Based on the function above | [95] | ✓ | The flow regime is considered only in the calculation of the coagulation (collision) rate of two particles. | [97] |
| Orientation of the selected particle | Isotropic | – | – | Isotropic | – | [95] | Random | The two particles chosen for coagulation are randomly rotated around their centers of mass before undergoing ballistic cluster-cluster aggregation with a random impact parameter. | [97] |
| Probability of selection of a particle displacement along its mean free path | Ø | Particles move across their mean free path based on their velocities that have a Maxwellian distribution | [93] | $P_{\text{select}} = \frac{\Delta t^{-1}}{\sum_i \Delta t^{-1}}$ | Particle are randomly selected with weighting related to their mobility | [95] | Ø | The motion of particles in the simulation volume is not tracked. | |
| Persistent distance (in the absence of collisions) | $\lambda_p = \tau\sqrt{\frac{8k_BT}{\pi m}}$ | Computed to determine whether the particles continue their ballistic trajectory or change their motion to a random direction. | [93] | $\lambda_p = 3\tau\sqrt{\frac{2k_BT}{m}}$ with $\tau = m/f$ | Persistent distance computed to enable the hypothesis of isotropy. | [95] | Ø | The motion of particles is not tracked. | |

(*continued on next page*)

**Table 3** (*continued*).

| | | | | | | | | | |
|---|---|---|---|---|---|---|---|---|---|
| Validation of the particle's mobility | ✓ | The EDEM-derived collision frequency was validated with the theoretical one for coalescing spheres in the free molecular, transition & continuum regimes. SPSDs of agglomerates and coalescing spheres have been validated with population balance models and analytical relations. | [93] | ✓ | Based on Langevin dynamics and Einstein's theory. | [95] | Ø | Limited attention was paid to particle's mobility, mainly because the motion of particles was not simulated. The particle mobility diameter was estimated only for the purpose of comparing the prediction to particle mobility size distribution measured by SMPS. | [197, 205] |
| Corresponding time duration | Ø | Estimated by considering all potential particle collisions and choosing the one that would take place faster. This is compared to the particle's time to travel the mean free path, and the smaller time is selected. | [93] | $\Delta t=3\tau$ or $\Delta t=(\sum_i \Delta t_i^{-1})^{-1}$ | Respectively the duration time corresponding to the persistent distance, the increment of residence time for the population after displacement of an individual particle. | [95] | Ø | The time step (also termed waiting time) is sampled from an exponential distribution based on a uniformly distributed random variable and the total rate of inception and coagulation. | [97] |
| Sticking probability at contact between particles | $P_{\text{stick}}=1$ | Considered to be true for $D_p > 10$ nm but applicable for $D_p > 2.4$ nm in flame conditions | [93] | $P_{\text{stick}}=1$ | Considered to be true for $D_p > 10$ nm but applicable for $D_p > 2.4$ nm in flame conditions | [206] | Variable | It is termed collision efficiency and was treated as a model parameter. In a recent study by Hou et al. [209], it was calculated from the interaction potentials between the two colliding particles. | [97, 205] |
| Inception | Ø | Initial number concentration of soot nanoparticles is obtained based on measurements at a height above the burner where inception peaks. | [94] | $\left.\frac{dN}{dt}\right\|_{\text{Incep}} = \frac{\dot{\omega}_{\text{Incep}}}{m_{\text{Incep}}}$ | New particles of diameter $D_c$ are injected. | [163] | Simulated | Modeled as dimerization of two PAHs. | [198] |
| Surface growth | $4\pi R_p^3(t+\Delta t)\rho_p = 4\pi R_p^3(t)\rho_p + 3m_{2C}$ | $R_p$ is increased for every acetylene molecule that reacts with its surface. The amount reacting with each primary particle in a $\Delta t$ is obtained based on reaction kinetics and collision dynamics. $m_{2C}$ is proportional to the primary sphere surface. | [94] | $R_p(t+\Delta t) = R_p(t)+\frac{\varphi}{\rho_p}\Delta t$ | $\varphi > 0$ is the specific mass flux density. | [206] | $R_i(t+\Delta t) = R_i(t) + \frac{\omega_g A_{free}}{A_i \rho_p}\Delta t$ | $\omega_g > 0$ is the surface growth rate, $A_{free}$ and $A_i$ are respectively the total aggregate free surface and the free surface of the $i$th primary particle. | [97] |
| Oxidation | $R_p(t+\Delta t) = R_p(t) - \frac{\omega}{\rho_p}\Delta t$ | The shrinking particle model for surface oxidation is applied for each soot primary particle given a specific oxidation rate, $\omega$. | [185] | $R_p(t+\Delta t) = R_p(t) + \frac{\varphi}{\rho_p}\Delta t$ | $\varphi < 0$ is the specific mass flux density | [163] | Ø | Not considered in all recent studies. Oxidation was considered perhaps only in a few early studies, e.g. Balthaser and Kraft [278] and [203]. | |
| Oxidation-induced Fragmentation | Ø | Not considered | | ✓ | When a pair of primary particles belonging to an aggregate is no longer in contact, then fragmentation occurs (no consideration of vdW attraction) | [163] | Ø | Not considered | |

(*continued on next page*)

**Table 3** (*continued*).

| | | | | | | | | | |
|---|---|---|---|---|---|---|---|---|---|
| Time dependence | $T, P, \rho_p$ | $T$ and $\rho_p$ are varied with $D_m$ based on experimental data and empirical power-laws. High pressures (>1 bar) have also been considered. | [185, 360, 361] | $T, P, \rho_p, \varphi, \dot{\omega}_{\text{Incep}}$ | If MCAC is using temporal variation of these quantities based on CFD results along trajectories | [163] | $T, P, \rho_p, \omega_g, \dot{\omega}_{\text{Incep}}$ | The flame properties are predicted using detailed gas-phase chemistry and MOM. These residence-time dependent properties are used as input to the DSPB modeling. | [205] |
| Morphological descriptors | ✓ | Fractal law for population fractal dimension, Mass-mobility exponent, Effective density distribution | [94] | ✓ | Pair correlation function and anisotropy for individual particles, fractal law for population fractal dimension | [163] | ✓ | Current DSPB models track the positions of primary particles (relative to the particle center of mass). The gyration radius can be calculated from its definition. Then the particle collision diameter and mobility diameter can be calculated. | [97, 205] |
| Size distribution | ✓ | Log-normal/Self-preserving, based on mobility, gyration or volume equivalent spherical diameter | [93, 360] | ✓ | Log-normal/Self-preserving, based on mobility, gyration or volume equivalent spherical diameter | [95] | ✓ | Lognormal type based on mobility diameter. There seems a lack of rigorous validation of DSPB predicted aggregate size distribution against either aggregation theory or other methods. The DSPB results have been compared with experimental measurements. | [97, 203, 205] |

**Table 4**
A survey of soot agglomeration studies using meso-scale approaches and the corresponding flame conditions, key parameters, and the mechanisms of soot particle growth considered. Unless otherwise indicated, all simulations were performed in laminar flows. The considered particle growth mechanisms include agglomeration (Agg.), surface growth (SG), oxidation (Ox.), and inception (Incep.). The key parameters include the initial primary particle size distribution (PPSD), volume fraction $f_v$, temperature $T$, and the maximum residence time $t_{res}$. The surveyed methods include MC: Monte Carlo, LD: Langevin Dynamics, EDEM: Event-driven DEM, MCAC: Monte Carlo Aggregation Code, and DSPB: detailed stochastic population balance model. The abbreviation N.C. refers to not clear or unknown.

| Year | Reference | Flame type | Method | Initial PPSD: $D_p$ (nm) [$\sigma_{p,geo}$] | Volume fraction (ppm) | Temperature (K) | Maximum $t_{res}$ (ms) | Soot mechanisms |
|---|---|---|---|---|---|---|---|---|
| 1999 | Hayashi et al. [366] | Premixed | Ballistic MC | N.C. | N.C. | 1573 | 30–500 | Agg. |
| 2005 | Balthasar and Frenklach [32] | Premixed | Dynamic MC | 1.32 [1] | 0.2 | 1460–1890 | 100 | Agg.; Incep; SG[a] |
| 2014 | Camejo et al. [367] | Premixed | Diffusion-limited MC | 50 [1] | 0.65–6544 | 1900 | 1000–6000 | Agg. |
| 2015 | Ono et al. [368] | Premixed | Ballistic MC | 15–22 [1] | 0.17–30 | 1800 | 50 | Agg. |
| 2015 | Yapp et al. [353] | Premixed | DSPB[b] | Incep. model | N.C. | 1300–1800 | N.C. | Agg.; Incep.; SG |
| 2016 | Inci et al. [345] | N.C.[c] | LD | 5, 20, 100 [1] | 3270 | 600 | 0.0008–1.46 | Agg.[d] |
| 2017 | Kelesidis et al. [33] | Premixed | EDEM | 2 [1] | 0.002–0.01 | 1830 | 100 | Agg.; SG |
| 2017 | Kelesidis et al. [94] | Premixed | EDEM | 2 [1] | 0.002–0.01 | 1830 | 100 | Agg.; SG |
| 2019 | Wang et al. [369] | Diffusion | LD | N.C. | 3–6 | 1750–2120 | 8–20 | Agg. |
| 2019 | Kelesidis and Pratsinis [185] | N.C. | EDEM | 2 [1] | N.C. | 900–1800 | 0.4–400 | Agg.; SG; Ox. |
| 2019 | Hou et al. [205] | Premixed | DSPB | Incep. model | 0–0.0075 | 550–1900 | 60 | Agg.; Incep.; SG |
| 2021 | Morán et al. [34] | Premixed | MCAC | 8 [1.2] | 0.118–3.5 | 1700 | 30 | Agg.; SG |
| 2021 | Morán et al. [206] | Premixed | MCAC | 2.4 [1.2] | 0.002 | 1700 | 30 | Agg.[e] |
| 2021 | Kholghy and Kelesidis [243] | Premixed | EDEM | 2 [1] | 0.002–0.01 | 1830 | 100 | Agg.; SG; Ox. |
| 2022 | Qian et al. [231] | Premixed | LD | 5 [1] | 409 | 600 | N.C. | Agg.[d] |
| 2023 | Trivanovic et al. [361] | Spray combustion reactors | EDEM | 2 [1] | 0.00063–0.1 | 500–1600 | 400 | Agg.; SG |
| 2023 | Kelesidis et al. [7] | Laminar flow reactors | EDEM | 3 [1] | 0.029–24 | 1473–1673 | 18–370 | Agg.; SG |
| 2023 | Qian et al. [188] | Premixed | LD | 2, 5, 8 [1.2] | 0.118–N.C. | 1200–1700 | 30–80 | Agg.; SG; Ox |
| 2023 | Morán et al. [163] | Diffusion | MCAC | 4.8–5.8 [1.2] | 0.002–8 | 400–1900 | 43–136 | Incep.; Agg.; SG; Ox. |

[a] Agg. and Incep. were accounted for the first 3 ms, afterwards only SG was considered.
[b] This version of DSPB model assumed $D_f = 1.8$ to calculate aggregate collision diameter.
[c] Turbulent flow.
[d] Considered inter-particle forces.
[e] Considered soot maturity, van der Waals interactions, and electric charges.

inception model [197,205,353]. Soot particles are treated as fractal-like aggregates formed by overlapping spherical primary particles while each primary particle is composed of several PAHs. The DSPB modeling is initiated by adding gaseous PAH species, for example, pyrene (A4), into the particle simulation volume according to its formation rate from CFD modeling [205].

### 5.3.2. Particle motion and coagulation

Due to the low inertia of nanoparticles generated in flames, they are sensitive to individual collisions with the surrounding gas. This gas-particle interaction is commonly modeled as a Stokes drag and a stochastic force uncorrelated in time and null on average. In the time-scale $t < \tau$, where $\tau$ is the particle momentum relaxation time defined as $\tau = m/f$ (ratio between the particle mass $m$ and the friction coefficient $f$), the particles move approximately ballistically. In this time scale, the particles move along a characteristic distance $\lambda_p$ referred to as the persistent or stopping distance. On the other hand, in the time-scale $t \gg \tau$ the particle movement becomes diffusive and can be described by Einstein's diffusion theory, i.e., the mean squared displacement is $\langle r^2 \rangle = 6Dt$, where $D = k_B T/f$ is the particle diffusion coefficient. In DEM, this movement can be simulated using different stochastic methods including (1) Event-driven DEM [93,94], (2) Monte Carlo [95,96,334], and (3) Langevin Dynamics [87,188,224,344,345].

Collisions between single particles, aggregates and/or agglomerates continuously reduce the number of particles in the simulation cell. When the number of particles is halved, the cell volume is doubled consecutively in $x$-, $y$-, and $z$-directions [225] in both the EDEM and MCAC approaches, similar to the DSPB method. This adjustment ensures that the number of single particles, aggregates, and agglomerates always remains between 500 and 1000. The purpose of volume-doubling is to maintain statistically significant particle dynamics, which can be validated against classic theories and population balance models. For example, the EDEM-derived collision frequency of coalescing spheres in the free molecular, transition, and continuum regimes has been

validated with the analytical relation derived by Fuchs [93]. Similarly, the EDEM-derived self-preserving size distributions in the free molecular and continuum regimes have been validated against those obtained from polydisperse population balance models [93]. Additionally, the dynamics of soot total number concentration and mean $D_m$ during coagulation in the transition regime have been validated using a monodisperse population balance model [297].

*Event-driven DEM*

Soot particle motion and coagulation from the free-molecular to the transition regime are simulated using an event-driven method [93]. As shown in Fig. 21(a), every soot primary particle follows ballistic trajectories based on the Maxwell–Boltzmann distribution of velocities [93]. A particle changes direction once it collides with another particle or has traveled a distance equal to its mean free path, $\lambda_p$. The latter is estimated by [365]

$$\lambda_p = \tau \cdot \bar{c} \tag{64}$$

where $\tau$ is the particle relaxation time given by [365]

$$\tau = \frac{mC_c(D_m)}{3\pi\eta D_m} \tag{65}$$

where $C_c$ is the Cunningham correction factor estimated based on the mobility diameter $D_m$ and $\eta$ is the fluid viscosity.

Unlike standard methods for molecular and particle dynamics that rely on explicit forward integration schemes with a finite time step, in event-driven methods the time is propagated based on the smallest time required for two particles/agglomerates to collide [349] or for a single particle to change direction after it has traveled its $\lambda_p$ [93]. The smallest collision time is estimated based on the particle positions and velocities, assuming that particles stick upon collision, i.e., a unity collision efficiency is assumed, to form agglomerates [349]. The velocity of the newly formed agglomerate is obtained based on the momentum conservation [93]. The agglomerate mass is obtained based on the diameter, $D_p$, and number, $N_p$, of primary particles in the aggregate or agglomerate, as well as the soot bulk density. A constant soot bulk density $\rho$ = 1800 kg/m$^3$ for mature soot has been used in most EDEM investigations [33,94,361]. Comparable values of $\rho$ = 1400 kg/m$^3$ have been reported for the bulk density of incipient soot consisting of benzopyrene molecules [371]. Using such incipient soot bulk density increases $D_p$ by only 4% and does not practically affect soot dynamics or the evolution of soot $D_m$ (see Fig. S3 in [360]). The agglomerate size is characterized by its diameter of gyration, $D_g$, and mobility diameter, $D_m$. The aggregate or agglomerate $D_g$ is obtained based on its radial density distribution, while its $D_m$ is estimated by its projected area $a_a$, as detailed in Section 2.3.

*MCAC*

As shown in Fig. 21(c), in the Monte Carlo Aggregation Code (MCAC), particles move in a ballistic trajectory along their persistent distance $\lambda_p$ during a time step $\Delta t$. The description of the particle motion as a random walk concludes that $\lambda_p^2 = 6D\Delta t$ is needed to ensure an accurate transition from ballistic to diffusive motion when $t \gg \tau$. Taking a random change in direction after the particle traveled a characteristic distance is the approach commonly taken in Monte Carlo simulations [348,372]. Furthermore, by describing the particle trajectory based on the Langevin equation and determining the distribution of angles between consecutive displacements for different $\Delta t$ concluded that at least $\Delta t = 3\tau$ should be taken in Monte-Carlo simulations to consider a random change of orientation in space when the particle has traveled along,

$$\lambda_p = \sqrt{6D\Delta t}, \qquad \Delta t = 3\tau. \tag{66}$$

The latter is determined by calculating the minimum time step required for the information entropy of the distribution of angles between consecutive displacements to reach 99% of its asymptotic value [95].

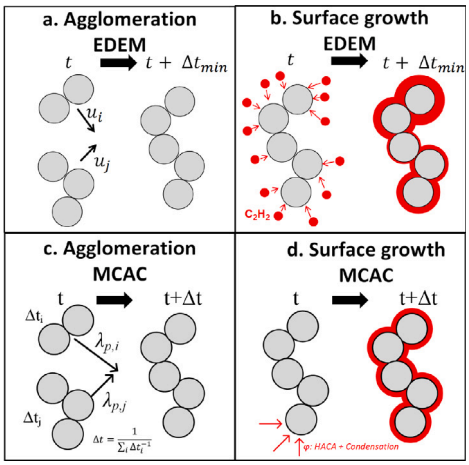


**Fig. 21.** Schematic of EDEM and MCAC agglomeration and surface growth modeling.

Thus, this approach will guarantee a good agreement between Monte Carlo and Langevin Dynamics for an individual particle. In addition, the dynamics of a population of polydisperse particles can be serialized (move one particle at the time) by defining a displacement probability $p_i \propto 1/\Delta t_i$. This probability simply means that smaller particles (with smaller $\tau$) will be displaced more frequently than larger particles (with larger $\tau$). Then, the probability of particle displacement can be normalized as,

$$p_i = \Delta t_i^{-1} / \sum_j \Delta t_j^{-1}. \tag{67}$$

The time advancement of the population of particles will be determined by the slowest particle in the domain having a displacement time $\Delta t_{\max} = \max_i\{\Delta t_i\}$. In this time-scale, any other particle will be displaced a fraction $\sum_i 1/(\Delta t_{\max}/\Delta t_i)$ of $\Delta t_{\max}$, and the physical residence time of the population of particles between time iteration $k$ and $k+1$ will be

$$t_{\text{res}}^{(k+1)} = t_{\text{res}}^{(k)} + \frac{1}{\sum_i \Delta t_i^{-1}}. \tag{68}$$

*Detailed stochastic population balance model*

Unlike EDEM or MCAC, the DSPB model does not track the motion of soot particles in the simulation volume. In the DSPB model, a particle (a soot aggregate) is described mathematically using a type-space schematically shown in Fig. 22. An aggregate $P_q$ formed by $N_p$ overlapping primary particles is expressed as

$$P_q = P_q(p_1, p_2, \ldots, p_{N_p}, \mathbf{C}) \tag{69}$$

where a primary particle $p_i$ in particle $P_q$ is represented as

$$p_i = p_i(\boldsymbol{\eta}_\mathbf{i}, r_i, \mathbf{x}_\mathbf{i}) \tag{70}$$

where $\boldsymbol{\eta}_\mathbf{i}$ denotes the composition, such as the numbers of C and H, $r_i$ is the primary particle radius, and $\mathbf{x}_\mathbf{i}$ is the position of the $i$th primary particle relative to the center of mass of aggregate $P_q$. The primary particles in aggregates are stored in a binary tree data structure, which enhances the computational performance but also imposes some constraints on the primary particle connectivity [41,97,352]. The binary tree data structure is embedded in the connectivity matrix $\mathbf{C}$ in Eq. (69), which is a binary lower triangular matrix of dimension $N_p(P_q) \times N_p(P_q)$

$$C_{ij} = \begin{cases} 0, & \text{if } p_i \text{ and } p_j \text{ are not in contact} \\ 1, & \text{if } p_i \text{ and } p_j \text{ are in contact} \end{cases} \tag{71}$$

The binary tree data structure has been described in detail in [97,99]. Although this data structure permits efficient access to primary particles and their properties, it does not allow for multiple overlaps between primary particles or looped structures [97].

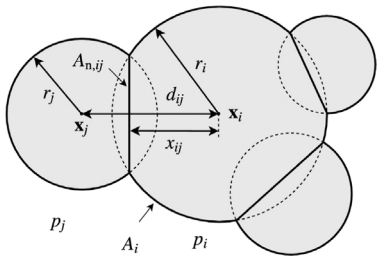


**Fig. 22.** Schematic representation of the detailed particle model type-space used in the DSPB model. A particle is modeled as a fractal-like aggregate composed of several overlapping spherical primary particles. The various geometric quantities of two overlapping primary particles $p_i$ and $p_j$ are indicated.
*Source:* Reproduced from Lindberg et al. [97]

In DSPB modeling, the rate of coagulation between two particles $P_q$ and $P_r$ is modeled by the transition regime kernel, which is the harmonic mean of the slip flow regime kernel and the free-molecular regime kernel [97,249]

$$K_{cg}^{tr}(P_q, P_r) = \left( \frac{1}{K^{sf}(P_q, P_r)} + \frac{1}{K^{fm}(P_q, P_r)} \right)^{-1} \tag{72}$$

The slip flow regime and free-molecular regime kernels are given as

$$K^{sf}(P_q, P_r) = \frac{2k_B T}{3\mu} \left( \frac{1 + 1.257\mathrm{Kn}(P_q)}{D_c(P_q)} + \frac{1 + 1.257\mathrm{Kn}(P_r)}{D_c(P_r)} \right) \times (D_c(P_q) + D_c(P_r)) \tag{73}$$

$$K^{fm}(P_q, P_r) = 2.2\sqrt{\frac{\pi k_B T}{2} \left( \frac{1}{m(P_q)} + \frac{1}{m(P_r)} \right)} (D_c(P_q) + D_c(P_r))^2 \tag{74}$$

where $D_c$ is the particle collision diameter, $m$ is the particle mass, $\mu$ is the gas viscosity, and $K_n$ is the Knudsen number defined as

$$K_n(P_q) = \frac{2\lambda_g}{D_c(P_q)} \tag{75}$$

The gas viscosity (in kg $m^{-1}$ $s^{-1}$) and mean free path (in m) are evaluated as [97]

$$\mu_g = 1.458 \times 10^{-6} \frac{T\sqrt{T}}{T + 110.4} \tag{76}$$

$$\lambda_g = 2.371 \times 10^{-5} \frac{T}{p} \tag{77}$$

In DSPB modeling, the positions of primary particles relative to the center of mass of the aggregate are tracked, the particle collision diameter is assumed to be the same as the gyration diameter [97]

$$D_c = \left( \frac{4}{\sum_i m_i} \sum_i m_i (|\mathbf{x_i}|^2 + \mathbf{r_i^2}) \right)^{0.5} \tag{78}$$

When a coagulation event between two particles, say $P_q$ and $P_r$, is chosen based on their coagulation rate given in Eq. (72) [373], the orientations and contact point between the two colliding particles are determined by performing ballistic cluster-cluster aggregation (BCCA) with a random impact parameter. The colliding and sticking of particles $P_q$ and $P_r$ are schematically illustrated in Fig. 23. Modeling of particle coagulation starts by randomly rotating particles $P_q$ and $P_r$ around their centers of mass and calculating their bounding spheres. A random direction is then generated, which is the collision direction, by uniformly selecting a point on a sphere centered on particle $P_q$. Next, a random impact parameter is applied by placing particle $P_r$ at a random point in the plane perpendicular to the collision direction. Further details of BCCA algorithm can be found in [97]. Upon coagulation of particles, $P_q$ and $P_r$, a new particle $P_s$ is formed and the connectivity matrix is updated.

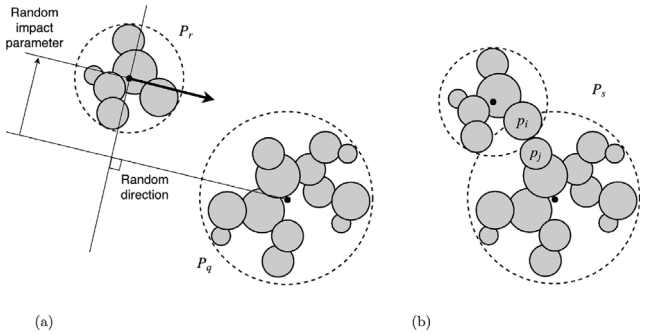


**Fig. 23.** Schematic representation of the ballistic cluster-cluster aggregation of particles $P_q$ and $P_r$ with a random impact parameter in the DSPB model. (a) Particles $P_q$ and $P_r$ before collision and (b) A new particle $P_s$ formed after successful coagulation in which a primary particle $p_i$ in $P_q$ is in point-contact with a primary particle $p_j$ in $P_r$.
*Source:* Reproduced from Lindberg et al. [97].

### 5.3.3. Surface growth and oxidation

*EDEM*

Although PAH adsorption may play a more important role to soot surface growth than HACA under some flame conditions or in a certain region of diffusion flames, such as in the centerline region of laminar coflow diffusion flames [254], in inverse diffusion flames [255], in normal diffusion flames at elevated pressures [256], and in rich premixed flames [257], only the HACA mechanism has currently been implemented into EDEM as the soot surface growth process. The contribution of PAH adsorption to soot surface growth can be incorporated into EDEM in a similar manner as HACA described below. That way, as shown in Fig. 21(b), the total number of $C_2H_2$ reactions with soot taking place between two particle collisions is obtained [33]. The $C_2H_2$ reactions are not distributed uniformly among all primary particles to account for the random walk of $C_2H_2$ molecules and H atoms that are present at very low concentrations in typical flame conditions [29]. Each $C_2H_2$ molecule reacts sequentially with a single soot primary particle (either spherical or within an aggregate/agglomerate) selected stochastically based on the probability, $\gamma$, obtained by the ratio of $C_2H_2$ reaction rate over its collision rate [33]. So, large soot particles have higher probabilities to react with an acetylene molecule than small particles [33]. This results in the formation of polydisperse soot primary particles that significantly impact soot light absorption [371] and scattering [81]. The increase in primary particle diameter is estimated by a mass balance [94]

$$\frac{1}{6}\pi D_p^3 \rho_p = \frac{1}{6}\pi D_{p,0}^3 \rho_p + m_{2C} \tag{79}$$

where $D_{p,0}$ is the initial primary particle diameter before the reaction takes place and $m_{2C}$ is the mass of two carbon atoms contributed by the addition of one acetylene molecule [239].

When acetylene molecules collide and react with primary particles within aggregates or agglomerates, they increase the particle mass by two carbon atoms [94], forming chemical bonds and necking between these primary particles (aggregation). The real mass and surface area of such chemically-bonded primary particles are estimated using the Vorlume software [358]. This is an exact method that decomposes the volume of the union of primary particles into convex regions. The volume estimated this way has been validated with analytical relations for nanoparticle sintering [359].

The EDEM-derived surface growth dynamics have been validated with a moving sectional model for spheres [33], as well as with a monodisperse population balance model for aggregates [243]. Most importantly, the EDEM-derived surface growth, aggregation, and agglomeration dynamics are in excellent agreement with data from premixed [94], diffusion [360] and spray [361] flames.

Surface oxidation of EDEM-derived soot aggregates and agglomerates has been elucidated only at high $O_2$ concentrations (21 vol%)

[185]. At these conditions, all soot primary particles can be accessed by $O_2$ molecules and thus oxidation reactions can be distributed uniformly. So, the diameter of each primary particle can be derived using the shrinking particle model [185]:

$$D_p = D_{p,0} - \frac{2\omega}{\rho}\Delta t \tag{80}$$

where $\omega$ is the specific oxidation rate of soot and $\Delta t$ is the time step. In essence, this model considers soot oxidation as a negative surface growth process. This shrinking particle model has been validated [185] with experiments of diffusion flame soot [374] and carbon black [375] oxidized at high temperatures.

*MCAC*

As shown in Fig. 21(d), the increase in primary particle diameter from $D_p(t)$ to $D_p(t+\Delta t)$ during a time step $\Delta t$ is determined as follows [31,34],

$$D_p(t+\Delta t) = D_p(t) + 2u\Delta t \tag{81}$$

where $u$ is the particle surface growth speed (m $s^{-1}$). The latter is determined as $u = \varphi_g/\rho_p$ where $\varphi_g$ is the local surface reaction flux (kg $m^{-2}$ $s^{-1}$) and can be provided by macro-scale approaches, and $\rho_p$ is the particle bulk mass density (kg $m^{-3}$). In this context, when $\varphi_g < 0$, oxidation takes place while $\varphi_g > 0$ leads to surface growth. It is useful to emphasize that while surface growth is treated stochastically based on probability in EDEM discussed above, surface growth is treated in a deterministic manner in MCAC. Such a fundamental difference in handling soot particle surface growth results in different predictions of primary particle polydispersity.

In MCAC, the surface and volume of aggregates containing overlapped spheres can be done accurately as a post-process using the SBL libraries [358]. But this process is time-consuming and to speed up calculation, these volumes and surfaces are approximated during MCAC simulation by the following laws. For an aggregate consisting of $N_p$ overlapped primary particles, its volume and surface are determined as $v = \alpha_v \sum_{i=1}^{i=N_p} (\pi/6) D_{p,i}^3$ and $s = \alpha_s \sum_{i=1}^{i=N_p} \pi D_{p,i}^2$, respectively. The volume and surface area correction factors $\alpha_v$ and $\alpha_s$ are determined as [34],

$$\alpha_v = 1 - \frac{1}{4}\overline{n_c}(3c_{20}^2 - c_{30}^3) + \beta_v \tag{82a}$$

$$\alpha_s = 1 - \frac{1}{2}\overline{n_c}c_{10} + \beta_s \tag{82b}$$

where $\overline{n_c}$, $c_{i0}$ are the average and $i$'th moment of the overlapping coefficients, respectively. Also, $\beta_v$ and $\beta_s$ are constants [34]. The overlap of two primary particles $i$ and $j$ is determined by the overlapping coefficient $C_{ov} = (r_i + r_j - d_{ij})/(r_i + r_j)$ where $d_{ij}$ is their center-center distance and $r_i + r_j$ the sum of their radii. On the other hand, oxidation leads to a continuous reduction in primary particle size and therefore possible bond breaking or fragmentation, as discussed in a recent study [163]. In practical terms, for any pair of primary particles $i$ and $j$ belonging to an aggregate, their overlapping coefficient can be monitored and aggregates are detached when $C_{ov} < 0$. In addition, considering that MCAC simulations only consider primary particles with a diameter larger than the critical coalescence diameter defined in Section 1.1, particles should be deleted from the simulation system when they reach this threshold value [163].

*DSPB*

In DSPB modeling, surface growth is treated as a linear process, i.e., surface growth affects only single particles independently of other particles in the simulation volume. Linear processes are delayed and performed only at the end of each simulation time step to speed up the DSPB modeling [99,280]. However, this treatment may introduce errors in the calculation of particle–particle coagulation rates. A mitigation strategy is to perform surface growth to the two particles chosen for coagulation before they coagulate [99]. As discussed in Section 3.4, soot particle surface growth is attributed to both surface reactions with gaseous hydrocarbons, i.e., the HACA mechanism, and the PAH adsorption. In the DSPB algorithm, the surface reactions on a soot particle undergoing surface growth are described by the KMC-ARS model [247,370] for the growth of PAHs inside the particle. Assuming the surface growth rate $\omega_g$ (particle mass gain per unit surface area per unit time) is known, which is typically obtained from the macro-scale modeling, the amount of mass added to particle $P_q$ during a time step $\Delta t$ through surface growth is

$$\Delta m = \omega_g A_{\text{free}} \Delta t \tag{83}$$

where $A_{\text{free}}$ is the total free or available surface area of particle $P_q$ for surface reactions, i.e., $A_{\text{free}} = \sum_{j=1}^{N_p(P_q)} A_j$ with $N_p(P_q)$ and $A_j$ being the number of primary particles in particle $P_q$ and the free surface area of primary particle $p_j$, respectively. The change in particle mass $\Delta m$ can be converted to a change in particle volume by using the particle density, i.e., $\Delta v = \Delta m/\rho_p$. A schematic representation of particle $P_q$ formed by overlapping spherical primary particles and undergoing surface growth is shown in Fig. 24. It is noticed that the free surface area of a primary particle refers only to its exposed area to gaseous species and can be calculated by its radius and the center-to-center distances between this primary particle and its neighbors. For example, for primary particle $p_i$ in Fig. 24, its free surface can be calculated from $r_i$ and $d_{ij}$ (here $j$ refers to all primary particles that overlap with $p_i$).

In DSPB modeling, the amount of volume increase to particle $P_q$ due to surface growth, $\Delta v$, is added solely to a primary particle $p_i$, which is indicated by the shaded area in Fig. 24, selected according to the probability

$$P(p_i) = \frac{A_i}{\sum_{j=1} N_p(P_q) A_j}. \tag{84}$$

Consequently, the radius of primary particle $p_i$ becomes larger as shown schematically in Fig. 24 by the red dashed lines. This implementation of soot particle surface growth in DSPB shares similarities with that in EDEM, i.e., it is stochastic in nature and the mass gain from surface reactions is all added to a single primary particle within the selected aggregate, though the probability for the selection of primary particle is different. The radius of primary particle $p_i$ after the event of surface growth becomes

$$r_i(t+\Delta t) = r_i(t) + \frac{\Delta v}{A_i}. \tag{85}$$

When the radius of the primary particle $p_i$ is enlarged, it not only increases the volume of $p_i$ but also reduces the volumes of adjacent primary particles that either overlap or are in point contact with $p_i$. These changes in the volumes of $p_i$ lead to corresponding changes in their compositions if the compositions of individual $p_i$ within an aggregated are being tracked [97]. Although soot oxidation has not been explicitly incorporated into DSPB modeling, it can be treated in a similar manner to surface growth but accounting for mass loss instead of mass gain [99].

### 5.4. Applications of meso-scale methods to soot modeling

Table 4 presents a list of soot formation studies using meso-scale approaches conducted in the last two decades or so. The list is by no means exhaustive, especially regarding DSPB simulations reviewed in detail in Ref. [99]. Nevertheless, it is evident that meso-scale approaches have been increasingly used to simulate soot particle aggregation with concurrent surface growth in laminar flames, spray combustion reactors, and laminar flow reactors. This trend is likely related to the increasingly available computational resources needed for meso-scale simulations. Common assumptions in these simulations involve decoupled aggregation from inception, constant particle and flame properties. Most of these studies took soot aggregation into account. Early DEM works considered a constant aggregation regime,

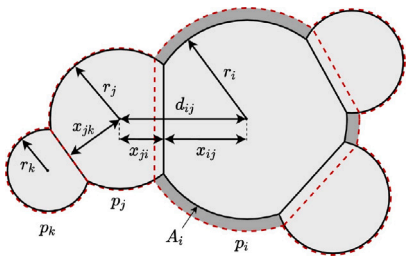


**Fig. 24.** Schematic representation of a particle formed by spherical and overlapping primary particles and undergoing surface growth. The shaded area indicates the volume added to primary particle $p_i$ over the current time step $\Delta t$ due to surface growth. The solid black and red dashed lines mark the outer boundary and the boundaries between primary particle $p_i$ and its overlapping neighboring primary particles before and after the surface growth of primary particle $p_i$, respectively.
*Source:* Reproduced from Lindberg et al. [97].

notably ballistic [366,368], or diffusive [367]. However, the residence time of diffusion-limited models is extremely long (~ h) compared to common flame conditions (~ hundreds of ms). The assumption of ballistic aggregation may only hold for early residence times when particles are commonly much smaller than their persistent distance. Soot aggregation commonly takes place in the transition regime [206]. Only a few DEM studies have included additional mechanisms relevant to soot formation in flames such as continuous inception [163], surface growth [33,34,94], and oxidation without fragmentation [185] and with oxidation-induced fragmentation [163,188].

In addition, due to their quasi-first principles nature and their ability to predict detailed morphology of aggregates, meso-scale models can be used to improve continuum dynamics or macroscopic modeling of soot formation. As mentioned in Section 3.3, meso-scale simulations have been used in previous works to propose accurate interpolation formulas for collision kernels in the transition regime, to account for van der Waals and Coulomb interactions, and high particle concentrations. This also includes models for aggregate's mobility diameter as discussed in Section 2.3. Power laws and analytical relations for the fractal dimension have been derived from DEM simulations [93]. As mentioned in Section 5.3.3, meso-scale simulations can also help improve models for the power-law correlation between the ratio of aggregate projected area $A_a$ to that of the primary particle $A_p$ with the number of monomers $N_p$ as originally proposed by Medalia [116]. Brasil et al. [92] observed an increase in the correlation constants $k_\alpha$ and $\alpha$ with increasing the degree of primary particle overlap coefficient $C_{ov}$ using numerically generated aggregates of monodisperse primary particles with varying degree of overlap added as a post-processing step. More recent works based on DEM simulations have proposed corrected expressions for more realistic overlapping related to sintering [376], and soot surface growth [377]. Both parameters $k_\alpha$ and $\alpha$ may also depend on primary particle polydispersity as proposed by Eggersdorfer et al. [378]. A monodisperse population balance model interfaced with these relations was able to simulate accurately the soot coagulation and surface growth dynamics at high [243] and low [297] temperatures, finding excellent agreement with several experimental data. So the relations for the soot morphology derived by meso-scale methods can improve substantially the accuracy of macro-scale combustion models.

Another important application of meso-scale methods is to generate soot aggregates. Such soot aggregates produced on physical ground are clearly more realistic than those simulated using a tunable algorithm discussed in Section 5.1 in terms of morphological features (PPSD, primary particle overlap, and fractal parameters) and can be used as input into other numerical methods for detailed investigation of the physical and optical properties of soot particles, such as the DDA code [112].

### 5.5. Meso-scale codes validation

MCAC is a public access project available via GitLab [379], which is constantly maintained and contains validated codes tested any time a modification is introduced. The trajectories of individual particles simulated by MCAC have been validated by a rigorous comparison with theory and Langevin Dynamics simulations and have been theoretically shown to be described as a binomial process characteristic of random walks [95]. This mathematical tool is used to ensure that the asymptotic particle trajectories are consistent with a diffusive motion predicted by Einstein theory. The physical properties defining the trajectories of MCAC simulated particles, namely the particle persistence distance and its corresponding time step, were derived to accurately match the Langevin equation [95]. Thus, the MCAC predicted particles trajectories exhibit a transition between ballistic and diffusive motion consistent with the Langevin equation. In addition, the accurate and consistent model of a population of polydisperse particles in a Monte Carlo approach has been achieved for the first time in MCAC simulations [95,96] and validated through a detailed comparison with theory [218] and sectional simulations [34]. The agglomeration kinetics at early stages (before reaching self-preserving) were found satisfactory compared with proven coagulation theories [166]. MCAC-derived collision kernels have also been validated by a detailed comparison with those predicted by Langevin Dynamics first time passage simulations [96]. Homogeneity coefficients describing the particle kinetics under different regimes have been validated by comparison to theory and simulations showing the correct asymptotic limits of aggregation [96]. MCAC modeling under more realistic conditions related to soot formation including surface reactions (surface growth and oxidation including fragmentation) and inception has been validated by comparison in simple cases with analytical solutions [377].

Similarly, EDEM has been validated with literature theories and numerical models. For example, the collision frequency of coalescing spheres derived by EDEM [93] closely followed the Fuchs interpolation formula that bridges the free molecular and continuum regimes [215]. The EDEM-derived self-preserving size distributions of particles coagulating by coalescence (forming single spheres) or agglomeration (forming agglomerates of spheres in point contact) were in excellent agreement with those obtained in the free molecular and continuum regimes by fixed sectional models [93]. The impact of numerical diffusion on EDEM has been quantified by simulating the dynamics of polydisperse soot particles during surface growth. As expected, the soot particle size distribution was narrowed by surface growth [33]. So, the EDEM-derived geometric standard deviation of the particle size distribution decreased with increasing time, following closely that obtained by a moving sectional model (MSM) for surface growth and confirming that EDEM simulations are not impacted by numerical diffusion [33]. The evolution of the soot volume fraction and number density during coagulation by coalescence and surface growth obtained by EDEM closely followed those calculated by MSM [33]. The real volume and surface area of EDEM-derived soot aggregates formed by concurrent surface growth and agglomeration were estimated by the exact method of the Vorlume software [358]. The evolution of the aggregate surface area and neck radius derived by a DEM for sintering of particle chains using this Vorlume software [359] was in good agreement with those estimated by Kirchhof et al. [380] using the fractional volume of fluid method, Pokluda et al. [381] using the extended Frenkel-Eshelby model, and Koch & Friedlander [382] using a phenomenological fusion model. The EDEM-derived gyration diameter of soot particles under surface growth and agglomeration [33] was also in good agreement with the Monte Carlo simulations of Mitchell [383] at small residence times in flames when particle-cluster agglomeration and surface growth dominate. In summary, the dynamics of spheres, aggregates, and agglomerates obtained by EDEM have been thoroughly validated with plenty of literature theoretical and numerical models.

In Fig. 25, we compile a range of experimental data pertaining to the fractal dimension, mass-mobility exponent, effective density, geometric standard deviation, particle size distributions, and mobility diameters of soot particles generated under both premixed and diffusion flame conditions. Where possible, we also include previously published numerical results obtained using EDEM and MCAC methodologies, facilitating a direct comparison between simulations and experiments. As shown in Fig. 25a, a surprising decrease in the fractal dimension of aggregates as a function of the primary particle diameter has been observed when compiling data from different experiments involving different types of colloid particles [384]. It is even more intriguing that such fractal dimension can even be below the DLCA limit. MCAC simulations [34] have lead to a similar conclusion for the aggregation of particles under flame conditions but different diameters up to around 200 nm. This evolution has been attributed to considering the simultaneous transition in aggregation (particle–particle) and flow regimes (particle-gas) which was not the case of previous works (e.g., DLCA and BLCA). In addition, MCAC simulations consider a specific method to describe the friction coefficient of aggregates by considering the size and regime of primary particles which may explain the strong importance of primary particle size in DEM derived aggregates fractal dimension.

In this regard, EDEM simulations of soot dynamics were able to explain several experimental datasets available in the literature. For example, the mobility size distribution derived by EDEM for soot surface growth and agglomeration (Fig. 25(e): red line) [33] was in excellent agreement with scanning mobility particle sizer (SMPS; Fig. 25(e): triangles) [155] and helium ion microscopy (HIM; Fig. 25(e): squares) [363] measurements in the benchmark premixed burner-stabilized stagnation ethylene flame, explaining, for the first time, the formation of small, compact nascent soot aggregates observed at these conditions. The primary particle and quasi self-preserving mobility size distributions derived by EDEM [360] closely followed the size distributions measured commonly in diffusion flames [385] and commercial CAST generators [386]. The morphology of the EDEM-derived soot aggregates and agglomerates has been quantified by their $D_f$ (Fig. 25(b): solid line) and mass-mobility exponent [94]. That way, the asymptotic $D_f = 3$ and 1.91 of small nascent soot spheres ($N_p = 1$) and large mature soot agglomerates ($N_p > 100$) were bridged [94], finding excellent agreement with experimental data from premixed ethylene (Fig. 25(b): squares) [363] and diffusion 1-decene (Fig. 25(b): triangles) flames [387]. It should be noted that the EDEM-derived fractal dimension reported in Fig. 25(b) has been obtained assuming that single spheres have a fractal dimension of 3, as the fractal scaling law is not accurate for clusters consisting just a few primary particles. If there are both single spheres and aggregates/agglomerates in the simulation box, the fractal dimension of EDEM-derived aggregates/agglomerates is estimated excluding the spheres. Based on the aggregate/agglomerate fractal dimension obtained that way, the assumed fractal dimension of spheres and the number-based fraction of spheres in the simulation box, the average fractal dimension is estimated.

The mass distribution and mass-mobility exponent of EDEM-derived nascent soot aggregates were also in good agreement with those measured by CPMA in a premixed ethylene flame. So, easy-to-use relations for the soot $N_p$ and effective density, $\rho_{\text{eff}}$, were derived by EDEM to assist macro-scale models to account for the realistic fractal-like soot structure. These power laws have been validated with several experimental datasets of flame-made organic and even inorganic nanoparticles. For instance, in Fig. 25(c), the soot $\rho_{\text{eff}}$ estimated by the EDEM-derived power law is compared to those measured for soot nanoparticles having $D_p = 16.2$ (triangles), 29.6 (circles), 9 (squares), and 18 nm (diamonds) produced using the CAST generator or premixed flames. Based on the EDEM-derived power law, the soot $\rho_{\text{eff}}$ is invariant with the particle $D_p$ when presented as a function of the normalized mobility diameter, $D_m/D_p$. This explains the small variation of the measured soot $\rho_{\text{eff}}$ between the various datasets presented in Fig. 25(c). The EDEM-derived power law can describe rather accurately the measured soot $\rho_{\text{eff}}$, resulting in average errors of 12.5 and 9.4% for CAST and premixed flame soot, respectively. In order to assess the relative accuracy of the mesoscale models presented in this manuscript, MCAC was also compared to some of the experimental datasets shown in Fig. 25. The nascent soot mobility size distribution derived by MCAC (Fig. 25(e): black line) is in good agreement with that obtained EDEM (Fig. 25(e): red line) and those measured by SMPS (Fig. 25(e): triangles) and HIM (Fig. 25(e): squares) in a premixed ethylene flame. However, the soot $\rho_{\text{eff}}$ estimated by MCAC deviates significantly from that obtained using EDEM. In particular, MCAC estimates the soot $\rho_{\text{eff}}$ based on a semi-empirical relation derived using experimental measurements of CAST soot. The soot $\rho_{\text{eff}}$ obtained that way varies with $D_p$. So, the soot $\rho_{\text{eff}}$ estimated using this relation results in, on average, 12.3 and 82.2% error when compared to those measured for CAST and premixed flame soot, respectively.

On the other hand, Fig. 25d shows a comparison of the geometric standard deviation of MCAC simulations in terms of mobility, gyration, and volume-equivalent diameters of soot particles under aggregation and surface growth in a premixed flame [34]. Fig. 25f, compares a $D_f$-moment average gyration diameter predicted by MCAC simulations and compared to multi-angle light-scattering measurements [388]. Even though the simulations and measurements show diameters in the same order of magnitude, these MCAC simulations seem to underestimate the experimentally measured gyration diameters, which has been attributed to difficulties to accurately predict volume fraction and surface reactions, including surface growth, in the current version of macro-scale CoFlame used as an input for MCAC. Thus, although meso-scale methods generally show a good agreement with experiments related to premixed flames, the accurate prediction of soot in diffusion flames remains challenging due to the different simultaneous phenomena including nucleation, aggregation, and surface reactions.

The DSPB model developed by Kraft and co-workers [97,99,252,278,352,390] has been implemented into the MOpS Particle Simulator code, also available on GitHub [391]. The code has been validated against benchmark solutions to simple problems of spherical particle coagulation. Patterson et al. [373] validated the DSPB model in the prediction of dynamics of particles undergoing pure coalescence in air at 500 K and 600 bar under two different conditions against direct solution of PBE using an ODE (ordinary differential equation) solver. In the first test case, the initial monodisperse particle diameter and number density are 0.88 nm and $6.56 \times 10^{11}/\text{cm}^3$, respectively. In the second case, there are no particles initially and particles of 0.88 nm in diameter are incepted at a rate of $2.63 \times 10^{13} \times [(0.05 - t)/0.05]^2$ $\text{cm}^{-3}$ $\text{s}^{-1}$. The particle density takes the value of 1.8 $\text{g/cm}^3$. Under these conditions, the Knudsen numbers are approximately in the range of 5 to 20, i.e., in the transition and near-continuum regimes. The results of DSPB model are compared with the direct solutions in Fig. 26. The results of DSPB model are in very good agreement with the benchmark solutions in both cases, though they display some scatters at large particle diameters.

The DSPB model has also been tested in pure coagulation of mono disperse spherical primary particles undergoing ballistic-limited cluster-cluster agglomeration (BLCA) [78]. The DSPB model predicted sizes of agglomerate as measured by the number of primary particles, $N_p$, against the ratio of collision diameter to the primary particle diameter, $D_c/D_p$, in log–log scale are plotted in Fig. 27. It is noticed that the agglomerate collision diameter is defined as the gyration diameter. A linear fit to all the agglomerates returns a fractal dimension of 1.93 (the slope of the linear fit), which is in close agreement with the value ($1.91 \pm 0.03$) reported by Jullien [392].

In addition to the above validation against pure particle coagulation under coalescence and agglomeration conditions, the DSPB model has also been applied to model soot volume fraction and particle size distributions in a plug flow reactor [279], soot particle size distributions in premixed flames at atmospheric pressure [197,198,205,353] and at

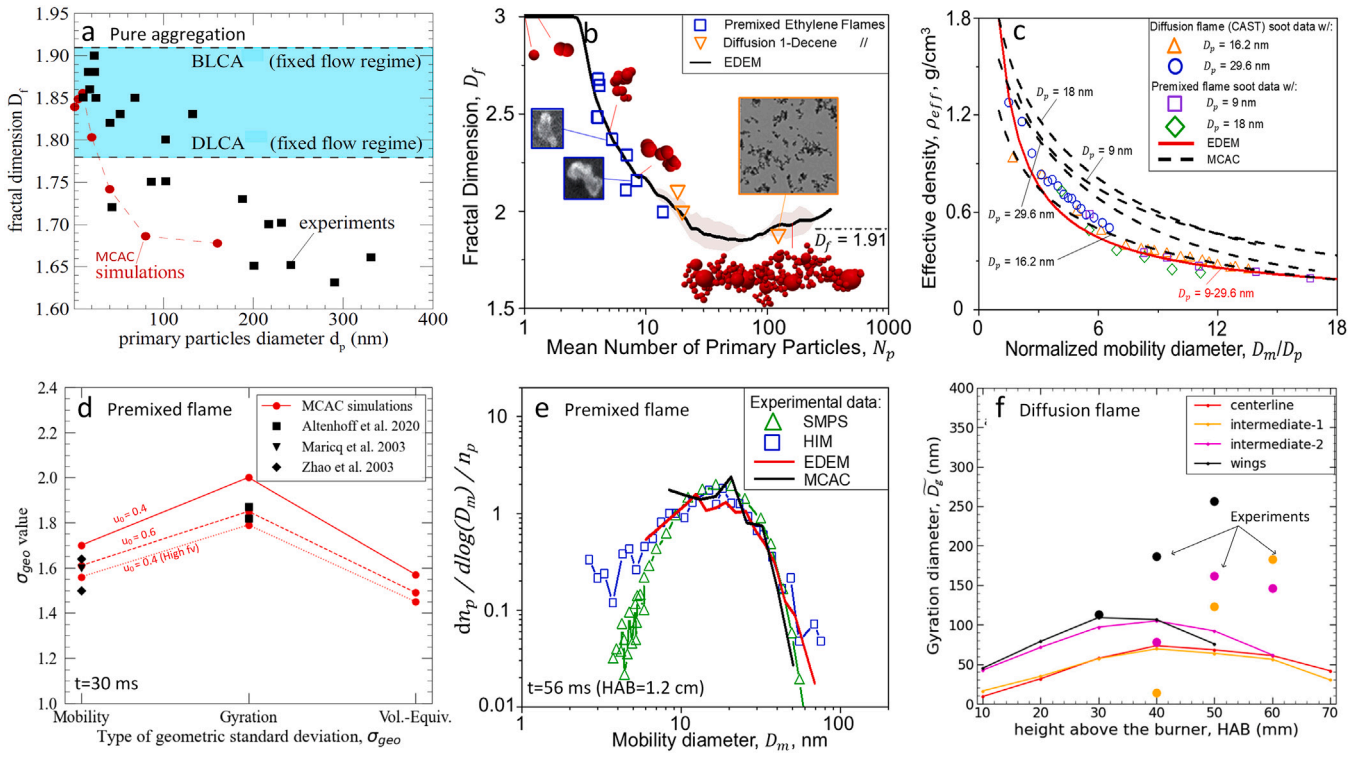


**Fig. 25.** Comparison of MCAC and EDEM simulations with available experimental results. Panel (a) shows the asymptotic population-based fractal dimensions of aggregates formed by pure aggregation (under flame conditions; adapted from [96]) compared to experimental data of Wu et al. [384]. Panels (b–e) corresponds to results under simultaneous soot aggregation and surface growth (Panels (b), (c), and (e) are adapted from [94], Panel (d) is adapted from [34]). Panel (b) shows the evolving weighted population-based fractal dimension and mobility-based fractal dimension of aggregates under simultaneous aggregation and surface growth. On Panel (c), the CAST experimental data are from Ref. [153], and the premixed flame data from Ref. [81]. Panel (d) compares different geometric standard deviations at a residence time $t = 30$ ms (adapted from [34]), compared to experimental data from Altenhoff et al. [389], Maricq et al. [364], and Zhao et al. [107]. Panel (e) compares the mobility diameter size distribution at a residence time of $t = 56$ ms (corresponding to height above burner HAB = 1.2 cm) with SMPS [155] and HIM [363] experimental data. Panel (f) compares a $D_f$-moment average gyration diameter as a function of HAB in a diffusion flame (adapted from [163]) compared to experimental data from Yon et al. [388].

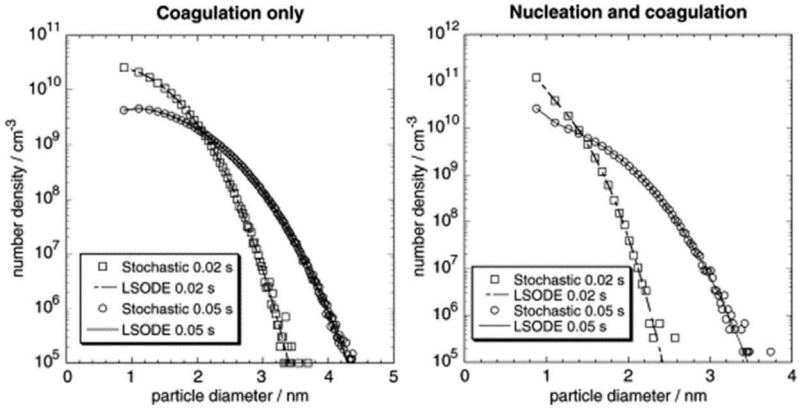


**Fig. 26.** Particle size distributions at 0.02 and 0.05 s calculated by the direct PBE solver (Livermore ODE solver, LSODE) and the DSPB model for the first case (left plot) and the second case (right plot).
*Source:* Adapted from Patterson et al. [373].

elevated pressures [373]. In these studies, the results of DSPB model have been compared with experimental data. In [373], the DSPB model results of soot volume fraction were also shown to agree better with the experimental data than the results of MOM.

### 5.6. Summary of meso-scale methods

Meso-scale methods, especially the three commonly used ones, namely EDEM, MCAC, and DSPB model, have been increasingly applied to study soot particle aggregation at individual particle level in the presence of surface growth and oxidation (see Table 4). As concluded from Table 4 and Fig. 25, some important progress has been achieved in simulating soot formation in premixed flames however, diffusion and turbulent flames remain challenging. Although the three meso-scale methods discussed above have all been developed on the same underlying physics governing interactions between particles and gas molecules, they differ in some important aspects concerning the complex fractal-like morphology of soot particles as compared in Table 3, such as the aggregate mobility size and how surface growth is handled. These differences among the meso-scale methods will likely result in different soot aggregate size and morphological properties. A direct comparison

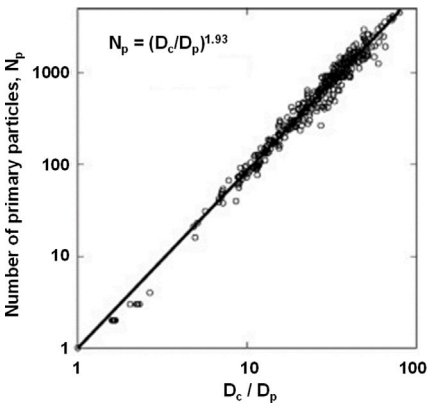


**Fig. 27.** The number of primary particles in agglomerates predicted by the DSPB model in BLCA of monodisperse primary particles against $D_c/D_p$ in log–log scale. The collision diameter $D_c$ is defined as the agglomerate gyration diameter.
*Source:* Modified from Morgan et al. [78].

of the results obtained by EDEM and MCAC in several well-defined test cases is provided in the next section.

## 6. Case study of modeling soot particle agglomeration using meso- and macro-scale methods

In this section, test cases of particle agglomeration without and with surface growth are simulated using different approaches. These methods include the meso-scale MCAC and EDEM approaches and two macro-scale methods (moment and sectional methods). Through a direct comparison and analysis of the results of these four approaches for simple and well controlled conditions, we hope to gain a clear understanding of the causes responsible for the differences in their results, especially in the predicted particle morphology by the two meso-scale methods. A total of 3 cases are simulated considering pure agglomeration (without surface growth) of monodisperse (Case 1) and polydisperse (Case 2) primary particles. Case 3 considers particle agglomeration with surface growth. The focus of this case study is particle agglomeration kinetics and surface growth. Hence soot oxidation was not considered. Although these test cases are much simpler than soot formation in flames, they are selected based on the considerations that only under simple and well controlled conditions that the causes for discrepancies in the predicted particle size distributions and particle morphology can be clearly identified and understood.

In all the meso-scale simulations the domain consists of a cubic box with periodic boundary conditions. The simulations are initialized with a total of 1000 (EDEM) or 1024 (MCAC) randomly distributed primary particles in the simulation box. The initial size of the simulation domain is determined based on the particle volume fraction. Primary particles are assumed spherical and they stick or agglomerate upon collision with unitary probability. Agglomeration of particles leads to a reduction of the number of particles in the domain and thus both EDEM and MCAC consider domain duplication as previously discussed in Section 5.3.2. When surface growth is present, the volume and surface area of soot aggregates considering primary particle overlapping are determined based on specific methods as detailed below. In addition, aggregates are simulated as rigid bodies without considering rotation. In all the simulations, the particle bulk density (or true density) is constant at 1.8 g/cm$^3$ corresponding to mature soot [393,394]. Unless otherwise indicated, the simulations are conducted at a constant temperature of 1830 K and atmospheric pressure. Additional details related to these simulations are given in the following sub-sections. It should be noted that some of the simplified conditions considered in this section can be used to describe accurately soot dynamics in premixed flames. For example, the mass [81] and mobility [33] size distributions derived by EDEM of soot surface growth and agglomeration at the conditions specified in the third test case were in excellent agreement with those measured by microscopy and scanning mobility particle sizers in a premixed ethylene flame having a maximum temperature of 1830 K [155]. Similarly, the mobility size distribution derived by EDEM of carbon black surface growth and agglomeration under the conditions of the third test case were in excellent agreement with those measured for carbon black produced in a furnace reactor [149]. So, the conditions considered in the third test case are representative of soot and carbon black formation in rich premixed flames and furnace reactors, respectively.

The sectional method and method of moments are selected as representative macro-scale methods of particle dynamics as these types of method have often been used in sooting flame modeling. For these test cases, the PBE does not include advection, thermophoresis, and diffusion (see Eq. (35) for the generic form of PBE). In both the SM and MOM, we assume a constant fractal dimension of 1.78 and a prefactor of 1.30. These values are selected since similar values have commonly been imposed in PBE simulations of soot formation in flames in the literature [43,196,211,254]. We note that some efforts to implement variable fractal dimension in time have been made in the literature [243,297,307,350]. The sectional method used here is a modified version of the NGDE code developed by Prakash et al. [395] which has been adapted to simulate aggregation [95] and is publicly available through GitLab [218]. A detailed description of this sectional method can be found in the referenced studies and here we only provide a brief description. The size distribution of aggregates is distributed logarithmically in terms of aggregate volume considering a total of 41 sections (or size bins) starting at the initial primary particle geometric mean diameter up to 4 orders of magnitude from this value. This number of sections represents a good compromise between accuracy and computational cost which is especially relevant when considering the resolution of the flow and chemical species transport equations. The size distribution is integrated in time considering a dynamic time step calculated from the coagulation kernels as explained in [218]. For both the sectional and moments method, the coagulation kernels are determined based on the transition regime model proposed by Gopalakrishnan et al. [234] (Equation 14 in this reference). The collision radius of aggregates is determined based on Thajudeen et al. [223] (Equations 21 to 23 in this reference). The friction coefficient of aggregates is determined as for MCAC, based on the method of Yon et al. [153].

For the MOM simulations, the DQMOM in a volume-surface formulation was selected, as explained in Section 4.2.4. Two delta functions ($N_\delta = 2$) are used for the quadrature approximation. In terms of the selected set of moments, the results of DQMOM are not unique but depend somewhat on this set. The best results of DQMOM, which give the closest agreement with those of EDEM and MCAC, were found for the following set of $3N_\delta$ moments: $m_{0,0}$, $m_{1,0}$, $m_{0,1}$, $m_{2,0}$, $m_{4,-3}$, and $m_{-2,3}$. These are physically related to number density, soot volume fraction, specific surface, volume squared, mean diameter $d_{6,3}$, and mean number of primary particles, respectively. For the numerical integration, a simple forward Euler method was used, ensuring time-step independence.

### 6.1. Case 1: Agglomeration of monodisperse primary particles

Primary particles of diameters $D_{p,geo} = 40$ nm and $D_{p,geo} = 8$ nm are simulated. The particle volume fraction is 10 ppb and simulations end at a residence time of 8 s and 100 ms for $D_{p,geo} = 40$ nm and $D_{p,geo} = 8$ nm, respectively. These diameters are selected based on the considerations that they are representative primary soot particles in the early stage of soot formation ($D_{p,geo} = 8$ nm) or in flames of heavily sooting liquid fuels ($D_{p,geo} = 40$ nm), e.g. Jet A-1 [396]. The results of Cases 1 and 2 are compared in Fig. 28. Columns 1 and 2 of Fig. 28 show a direct comparison of MCAC, EDEM, and population balance

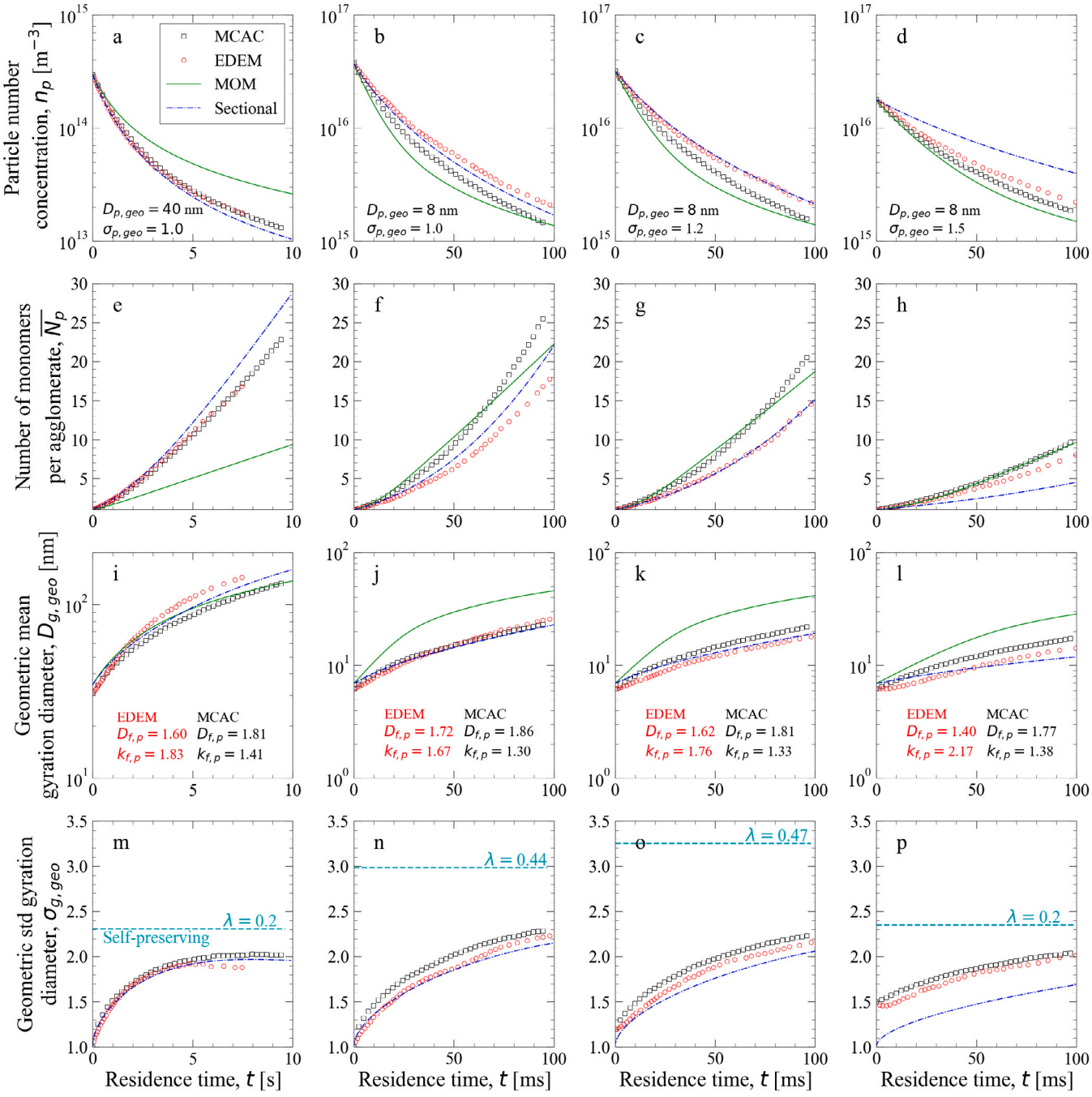


**Fig. 28.** Comparison of the results of MCAC, EDEM, sectional, and MOM simulations for pure agglomeration cases considering different primary particle size distributions. Column 1 compares the results of monodisperse primary particles ($\sigma_{p,geo}$ = 1) with $D_{p,geo}$ = 40 nm, while columns 2, 3 and 4 show results of the same $D_{p,geo}$ = 8 nm but different $\sigma_{p,geo}$ of 1, 1.2, and 1.5, respectively. Each row represents a different agglomerate property of the simulation including the total aggregate number concentration ($n_p$), average primary particle number per agglomerate ($\overline{N_p}$), geometric mean and standard deviation of gyration diameter $D_{g,geo}$ and $\sigma_{g,geo}$, respectively. Fractal parameters ($D_{f,p}$, $k_{f,p}$) are obtained by fitting Eq. (1) considering $N_p > 2$ (the fractal plot are available in Supporting Material). The cyan dashed lines represent the self-preserving $\sigma_{g,geo}$. Both the fractal parameters and self-preserving $\sigma_{g,geo}$ are evaluated nearly the last residence time shown in the figure based on Eq. (17c) and MCAC simulations (see S2 of the Supporting Material).

simulations of pure agglomeration of monodisperse particles ($\sigma_{p,geo}$ = 1) for $D_{p,geo}$ = 40 nm and $D_{p,geo}$ = 8 nm, respectively. The variations of particle number concentration with time predicted by MCAC and EDEM are in good agreement for $D_{p,geo}$ = 40 nm while in the case of $D_{p,geo}$ = 8 nm EDEM predicted a slower decrease in the particle number concentration, i.e., it predicted slower coagulation dynamics than MCAC. These two cases correspond to near-transition (initial $K_{n_D}$ = 17) and ballistic (initial $K_{n_D}$ = 190) agglomeration regimes, respectively. The difference in agglomeration dynamics is explained by two main factors, namely the particle persistent distances $\lambda_p$ (and their corresponding time step $\Delta t$), and the particle mobility diameter. The average ratio $\lambda_p/\Delta t$ leads to an average characteristic velocity of particle displacement, which is 12% higher for EDEM compared to MCAC. We thus would expect larger coagulation kernels for EDEM in the ballistic regime. However, both codes also have different models for mobility diameters as discussed in Section 2.3.

Indeed, as shown in Fig. 6, for $N_p$ larger than 1, the mobility diameter as modeled by MCAC is systematically smaller than the one predicted by EDEM indicating that the mobility as modeled by MCAC is larger than the one predicted by EDEM, especially at small $D_p$. This

explain the faster coagulation dynamics of MCAC compared to EDEM simulations observed in Fig. 28, particularly for $D_{p,geo} = 8$ nm.

The differences in coagulation kinetics lead to larger agglomerates, in terms of $\overline{N_p}$, by MCAC as compared to EDEM in the ballistic regime under the studied residence times, Fig. 28(f). In addition, both codes predicted very similar evolution of $\overline{N_p}$ in the near-transition regime, Fig. 28(e). A different trend is however observed in terms of the aggregate's geometric mean gyration diameter $D_{g,geo}$. The $D_{g,geo}$ predicted by EDEM is generally larger or equal to the one predicted by MCAC, Fig. 28(i) and (j), suggesting that the agglomerates predicted by EDEM must have a lower fractal dimension as compared to those by MCAC. As observed in Fig. 28(i) and (j), slightly more compact agglomerates are obtained with MCAC as compared to EDEM due to the larger persistent distance (by a factor of 2.65) in EDEM simulations (cf. Eqs. (66) and (64)). These population fractal parameters were determined by fitting Eq. (1) considering $N_p > 2$ to find $D_{f,p}$ and $k_{f,p}$ (see S2 in the Supporting Material). It should be noted that the fractal parameters obtained here for EDEM-derived agglomerates are lower than those reported previously [33,33,93], which included single spherical particles in the fractal parameter estimation. In addition, the aggregate size polydispersity is quantified by the gyration diameter geometric standard deviation $\sigma_{g,geo}$ shown in the last row of Fig. 28. The latter is naturally increasing with time due to agglomeration and remains below the self-preserving limit predicted by Eq. (17c) determined based on the homogeneity coefficient of the gyration diameter size distribution of MCAC simulations evaluated at the end of the simulation time. It should be noted that the self-preserving limit requires large aggregates (at least 20 primary spheres, see [96]) to be reached, which is hardly the case in the current simulation. In addition, the self-preservation approach is theoretically based on a constant homogeneity coefficient during time, which is not the case here since the particles undergo a change in flow regime over time. The MCAC and EDEM predicted similar evolution of $\sigma_{g,geo}$ for the $D_{p,geo} = 40$ nm case at relatively short residence times up to about 5 s, Fig. 28(m). At longer residence times, however, the discrepancies between the two codes grow and the $\sigma_{g,geo}$ of MCAC reaches a maximum polydispersity closer to the one expected for the self-preserving limit while the EDEM predicted a lower polydispersity. For the case of $D_{p,geo} = 8$ nm, MCAC predicted consistently larger $\sigma_{g,geo}$ than EDEM, though both codes predicted a maximum value of $\sigma_{g,geo}$ at 100 ms close to the self-preserving polydispersity expected for the ballistic regime $\sigma_{g,geo} = 2.27$ according to [93], Fig. 28(n). The asymptotic geometric standard deviation of the gyration diameter, $\sigma_{g,geo} \approx 2$ derived by both EDEM and MCAC is in good agreement with the asymptotic $\sigma_{g,geo} = 2.04$ measured for $ZrO_2$ agglomerates of polydisperse primary particles growing mostly by coagulation in a spray flame [397]. We also note that $\sigma_{g,geo}$ derived from TEM image analysis of soot particles has been found between 1.82 to 1.87 [389] in premixed and between 1.61 to 2.9 in diffusion flames [398,399]. The asymptotic $\sigma_{g,geo}$ derived by MCAC and EDEM are within this range considering that surface growth and oxidation are not considered in these simulations. It should also be noted that the substantially different diffusion models used by EDEM and MCAC resulted in practically identical coagulation dynamics in the absence of surface growth. However, the soot aggregates derived by EDEM have a smaller fractal dimension, $D_{f,p}$, but a larger prefactor, $k_{f,p}$, compared to those obtained by MCAC. These differences could be attributed partly to the different particle diffusion modeling used in EDEM and MCAC.

Good agreement is observed between the sectional and EDEM approaches for both $D_{p,geo} = 40$ nm and $D_{p,geo} = 8$ nm cases in terms of $n_p$, $\overline{N_p}$, $D_{g,geo}$, and $\sigma_{g,geo}$ especially at early residence times. At larger residence times, the sectional method predicted a faster decrease of $n_p$ for the $D_{p,geo} = 40$ nm case, which may be explained by the lower fractal prefactor assumed in these simulations as compared to EDEM leading to slightly enhanced coagulation kernels. In the $D_{p,geo} = 8$ nm case, the sectional method still shows faster coagulation than EDEM but slower than MCAC. The latter may be explained by the more ballistic agglomeration of this case leading to larger fractal dimensions but lower fractal prefactors. The $D_{g,geo}$ predicted by the sectional method is in excellent agreement with EDEM. The differences observed at early residence times, when agglomerates are small, are likely due to the poor accuracy of the fractal law (Eq. (1)) used here to determine $D_g$ for each section from the agglomerate volume, primary particle volume, and diameter. The closer agreement between the sectional method and EDEM, as compared to MCAC, for the $D_{p,geo} = 8$ nm case could be attributed to the similarity between the selected fractal parameters and those obtained from EDEM for this particular case.

In terms of particle number density, computed as $m_{0,0}$, the MOM approach shows good agreement with the other methods just at the beginning of the simulation, up to approximately 1 s for the $D_{p,geo} = 40$ nm case. However, for longer residence times, the aggregation process is slower in MOM, indicating an underprediction of the aggregation rate. Conversely, for the $D_{p,geo} = 8$ nm case, MOM aligns well with MCAC up to 10 ms, after which it underpredicts the particle number density compared to all the other methods. As a result, the number of monomers per aggregate ($N_p = 1/(36\pi)\, m_{-2,3}/m_{0,0}$) is underpredicted on the whole for the high $D_{p,geo}$ case and overpredicted for the low $D_{p,geo}$ case. In terms of gyration diameter ($D_g = 6/(36\pi k_f)^{1/D_f}\, m_{1-2/D_f,3/D_f-1}/m_{0,0}$), MOM presents an overall good agreement for the high $D_{p,geo}$ with other methods, while it overpredicts its evolution on the whole for the low $D_{p,geo}$ case. This highlights the limitations of MOM in capturing the detailed properties of soot particles when reducing the problem to a few statistical properties. Nevertheless, given its substantially reduced computational requirements, solving only six differential equations, MOM provides an efficient and fast method for obtaining preliminary estimates.

### 6.2. Case 2: Agglomeration of polydisperse primary particles

The primary particle diameters are now considered log-normally distributed with a geometric mean $D_{p,geo} = 8$ nm and different geometric standard deviations, namely $\sigma_{p,geo} = 1$, 1.2 and 1.5. The results of these simulations are reported in Fig. 28, from the second to fourth columns, respectively. Soot primary particle diameters in flames are in general fairly monodisperse, i.e., narrowly distributed, especially within individual aggregates [400], with values of $\sigma_{p,geo}$ up to 1.54 have been previously reported in the literature for soot particles sampled from diffusion or premixed flames [118,401]. The particle volume fraction, bulk density, and flame temperature are the same as the simulations presented in the previous section for Case 1. We note that in the first row of Fig. 28 the initial particle number concentration decreases monotonically with increasing the $\sigma_{p,geo}$ due to the increase in the total particle volume when keeping constant the initial particle volume fraction. It is intriguing to observe that increasing the $\sigma_{p,geo}$ leads to better agreement in most quantities predicted by MCAC and EDEM in Fig. 28, except $D_{g,geo}$. This may be explained by the predominant effect of larger particles in the system which makes the agglomeration closer to the transition regime where the results of the two meso-scale methods were seen in better agreement than in the ballistic regime (see the results of Case 1 in columns 1 and 2 of Fig. 28 discussed in the previous section). As shown in the bottom row of Fig. 28, the geometric standard deviation of gyration diameter predicted by MCAC is consistently larger than that by EDEM. In addition, the agglomerate polydispersity in terms of $\sigma_{g,geo}$ increases with time for all the cases but reaches a lower maximum value at the end of the simulation (100 ms) for larger $\sigma_{p,geo}$. These results may be explained by the longer time required by agglomerates consisting of polydisperse monomers to reach the self-preserving limit [96,350]. We also observe that both EDEM and MCAC show a lower fractal dimension as $\sigma_{p,geo}$ is increased which is also in agreement with previous observations from the literature [96, 350]. In addition, the performance of the sectional method consistently degrades in terms of $n_p$, $\overline{N_p}$, $D_{g,geo}$, and $\sigma_{g,geo}$ as we increase the primary particle polydispersity. Neglecting primary particle polydispersity as

done in this sectional approach leads to over-prediction of $n_p$ and under-prediction of $\overline{N_p}$. This is a natural limitation of the sectional approach as accurately simulating the evolution of primary particle polydispersity may require a multi-dimensional population balance approach where multiple additional differential equations are solved to obtain the polydispersity of each section of the aggregate size distribution. Such an approach is not considered here. A similar but likely less accurate approach may be to model the evolution of the primary particle size distribution assuming the same monomer distribution for all sections of aggregates as done in [43]. In this regard, monodisperse population balance models used EDM-derived collision frequencies enhanced by 1.35 [350] or 1.8 [360] to simulate soot dynamics in the free molecular [243] and transition [297] regimes, respectively, displaying good agreement with experimental data. We also observe that despite the limited accuracy of the sectional method in resolving both the $n_p$ and $\overline{N_p}$, it predicted fairly accurate geometric mean $D_g$, suggesting that $D_{g,geo}$ seems a robust parameter during particle agglomeration. Similarly to the sectional method, results from the MOM approach are also presented for the polydisperse case. The difference here lies in the initial conditions, as the MOM formulation cannot deal with polydispersity within aggregates. The MOM predictions are similar to MCAC at higher levels of initial polydispersity (e.g., $\sigma_{p,geo} = 1.5$), likely because the fractal parameters assumed in the MOM resemble those obtained through the MCAC simulations. However, the MOM consistently overpredicts the gyration diameter, which can be attributed to its inability to fully capture the evolving polydispersity and morphology of the aggregates. While the MOM provides reasonable agreement under certain conditions, particularly when its prescribed parameters closely match those determined by more detailed simulations, it still remains less accurate in reflecting the distribution of primary particle sizes and aggregate structures that arise as agglomeration proceeds.

Fig. 29 compares the aggregate size distributions predicted by MCAC, EDEM, sectional method and method of moments in terms of the volume equivalent diameter $D_v$ and the gyration diameter $D_g$. While $D_v$ is a direct output from the sectional method allowing a comparison with the results of EDEM and MCAC, the value of $D_g$ is determined based on Eq. (1) along with the assumed fractal parameters in the sectional and method of moments code. Since the size distributions are evaluated near the end of simulations, most of them look unimodal and in good agreement between MCAC and EDEM. As observed previously in terms of the geometric mean and geometric standard deviation of the gyration size distribution (Fig. 28), the agreement between the two meso-scale methods and the sectional approach is good when the primary particle polydispersity is low ($\sigma_{p,geo} \leq 1.2$). However, we notice the difficulties for the sectional method to predict the peak and the left-tail of the size distributions when $\sigma_{p,geo}$ further increases. A similar trend is observed for the method of moments, which also fails to accurately represent the details of the distribution, specially for high primary particle polydispersity. Notably, the only scenario in which this method aligns reasonably well with the other approaches occurs when $D_{p,geo} = 40$ nm and the initial distribution is monodisperse. Under all other conditions, the method of moments produces narrower distributions than those obtained from the other methods.

### 6.3. Case 3: Soot aggregation with surface growth

Two different sub-cases of simultaneous soot aggregation and surface growth are simulated. The prescribed total surface growth rates, $\dot{\omega}$ in kg m$^{-3}$ s$^{-1}$, for the two sub-cases are reported in Fig. 30(a). Here, $\dot{\omega}$ represents the total mass gained by particles, per unit of soot aerosol volume, per unit of time, from the gas-phase through surface growth. The first sub-case simulated is representative of a premixed flame [94] and considers a constant flame temperature of 1830 K, an initially monodisperse primary particle distribution with diameter $D_{p,geo} = 2$ nm, and initial volume fraction of $f_{v,0} = 0.1885$ ppb. These conditions are consistent with the measurements of incipient soot in the benchmark premixed ethylene flame [155]. The second sub-case simulated is representative of a carbon black furnace (the case referred to as $f_v = 2.4 \times 10^{-5}$ in Ref. [7]) and considers a constant temperature of 1673 K, an initially monodisperse primary particle distribution with diameter $D_{p,geo} = 3$ nm, and an initial volume fraction of $f_{v,0} = 1.18$ ppb. Both sub-cases are simulated until a total residence time of 100 ms.

Fig. 30(b) and (c) show the evolution of the particle volume fraction, $f_v$, with time in the premixed flame and carbon black furnace, respectively. The results of both MCAC and EDEM in the premixed flame sub-case exhibit a rapid increase in $f_v$ within about the first 10 ms, which is expected from the initially high surface growth rate shown in Fig. 30(a). After this time, the $f_v$ of MCAC reaches an asymptotic value of $f_v = 11$ ppb, which is consistent with the expected volume fraction based on the prescribed surface growth rate. The latter is determined as $f_v(t) = \rho_p^{-1} \int_{\tau=0}^{\tau=t} \dot{\omega}(\tau)\, d\tau$, where $\rho_p$ is the soot bulk mass density. The accuracy of MCAC depends on the method used for the determination of the volume and surface area of aggregates formed by overlapping primary particles, which is achieved here by using the $\alpha_v$ and $\alpha_s$ functions given in Eq. (82). The EDEM derived soot $f_v$ approaches slowly the prescribed final $f_v$. This can be attributed to the discrete number of acetylene molecules and hydrogen atoms present in the EDEM simulation by surface growth at $t > 10$ ms. Hence, the limited number of surface growth species can result in statistical variations of soot $f_v$ at long residence times. The difference in the predicted $f_v$ between MCAC and EDEM is predominantly attributed to their different computational implementation of surface growth (Section 5.3.3). MOM accurately predicted the evolution of $f_v$ under prescribed surface growth rates as compared to the reference (black dashed lines). This high accuracy is expected because under these conditions and assuming primary particles are in point contact, the evolution of $f_v$ becomes independent of particle morphology. It is important to note that the usual implementation of MOM in soot formation modeling involves calculating surface growth rates based on particle morphology and flow conditions, which can introduce discrepancies when compared to more detailed methods such as EDEM and MCAC.

A very different evolution of $f_v$ is observed in the carbon black furnace sub-case, where its evolution is slow at early residence times but continuously increases with residence time leading to $f_v > 16$ ppm at $t = 100$ ms. Such evolution of $f_v$ is expected from the monotonically increasing prescribed surface growth rate. In the carbon black furnace sub-case, while the deterministic surface growth model implemented in MCAC can accurately reproduce the theoretical volume fraction, EDEM shows difficulties in predicting accurately $f_v$, especially at residence times longer than about 60 ms. Once again, the accuracy of MCAC is dependent on the method for aggregate volume and surface area determination when primary particles are overlapped. In the carbon black furnace sub-case the results of MCAC were obtained by using the SBL library [358] instead of the $\alpha_v$ and $\alpha_s$ functions given in Eq. (82) used for the premixed flame sub-case. The latter method was needed in the carbon black furnace sub-case because of the high levels of primary particle overlapping between monomers whose diameters increase by almost 2 orders of magnitude in time. The difference between EDEM-derived and the prescribed $f_v$ evolution for this case can again be attributed to the statistical variation of the EDEM simulations using a stochastic algorithm for surface growth as explained above and in Section 5.3.3. MOM again predicted $f_v$ evolution in excellent agreement with the theoretically expected $f_v$.

Fig. 31 compares the particle (aggregate) number concentration and geometric mean gyration diameter predicted by MCAC, EDEM, and MOM (top row), and the aggregate gyration diameter geometric standard deviation predicted by MCAC and EDEM for both the premixed flame (plots on the left column) and carbon black furnace (plots on the right column) sub-cases of Case 3. Also plotted in Fig. 31(a) are the experimental data from [155]. For the premixed flame sub-case, MOM predicted the particle concentration evolution in excellent agreement with MCAC. For this case, the results from all these methods,

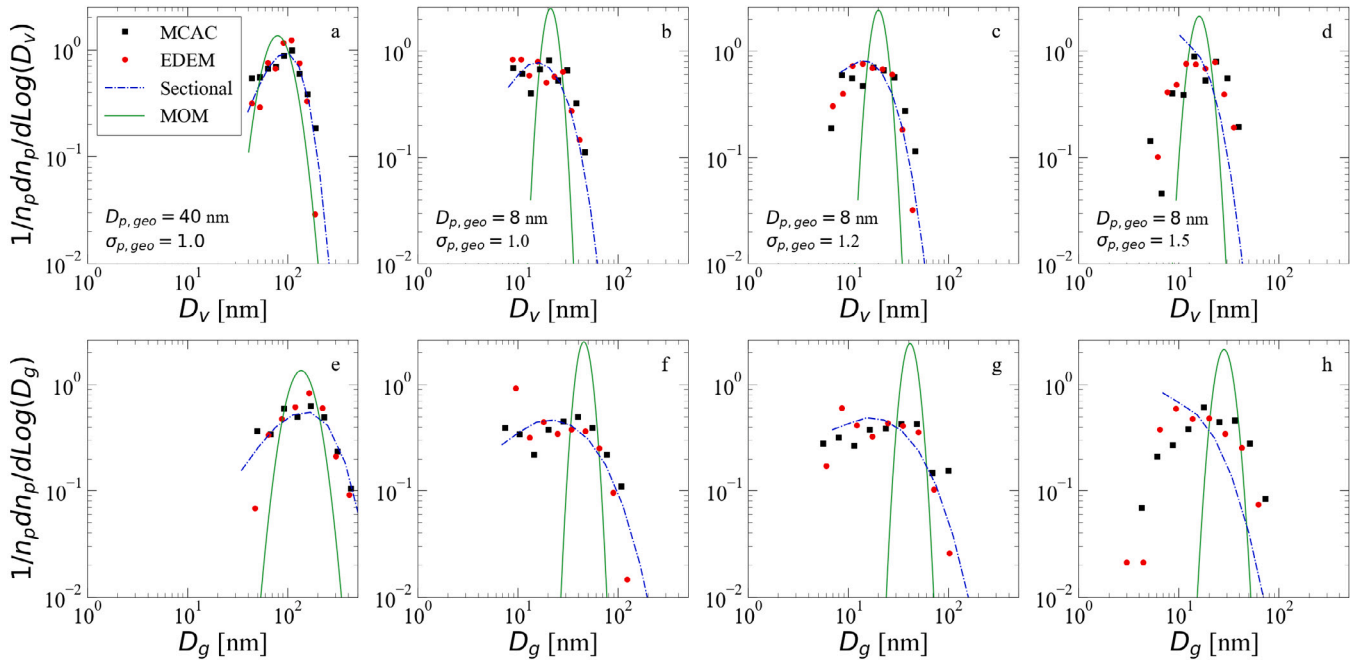


**Fig. 29.** Comparison of aggregate size distributions predicted by MCAC, EDEM, MOM, and the sectional method in terms of volume-equivalent diameter (top row) and gyration diameter (bottom row) for the pure agglomeration cases. Distributions are normalized by the total number concentration $N_{tot}$. Distributions evaluated at $t$ = 7.5 s for the $D_{p,geo}$ = 40 nm case and $t$ = 100 ms for the three cases of $D_{p,geo}$ = 8 nm.

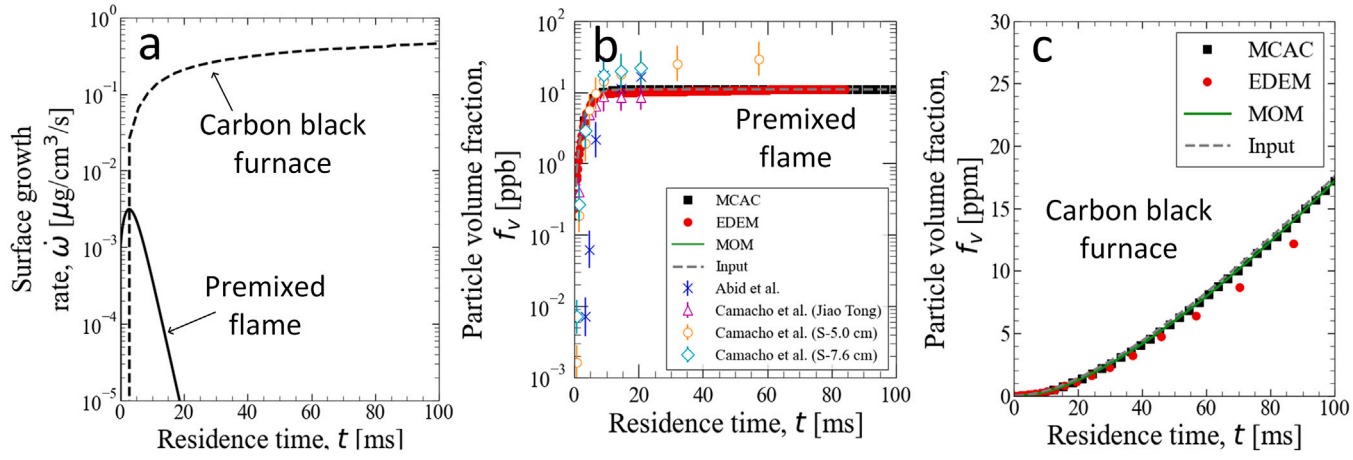


**Fig. 30.** Results of MCAC, EDEM, and MOM simulations of Case 3. The prescribed time-dependent total surface growth rates $\dot{\omega}$ in a premixed flame and a carbon black furnace, (a), the predicted particle volume fraction $f_v$ in the premixed flame, (b), and in the carbon black furnace, (c). Plots (b) and (c) share the same legend. The gray dashed line (referred to as Input) in these figures represents the theoretically expected soot volume fraction $f_v(t) = \rho_p^{-1} \int_{\tau=0}^{\tau=t} \dot{\omega}(\tau)\, d\tau$, where $\rho_p$ is the soot particle bulk mass density.
*Source:* Experimental volume fractions corresponding to the premixed flame from Camacho et al. [155] and Abid et al. [154].

i.e., MCAC, EDEM, and MOM, are in reasonable agreement with the experimental data, though the particle concentrations predicted by EDEM at about < 35 ms seem to be higher than the uncertainty range of the data. For the carbon black furnace sub-case, Fig. 31(b), MCAC again predicted a persistently lower particle concentration (or fast particle coagulation) than EDEM. On the other hand, MOM predicted particle concentrations in good agreement with the results of MCAC and EDEM at short residence times (<15 ms), but predicted increasingly higher particle concentrations than those of MCAC and EDEM with increasing residence time. Although MOM is able to predict accurately the evolution of soot volume fraction in both sub-cases of Case 3, Fig. 30, its ability to predict particle dynamics or coagulation is affected by the assumed particle morphological parameters, namely $D_f$ and $k_f$. The increasingly larger deviation of particle concentration predicted by MOM from MCAC and EDEM in the carbon black furnace sub-case is likely attributed to the inappropriate assumption of $D_f$ = 1.78 and/or $k_f$ = 1.3.

The differences in the particle number concentration evolution shown in Fig. 31(a) and (b), predicted by MCAC and EDEM, notably the faster decrease predicted by MCAC, are explained by the differences in the particle dynamics and thus in particle coagulation rate as discussed in Section 5.3.2. This also explains the slightly lower geometric mean gyration diameter by EDEM as compared to MCAC in both the premixed flame (Fig. 31(c)) and carbon black furnace (Fig. 31(d)). A similar trend to this property is predicted by the MOM approach, which displays the same overall behavior as in the pure aggregation cases. Specifically, in this scenario, MOM overpredicts the gyration diameter by up to a factor of two compared to MCAC and EDEM, reflecting the limitations of lower-order moment representations of particle dynamics in the presence of surface growth. In addition, while fairly good agreement is observed in terms of the gyration diameter geometric standard

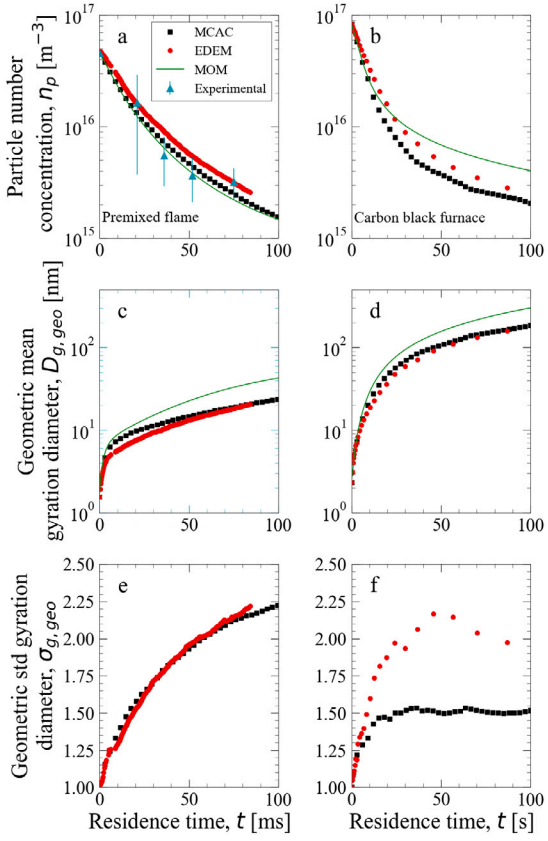


**Fig. 31.** Comparison of particle (aggregate) number concentration evolution predicted by MCAC, EDEM, and MOM for Case 3 in premixed flame (a) and carbon black furnace (b) and the geometric mean and geometric standard deviation of gyration diameter predicted by MCAC and EDEM. Plots (c) and (e) are for the premixed flame sub-case and plots (d) and (f) are for the carbon black furnace sub-case of Case 3.
*Source:* Experimental data from Camacho et al. [155].

deviation $\sigma_{g,geo}$ in the premixed flame (Fig. 31(e)), a considerably larger $\sigma_{g,geo}$ is observed from the EDEM results (Fig. 31(f)) for the carbon black furnace. Considering that the opposite trend was observed for pure coagulation cases studied in Sections 6.1 and 6.2, the larger $\sigma_{g,geo}$ of EDEM compared to MCAC may be explained by their different implementations of surface growth. There are two distinct effects that may contribute to this explanation, namely (1) the polydispersity of primary particles tends to decrease with surface growth in MCAC while it tends to increase in EDEM, and (2) the strong surface growth effect in the carbon black furnace sub-case may lead to particle coagulation evolution towards the transition and near diffusive regime where the MCAC predicted $\sigma_{g,geo}$ has been observed to be smaller than the one of ballistic regime [96].

Fig. 32 compares the average number of monomers per aggregate and properties of primary particles as a function of residence time in the premixed flame and carbon black furnace of Case 3 simulated by both MCAC and EDEM. Results from MOM are also included for number of monomers and primary particle diameter. The experimental mean numbers of primary particles per agglomerate obtained based on average mass measured using CPMA by Camacho et al. [155] are also included in Fig. 32(c). While coagulation is faster in MCAC simulations as compared to EDEM, it is not surprising to have larger $\overline{N_p}$ for MCAC compared to EDEM, Fig. 32(a,b). Additionally, the MOM results align closely with MCAC predictions for the premixed flame case, whereas for the carbon black furnace scenario, MOM predictions more closely match those of EDEM, demonstrating that its performance can vary depending on the operating conditions. The larger $\overline{N_p}$ for MCAC is still observed in terms of the volume-surface equivalent number of monomers $\overline{N_{va}}$ for the premixed flame, Fig. 32(c). It is noticed that at about 20 ms the mean number of primary particles per agglomerate predicted by EDEM agrees better with the experimental data. At 50 ms, however, the mean number of primary particles per agglomerate predicted by MCAC agrees well with the experimental data. It is interesting to observe that a crossover in the predicted mean numbers of primary particles per agglomerate by MCAC and EDEM occurs for the carbon black furnace sub-case, Fig. 32(d). The latter may be explained by the differences in aggregate morphology as discussed in the next section. The second row plots of Fig. 32 display the primary particle geometric mean volume-area equivalent diameter (Fig. 32(e–f)) and geometric mean diameter (Fig. 32(g–h)). Larger primary particles obtained in MCAC simulation for both the premixed flame and carbon black furnace sub-cases can be explained by the differences observed in Fig. 30 related to the different implementations of surface growth. We also observe that the MOM-predicted particle diameter for the premixed flame case remains intermediate between MCAC and EDEM, Fig. 32(e), yet continues to grow from 10 to 100 ms, whereas the results of MCAC and EDEM remain approximately constant. In contrast, for the carbon black furnace scenario, the MOM underestimates particle diameter relative to both MCAC and EDEM for the entire simulation, Fig. 32(f), displaying the method's sensitivity to the underlying conditions. Finally, as shown in the bottom row of Fig. 32, the primary particles have a relatively narrow distribution with geometric standard deviations below 1.25 predicted by EDEM for both cases. The asymptotic $\sigma_{p,geo}$ derived by EDEM is in reasonably good agreement with that measured in laminar sooting flames. In addition, the $\sigma_{p,geo}$ remains constant at the initial value (unity) for MCAC while it increases monotonically to reach a fairly asymptotic value for EDEM. The difference in the predicted $\sigma_{p,geo}$ by EDEM and MCAC is entirely attributed to their different treatments of particle surface growth. While in EDEM simulations the surface growth is treated stochastically at the primary particle level (the mass is added only to a selected primary particle in an aggregate), in MCAC all the primary particles are subject to surface growth uniformly within the aggregate. Therefore, EDEM can account for soot primary particle polydispersity through inception (polydisperse incipient soot particles are initialized as in Case 2) or surface growth (Case 3), while MCAC can predict polydisperse primary particles only if the initial incipient soot particles are polydisperse, as in Case 2, since MCAC does not produce primary particle polydispersity during surface growth for initially monodisperse incipient soot particles.

Fig. 33 shows an EDEM/MCAC comparison of aggregates size distribution in terms of volume equivalent diameter $D_v$ (top row) and gyration diameter $D_g$ (bottom row) for the premixed (left column) and carbon black furnace (right column). In addition, the results from the MOM are also presented, assuming a log-normal size distribution. All distributions are unimodal as expected from the simultaneous aggregation and surface growth. The agreement between both codes (EDEM and MCAC) is excellent in the premixed flame case in terms of $D_v$ while a small shift to larger diameters is observed in terms of $D_g$ for MCAC as compared to EDEM. Interestingly, in the carbon black furnace, we observe similar size distributions in terms of $D_v$ for both MCAC and EDEM. However, the $D_g$ distribution is much broader for EDEM than for MCAC. Both codes show the same main mode, which peaks at about 200 nm, but the $D_g$ distribution of EDEM shows a larger amount of smaller particles. The agreement in terms of the main mode of the distribution is attributed to the similarities between both codes for simulating coagulation as discussed in Sections 6.1 and 6.2. The broader left-tail in the $D_g$ distribution observed for EDEM as compared to MCAC may be explained by the preferential surface growth of larger primary particles in EDEM leading to aggregates with large friction coefficient and thus smaller collision frequency. Regarding the MOM, its predicted distributions are generally narrower, especially for $D_g$, as previously noted in the pure aggregation case. However, under the premixed flame conditions, MOM still provides a reasonably good

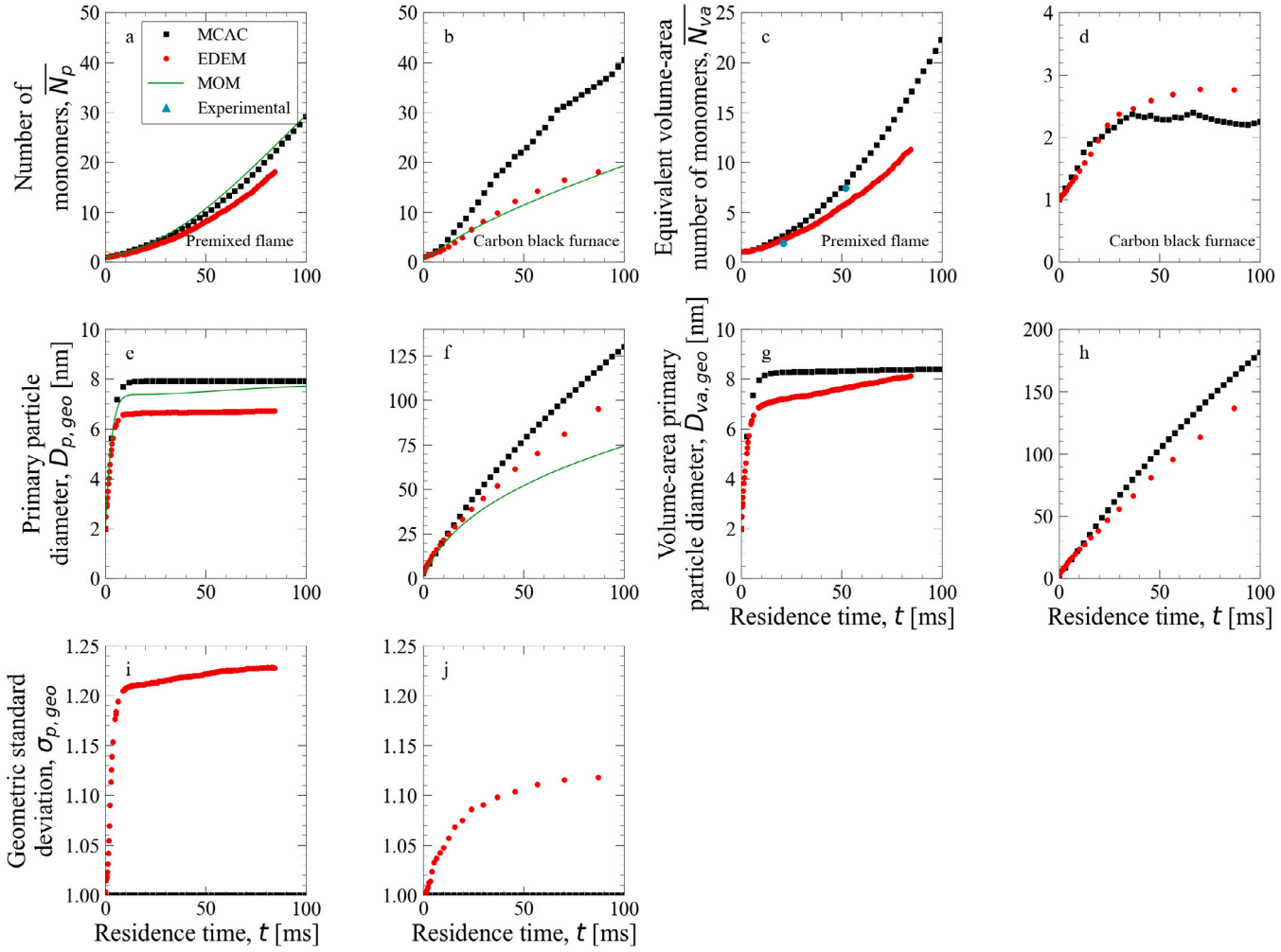


**Fig. 32.** Comparison of primary particle size distributions and the average number of monomers predicted by MCAC, EDEM, and MOM for Case 3. Plots (a, c, e, g, and i) are for the premixed flame sub-case and plots (b, d, f, h, and j) are for the carbon black furnace sub-case.
*Source:* Experimental data from Camacho et al. [155].

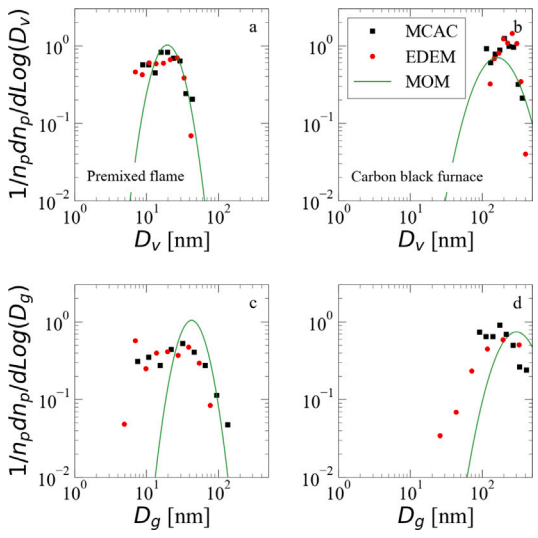


**Fig. 33.** Comparison of aggregate size distributions predicted by MCAC, EDEM, and MOM in terms of volume-equivalent diameter (top row) and gyration diameter (bottom row), the left column corresponds to the premixed flame, the right one to the CB case. Distributions are normalized by the total number concentration $N_{tot}$. Distributions are evaluated at a residence time $t = 100$ ms.

match in terms of $D_v$, and the mean particle sizes are not significantly different from those predicted by EDEM and MCAC, even with various underlying simplifications. Thus, while the MOM cannot fully capture the complexity of evolving aggregate structures under different conditions, it can offer a useful approximation in scenarios where a log-normal assumption and a limited set of parameters can adequately describe the particle population.

### 6.4. Detailed morphological analysis for Cases 1, 2 and 3

The aim of this section is to present the morphological parameters of a small number of arbitrarily selected large particles out of all those generated by the two meso-scale codes. As such, this analysis is by no means of statistical significance. For example, the aggregate sizes reported hereafter are not representative of those generated, as discussed in the previous sections. As explained in Section 2.2, a detailed morphological analysis of each numerically produced aggregate can be performed by examining its volume-based pair correlation function. In this section, we consider the largest aggregates (in terms of the number of primary particles $N_p$) produced by each meso-scale simulation (without surface growth in Cases 1 and 2, $D_{p,geo} = 40$ and 8 nm respectively with $\sigma_{p,geo} = 1.0$, 1.2 and 1.5 and with surface growth in the premixed flame sub-case of Case 3 at residence times of 25, 50, 75 and 100 ms).

Fig. 34 displays the normalized pair correlations of four aggregates generated by EDEM and MCAC, without surface growth (Case 1 with

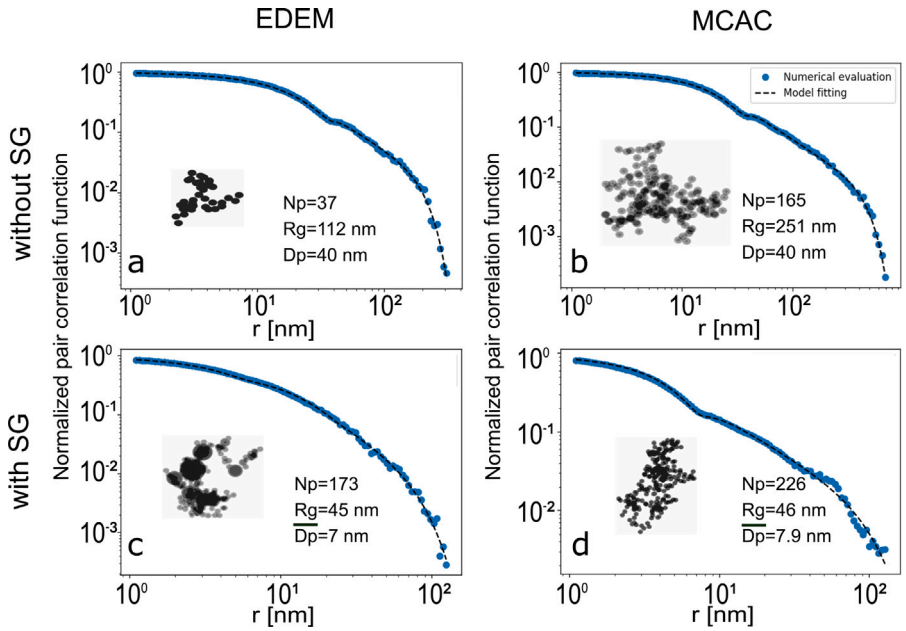


**Fig. 34.** Examples of pair correlation calculations and analysis for EDEM (a and c) and MCAC (b and d) without (a and b) or with (c and d) surface growth for Case 1 (first row) at $t$ = 8 s and the premixed flame sub-case of Case 3 at $t$ = 100 ms.

$D_{p,geo}$ = 40 nm, $\sigma_{p,geo}$ = 1.0, and at $t$ = 8 s) and with surface growth (the premixed flame sub-case of Case 3, at $t_{res}$ = 100 ms). For both Cases 1 (first row) and 3 (second row), we can clearly see the transition between $A_{pp}$ (which corresponds to the pair correlation of primary particles with themselves) and $A_{agg}$ (which corresponds to the pair correlation between different primary particles with each other). This transition becomes less visible as the primary particles become more polydispersed (see plot c). In any case, the results based on Eq. (4), reported as dashed curves, are in good overall agreement with the data points, enabling the evaluation of quantities of interest. For example, we found the individual fractal dimension $D_{fi}$ = 1.69, 1.69, 1.39, and 1.91, packing factor $\varphi$ = 0.75, 0.85, 2.8, and 0.68, and the stretching exponent $\beta$ = 3.48, 3,42, 2.37, and 2.12 for the aggregates shown in plots a, b, c and d, respectively.

Fig. 35(a) reports the individual fractal dimensions of the selected aggregates. As a reference, we also plot the asymptotic value observed for the DLCA case [129] (the blue dashed line), which is relatively well found in this study for the largest analyzed aggregates. For smaller aggregates, a fractal signature is not distinguishable, explaining the variability of the reported individual fractal dimensions. From this point of view, there is no specific difference between MCAC and EDEM. Fig. 35(b) displays the corresponding packing factors. This parameter reveals the local compactness. It is larger in the case of polydisperse aggregates (the larger values are found here for the EDEM simulation for $D_{\mathrm{p,geo}}$ = 8 nm with $\sigma_{\mathrm{p,geo}}$ = 1.5). Surface growth activates the primary particle overlapping which also explains the increase of the packing factor as well as the coordination number [34]. Most of the reported values are similar to the asymptotic behavior $\phi$ = 0.68 obtained in [131]. Nevertheless, much larger values (even larger than 1) can be found as reported in [34].

Each analyzed aggregate can also be discretized enabling the evaluation of the particle anisotropy and exact gyration radius when overlapping is present [130]. Heinson et al. [131] have shown the anticorrelation property of this parameter with the stretching exponent for DLCA aggregates as reported by the cyan crosses in Fig. 36(a). The present study reveals a similar dispersion for the MCAC and EDEM simulations without and with surface growth.

Primary particle overlapping occurs when surface growth is activated. This is quantified by the overlapping coefficient introduced by [92] and reported in Fig. 36(b). It appears that MCAC produces larger overlapping than EDEM. Nevertheless, it must be noticed that this scenario of surface growth produces smaller $C_{ov}$ compared to experimental observations. Larger values (up to 0.5) have been observed with MCAC for the simulation of a laminar ethylene diffusion flame [163].

Based on the above discussion, we can conclude that the morphological parameters of MCAC and EDEM produced aggregates are similar and not too different from those of the reference DLCA aggregates, except the primary particle polydispersity that is found to be larger for EDEM aggregates when surface growth is activated. This is primarily due to the different ways to implement the particle surface growth under a given mass flux in EDEM and MCAC. In particular, each acetylene reaction takes place stochastically and sequentially on the surface of EDEM-derived soot primary particles, increasing their polydispersity. In contrast, acetylene reactions are distributed uniformly among all MCAC-derived primary particles without affecting their polydispersity.

### 6.5. Comparison of CPU times for Cases 1, 2, and 3

Table 5 compares the CPU times (in hours) of selected simulations from Cases 1, 2, and 3 based on EDEM, MCAC, sectional, and MOM simulations. In all cases, a total flame residence time of 100 ms was considered. Unsurprisingly, the table shows up to 5 orders of magnitude difference between meso-scale and macro-scale codes. Two points can be noticed from the CPU time scaling for meso-scale models when surface growth is included. Firstly, the inclusion of surface growth significantly increases the CPU time of both MCAC and EDEM, especially for the latter. This is because additional calculations of volume and surface area of overlapping primary particles must be performed to account for surface growth. The much higher increase in CPU time for EDEM is attributed to its stochastic way to handle soot surface growth. In contrast, MCAC assumed that surface growth occurs uniformly and deterministically over all the primary particles in an aggregate (though mass is only added to free surface area). Although the stochastic approach used to simulate surface growth in EDEM requires larger computational times than MCAC, it resulted in favorable agreement in the predicted polydispersity of primary particle size with available experimental measurements in premixed [81] and diffusion [360] flames. Similar distributions can also be obtained by MCAC, though a proper

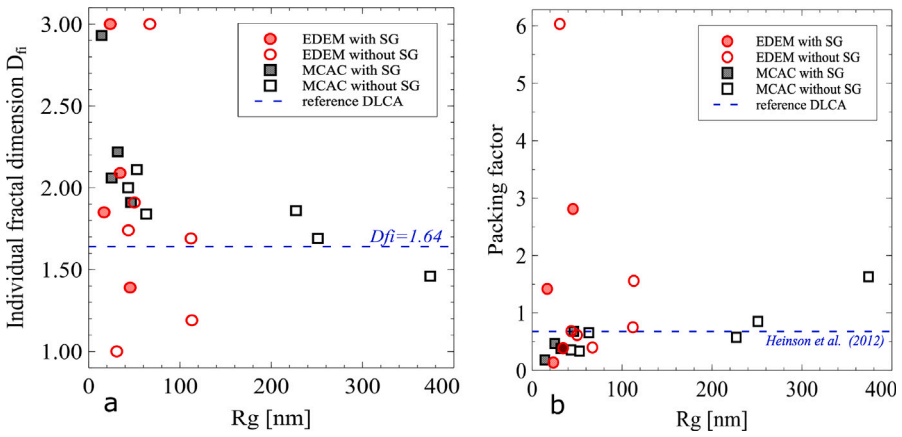


**Fig. 35.** Individual fractal dimension $D_{fi}$, (a), and packing factor $\varphi$, (b), as a function of the gyration radius for the set of selected aggregates.

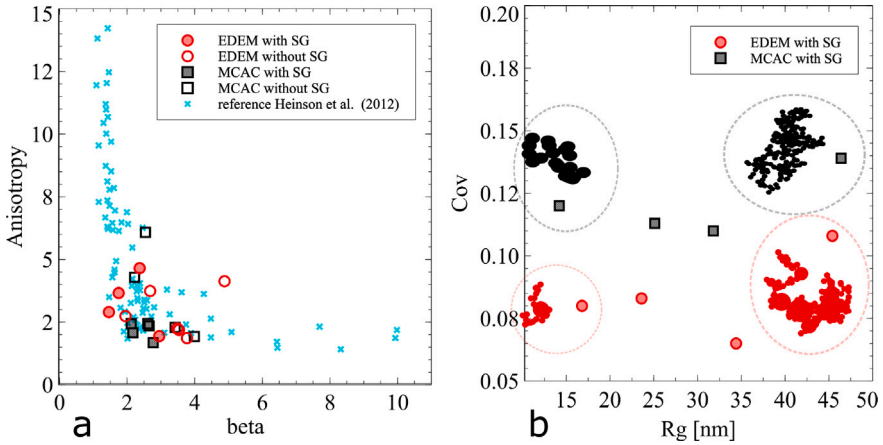


**Fig. 36.** Anisotropy vs. stretching exponent, (a), and primary particle overlapping coefficient as a function of the gyration radius, (b), for the set of selected aggregates.

**Table 5**
Comparison of CPU times (in hours) for EDEM, MCAC, Sectional, and MOM simulations corresponding to 100 ms of flame residence time. Case 1 and Case 2 refer to $D_{p,geo}$ = 8 nm with $\sigma_{p,geo}$ = 1 and $\sigma_{p,geo}$ = 1.5, respectively. Case 3(PF) and Case 3(BCF) refer to the premixed flame (PF) and black carbon furnace (BFC) sub-cases of Case 3, respectively. N.A. stands for "not available".

| Method | Case 1 | Case 2 | Case 3(PF) | Case 3(BCF) |
|---|---|---|---|---|
| EDEM[a] | 2.84 | 7.96 | 91 | 250 |
| MCAC[b] | 2.71 | 2.52 | 7.46 | 252 |
| Sectional[b] | $1.5 \cdot 10^{-3}$ | $1.4 \cdot 10^{-3}$ | – | – |
| MOM[c] | $2.4 \cdot 10^{-4}$ | $2.4 \cdot 10^{-4}$ | $2.9 \cdot 10^{-3}$ | $3.6 \cdot 10^{-3}$ |

[a] Based on Euler (VI-IX) ETH Supercomputer [402]. All these CPUs are AMD with clock speed between 2.25 to 2.6 GHz nominal and maximum RAM between 256 to 512 Gb.
[b] Based on a 11th Gen Intel(R) Core(TM) i5-1135G7 with 2.40 GHz CPU clock speed, and 8 Gb of RAM memory.
[c] Based on a 12th Gen Intel(R) Core(TM) i7-12700K with 3.60 GHz CPU clock speed, and 32 Gb of RAM memory.

initial level of primary particle polydispersity is required. Secondly, the carbon black furnace (CBF) sub-case involves much bigger soot primary particles than the premixed flame sub-case, which means that particle aggregation is more diffusive in the CBF case than in the premixed flame case. As described in previous sections, both MCAC and EDEM consider a persistent distance to simulate the particle displacement which becomes smaller as aggregation becomes more diffusive, making the simulation more challenging in both EDEM and MCAC. In addition, the much higher CPU time of the CBF sub-case of Case 3 compared to that of the premixed flame sub-case for MCAC is also explained by the different method of aggregate's volume and surface area calculation as explained above.

## 7. Challenges and future prospects

Meso-scale methods have been increasingly used to predict the size and detailed morphology of individual soot particles under conditions relevant to laminar sooting flames. This type of method was developed to incorporate most of the physical and chemical processes associated with soot formation and soot particle dynamics and to resolve the positions of primary particles within individual aggregates. The main features of the three commonly used meso-scale methods, namely the detailed stochastic population balance (DSPB) algorithm, the event-driven discrete element method (EDEM), and the Monte Carlo aggregation code (MCAC), were discussed with their differences highlighted in Section 5. In particular, the performance of EDEM and

MCAC was directly compared in several test cases of soot particle aggregation without and with surface growth. It is unexpected that EDEM and MCAC performed somewhat differently even in the simplest cases of pure agglomeration of either monodisperse primary particles, especially in the free-molecular regime, or polydisperse primary particles. In the cases of pure particle agglomeration MCAC typically predicted faster particle coagulation and hence a faster decay in the particle number concentration and a larger number of monomers per agglomerate. Larger discrepancies in the results of EDEM and MCAC were produced in the simulation of particle aggregation in the presence of surface growth, which can be primarily attributed to the difference in how they model surface growth of fractal aggregates formed by overlapping primary particles discussed in Section 5. In fact, the surface growth of fractal aggregates is handled differently in all three meso-scale methods reviewed in this article. Apart from other differences in the predicted particle morphology and aggregate size distribution, a distinct consequence is the primary particle polydispersity. Specifically, for initially monodisperse primary particles subject to surface growth EDEM and DSPB will produce fractal soot aggregates formed by polydisperse primary particles with overlapping. In contrast, MCAC will produce soot fractal aggregates formed by overlapping monodisperse primary particles. Therefore, how to properly model the surface growth of fractal aggregates formed by either point-contact or overlapping primary particles remains a challenge. This question may perhaps be answered by performing a detailed DSMC simulation of a fractal soot aggregate submerged in surface growth gaseous species and calculating soot surface growth based on collision between surface growth species and the soot particle without prescribing how mass is added to the soot particle. It is noticed that benchmark meso-scale solutions of nanoparticle aggregation in the presence of surface growth are currently unavailable to our knowledge, but certainly needed for validating meso-scale methods. It should also be noticed that EDEM and MCAC modeled the mobility diameter of fractal aggregates differently. While the $D_m/D_p$ ratio of MCAC depends on $D_p$, it is independent of $D_p$ in EDEM in both the free-molecular and transition flow regimes. The mobility diameter of fractal aggregates in different flow regimes should be further investigated.

As can be seen in Table 4, there is no agreement in the criteria for selecting the initial primary particle size distribution considered in DEM simulations for soot formation in flames. It is also currently unknown how soot primary particle polydispersity arises from the following three plausible reasons: (1) polydispersity of incipient soot particles (as commonly considered in MCAC simulations [334]), (2) as the result of continuous soot inception in time in the presence of surface growth [163], or (3) as the result of surface growth itself (as proposed in EDEM simulations [33]). It is possible that the soot primary particle polydispersity is the dominant one among the three causes in reality, though their relative importance may vary with flame conditions.

In addition to the challenges of detailed modeling of soot surface growth discussed above at meso-scale, there are several other important yet unresolved issues in modeling the detailed soot particle morphology in sooting flames, such as coalescence, sintering, and maturity.

Coalescence refers to the process in which two colliding spherical particles fuse into a larger spherical particle instantaneously, which results in reduced particle number concentration and the available area for surface growth. It is noticed that coalescence is commonly used to describe the instantaneous merging of two liquid drops upon collision. Coalescence has been believed to play an important role in the very early stage of soot formation [21]. The current status of modeling soot coalescence was reviewed in Section 3.1. More fundamental research is clearly needed to understand the coalescence of incipient soot particles and to explore how to differentiate incipient soot coalescence from PAH coalescence. It is noticed that coalescence of liquid-like incipient soot has not always been taken into account in soot models, either at meso- or macro-scale. For example, particle coalescence was implemented in the DSPB method in which a soot particle smaller than a critical diameter coalesces with another particle upon collision [197,205]. Continuous coalescence of 2 nm soot [33] and silica [360] nanoparticles has been simulated by EDEM. It was shown that coalescence and surface growth of small nascent soot particles in the absence of aggregation resulted in narrow size distributions and underestimated the measured mean $D_m$ of premixed flame soot by 25% [33]. Coalescence of soot has not been considered in MCAC. Even though coalescence of flame-made silica nanoparticles has been considered by EDEM [360], coalescence of soot has not been considered in either EDEM or MCAC. The potential importance of coalescence in the early growth of incipient soot particles is strongly dependent on their coagulation efficiency. Quite different coagulation efficiencies of incipient soot particles have been reported in the literature as reviewed in Section 3.2.

Further studies are needed to reconcile the large differences in the sticking probability of young soot particles less than 10 nm predicted by Hou et al. [209], Morán et al. [206], and Hou et al. [214] on one hand, and Huo et al. [202] on the other hand.

In the context of aerosol science, sintering commonly refers to the process of compacting and bonding of two or more touching solid particles by pressure or heat, causing the atoms of these particles in the contacting region to diffuse across their surfaces to fuse into each other. Different mechanisms of sintering have been proposed [403], such as surface diffusion, grain boundary diffusion, and plastic/viscous flow. Because coalescence and sintering describe a similar phenomenon, they are sometimes used inconsistently in the literature [30,98]. The relevance of sintering in soot formation has been subject to confusion and debate. On one hand, it is believed that carbonaceous soot particles do not undergo sintering since they possess a turbostratic structure and do not melt [32,158]. On the other hand, sintering has been considered important in the studies of Kraft and co-workers, e.g. [98,194,197,205,353]. It is worth noting that sintering and coalescence are modeled the same way in these studies and the subtle difference between them lies in the characteristic sintering time, i.e., sintering is a relatively slow process (relative to coalescence) while coalescence takes place nearly instantaneously [205]. Besides surface growth, sintering is potentially another mechanism for the overlap between neighboring soot primary particles in aggregates observed in TEM images of sampled soot. Although Michelsen et al. [30] have recently recommended to use *coalescence* to describe the instantaneous merging of liquid-like incipient soot particles and favored the viewpoint that sintering is not relevant to soot, the transition of incipient soot from coalescence to aggregation growth deserves further research to ascertain if young soot particles undergo sintering under different flame conditions. However, sintering should be taken into account for the simulation of particles composed of other materials at high temperatures, such as $TiO_2$.

Soot maturity has received increasing research attention in recent years because it is closely related to the chemical and physical properties of soot. Maturity has been used to describe the maturity level of soot during its evolution from incipient soot to fully mature soot. Conceptually, the maturity level of soot can be linked to its chemical composition and/or its internal nanostructure, and different techniques (most of these techniques are *ex-situ*) can be used to characterize the chemical, morphological, and structural properties of soot particles, depending on their maturity level [404]. There is currently no established indicator to quantify the level of soot maturity, though the soot absorption function $E(m)$ and the Ångstrom absorption exponent (AAE) have often been used for this purpose [12–14,405]. This is likely because $E(m)$ and AAE can be obtained *in-situ* and fairly easily from extinction measurements. Kholghy et al. [189] defined mature soot by the presence of a graphitic shell, regardless of H/C ratio, shell thickness, or size. It has been well known that soot maturity affects the surface reactivity of soot particles as discussed in Section 3; however, little attention has been paid to the effect of soot maturity on soot particle dynamics, i.e., the bulk density increase with maturity and soot maturity as characterized by the soot particle surface structure can potentially affect the collision and sticking efficiencies. Although

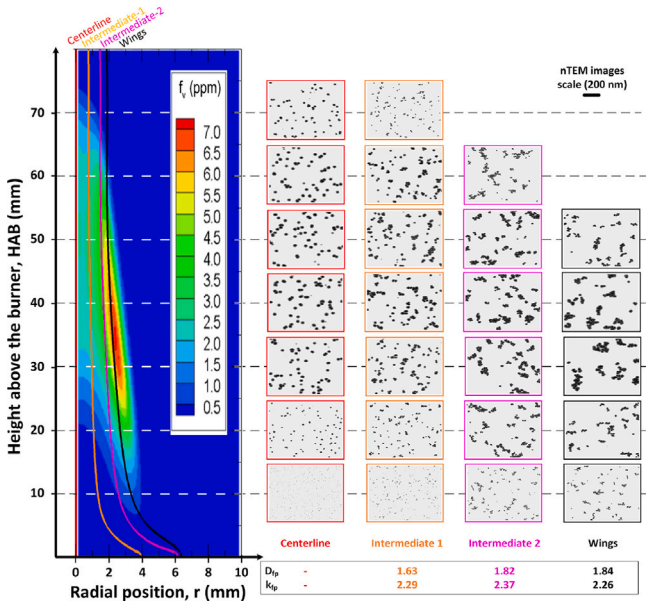


**Fig. 37.** Multi-scale simulations of soot formation in an ethylene diffusion flame along 4 different trajectories including one through the flame wing and one through the flame centerline. The left plot shows the soot volume fraction predicted by the macro-scalemarcoscale code (CoFlame [43]) and the right plots display numerical TEM of sampled aggregates simulated using MCAC [163].
*Source:* Reproduced from Morán et al. [163].

the DSPB model is able to track the average H/C ratio and the detailed PAH composition of soot particles, carbonization, which is believed to be the driving force of soot maturity, has not been considered in the other two meso-scale methods discussed in this review.

Recently, Morán et al. [206] have made an attempt to investigate the effect of soot maturity on soot particle aggregation kinetics. In their study, however, soot maturity was related only to particle size and bulk mass density, without accounting for detailed particle surface structure characterized by PAH size and orientation [189]. The impact of the particle bulk density and maturity on soot dynamics has also been quantified in EDEM [360]. That way, it was shown that reducing the bulk density from 1.8 to 1.4 g/cm$^3$ did not affect the evolution of the soot $D_m$ and $D_p$.

As can be seen in Table 4, other limitations of the meso-scale approaches include a detailed consideration of the local flame conditions, such as temperature and gas species concentrations, as well as modeling the particle-gas mass transfer. Also, as tracking the positions of individual primary particles, as done in DEM meso-scale approaches, is commonly computationally expensive, simulating a whole flame remains a challenge. An alternative to tackle these limitations has been recently proposed in Ref. [163]. In this work, the authors proposed a strategy for simulating soot formation in a diffusion flame based on DEM simulations. For this purpose, they coupled both macro- and meso-scale codes (CoFlame and MCAC). This multi-scale approach accounted for the local flame conditions to predict the evolution of soot particle size and morphology along specified pathlines in the flame as shown in Fig. 37.

Indeed, both meso- and macro-scale modeling should be conducted as they complement each other. Macro-scale methods provide a more detailed description of soot kinetics (chemical aspects dealing with interactions with gas-phase species), but cannot track soot particle dynamics at the level of meso-scale methods. Specifically, macro-scale methods are capable of providing soot inception, surface growth, and oxidation rates and soot particle size distribution because they solve the conservation equations of the system, including the gas-phase and the particle phase, i.e., the focus of macro-scale methods is the statistical behavior of the reacting system. However, macro-scale methods are unable to describe certain particle behavior, especially for fractal-like soot particles, such as the fractal parameters ($D_f$ and $k_f$), collision diameter, and mobility diameter. Such information has to be obtained either from experiments or from meso-scale modeling. On the other hand, the focus of meso-scale methods is the particle behavior, though some gas-phase properties affecting the particle process are still needed, such as temperature, viscosity, and mean-free-path. To model soot formation in flames, meso-scale methods typically depend on macro-scale methods to provide temperature, gas-phase species, and soot inception, surface growth, and oxidation rates along the trajectory of the meso-scale domain in the flame. Several studies have been conducted to use a meso-scale method as a post-processor to provide more detailed modeling of soot particle morphology [163,205]. From these points of view, such multiscale modeling should be coupled in the future to achieve overall better description of soot formation and particle dynamics. Specifically, the detailed soot particle morphology from the meso-scale modeling should be used to update the macro-scale modeling. This is because soot particle morphology affects not only particle coagulation but also soot particle surface growth and oxidation through surface area. In this regard, simple analytical power laws for the soot collision frequency [350,360], $D_m$ and $D_g$ [94] derived by EDEM have been interfaced with macro-scale population balance models to account for the realistic soot structure, improving substantially their agreement with experimental data [243,297]. Nevertheless, with the perspective of coupling simulations at meso- and macro-scales, an effort must be made to improve the modeling of certain forces. Indeed, simulating aggregation in a domain (meso-scale) moving along a streamline in the macro-scale simulation is not enough. While it has been shown that molecular diffusion plays a negligible role due to short residence times, the thermophoretic force seems to play a non-negligible role in the extraction of the domain trajectory [163]. In fact, it has been shown that in identical temperature gradients, at the same mobility diameter, the thermophoretic velocity of aggregates is much higher than that of a spherical particle [406].

Another remaining challenge is adapting DEM codes for turbulent flames. Although the length scales studied in meso-scale simulations are much smaller than the smallest turbulent scales. However, the time scale involved in particle coagulation in meso-scale simulations (on the order of ms to s) is much longer than turbulent time scales (typically on the order of μs). Consequently, turbulent effects cannot be ignored during meso-scale modeling of soot particle aggregation. A remarkable pioneer work has been conducted by Inci et al. [345] where Langevin Dynamics DEM simulations have been combined with a DNS approach to account for the flame turbulence. The authors highlight the importance of determining the Péclet number corresponding to the ratio between the Brownian diffusion and Kolmogorov characteristic times. They tend to observe an increase in the population fractal dimension as the Péclet increases from $D_{fp} \approx 1.65$ for pure diffusive aggregation to $1.91 \leq D_{fp} \leq 2.1$ for Péclet numbers as high as 1. In addition, DEM and DNS simulations have shown that the collision rate of droplets growing by turbulent coalescence is smaller compared to that obtained by kinetic theory valid for laminar conditions [407]. There is a limited understanding though about the impact of turbulence on soot agglomeration during combustion. In this regard, the soot mobility and primary particle size distributions measured in a rather turbulent flame environment in an enclosed spray combustion burner were described accurately by EDEM for surface growth and agglomeration [361]. This may indicate that the impact of turbulence is rather small for soot formation during combustion. Further research is certainly essential to explore the effects of turbulence on soot dynamics.

Much effort needs to be made to access experimentally in a non-intrusive *in-situ* manner to the measurands of interest for the simulation discussed in this review. Indeed, DEM simulation provides access to detailed information on the size and morphology of soot. In order to ensure the relevance of this modeling, it is appropriate to validate them

on reference flames. To date, while reference flames are fairly well detailed in terms of soot volume fraction, few studies reported information on their size and even fewer presented detailed soot morphology (generally limited to $D_{fp}$ and $D_p$). Therefore, efforts need to be made to better determine experimentally the size and morphology of particles with the best possible spatial and temporal resolution. Techniques based on light scattering (visible or X-ray) have great potential in this perspective. For example, a very recent study has improved an angular light scattering technique for determining the size of aggregates in an axisymmetric scattering flame with high spatial resolution and by correcting the bias induced by light trapping occurring in such heavily sooting flames [408]. With such advanced experimental techniques, we hope to be able to validate the simulations and also to gain more clarity on certain pending questions such as those raised in this review concerning the nature of the size distribution during particle formation (lognormal or self-preserving) and if sintering plays a role in primary particle overlap.

## 8. Concluding remarks

Developing capabilities of predicting the detailed soot particle size and morphology is of both great fundamental interest and vital importance to optimization of carbon black furnace design, evaluation of soot particle physical and optical properties, and mitigation of soot emissions from combustion systems. Although the details of soot formation, such as inception, maturity, surface growth, and oxidation-induced fragmentation, remain not fully resolved, significant progress has been achieved in our understanding of PAH formation and growth of PAH clusters leading to incipient soot under flame conditions from experiments and multi-scale modeling. Reactive molecular dynamics simulations and meso-scale discrete element methods have been increasingly used to investigate soot inception and particle dynamics and the evolution of particle size distribution and detailed morphology of individual soot particles. Macro-scale models of soot formation in flames, either solve the PBE explicitly or implicitly using the sectional soot kinetics models, have also been advanced to the level that the soot volume fraction, particle size distribution, and mean primary particle size in laminar flames can be predicted reasonably well compared to experimental data. In this review, we discussed various physical and chemical processes that play an important role in the growth of mass and size of soot particle after inception. The subjects reviewed in this article include the properties of fractal-like soot agglomerates, the physics of particle agglomeration, coalescence, mechanisms and modeling of particle surface growth, the three commonly used state-of-the-art meso-scale (namely, the Event-driven Discrete Element Method, Monte Carlo Aggregation Code, and Detailed Stochastic Population Balance) approaches to model the details of individual soot particle morphology without and with the presence of surface growth, and the commonly used macro-scale sectional method and the methods of moments for modeling particle dynamics and the sectional soot kinetics models. The focus of this review was on how particle aggregation and surface growth were modeled in the meso-scale methods.

With adequately assumed particle morphological parameters, namely the fractal dimension and fractal prefactor, the macro-scale sectional method and the methods of moments provide reasonably accurate results of particle agglomeration, especially the sectional method, in comparison with the meso-scale approaches. Despite the inability to predict the particle morphology, the macro-scale PBE methods offer high computational efficiency, in particular the methods of moments, and can be used to model particle dynamics in a fully coupled manner with mass, momentum, energy, species, and soot related transport equations.

Meso-scale methods are a powerful tool for modeling the evolution of a particle system containing initially a relatively large number of isolated spherical primary particles under agglomeration without or with surface growth. Unlike the macro-scale methods that require assumed particle morphological parameters to estimate particle collision rate, meso-scale approaches track the positions of primary particles and hence are able to predict the morphology of individual soot particles. Owing to the complex shape of fractal-like soot aggregates, however, different models of soot particle mobility diameter have been implemented in the three meso-scale approaches reviewed in this paper. One of our main motivations for this review was to understand the quite different levels of primary particle polydispersity under similar flame conditions predicted by the event-driven discrete element method (EDEM) and the Monte-Carlo aggregation code (MCAC) in previous publications. To this end, all the models implemented in EDEM and MCAC have been comprehensively reviewed and their results were directly compared in three test cases: two pure agglomeration cases (no surface growth) of different initial primary particle sizes and one case with surface growth of different initial particle volume fractions. To better focus on the impact of different implementations of particle agglomeration kinetics and surface growth, soot oxidation was excluded from this exercise.

EDEM and MCAC predicted different soot particle agglomeration kinetics even for the pure agglomeration cases, especially for the case where the flow is in the near-transition regime. The difference can be mainly attributed to the different particle mobility models used. For the test with surface growth, EDEM and MCAC predicted a similar evolution of the soot volume fraction, particle morphology, and mean aggregate size. However, EDEM predicted significantly broader primary particle size distributions than MCAC. In cases of extensive surface growth (for example in a CB furnace), the aggregate size distribution obtained by EDEM is also broader than the MCAC one. The different behavior of EDEM and MCAC in the presence of surface growth is primarily caused by the different ways to implement surface growth. In MCAC, the evolution of primary particle polydispersity is entirely dependent on the initial primary particle polydispersity and surface growth does not qualitatively alter it. In contrast, EDEM always predicts polydisperse primary particles when there is surface growth, even when initially the primary particles are monodisperse. In this regard, it is expected that the detailed stochastic population balance (DSPB) method performs similarly to EDEM since they handle soot surface growth in a similar way.

Despite different implementations of fractal aggregate dynamics and surface growth, meso-scale simulations have advanced our quantitative understanding of soot particle dynamics and the evolution of soot particle size and morphology in laminar flames and also help develop accurate correlations required in macro-scale modeling.

However, meso-scale methods are computationally expensive and can currently only be used to predict detailed soot particle size distribution and morphology in a decoupled fashion. Although meso-scale approaches can predict more realistic morphologies of individual soot particles revealed from TEM images and even if enormous progress has been made since the first models of the aggregate formation, i.e., DLCA and BLCA, significant challenges remain to establish a benchmark solution to particle agglomeration in the presence of surface growth and to incorporate soot maturity characterized by carbonization and oxidation-induced fragmentation.

The impact of turbulence on soot dynamics, especially at meso-scales, should be explored further. There is limited understanding about the impact of turbulence on soot agglomeration during combustion. Limited research suggests that turbulence appears to have a fairly weak impact on soot formation during combustion, but this conclusion should be verified.

As a summary, the limitations and capabilities of the macro- and meso-scale methods reviewed are highlighted in Table 6.

Although significant progress has been made in both macro- and meso-scale modeling of soot formation, several challenges remain as outlined above, such as sintering, modeling surface growth at meso-scale, coupling of meso- and macro-scale modeling, and modeling the

**Table 6**
The limitations and capabilities of macro- and meso-scale methods in terms of prediction of key soot morphological properties.

| Class | Method | $D_f$ | $k_f$ | $D_p$ ($\sigma_{p,geo}$) | $N_p$ ($\sigma_{Np,geo}$) | $f_v$ | $C_{ov}$ ($\sigma_{Cov}$) |
|---|---|---|---|---|---|---|---|
| Macro-scale | MOM[a] | × | × | ✓(✓[c]) | ✓(✓[c]) | ✓ | ×(×) |
| | Sectional[a] | × | × | ✓(×) | ✓(✓) | ✓ | ×(×) |
| | SSKM | × | × | ×[b] (×[b]) | ✓(✓) | ✓ | ×(×) |
| Meso-scale | EDEM | ✓ | ✓ | ✓(✓) | ✓(✓) | ✓ | ✓(✓) |
| | MCAC | ✓ | ✓ | ✓(✓) | ✓(✓) | ✓ | ✓(✓) |
| | DSPB | ✓ | ✓ | ✓(✓) | ✓(✓) | ✓ | ✓(✓) |

[a] Quasi-bivariate versions. They can only predict a locally monodisperse PP diameter $D_p$.
[b] Monodisperse $D_p$ was generally assumed, though a recent development of SSKM removed this limitation at a cost of significant extra computing time. This recent SSKM of Nobili et al. [314] is capable of predicting $D_p$ distribution.
[c] The geometric standard deviations can only be estimated if a particle size distribution is assumed.

effects of turbulence. It is anticipated that multi-scale approaches will continue to play a vital role in resolving these remaining challenges, in the development of more capable and more accurate soot models, in the design of more efficient and cleaner combustion devices, and in the optimization of carbon black furnaces.

## CRediT authorship contribution statement

**Fengshan Liu:** Writing – review & editing, Writing – original draft, Conceptualization. **Jérôme Yon:** Writing – original draft, Formal analysis, Data curation. **José Morán:** Writing – review & editing, Writing – original draft, Formal analysis, Data curation. **Georgios A. Kelesidis:** Writing – review & editing, Writing – original draft, Formal analysis, Data curation. **Felipe Escudero:** Writing – review & editing, Writing – original draft, Formal analysis, Data curation. **Andrés Fuentes:** Conceptualization.

## Declaration of competing interest

The authors declare that they have no known competing financial interests or personal relationships that could have appeared to influence the work reported in this paper.

## Acknowledgments

José Morán and Jérôme Yon thank Alexandre Poux for his assistance in MCAC simulations. José Morán thanks the University of Minnesota for the provided computational resources for running MCAC simulations.

## Appendix A. Supplementary data

Supplementary material related to this article can be found online at https://doi.org/10.1016/j.pecs.2025.101234.

## Data availability

Data will be made available on request.

## References

[1] Key world energy statistics. International Energy Agency; 2020, https://www.iea.org/reports/key-world-energy-statistics-2020.
[2] Shiraiwa M, Selzle K, Pöschl U. Hazardous components and health effects of atmospheric aerosol particles: reactive oxygen species, polycyclic aromatic compounds and allergenic proteins. Free Radic Res 2012;46:927–39.
[3] Bond TC, Doherty SJ, Fahey DW, Forster PM, Berntsen T, DeAngelo BJ, Flanner MG, Ghan S, Kärcher B, Koch D, Kinne S, Kondo Y, Quinn PK, Sarofim MC, Schultz MG, Schulz M, Venkataraman C, Zhang H, Zhang S, Bellouin N, Guttikunda SK, Hopke PK, Jacobson MZ, Kaiser JW, Klimont Z, Lohmann U, Schwarz JP, Shindell D, Storelvmo T, Warren SG, Zender CS. Bounding the role of black carbon in the climate system: A scientific assessment. J Geophys Res: Atmos 2013;118:5380–552.
[4] Jacobson MZ. Strong radiative heating due to the mixing state of black carbon in atmospheric aerosols. Nature 2001;409:695–7.
[5] Carbon black users' guide. International Carbon Black Association; 2016, https://www.carbon-black.org/resources-from-icba.
[6] Watson AY, Valberg PA. Carbon black and soot: two different substances. AIHAJ- Am Ind Hyg Assoc 2001;62(2):218–28.
[7] Kelesidis GA, Benz S, Pratsinis SE. Process design for carbon black size and morphology. Carbon 2023;213:118255.
[8] Sánchez-Bastardo N, Schlögl R, Ruland H. Methane pyrolysis for zero-emission hydroen production: A potential bridge technology from fossil fuels to a renewable and sustainable hydrogen economy. Ind Eng Chem Res 2021;60:11855–81.
[9] Ahmed S, Aitani A, Rahman F, Al-Dwood A, Al-Muhaish F. Decomposition of hydrocarbons to hydrogen and carbon. Appl Catal A: Gen 2009;359:1–24.
[10] Donaldson K, Tran L, Jimenez LA, Duffin R, Newby DE, Mills N, MacNee W, Stone V. Combustion-derived nanoparticles: A review of their toxicology following inhalation exposure. Part Fibre Toxicol 2005;2:10.
[11] Park SH, Gong SL, Bouchet VS, Gong W, Makar PA, Moran MD, Stroud CA, Zhang J. Effects of black carbon aging on air quality predictions and direct radiative forcing estimation. Tellus B: Chem Phys Meteorol 2011;63:1026–39.
[12] López-Yglesias X, Schrader P, Michelsen H. Soot maturity and absorption cross sections. J Aerosol Sci 2014;75:43–64.
[13] Michelsen HA. Probing soot formation, chemical and physical evolution, and oxidation: A review of in situ diagnostic techniques and needs. Proc Combust Inst 2017;36(1):717–35.
[14] Yon J, Cruz J, Escudero F, Morán J, Liu F, Fuentes A. Revealing soot maturity based on multi-wavelength absorption/emission measurements in laminar axisymmetric coflow ethylene diffusion flames. Combust Flame 2021;227:147–61.
[15] Liu S, Mohammadi MM, Swihart MT. Fundamentals and recent applications of catalyst synthesis using flame aerosol technology. Chem Eng J 2021;405:126958.
[16] Baldelli A, Esmeryan KD, Popovicheva O. Turning a negative into a positive: Trends, guidelines and challenges of developing multifunctional non-wettable coatings based on industrial soot wastes. Fuel 2021;301:121068.
[17] Drakon A, Gurentsov E, Eremin A, Kolotushkin R, Khodyko E, Jander H. Special features of soot formation in a standard premixed ethylene/air flame diluted with DME. Combust Flame 2022;246:112309.
[18] Juarez-Facio AT, Castilla C, Corbière C, Lavanant H, Afonso C, Morin C, Merlet-Machour N, Chevalier L, Vaugeois J-M, Yon J, Monteil C. Development of a standardized in vitro approach to evaluate microphysical, chemical, and toxicological properties of combustion-derived fine and ultrafine particles. J Environ Sci 2022;113:104–17.
[19] Khalizov AF, Xue H, Wang L, Zheng J, Zhang R. Enhanced light absorption and scattering by carbon soot aerosol internally mixed with sulfuric acid. J Phys Chem A 2009;113(6):1066–74.
[20] He Q, Guo Q, Umeki K, Ding L, Wang F, Yu G. Soot formation during biomass gasification: A critical review. Renew Sustain Energy Rev 2021;139:110710.
[21] Haynes BS, Wagner HG. Soot formation. Prog Energy Combust Sci 1981;7:229–73.
[22] Bockhorn H. Soot formation in combustion. Springer-Verlag; 1994.
[23] Bockhorn H, D'Anna A, Sarofim AF, Wang H. Combustion generated fine carbonceous particles. KIT Scientific Publishing; 2009.
[24] D'Anna A. Combustion-formed nanoparticles. Proc Combust Inst 2009;32:593–613.
[25] Desgroux P, Mercier X, Thomson KA. Study of the formation of soot and its precursors in flames using optical diagnostics. Proc Combust Inst 2013;34(1):1713–38.
[26] Wang Y, Chung SH. Soot formation in laminar counterflow flames. Prog Energy Combust Sci 2019;74:152–238.

[27] Martin JW, Salamanca M, Kraft M. Soot inception: Carbonaceous nanoparticle formation in flames. Prog Energy Combust Sci 2022;88:100956.
[28] Thomson MJ. Modeling soot formation in flames and reactors: Recent progress and current challenges. Proc Combust Inst 2023;39:111–222.
[29] Wang H. Formation of nascent soot and other condensed-phase materials in flames. Proc Combust Inst 2011;33:41–67.
[30] Michelsen HA, Colket MB, Bengtsson P-E, D'Anna A, Desgroux P, Haynes BS, Miller JH, Nathan GJ, Pitsch H, Wang H. A review of terminology used to describe soot formation and evolution under combustion and pyrolytic conditions. ACS Nano 2020;14:12470–90.
[31] Mitchell P, Frenklach M. Monte Carlo simulation of soot aggregation with simultaneous surface growth – why primary particles appear spherical. Proc Combust Inst 1998;27:1507–14.
[32] Balthasar M, Frenklach M. Monte-Carlo simulation of soot particles coagulation and aggregation: the effect of a realistic size distribution. Proc Combust Inst 2005;30:1467–75.
[33] Kelesidis GA, Goudeli E, Pratsinis SE. Flame synthesis of functional nanostructured materials and devices: Surface growth and aggregation. Proc Combust Inst 2017;36:29–50.
[34] Morán J, Poux A, Yon J. Impact of the competition between aggregation and surface growth on the morphology of soot particles formed in an ethylene laminar premixed flame. J Aerosol Sci 2021;152:105690.
[35] Medalia AI, Heckman FA. Morphology of aggregates VII. Comparison chart method for electron microscopic determination of carbon black aggregate morphology. J Colloid Interface Sci 1971;36(2):173–90.
[36] Dobbins RA, Megaridis CM. Morphology of flame-generated soot as determined by thermophoretic sampling. Langmuir 1987;3(2):254–9.
[37] Megaridis CM, Dobbins RA. Morphological description of flame-generated materials. Combust Sci Technol 1990;71:95–109.
[38] Friedlander SK. Smoke, dust, and haze: fundamentals of aerosol dynamics. 2nd ed.. New York: Oxford University Press; 2000.
[39] Rigopoulos S. Population balance modelling of polydispersed particles in reactive flows. Prog Energy Combust Sci 2010;36:412–43.
[40] Solsvik J, Jakobsen HA. The foundation of the population balance equation: A review. J Dispers Sci Technol 2015;36:510–20.
[41] Sander M, West RH, Celnik MS, Kraft M. A detailed model for the sintering of polydispersed nanoparticle agglomerates. Aerosol Sci Technol 2009;43:978–89.
[42] Zhang Q, Guo H, Liu F, Smallwood GJ, Thomson MJ. Modeling of soot aggregate formation and size distribution in a laminar ethylene/air coflow diffusion flame with detailed PAH chemistry and an advanced sectional aerosol dynamics model. Proc Combust Inst 2009;32:761–8.
[43] Eaves NA, Zhang Q, Liu F, Guo H, Dworkin SB, Thomson MJ. CoFlame: a refined and validated numerical algorithm for modeling sooting laminar coflow diffusion flames. Comput Phys Comm 2016;207:464–77.
[44] Frenklach M. Method of moments with interpolative closure. Chem Eng Sci 2002;57:2229–39.
[45] Mueller ME, Blanquart G, Pitsch H. A joint volume-surface model of soot aggregation with the method of moments. Proc Combust Inst 2009;32(1):785–92.
[46] Xing JY, Groth CPT, Hu JCT. On the use of fractional-order quadrature-based moment closures for predicting soot formation in laminar flames. Combust Sci Technol 2022;194(1):22–44.
[47] Park SH, Rogak SN, Bushe WK, Wen JZ, Thomson MJ. An aerosol model to predict size and structure of soot particles. Combust Theory Model 2005;9:499–513.
[48] Rodrigues P, Franzelli B, Vicquelin R, Gicquel O, Darabiha N. Coupling an LES approach and a soot sectional model for the study of sooting turbulent non-premixed flames. Combust Flame 2018;190:477–99.
[49] Tian L, Schiener MA, Lindstedt RP. Fully coupled sectional modelling of soot particle dynamics in a turbulent diffusion flame. Proc Combust Inst 2021;38:1356–73.
[50] Salenbauch S, Hasse C, Vanni M, Marchisio DL. A numerically robust method of moments with number density function reconstruction and its application to soot formation, growth and oxidation. J Aerosol Sci 2019;128:34–49.
[51] Ferraro F, Gierth S, Salenbauch S, Han W, Hasse C. Soot particle size distribution reconstruction in a turbulent sooting flame with the split-based extended quadrature method of moments. Phys Fluids 2022;34(7).
[52] Wu S, Lao CT, Akroyd J, Mosbach S, Yang W, Kraft M. A joint moment projection method and maximum entropy approach for simulation of soot formation and oxidation in diesel engines. Appl Energy 2020;258:114083.
[53] Frenklach M. Dynamics of discrete distribution for Smoluchowski coagulation model. J Colloid Interface Sci 1985;108(1):237–42.
[54] Frenklach M, Harris SJ. Aerosol dynamics modeling using the method of moments. J Colloid Interface Sci 1987;118(1):252–61.
[55] Markatou P, Wang H, Frenklach M. A computational study of sooting limits in laminar premixed flames of ethane, ethylene, and acetylene. Combust Flame 1993;93(4):467–82.
[56] Mauss F, Schäfer T, Bockhorn H. Inception and growth of soot particles in dependence on the surrounding gas phase. Combust Flame 1994;99(3–4):697–705.
[57] Kazakov A, Wang H, Frenklach M. Detailed modeling of soot formation in laminar premixed ethylene flames at a pressure of 10 bar. Combust Flame 1995;100(1–2):111–20.
[58] Kazakov A, Frenklach M. Dynamic modeling of soot particle coagulation and aggregation: Implementation with the method of moments and application to high-pressure laminar premixed flames. Combust Flame 1998;114(3–4):484–501.
[59] Balthasar M, Frenklach M. Detailed kinetic modeling of soot aggregate formation in laminar premixed flames. Combust Flame 2005;140(1–2):130–45.
[60] McGraw R. Description of aerosol dynamics by the quadrature method of moments. Aerosol Sci Technol 1997;27(2):255–65.
[61] Marchisio DL, Vigil RD, Fox RO. Quadrature method of moments for aggregation–breakage processes. J Colloid Interface Sci 2003;258(2):322–34.
[62] Marchisio DL, Fox RO. Solution of population balance equations using the direct quadrature method of moments. J Aerosol Sci 2005;36(1):43–73.
[63] Mueller ME, Blanquart G, Pitsch H. Hybrid method of moments for modeling soot formation and growth. Combust Flame 2009;156:1143–55.
[64] Rigopoulos S. Modelling of soot aerosol dynamics in turbulent flow. Turbul Combust 2019;103:565–604.
[65] Colket MB, Hall RJ. Successes and uncertainties in modeling soot formation in laminar, premixed flames. In: Soot formation in combustion: mechanisms and models. Springer; 1994, p. 442–70.
[66] Smooke M, McEnally C, Pfefferle L, Hall R, Colket M. Computational and experimental study of soot formation in a coflow, laminar diffusion flame. Combust Flame 1999;117(1–2):117–39.
[67] Park S, Rogak S. A novel fixed-sectional model for the formation and growth of aerosol agglomerates. J Aerosol Sci 2004;35(11):1385–404.
[68] Wu JJ, Flagan RC. A discrete-sectional solution to the aerosol dynamic equation. J Colloid Interface Sci 1988;123(2):339–52.
[69] Richter H, Granata S, Green WH, Howard JB. Detailed modeling of PAH and soot formation in a laminar premixed benzene/oxygen/argon low-pressure flame. Proc Combust Inst 2005;30:1397–405.
[70] D'Anna A, Kent J. Modeling of particulate carbon and species formation in coflowing diffusion flames of ethylene. Combust Flame 2006;144:249–60.
[71] D'Anna A, Kent J. A model of particulate and species formation applied to laminar, nonpremixed flames for three aliphatic-hydrocarbon fuels. Combust Flame 2008;152(4):573–87.
[72] D'Anna A, Sirignano M, Kent J. A model of particle nucleation in premixed ethylene flames. Combust Flame 2010;157:2106–15.
[73] Sirignano M, Kent J, D'Anna A. Modeling formation and oxidation of soot in nonpremixed flames. Energy Fuels 2013;27:2303–15.
[74] Cuoci A, Frassoldati A, Faravelli T, Ranzi E. Soot formation in unsteady counterflow diffusion flames. Proc Combust Inst 2009;32(1):1335–42.
[75] Cuoci A, Frassoldati A, Faravelli T, Ranzi E. Kinetic modeling of soot formation in turbulent nonpremixed flames. Environ Eng Sci 2008;25(10):1407–22.
[76] Cuoci A, Frassoldati A, Faravelli T, Ranzi E. OpenSMOKE++: An object-oriented framework for the numerical modeling of reactive systems with detailed kinetic mechanisms. Comput Phys Comm 2015;192:237–64.
[77] Medalia AI, Heckman FA. Morphology of aggregates - II. Size and shape factors of carbon black aggregates from electron microscope. Carbon 1969;7:567–82.
[78] Morgan N, Kraft M, Balthasar M, Wong D, Frenklach M, Mitchell P. Numerical simulations of soot aggregation in premixed laminar flames. Proc Combust Inst 2007;31:693–700.
[79] Yon J, Bescond A, Liu F. On the radiative properties of soot aggregates part 1: Necking and overlapping. J Quant Spectrosc Radiat Transfer 2015;162:197–206.
[80] Teng S, Liu C, Schnaiter M, Chakrabarty RK, Liu F. Accounting for the effects of nonideal minor structures on the optical properties of black carbon aerosols. Atmos Chem Phys 2019;19:2917–31.
[81] Kelesidis GA, Kholghy MR, Zuercher J, Robertz J, Allemann M, Duric A, Pratsinis SE. Light scattering from nanoparticle agglomerates. Powder Technol 2020;365:52–9.
[82] Filippov A, Zurita M, Rosner D. Fractal-like aggregates: Relation between morphology and physical properties. J Colloid Interface Sci 2000;229(1):261–73.
[83] Johnsson J, Bladh H, Olofsson N-E, Bengtsson P-E. Influence of soot aggregate structure on particle sizing using laser-induced incandescence: importance of bridging between primary particles. Appl Phys B 2013;112:321–32.
[84] Zhang C, Thajudeen T, Larriba C, Schwartzentruber TE, Hogan Jr CJ. Determination of the scalar friction factor for nonspherical particles and aggregates across the entire Knudsen number range by direct simulation Monte Carlo (DSMC). Aerosol Sci Technol 2012;46(10):1065–78.
[85] Lin MY, Lindsay HM, Weitz DA, Ball RC, Klein R, Meakin P. Universality in colloid aggregation. Nature 1989;339(1):360–2.
[86] Fry D, Mohammad A, Chaktabarti A, Sorensen CM. Cluster shape anisotropy in irreversibly aggregating particulate systems. Langmuir 2004;20:7871–9.
[87] Thajudeen T, Deshmukh S, Hogan Jr CJ. Langevin simulation of aggregate formation in the transition regime. Aerosol Sci Technol 2015;49(2):115–25.
[88] Mao Q, van Duin ACT, Luo KH. Formation of incipient soot particles from polycyclic aromatic hydrocarbons: A ReaxFF molecular dynamics study. Carbon 2017;121:380–8.

[89] Skorupski K, Mroczka J, Wriedt T, Riefler N. A fast and accurate implementation of tunable algorithms used for generation of fractal-like aggregate models. Phys A 2014;404:106–17.

[90] Morán J, Fuentes A, Liu F, Yon J. FracVAL: An improved tunable algorithm of cluster–cluster aggregation for generation of fractal structures formed by polydisperse primary particles. Comput Phys Comm 2019;239:225–37.

[91] Oh C, Sorensen CM. The effect of overlap between monomers on the deterination of fractal cluster morphology. J Colloid Interface Sci 1997;193(1):17–25.

[92] Brasil AM, Farias TL, Carvalho MG. A recipe for image characterization of fractal-like aggregates. J Aerosol Sci 1999;30(10):1379–89.

[93] Goudeli E, Eggersdorfer ML, Pratsinis SE. Coagulation-agglomeration of fractal-like particles: structure and self-preserving size distribution. Langmuir 2015;31:1320–7.

[94] Kelesidis GA, Goudeli E, Pratsinis SE. Morphology and mobility diameter of carbonaceous aerosols during agglomeration and surface growth. Carbon 2017;121:527–35.

[95] Morán J, Yon J, Poux A. Monte Carlo aggregation code (MCAC) part 1: Fundamentals. J Colloid Interface Sci 2020;569:184–94.

[96] Morán J, Yon J, Poux A, Corbin F, Ouf F-X, Siméon A. Monte Carlo aggregation code (MCAC) part 2: Application to soot agglomeration, highlighting the importance of primary particles. J Colloid Interface Sci 2020;575:274–85.

[97] Lindberg CS, Manuputty MY, Yapp EK, Akroyd J, Xu R, Kraft M. A detailed particle model for polydisperse aggregate particles. J Comput Phys 2019;397:108799.

[98] Hou D, Lindberg CS, Wang M, Manuputty MY, You X, Kraft M. Simulation of primary particle size distribution in a premixed ethylene stagnation flame. Combust Flame 2020;216:126–35.

[99] Boje A, Kraft M. Stochastic population balance methods for detailed modelling of flame-made aerosol particles. J Aerosol Sci 2022;159:105895.

[100] Singh M, Ranade V, Shardt O, Matsoukas T. Challenges and opportunities concerning numerical solutions for population balances: a critical review. J Phys A 2022;55:383002.

[101] Endres S, Ciacchi L, Mädler L. A review of contact force models between nanoparticles in agglomerates, aggregates, and films. J Aerosol Sci 2021;153:105719.

[102] Li DD, Wang C, Chan QN, Yeoh GH. Soot: A review of computational models at different scales. Exp Comput Multiph Flow 2023;5(1):1–14.

[103] Mao Q, Feng M, Jiang XZ, Ren Y, Luo KH, van Duin AC. Classical and reactive molecular dynamics: Principles and applications in combustion and energy systems. Prog Energy Combust Sci 2023;97:101084.

[104] Buesser B, Pratsinis SE. Design of nanomaterial synthesis by aerosol processes. Annu Rev Chem Biomol Eng 2012;3:103–27.

[105] Eggersdorfer ML, Pratsinis SE. Agglomerates and aggregates of nanoparticles in the gas phase. Adv Powder Technol 2014;25:71–90.

[106] Wu S, Wu G, Wang P, Guo G. Investigation on the effect of water addition on benzene oxidation over palladium-oxide nanoparticle via ReaxFF molecular dynamics. Int J Hydrog Energy 2023;48(27):10288–98.

[107] Zhao B, Yang Z, Johnston MV, Wang H, Wexler AS, Balthasar M, Kraft M. Measurement and numerical simulation of soot particle size distribution functions in a laminar premixed ethylene-oxygen-argon flame. Combust Flame 2003;133(1–2):173–88.

[108] Bouaniche A, Yon J, Domingo P, Vervisch L. Analysis of the soot particle size distribution in a laminar premixed flame: A hybrid stochastic/fixed-sectional approach. Flow, Turbul Combust 2020;104:753–75.

[109] Kelesidis GA, Pratsinis SE. Determination of the volume fraction of soot accounting for its composition and morphology. Proc Combust Inst 2021;38:1189–96.

[110] Qiu Z, Wang X, Liu Z, Luo J. Quantitative assessment of cyclists' exposure to PM and BC on different bike lanes. Atmos Pollut Res 2022;13:101588.

[111] Lizonova D, Nagarkar A, Demokritou P, Kelesidis GA. Effective density of inhaled environmental and engineered nanoparticles and its impact on the lung deposition and dosimetry. Part Fibre Toxicol 2024;21:7.

[112] Draine BT, Flatau PJ. Discrete-dipole approximation for scattering calculations. J Opt Soc Amer A 1994;11(4):1491–9.

[113] Liu F, Yon J, Fuentes A, Lobo P, Smallwood GJ, Corbin JC. Review of recent literature on the light absorption properties of black carbon: Refractive index, mass absorption cross section, and absorption function. Aerosol Sci Technol 2020;54(1):33–51.

[114] Kelesidis GA, Neubauer D, Fan L-S, Lohmann U, Pratsinis SE. Enhanced light absorption and radiative forcing by black carbon agglomerates. Environ Sci Technol 2022;56:8610–8.

[115] Cohan L, Watson J. Shape factor and other fundamental properties of carbon black. Rubber Age 1951;63.

[116] Medalia A. Morphology of aggregates: I. Calculation of shape and bulkiness factors; application to computer-simulated random flocs. J Colloid Interface Sci 1967;24(3):393–404.

[117] Grishin I, Thomson K, Migliorini F, Sloan JJ. Application of the Hough transform for the automatic determination of soot aggregate morphology. Appl Opt 2012;51(5):610–20.

[118] Bescond A, Yon J, Ouf F, Ferry D, Delhaye D, Gaffié D, Coppalle A, Rozé C. Automated determination of aggregate primary particle size distribution by TEM image analysis: application to soot. Aerosol Sci Technol 2014;48(8):831–41.

[119] Sipkens TA, Frei M, Baldelli A, Kirchen P, Kruis FE, Rogak SN. Characterizing soot in TEM images using a convolutional neural network. Powder Technol 2021;387:313–24.

[120] Samson R, Mulholland GW, Gentry J. Structural analysis of soot agglomerates. Langmuir 1987;3(2):272–81.

[121] Köylü ÜÖ, Faeth GM. Structure of overfire soot in buoyant turbulent diffusion flames at long residence times. Combust Flame 1992;89(2):140–56.

[122] Köylü ÜÖ, Faeth GM, Farias TL, Carvalho MG. Fractal and projected structure properties of soot aggregates. Combust Flame 1995;100(4):621–33.

[123] Sorensen C. Light scattering by fractal aggregates: a review. Aerosol Sci Technol 2001;35(2):648–87.

[124] Adachi K, Chung SH, Buseck PR. Shapes of soot aerosol particles and implications for theie effects on climate. J Geophys Res 2010;115:D15206.

[125] Okyay G, Héripré E, Reiss T, Haghi-Ashtiani P, Auger T, Enguehard F. Soot aggregate complex morphology: 3D geometry reconstruction by SEM tomography applied on soot issued from propane combustion. J Aerosol Sci 2016;93:63–79.

[126] Haffner-Staton E, La Rocca A, Fay MW. Progress towards a methodology for high throughput 3D reconstruction of soot nanoparticles via electron tomography. J Microsc 2018;270:272–89.

[127] Lagana S, La Rocca A, Cairns A, Fay MW, Apicella B, Ciajolo A, Russo C. 2D and 3D TEM characterisation of benzene and ethylene soot. Fuels 2023;4:147–85.

[128] Jullien R, Botet R. Aggregation and fractal aggregates. Singapore: World Scientific; 1987.

[129] Yon J, Morán J, Ouf F-X, Mazur M, Mitchell J. From monomers to agglomerates: A generalized model for characterizing the morphology of fractal-like clusters. J Aerosol Sci 2021;151:105628.

[130] Heinson W, Sorensen C, Chakrabarti A. Does shape anisotropy control the fractal dimension in diffusion-limited cluster-cluster aggregation? Aerosol Sci Technol 2010;44(12):1–4.

[131] Heinson W, Sorensen C, Chakrabarti A. A three parameter description of the structure of diffusion limited cluster fractal aggregates. J Colloid Interface Sci 2012;375(1):65–9.

[132] Wozniak M, Onofri F, Barbosa S, Yon J, Mroczka J. Comparison of methods to derive morphological parameters of multi-fractal samples of particle aggregates from TEM images. J Aerosol Sci 2012;47:12–26. http://dx.doi.org/10.1016/j.jaerosci.2011.12.008, URL: https://www.sciencedirect.com/science/article/pii/S0021850211001984.

[133] Adachi K, Chung SH, Friedrich H, Buseck PR. Fractal parameters of individual soot particles determined using electron tomography: Implications for optical properties. J Geophys Res: Atmos. 2007;112(D14).

[134] Lattuada M, Wu H, Morbidelli M. A simple model for the structure of fractal aggregates. J Colloid Interface Sci 2003;268(1):106–20.

[135] Debye P, Anderson Jr H, Brumberger H. Scattering by an inhomogeneous solid. II. The correlation function and its application. J Appl Phys 1957;28(6):679–83.

[136] Naumann K-H. Van der waals interactions between fractal particles. J Aerosol Sci 1993;24:S181–2.

[137] Morán J, Yon J, Henry C, Kholghy MR. Approximating the van der Waals interaction potentials between agglomerates of nanoparticles. Adv Powder Technol 2023;34(12):104269.

[138] Naumann K-H, Bunz H. Aerodynamic properties of fractal aerosol particles. J Aerosol Sci 1991;22:S161–4.

[139] Naumann K-H. COSIMA—a computer program simulating the dynamics of fractal aerosols. J Aerosol Sci 2003;34(10):1371–97.

[140] Sorensen C. The mobility of fractal aggregates: a review. Aerosol Sci Technol 2011;45(7):765–79.

[141] Baron P, Sorensen C, Brockmann J. Nonspherical particle measurements: shape factors, fractals, and fibers. Aerosol Meas 2001;703–50.

[142] Park K, Kittelson DB, McMurry PH. Structural properties of diesel exhaust particles measured by transmission electron microscopy (TEM): Relationships to particle mass and mobility. Aerosol Sci Technol 2004;38(9):881–9.

[143] Maricq M, Xu N. The effective density and fractal dimension of soot particles from premixed flames and motor vehicle exhaust. J Aerosol Sci 2004;35(10):1251–74.

[144] Rogak SN, Flagan RC, Nguyen HV. The mobility and structure of aerosol agglomerates. Aerosol Sci Technol 1993;18(1):25–47.

[145] Meakin P. Fractal aggregates. Adv Colloid Interface Sci 1987;28:249–331.

[146] Jung H, Kittelson DB, Zachariah MR. Kinetics and visualization of soot oxidation using transmission electron microscopy. Combust Flame 2004;136(4):445–56.

[147] Eggersdorfer ML, Grohn AJ, Sorensen CM, McMurry PH, Pratsinis SE. Mass-mobility characterization of flame-made ZrO2 aerosols: Primary particle diameter and extent of aggregation. J Colloid Interface Sci 2012;387:12–23.

[148] Trivanovic U, Kelesidis GA, Pratsinis SE. High-throughput generation of aircraft-like soot. Aerosol Sci Technol 2022;56:732–43.

[149] Kelesidis GA, Pratsinis SE. A perspective on gas-phase synthesis of nanomaterials: Process design, impact and outlook. Chem Eng J 2021;421:129884.

[150] Kelesidis GA, Furrer FM, Wegner K, Pratsinis SE. Impact of humidity on silica nanoparticle agglomerate morphology and size distribution. Langmuir 2018;34:8532–41.

[151] Svensson CR, Ludvigsson L, Meuller BO, Eggersdorfer ML, Deppert K, Bohgard M, Pagels JH, Messing ME, Rissler J. Characteristics of airborne gold aggregates generated by spark discharge and high temperature evaporation furnace: Mass-mobility relationship and surface area. J Aerosol Sci 2015;87:38–52.

[152] Kim SC, Wang J, Emery MS, Shin WG, Mulholland GW, Pui DYH. Structural property effect of nanoparticle agglomerates on particle penetration through fibrous filter. Aerosol Sci Technol 2009;43:344–55.

[153] Yon J, Bescond A, Ouf F-X. A simple semi-empirical model for effective density measurements of fractal aggregates. J Aerosol Sci 2015;87:28–37.

[154] Abid AD, Camacho J, Sheen DA, Wang H. Quantitative measurement of soot particle size distribution in premixed flames–the burner-stabilized stagnation flame approach. Combust Flame 2009;156(10):1862–70.

[155] Camacho J, Liu CR, Gu C, Lin H, Huang Z, Tang QX, You XQ, Saggese C, Li Y, Jung HJ, Deng L, Wlokas I, Wang H. Mobility size and mass of nascent soot particles in a benchmark premixed ethylene flame. Combust Flame 2015;162:3810–22.

[156] Abid AD, Heinz N, Tolmachoff ED, Phares DJ, Campbell CS, Wang H. On evolution of particle size distribution functions of incipient soot in premixed ethylene–oxygen–argon flames. Combust Flame 2008;154(4):775–88.

[157] Schenk M, Lieb S, Vieker H, Beyer A, Gölzhäuser A, Wang H, Kohse-Höinghaus K. Morphology of nascent soot in ethylene flames. Proc Combust Inst 2015;35(2):1879–86.

[158] Mitchell P, Frenklach M. Particle aggregation with simultaneous surface growth. Phys Rev E 2003;67:061407.

[159] Wang G, Sorensen C. Aggregation kernel homogeneity for fractal aggregate aerosols in the slip regime. Aerosol Sci Technol 2001;34(3):297–306.

[160] Vemury S, Pratsinis SE. Self-preserving size distributions of agglomerates. J Aerosol Sci 1995;26(2):175–85.

[161] Dekkers PJ, Friedlander SK. The self-preserving size distribution theory: I. Effects of the Knudsen number on aerosol agglomerate growth. J Colloid Interface Sci 2002;248(2):295–305.

[162] Pierce F, Sorensen C, Chakrabarti A. Computer simulation of diffusion-limited cluster-cluster aggregation with an Epstein drag force. Phys Rev E 2006;74(2):021411.

[163] Morán J, Poux A, Cepeda F, Escudero F, Fuentes A, Gallen L, Riber E, Cuenot B, Yon J. Multi-scale soot formation simulation providing detailed particle morphology in a laminar coflow diffusion flame. Combust Flame 2023;256:112987.

[164] Harris SJ, Maricq MM. Signature size distributions for diesel and gasoline engine exhaust particulate matter. J Aerosol Sci 2001;32(6):749–64.

[165] Sorensen CM, Roberts GC. The prefactor of fractal aggregates. J Colloid Interface Sci 1997;186(2):447–52.

[166] Ehrl L, Soos M, Lattuada M. Generation and geometrical analysis of dense clusters with variable fractal dimension. J Phys Chem B 2009;113(31):10587–99.

[167] Mountain RD, Mulholland G. Light scattering from simulated smoke agglomerates. Langmuir 1988;4(6):1321–6.

[168] Mountain RD, Mulholland GW, Baum H. Simulation of aerosol agglomeration in the free molecular and continuum flow regimes. J Colloid Interface Sci 1986;114(1):67–81.

[169] Wu MK, Friedlander SK. Note on the power law equation for fractal-like aerosol agglomerates. J Colloid Interface Sci 1993;159(1):246–8.

[170] Brasil A, Farias TL, Carvalho MdG, Köylü ÜÖ. Numerical characterization of the morphology of aggregated particles. J Aerosol Sci 2001;32(4):489–508.

[171] Brasil A, Farias T, Carvalho M. Evaluation of the fractal properties of cluster-cluster aggregates. Aerosol Sci Technol 2000;33(5):440–54.

[172] Neoh K, Howard J, Sarofim A. Effect of oxidation on the physical structure of soot. Symp (Int) Combust 1985;20(1):951–7.

[173] Kennedy IM. Models of soot formation and oxidation. Prog Energy Combust Sci 1997;23:95–132.

[174] Guo H, Anderson PM, Sunderland PB. Optimized rate expressions for soot oxidation by OH and $O_2$. Fuel 2016;172. 284–252.

[175] Sediako AD, Soong C, Howe JY, Kholghy MR, Thomson MJ. Real-time observation of soot aggregate oxidation in an environmental transmission electron microscope. Proc Combust Inst 2017;36(1):841–51.

[176] Frenklach M, Liu Z, Singh RI, Galimova GR, Azyazov VN, Mebel AI. Detailed, sterically-resolved modeling of soot oxidation: Role of O atoms, interplay with particle nanostructure, and emergence of inner particle burning. Combust Flame 2018;188:284–306.

[177] Frenklach M. New form for reduced modeling of soot oxidation: Accounting for multi-site kinetics and surface reactivity. Combust Flame 2019;201:148–59.

[178] Toth P, Jacobsson D, Ek M, Wiinikka H. Real-time, in situ, atomic scale observation of soot oxidation. Carbon 2019;145:149–60.

[179] Khosousi A, Dworkin SB. Detailed modelling of soot oxidation by $O_2$ and OH in laminar diffusion flames. Proc Combust Inst 2016;35:1903–10.

[180] Gao M, Jang Y, Ding L, Gao Y, Dai S, Dai Z, Yu G, Yang W, Wang F. Mechanism of the noncatalytic oxidation of soot using in situ transmission electron microscopy. Nat Commun 2023;14(1):6256.

[181] Zhang Q, Thomson MJ, Guo H, Liu F, Smallwood GJ. Modeling of oxidation-driven soot aggregate fragmentation in a laminar coflow diffusion flame. Combust Sci Technol 2010;182:491–504.

[182] Mueller M, Blanquart G, Pitsch H. Modeling the oxidation-induced fragmentation of soot aggregates in laminar flames. Proc Combust Inst 2011;33:667–74.

[183] Ghiassi H, Toth P, Jaramillo IC, Lighty JS. Soot oxidation-induced fragmentation: Part 1: The relationship between soot nanostructure and oxidation-induced fragmentation. Combust Flame 2016;163:179–87.

[184] Sirignano M, Ghiassi H, D'Anna A, Lighty JS. Temperature and oxygen effects on oxidation-induced fragmentation of soot particles. Combust Flame 2016;171:15–26.

[185] Kelesidis GA, Pratsinis SE. Estimating the internal and surface oxidation of soot agglomerates. Combust Flame 2019;209:493–9.

[186] Kelesidis GA, Crepaldi P, Pratsinis SE. Oxidation dynamics of soot or carbon black accounting for its core-shell structure and pore network. Carbon 2024;219:118764.

[187] Liu Y, Zhang X, Lyu G, Qiao Y, Zhang W, Song C. Effect of the oxidation-induced fragmentation of primary particles on soot oxidation reactivity. Combust Flame 2022;240:112026.

[188] Qian W, Hui X, Wang B, Kronenburg A, Sung C-J, Lin Y. An investigation into oxidation-induced fragmentation of soot aggregates by Langevin dynamics simulations. Fuel 2023;334:126547.

[189] Kholghy MR, Veshkini AV, Thomson MJ. The core-shell internal nanostructure of soot – a criterion to model soot maturity. Carbon 2016;100:508–36.

[190] Johansson KO, Gabaly FE, Schrader P, Campbell M, Michelsen HA. Evolution of maturity levels of the particle surface and bulk during soot growth and oxidation in a flame. Aerosol Sci Technol 2017;51:1333–44.

[191] Sharma A, Mukut K, Roy S, Goudeli E. The coalescence of incipient soot clusters. Carbon 2021;180:215–25.

[192] Veshkini A, Dworkin SB, Thomson MJ. Understanding soot particle size evolution in laminar ethylene/air diffusion flames using novel soot coalescence models. Combust Theory Model 2016;20(4):707–34.

[193] Hou D, Chu Q, Chen D, Pascazio L, Kraft M, You X. Atomic insights into the sintering process of polycyclic aromatic hydrocarbon clusters. Proc Combust Inst 2021;38:1181–8.

[194] Botero M, Eaves N, Dreyer J, Sheng Y, Akroyd J, Yang W, Kraft M. Experimental and numerical study of the evolution of soot primary particles in a diffusion flame. Proc Combust Inst 2019;37:2047–55.

[195] Smooke M, Long M, Connelly B, Colket M, Hall R. Soot formation in laminar diffusion flames. Combust Flame 2005;143:613–28.

[196] Sun B, Rigopoulos S, Liu A. Modelling of soot coalescence and aggregation with a two-population balance equation model and a conservative finite volume method. Combust Flame 2021;229:111382.

[197] Chen D, Zainuddin Z, Yapp E, Akroyd J, Mosbach S, Kraft M. A fully coupled simulation of PAH and soot growth with a population balance model. Proc Combust Inst 2013;34:1827–35.

[198] Sander M, West RH, Celnik MS, Kraft M. Developing the PAH-PP soot particle model using process informatics and uncertainty propagation. Proc Combust Inst 2011;43:675–83.

[199] Wang M, Tang Q, Mei J, You X. On the effective density of soot particles in premixed ethylene flames. Combust Flame 2018;198:428–35.

[200] Chen D, Totton TS, Akroyd JW, Mosbach S, Kraft M. Size-dependent melting of polycyclic aromatic hydrocarbon nano-clusters: A molecular dynamics study. Carbon 2014;67:79–91.

[201] Seinfeld JH, Pandis SN. Atmospheric chemistry and physics. John Wiley & Sons; 2006.

[202] Huo Z, Cleary MJ, Sirignano M, Masri AR. A sectional soot formation kinetics scheme with a new model for coagulation efficiency. Combust Flame 2021;230:111444.

[203] Singh J, Patterson RIA, Kraft M, Wang H. Numerical simulation and sensitivity analysis of detailed soot particle size distribution in laminar premixed ethylene flames. Combust Flame 2006;145:117–27.

[204] Sirignano M, D'Anna A. Coagulation of combustion generated nanoparticles in low and intermediate temperature regimes: An experimental study. Proc Combust Inst 2013;34(1):1877–84.

[205] Hou D, Lindberg CS, Manuputty MY, You X, Kraft M. Modelling soot formation in a benchmark ethylene stagnation flame with a new detailed population balance model. Combust Flame 2019;203:56–71.

[206] Morán J, Henry C, Poux A, Yon J. Impact of the maturation process on soot particle aggregation kinetics and morphology. Carbon 2021;182:837–46.

[207] D'Alessio A, Barone A, Cau R, D'Anna A, Minutolo P. Surface deposition and coagulation efficiency of combustion generated nanoparticles in the size range from 1 to 10 nm. Proc Combust Inst 2005;30:2595–603.

[208] Lindstedt RP, Waldheim B. Modeling of soot particle size distributions in premixed stagnation flow flames. Proc Combust Inst 2013;34:1861–8.

[209] Hou D, Zong D, Lindberg CS, Kraft M, You X. On the coagulation efficiency of carbonaceous nanoparticles. J Aerosol Sci 2020;140:105478.

[210] Narsimhan G, Ruckenstein E. The Brownian coagulation of aerosols over the entire range of Knudsen numbers: Connection between the sticking probability and the interaction forces. J Colloid Interface Sci 1985;104(2):344–69.

[211] Saggese C, Ferrario S, Camacho J, Cuoci A, Frassoldati A, Ranzi E, Wang H, Faravelli T. Kinetic modeling of particle size distribution of soot in a premixed burner-stabilized stagnation ethylene flame. Combust Flame 2015;162(9):3356–69.
[212] Sgro L, De Filippo A, Lanzuolo G, D'Alessio A. Characterization of nanoparticles of organic carbon (NOC) produced in rich premixed flames by differential mobility analysis. Proc Combust Inst 2007;31(1):631–8.
[213] Sgro L, Barone A, Commodo M, D'Alessio A, De Filippo A, Lanzuolo G, Minutolo P. Measurement of nanoparticles of organic carbon in non-sooting flame conditions. Proc Combust Inst 2009;32(1):689–96.
[214] Hou D, Pascazio L, Martin J, Zhou Y, Kraft M, You X. On the reactive coagulation of incipient soot nanoparticles. J Aerosol Sci 2022;159:105866.
[215] Fuchs N. The mechanics of aerosols. Oxford: Pergamon Press; 1964.
[216] Sahni D. An exact solution of fokker-planck equation and brownian coagulation in the transition regime. J Colloid Interface Sci 1983;91(2):418–29.
[217] Gmachowski L. The aerosol particle collision kernel considering the fractal model of particle motion. J Aerosol Sci 2013;59:47–56.
[218] Morán J. On the link between the Langevin equation and the coagulation kernels of suspended nanoparticles. Fractal Fract 2022;6(9):529.
[219] Gopalakrishnan R, Thajudeen T, Hogan CJ. Collision limited reaction rates for arbitrarily shaped particles across the entire diffusive Knudsen number range. J Chem Phys 2011;135(5).
[220] Polovnikov P, Azarov I, Veshchunov M. Advancement of the kinetic approach to Brownian coagulation on the base of the Langevin theory. J Aerosol Sci 2016;96:14–23.
[221] Zurita-Gotor M, Rosner D. Effective diameters for collisions of fractal-like aggregates: Recommendations for improved aerosol coagulation frequency predictions. J Colloid Interface Sci 2002;255(1):10–26.
[222] Corson J, Mulholland GW, Zachariah MR. Friction factor for aerosol fractal aggregates over the entire Knudsen range. Phys Rev E 2017;95(1):013103.
[223] Thajudeen T, Gopalakrishnan R, Hogan Jr CJ. The collision rate of nonspherical particles and aggregates for all diffusive Knudsen numbers. Aerosol Sci Technol 2012;46(11):1174–86.
[224] Karsch M, Kronenburg A, Stein OT. Coagulation rate coefficients for fractal-like agglomerates in the diffusive and ballistic limits. Chem Eng Res Des 2022;187:611–22.
[225] Heine MC, Pratsinis SE. Brownian coagulation at high concentration. Langmuir 2007;23:9882–90.
[226] Morán J, Kholghy MR. Theoretical derivation of particle collision kernels and its enhancement at a high concentration from a first-time-passage approach in the diffusive regime. Aerosol Sci Technol 2023;57(8):782–96.
[227] Trzeciak TM, Podgórski A, Marijnissen JC. Brownian coagulation in dense systems: Thermal non-equilibrium effects. J Aerosol Sci 2014;69:1–12.
[228] Suresh V, Liu Z, Perry Z, Gopalakrishnan R. Modeling particle-particle binary coagulation rate constants for spherical aerosol particles at high volume fractions using langevin dynamics simulations. J Aerosol Sci 2022;164:106001.
[229] Ouyang H, Gopalakrishnan R, Hogan CJ. Nanoparticle collisions in the gas phase in the presence of singular contact potentials. J Chem Phys 2012;137(6).
[230] Gopalakrishnan R, Hogan Jr CJ. Coulomb-influenced collisions in aerosols and dusty plasmas. Phys Rev E— Stat Nonlinear Soft Matter Phys 2012;85(2):026410.
[231] Qian W, Kronenburg A, Hui X, Lin Y, Karsch M. Effects of agglomerate characteristics on their collision kernels in the free molecular regime. J Aerosol Sci 2022;159:105868.
[232] Dahneke B. Simple kinetic theory of Brownian diffusion in vapors and aerosols. In: Theory of dispersed multiphase flow. Elsevier; 1983, p. 97–133.
[233] Pratsinis SE. Simultaneous nucleation, condensation, and coagulation in aerosol reactors. J Colloid Interface Sci 1988;124(2):416–27.
[234] Gopalakrishnan R, Hogan Jr CJ. Determination of the transition regime collision kernel from mean first passage times. Aerosol Sci Technol 2011;45(12):1499–509.
[235] Karsch M, Kronenburg A. Modelling nanoparticle agglomeration in the transition regime: A comparison between detailed Langevin dynamics and population balance calculations. J Aerosol Sci 2023;106228.
[236] Corson J, Mulholland GW, Zachariah MR. Analytical expression for the rotational friction coefficient of DLCA aggregates over the entire Knudsen regime. Aerosol Sci Technol 2018;52(2):209–21.
[237] Jungblut S, Joswig J-O, Eychmüller A. Diffusion-limited cluster aggregation: Impact of rotational diffusion. J Phys Chem C 2018;123(1):950–4.
[238] Frenklach M, Wang H. Detailed modeling of soot particle nucleation and growth. Proc Combust Inst 1990;23(1):1559–66.
[239] Appel J, Bockhorn H, Frenklach M. Kinetic modeling of soot formation with detailed chemistry and physics: laminar premixed flames of $C_2$ hydrocarbons. Combust Flame 2000;121:122–36.
[240] Frenklach M. Reaction mechanism of soot formation in flames. Phys Chem Chem Phys 2002;4:2028–37.
[241] Liu F, Consalvi J-L, Nmira F. The importance of accurately modelling soot and radiation coupling in laminar and laboratory-scale turbulent diffusion flames. Combust Flame 2022;112573.
[242] Veshkini A, Dworkin SB, Thomson MJ. A soot particle surface reactivity model applied to a wide range of laminar ethylene/air flames. Combust Flame 2014;161(12):3191–200.
[243] Kholghy MR, Kelesidis GA. Surface growth, coagulation and oxidation of soot by a monodisperse population balance model. Combust Flame 2021;227:456–63.
[244] Chen D, Akroyd J, Mosbach S, Kraft M. Surface reactivity of polycyclic aromatic hydrocarbon clusters. Proc Combust Inst 2015;35:1811–8.
[245] Wang Y, Raj A, Chung SH. Soot modeling of counterflow diffusion flames of ethylene-based binary mixture fuels. Combust Flame 2015;162:586–96.
[246] Hoerlle CA, Pereira FM. Effect of $CO_2$ addition on soot formation of ethylene non-premixed flames under oxygen enriched atmospheres. Combust Flame 2019;203:407–23.
[247] Celnik M, Raj A, West R, Patterson R, Kraft M. Aromatic site description of soot particles. Combust Flame 2008;155:161–80.
[248] Di Domenico M, Gerlinger P, Aigner M. Development and validation of a new soot formation model for gas turbine combustor simulations. Combust Flame 2010;157:246–58.
[249] Lindberg CS, Manuputty MY, Akroyd J, Kraft M. A two-step simulation methodology for modelling stagnation flame synthesised aggregate nanoparticles. Combust Flame 2019;202:143–53.
[250] Harris SJ, Kennedy IM. The coagulation of soot particles with van der Waals forces. Combust Sci Technol 1988;59(4–6):443–54.
[251] Frenklach M, Wang H. Detailed mechanism and modeling of soot particle formation. In: Bockhorn H, editor. Soot formation in combustiom - mechanisms and models. Berlin: Springer-Verlag; 1994, p. 165–90, chapter 10.
[252] Menz WJ, Kraft M. A new model for silicon nanoparticle synthesis. Combust Flame 2013;160:947–58.
[253] Zhou Y, Chu Q, Hou D, Chen D, You X. Molecular dynamics study on the condensation of PAH molecules on quasi soot surfaces. J Phys Chem A 2022;126:630–9.
[254] Dworkin SB, Zhang Q, Thomson MJ, Slavinskaya NA, Riedel U. Application of an enhanced PAH growth model to soot formation in a laminar coflow ethylene/air diffusion flame. Combust Flame 2011;158(9):1682–95.
[255] Demarco R, Jerez A, Liu F, Chen L, Fuentes A. Modeling soot formation in laminar coflow ethylene inverse diffusion flames. Combust Flame 2021;232:111513.
[256] Guo H, Gu Z, Thomson K, Smallwood G. Soot formation in a laminar ethylene/air diffusion flame at pressures from 1 to 8 atm. Proc Combust Inst 2013;34:1795–802.
[257] Pejpichestakul W, Ranzi E, Pelucchi M, Frassoldati A, Cuoci A, Parente A, Faravelli T. Examination of a soot model in premixed laminar flames at fuel-rich conditions. Proc Combust Inst 2019;37:1013–21.
[258] Aubagnac-Karkar D, Bakali AE, Desgroux P. Soot particles inception and PAH condensation modelling applied in a soot model utilizing a sectional method. Combust Flame 2018;189:190–206.
[259] Saffaripour M, Kholghy M, Dworkin SB, Thomson MJ. A numerical and experimental study of soot formation in a laminar coflow diffusion flame of a jet A-1 surrogate. Proc Combust Inst 2013;34:1057–65.
[260] Zhang T, Thomson MJ. A numerical study of the effects of n-propylbenzene addition to n-dodecane on soot formation in a laminar coflow diffusion flame. Combust Flame 2018;190:416–31.
[261] Guo J, Liu P, Quadarella E, Yalamanchi K, Alsheikh I, Chu C, Liu F, Sarathy SM, Roberts WL. Assessment of physical soot inception model in normal and inverse laminar diffusion flames. Combust Flame 2022;246:112420.
[262] Zhang HB, Hou D, Law CK, You X. The role of carbon-addition and hydrogen-migration reactions in soot surface growth. J Phys Chem A 2016;120(5):683–9.
[263] Frenklach M, Singh RI, Mebel AM. On the low-temperature limit of HACA. Proc Combust Inst 2019;37:969–76.
[264] Johansson KO, Head-Gordon MP, Schrader PE, Wilson KR, Michelsen HA. Resonance-stabilized hydrocarbon-radical reactions may explain soot inception and growth. Science 2018;361:997–1000.
[265] Mao Q, Cai L, Langer R, Pitsch H. The role of resonance-stabilized radical chain reactions in polycyclic hydrocarbon growth: Theoretical calculations and kinetic modeling. Proc Combust Inst 2021;38:1459–66.
[266] Eaves NA, Dworkin SB, Thomson MJ. The importance of reversibility in modeling soot nucleation and condensation processes. Proc Combust Inst 2015;35:1787–94.
[267] Veshkini A, Eaves NA, Dworkin SB, Thomson MJ. Application of PAH-condensation reversibility in modeling soot growth in laminar premixed and nonpremixed flames. Combust Flame 2016;167:335–52.
[268] Pope C, Howard J. Simultaneous particle and molecule modeling (SPAMM): An approach for combining sectional aerosol equations and elementary gas-phase reactions. Aerosol Sci Technol 1997;27:73–94.
[269] Pejpichestakul W, Frassoldati A, Parente A, Faravelli T. Kinetic modeling of soot formation in premixed burner-stabilized stagation ethylene flames at heavily sooting condition. Fuel 2018;234:199–206.
[270] Sirignano M, Kent J, D'Anna A. Detailed modeling of size distribution functions and hydrogen content in combustion-formed particles. Combust Flame 2010;157:1211–9.

[271] Blacha T, Di Domenico M, Gerlinger P, Aigner M. Soot predictions in premixed and non-premixed laminar flames using a sectional approach for PAHs and soot. Combust Flame 2012;159:181–93.

[272] Eberle C, Gerlinger P, Aigner M. A sectional PAH model with reversible PAH chemistry for CFD soot simulations. Combust Flame 2017;179:63–73.

[273] Eigentler F, Gerlinger P. A detailed PAH and soot model for complex fuels in CFD applications. Flow Turbul Combust 2022;109:225–51.

[274] Leung KM, Lindstedt RP, Jones WP. A simplified reaction mechanism for soot formation in nonpremixed flames. Combust Flame 1991;87(3–4):289–305.

[275] Jeong JI, Choi M. A sectional method for the analysis of growth of polydisperse non-spherical particles undergoing coagulation and coalescence. J Aerosol Sci 2001;32(5):565–82.

[276] Tsantilis S, Kammler H, Pratsinis S. Population balance modeling of flame synthesis of titania nanoparticles. Chem Eng Sci 2002;57(12):2139–56.

[277] Park S, Rogak S. A one-dimensional model for coagulation, sintering, and surface growth of aerosol agglomerates. Aerosol Sci Technol 2003;37(12):947–60.

[278] Balthasar M, Kraft M. A stochastic approach to calculate the particle size distribution function of soot particles in laminar premixed flames. Combust Flame 2003;133(3):289–98.

[279] Celnik M, Patterson R, Kraft M, Wagner W. Coupling a stochastic soot population balance to gas-phase chemistry using operator splitting. Combust Flame 2007;148(3):158–76.

[280] Patterson RI, Singh J, Balthasar M, Kraft M, Norris JR. The linear process deferment algorithm: A new technique for solving population balance equations. SIAM J Sci Comput 2006;28(1):303–20.

[281] Lee K, Matsoukas T. Simultaneous coagulation and break-up using constant-N Monte Carlo. Powder Technol 2000;110(1–2):82–9.

[282] Gelbard F. Modeling multicomponent aerosol particle growth by vapor condensation. Aerosol Sci Technol 1990;12:399–412.

[283] Wu C-Y, Biswas P. Study of numerical diffusion in a discrete-sectional model and its application to aerosol dynamics simulation. Aerosol Sci Technol 1998;29:359–78.

[284] Gelbard F, Seinfeld JH. Simulation of multicomponent aerosol dynamics. J Colloid Interface Sci 1980;78(2):485–501.

[285] Xiong Y, Pratsinis SE. Formation of agglomerate particles by coagulation and sintering—Part I. A two-dimensional solution of the population balance equation. J Aerosol Sci 1993;24(3):283–300.

[286] Nakaso K, Fujimoto T, Seto T, Shimada M, Okuyama K, Lunden MM. Size distribution change of titania nano-particle agglomerates generated by gas phase reaction, agglomeration, and sintering. Aerosol Sci Technol 2001;35(5):929–47.

[287] Hounslow M, Ryall R, Marshall V. A discretized population balance for nucleation, growth, and aggregation. AIChE J 1988;34(11):1821–32.

[288] Kumar S, Ramkrishna D. On the solution of population balance equations by discretization—I. A fixed pivot technique. Chem Eng Sci 1996;51(8):1311–32.

[289] Saffaripour M, Veshkini A, Kholghy M, Thomson MJ. Experimental investigation and detailed modeling of soot aggregate formation and size distribution in laminar coflow diffusion flames of jet A-1, a synthetic kerosene, and n-decane. Combust Flame 2014;161(3):848–63.

[290] Saffaripour M, Chan TW, Liu F, Thomson KA, Smallwood GJ, Kubsh J, Brezny R. Effect of drive cycle and gasoline particulate filter on the size and morphology of soot particles emitted from a gasoline-direct-injection vehicle. Environ Sci Technol 2015;49(19):11950–8.

[291] Sun B, Rigopoulos S. Modelling of soot formation and aggregation in turbulent flows with the LES-PBE-PDF approach and a conservative sectional method. Combust Flame 2022;242:112152.

[292] Qamar S, Elsner MP, Angelov IA, Warnecke G, Seidel-Morgenstern A. A comparative study of high resolution schemes for solving population balances in crystallization. Comput Chem Eng 2006;30(6–7):1119–31.

[293] Bouaniche A, Vervisch L, Domingo P. A hybrid stochastic/fixed-sectional method for solving the population balance equation. Chem Eng Sci 2019;209:115198.

[294] Sewerin F, Rigopoulos S. An explicit adaptive grid approach for the numerical solution of the population balance equation. Chem Eng Sci 2017;168:250–70.

[295] Tang HY, Rigopoulos S, Papadakis G. A methodology for coupling DNS and discretised population balance for modelling turbulent precipitation. Int J Heat Fluid Flow 2020;86:108689.

[296] Kruis F, Kusters K, Pratsinis S. A simple model for the evolution of the characteristics of aggregate particles undergoing coagulation and sintering. Aerosol Sci Technol 1993;19:514–26.

[297] Kelesidis GA, Kholghy MR. A monodisperse population balance model for nanoparticle agglomeration in the transition regime. Materials 2021;14:3882.

[298] Wick A, Frenklach M, Pitsch H. Systematic assessment of the method of moments with interpolative closure and guidelines for its application to soot particle dynamics in laminar and turbulent flames. Combust Flame 2020;214:450–63.

[299] Wright DL, McGraw R, Rosner DE. Bivariate extension of the quadrature method of moments for modeling simultaneous coagulation and sintering of particle populations. J Colloid Interface Sci 2001;236(2):242–51.

[300] Yoon C, McGraw R. Representation of generally mixed multivariate aerosols by the quadrature method of moments: I. Statistical foundation. J Aerosol Sci 2004;35(5):561–76.

[301] Yoon C, McGraw R. Representation of generally mixed multivariate aerosols by the quadrature method of moments: II. Aerosol dynamics. J Aerosol Sci 2004;35(5):577–98.

[302] Fox RO. Higher-order quadrature-based moment methods for kinetic equations. J Comput Phys 2009;228(20):7771–91.

[303] Fox RO. Optimal moment sets for multivariate direct quadrature method of moments. Ind Eng Chem Res 2009;48(21):9686–96.

[304] Yuan C, Fox RO. Conditional quadrature method of moments for kinetic equations. J Comput Phys 2011;230(22):8216–46.

[305] Yuan C, Laurent F, Fox R. An extended quadrature method of moments for population balance equations. J Aerosol Sci 2012;51:1–23.

[306] Fox RO. Computational models for turbulent reacting flows. Cambridge University Press; 2003.

[307] Zucca A, Marchisio DL, Barresi AA, Fox RO. Implementation of the population balance equation in CFD codes for modelling soot formation in turbulent flames. Chem Eng Sci 2006;61(1):87–95.

[308] Blanquart G, Pitsch H. Analyzing the effects of temperature on soot formation with a joint volume-surface-hydrogen model. Combust Flame 2009;156(8):1614–26.

[309] Bruns MC, Ezekoye OA. Development of a hybrid sectional quadrature-based moment method for solving population balance equations. J Aerosol Sci 2012;54:88–102.

[310] Laurent F. Numerical analysis of Eulerian multi-fluid models in the context of kinetic formulations for dilute evaporating sprays. ESAIM Math Model Numer Anal 2006;40(3):431–68.

[311] Laurent F, Sibra A, Doisneau F. Two-size moment multi-fluid model: a robust and high-fidelity description of polydisperse moderately dense evaporating sprays. Commun Comput Phys 2016;20(4):902–43.

[312] Yang S, Mueller ME. A multi-moment sectional method (MMSM) for tracking the soot number density function. Proc Combust Inst 2019;37(1):1041–8.

[313] Colmán HM, Mueller ME. Large eddy simulation of the evolution of the soot size distribution in turbulent nonpremixed flames using the bivariate multi-moment sectional method. Combust Flame 2024;265:113496.

[314] Nobili A, Fanari N, Dinelli T, Cipriano E, Cuoci A, Pelucchi M, Frassoldati A, Faravelli T. Kinetic modeling of carbonaceous particle morphology, polydispersity and nanostructure through the discrete sectional approach. Combust Flame 2024;269:113697.

[315] Blanquart G, Pitsch H. A joint volume-surface-hydrogen multi-variate model for soot formation. In: Bockhorn H, D'Anna A, Sarofim AF, Wang H, editors. Combustion generated fine carbonceous particles. KIT Scientific Publishing: Springer-Verlag; 2009, p. 437–64, chapter 27.

[316] Desjardins O, Blanquart G, Balarac G, Pitsch H. High order conservative finite difference scheme for variable density low Mach number turbulent flows. J Comput Phys 2008;227(15):7125–59.

[317] Pitsch H. FlameMaster: A C++ computer program for 0D combustion and 1D laminar flame calculations. Cited in 1998;81.

[318] Goodwin DG, Moffat HK, Schoegl I, Speth RL, Weber BW. Cantera: An object-oriented software toolkit for chemical kinetics, thermodynamics, and transport processes. 2023, http://dx.doi.org/10.5281/zenodo.8137090, https://www.cantera.org. Version 3.0.0.

[319] CHEMKIN-PRO R. 15112, reaction design. Vol. 422, Inc., San Diego, CA; 2011, p. 396.

[320] Weller HG, Tabor G, Jasak H, Fureby C. A tensorial approach to computational continuum mechanics using object-oriented techniques. Comput Phys 1998;12(6):620–31.

[321] Hawkes ER, Sankaran R, Sutherland JC, Chen JH. Direct numerical simulation of turbulent combustion: fundamental insights towards predictive models. In: Journal of physics: conference series. Vol. 16, IOP Publishing; 2005, p. 65.

[322] Moureau V, Lartigue G, Sommerer Y, Angelberger C, Colin O, Poinsot T. Numerical methods for unsteady compressible multi-component reacting flows on fixed and moving grids. J Comput Phys 2005;202(2):710–36.

[323] Amsden AA. KIVA-3V, release 2: improvements to KIVA-3V. Tech. rep., Los Alamos National Lab.(LANL), Los Alamos, NM (United States); 1999.

[324] Thouy R, Jullien R. A cluster-cluster aggregation model with tunable fractal dimension. J Phys A: Math Gen 1994;27(9):2953–63.

[325] Mackowski DW. Electrostatics analysis of radiative absorption by sphere clusters in the Rayleigh limit: application to soot particles. Appl Opt 1995;34(18):3535.

[326] Thouy R, Jullien R. Structure factors for fractal aggregates built off-lattice with tunable fractal dimension. J Phys I 1996;6(10):1365–76.

[327] Thouy R, Jullien R. Geometrical properties of aggregates with tunable fractal dimension. J Phys A: Math Gen 1997;30(19):6725–35.

[328] Thouy R, Jullien R. Structure and dynamics of fractal aggregates with tunable fractal dimension. Philos Mag B 1998;77(2):321–31.

[329] Kätzel U, Bedrich R, Stintz M, Ketzmerick R, Gottschalk-Gaudig T, Barthel H. Dynamic light scattering for the characterization of polydisperse fractal systems: I. Simulation of the diffusional behavior. Part Part Syst Charact 2008;25(1):9–18.

[330] Chakrabarty RK, Garro MA, Chancellor S, Herald C, Moosmüller H. FracMAP: A user-interactive package for performing simulation and orientation-specific morphology analysis of fractal-like solid nano-agglomerates. Comput Phys Comm 2009;180(8):1376–81.
[331] Gilbert B, Ono RK, Ching KA, Kim CS. The effects of nanoparticle aggregation processes on aggregate structure and metal uptake. J Colloid Interface Sci 2009;339(2):285–95.
[332] Ringl C, Urbassek HM. A simple algorithm for constructing fractal aggregates with pre-determined fractal dimension. Comput Phys Comm 2013;184(7):1683–5.
[333] Guesnet E, Dendievel R, Jauffrès D, Martin C, Yrieix B. A growth model for the generation of particle aggregates with tunable fractal dimension. Phys A 2019;513:63–73.
[334] Morán J, Cuevas J, Liu F, Yon J, Fuentes A. Influence of primary particle polydispersity and overlapping on soot morphological parameters derived from numerical TEM images. Powder Technol 2018;330:67–79.
[335] Singh A, Thajudeen T. A hybrid particle swarm optimization-tuning algorithm for the prediction of nanoparticle morphology from microscopic images. Aerosol Air Qual Res 2023;23(4):220453.
[336] Yon J, Liu F, Morán J, Fuentes A. Impact of the primary particle polydispersity on the radiative properties of soot aggregates. Proc Combust Inst 2019;37(1):1151–9.
[337] Paulien L, Ceolato R, Fossard F, Rairoux P, Miffre A. (UV, VIS) laboratory evaluation of the lidar depolarization ratio of freshly emitted soot aggregates from pool fire in ambient air at exact backscattering angle. J Quant Spectrosc Radiat Transfer 2021;260:107451.
[338] Merkl P, Zhou S, Zaganiaris A, Shahata M, Eleftheraki A, Thersleff T, Sotiriou GA. Plasmonic coupling in silver nanoparticle aggregates and their polymer composite films for near-infrared photothermal biofilm eradication. ACS Appl Nano Mater 2021;4(5):5330–9.
[339] Luo J, Zhang Q, Zhang Y, Li Z. Radiative properties of non-spherical black carbon aerosols. In: Springer series in light scattering: volume 7: light absorption and scattering in turbid media. Springer; 2021, p. 69–124.
[340] Tomchuk OV, Avdeev MV, Bulavin LA. Modeling fractal aggregates of polydisperse particles with tunable dimension. Colloids Surf A: Physicochem Eng Asp 2020;605:125331.
[341] Tomchuk O. Models for simulation of fractal-like particle clusters with prescribed fractal dimension. Fractal Fract 2023;7(12).
[342] Langevin P. Sur la théorie du mouvement Brownien. C R 1908;146:530–3.
[343] Narsimhan G, Ruckenstein E. Monte Carlo simulation of brownian coagulation over the entire range of particle sizes from near molecular to colloidal: Connection between collision efficiency and interparticle forces. J Colloid Interface Sci 1985;107(1):174–93.
[344] Isella L, Drossinos Y. Langevin agglomeration of nanoparticles interacting via a central potential. Phys Rev E 2010;82(1):011404.
[345] Inci G, Kronenburg A, Weeber R, Pflüger D. Langevin dynamics simulation of transport and aggregation of soot nano-particles in turbulent flows. Flow Turbul Combust 2017;98:1065–85.
[346] Ermak DL, Buckholz H. Numerical integration of the Langevin equation: Monte Carlo simulation. J Comput Phys 1980;35(2):169–82.
[347] Suresh V, Gopalakrishnan R. Tutorial: Langevin dynamics methods for aerosol particle trajectory simulations and collision rate constant modeling. J Aerosol Sci 2021;155:105746.
[348] Meakin P. A historical introduction to computer models for fractal aggregates. J Sol-Gel Sci Technol 1999;15:97–117.
[349] Böttcher L, Herrmann HJ. Computational statistical physics. Cambridge University Press; 2021.
[350] Goudeli E, Eggersdorfer ML, Pratsinis SE. Coagulation of agglomerates consisting of polydisperse primary particles. Langmuir 2016;32(36):9276–85.
[351] Gillespie DT. An exact method for numerically simulating the stochastic coalescence process in a cloud. J Atmos Sci 1975;32:1977–89.
[352] Shekar S, Menz WJ, Smith AJ, Kraft M. On a multivariate population balance model to describe the structure and composition of silica nanoparticles. Comput Chem Eng 2012;43:130–47.
[353] Yapp EKY, Chen D, Akroyd J, Mosbach S, Kraft M, Camacho J, Wang H. Numerical simulation and parametric sensitivity study of particle size distributions in a burner-stabilised stagnation flame. Combust Flame 2015;162:2569–81.
[354] Patodia S, Bagaria A, Chopra D. Molecular dynamics simulation of proteins: A brief overview. J Phys Chem Biophys 2014;4(6):1.
[355] Allen MP, Tildesley DJ. Computer simulation of liquids. Oxford University Press; 2017.
[356] Inci G, Arnold A, Kronenburg A, Weeber R. Modeling nanoparticle agglomeration using local interactions. Aerosol Sci Technol 2014;48(8):842–52.
[357] Hamaker HC. The London—van der Waals attraction between spherical particles. Physica 1937;4(10):1058–72.
[358] Cazals F, Kanhere H, Loriot S. Computing the volume of a union of balls: A certified algorithm. ACM Trans Math Software 2011;38(1):3:1–20.
[359] Eggersdorfer ML, Kadau D, Herrmann HJ, Pratsinis SE. Multiparticle sintering dynamics: From fractal-like aggregates to compact structures. Langmuir 2011;27:6358–67.
[360] Kelesidis GA, Goudeli E. Self-preserving size distribution and collision frequency of flame-made nanoparticles in the transition regime. Proc Combust Inst 2021;38(1):1233–40.
[361] Trivanovic U, Martins MP, Benz S, Kelesidis GA, Pratsinis SE. Dynamics of soot surface growth and agglomeration by enclosed spray combustion of jet fuel. Fuel 2023;342:127864.
[362] Tsalikis DG, Mavrantzas VG, Pratsinis SE. A new equation for the mean free path of air. Aerosol Sci Technol 2024;1–12.
[363] Schenk M, Lieb S, Vieker H, Beyer A, Golzhauser A, Wang H, Kohse-Höinghaus K. Imaging nanocarbon materials: Soot particles in flames are not structurally homogeneous. Chem Phys Chem 2013;14:3248–54.
[364] Maricq MM, Harris SJ, Szente JJ. Soot size distributions in rich premixed ethylene flames. Combust Flame 2003;132:328–42.
[365] Hinds WC, Zhu Y. Aerosol technology: properties, behavior, and measurement of airborne particles. John Wiley & Sons; 2022.
[366] Hayashi S, Hisaeda Y, Asakuma Y, Aoki H, Miura T, Yano H, Sawa Y. Simulation of soot aggregates formed by benzene pyrolysis. Combust Flame 1999;117(4):851–60.
[367] Camejo M, Espeso D, Bonilla L. Influence of primary-particle density in the morphology of agglomerates. Phys Rev E 2014;90(1):012306.
[368] Ono K, Matsukawa Y, Saito Y, Matsushita Y, Aoki H, Era K, Aoki T, Yamaguchi T. Monte Carlo simulation for morphology of nanoparticles and particle size distributions: comparison of the cluster–cluster aggregation model with the sectional method. J Nanoparticle Res 2015;17:1–12.
[369] Wang Y-f, Huang Q-x, Wang F, Chi Y, Yan J-h. Brownian dynamics simulation of soot primary particle aggregation in laminar ethylene diffusion flames. Phys A 2019;514:936–47.
[370] Raj A, Celnik M, Shirley R, Sander M, Patterson R, West R, Kraft M. A statistical approach to develop a detailed soot growth model using PAH chatacteristics. Combust Flame 2009;156:896–913.
[371] Kelesidis GA, Pratsinis SE. Soot light absorption and refractive index during agglomeration and surface growth. Proc Combust Inst 2019;37:1177–84.
[372] Heinson WR, Pierce F, Sorensen CM, Chakrabarti A. Crossover from ballistic to Epstein diffusion in the free-molecular regime. Aerosol Sci Technol 2014;48(7):738–46.
[373] Patterson RIA, Singh J, Balthasar M, Kraft M, Wagner W. Extending stochastic soot simulation to higher pressures. Combust Flame 2006;145:638–42.
[374] Ma X, Zangmeister CD, Zachariah M. A comparison study of two tandem ion-mobility methods. J Phys Chem C 2013;117:10723–9.
[375] Kelesidis GA, Rossi N, Pratsinis SE. Porosity and crystallinity dynamics of carbon black during internal and surface oxidation. Carbon 2022;197:334–40.
[376] Eggersdorfer ML, Kadau D, Herrmann HJ, Pratsinis SE. Aggregate morphology evolution by sintering: Number and diameter of primary particles. J Aerosol Sci 2012;46:7–19.
[377] Morán J. Improving the numerical simulation of soot aerosol formation in flames (Ph.D. thesis), COMUE NORMANDIE UNIVERSITE; 2021.
[378] Eggersdorfer ML, Pratsinis SE. The structure of agglomerates consisting of polydisperse particles. Aerosol Sci Technol 2012;46(3):347–53.
[379] MCAC GitLab repository. CORIA Laboratory; 2017, URL: https://gitlab.coria-cfd.fr/MCAC/MCAC.
[380] Kirchhof MJ, Schmid H-J, Peukert W. Three-dimensional simulation of viscous-flow agglomerate sintering. Phys Rev E 2009;80:026319.
[381] Pokluda O, Bellehumeur CT, Vlachopoulos J. Modification of Frenkel's model for sintering. AIChE J 1997;43(2):3253–6.
[382] Koch W, Friedlander SK. The effect of particle coalescence on the surface area of a coalugating aerosol. J Colloid Interface Sci 1990;140(2):419–27.
[383] Mitchell P. Monte Carlo simulation of soot aggregation with simultaneous surface growth (ph.d. thesis) (Ph.D. thesis), University of California, Berkeley, U.S.A.; 2001.
[384] Wu H, Lattuada M, Morbidelli M. Dependence of fractal dimension of DLCA clusters on size of primary particles. Adv Colloid Interface Sci 2013;195:41–9.
[385] Rissler J, Messing ME, Malik AI, Nilsson PT, Nordin EZ, Bohgard M, Sanati M, Pagels JH. Effective density characterization of soot agglomerates from various sources and comparison to aggregation theory. JAerosol Sci Technol 2013;47:792–805.
[386] Maricq MM. Examining the relationship between black carbon and soot in flames and engine exhaust. Aerosol Sci Technol 2014;48:620–9.
[387] Kholghy MR, Afarin Y, Sediako AD, Barda J, Lapuerta M, Chu C, Weingarten J, Borshanpour B, Chernov V, Thomson MJ. Comparison of multiple diagnostic techniques to study soot formation and morphology in a diffusion flame. Combust Flame 2017;176:567–83.
[388] Yon J, Morán J, Lespinasse F, Escudero F, Godard G, Mazur M, Liu F, Fuentes A. Horizontal planar angular light scattering (HPALS) characterization of soot produced in a laminar axisymmetric coflow ethylene diffusion flame. Combust Flame 2021;232:111539.
[389] Altenhoff M, Aßmann S, Teige C, Huber FJ, Will S. An optimized evaluation strategy for a comprehensive morphological soot nanoparticle aggregate characterization by electron microscopy. J Aerosol Sci 2020;139:105470.

[390] Goodson M, Kraft M. An efficient stochastic algorithm for simulating nano-particle dynamics. J Comput Phys 2002;183:210–32.
[391] University of cambridge, department of chemical engineering and Biotechnology, computational modelling group. 2020, URL: https://github.com/ucam-ceb-como/MOpS.
[392] Jullien R. Transparency effects in cluster-cluster aggregation with linear trajectories. J Phys A: Math Gen 1984;17:L771–6.
[393] Ouf F-X, Bourrous S, Fauvel S, Kort A, Lintis L, Nuvoli J, Yon J. True density of combustion emitted particles: A comparison of results highlighting the influence of the organic contents. J Aerosol Sci 2019;134:1–13.
[394] Michelsen HA. Effects of maturity and temperature on soot density and specific heat. Proc Combust Inst 2021;38(1):1197–205.
[395] Prakash A, Bapat A, Zachariah M. A simple numerical algorithm and software for solution of nucleation, surface growth, and coagulation problems. Aerosol Sci Technol 2003;37(11):892–8.
[396] Kholghy MR, Saffaripour M, Yip C, Thomson MJ. The evolution of soot morphology in a laminar coflow diffusion flame of a surrogate for jet A-1. Combust Flame 2013;160:2119–30.
[397] Gröhn AJ, Eggersdorfer ML, Pratsinis SE, Wegner K. On-line monitoring of primary and agglomerate particle dynamics. J Aerosol Sci 2014;73:1–13.
[398] Cortés D, Morán J, Liu F, Escudero F, Consalvi J-L, Fuentes A. Effect of fuels and oxygen indices on the morphology of soot generated in laminar coflow diffusion flames. Energy Fuels 2018;32(11):11802–13.
[399] Bouvier M, Yon J, Lefevre G, Grisch F. A novel approach for in-situ soot size distribution measurement based on spectrally resolved light scattering. J Quant Spectrosc Radiat Transfer 2019;225:58–68.
[400] Dastanpour R, Rogak SN. Observations of a correlation between primary particle and aggregate size for soot particles. Aerosol Sci Technol 2014;48(10):1043–9.
[401] Kazemimanesh M, Dastanpour R, Baldelli A, Moallemi A, Thomson KA, Jefferson MA, Johnson MR, Rogak SN, Olfert JS. Size, effective density, morphology, and nano-structure of soot particles generated from buoyant turbulent diffusion flames. J Aerosol Sci 2019;132:22–31.
[402] LLC M. Euler ETH supercomputer. 2017, URL: https://scicomp.ethz.ch/wiki/Euler#Euler_VIII.
[403] Rahaman M. Sintering of ceramics. CRC Press: Boca Raton; 2008.
[404] Baldelli A, Trivanovic U, Sipkens TA, Rogak SN. On determining soot maturity: A review of the role of microscopy- and spectroscopy-based techniques. Chemosphere 2020;252:126532.
[405] Mannazhi M, Török S, Gao J, Bengtsson P-E. Soot maturity studies in methane-air diffusion flames at elevated pressures using laser-induced incandescence. Proc Combust Inst 2021;38:1217–24.
[406] Brugière E, Gensdarmes F, Ouf F, Yon J, Coppalle A. Increase in thermophoretic velocity of carbon aggregates as a function of particle size. J Aerosol Sci 2014;76:87–97. http://dx.doi.org/10.1016/j.jaerosci.2014.06.007, URL: https://www.sciencedirect.com/science/article/pii/S0021850214001049.
[407] Meyer DW, Eggersdorfer ML. Simulating particle collisions in homogeneous turbulence with kinematic simulation–a validation study. Colloids Surf A: Physicochem Eng Asp 2014;454:57–64.
[408] Littin M, Poux A, Lefevre G, Mazur M, Fuentes A, Yon J. On the consideration of signal trapping for soot sizing by angular light scattering in laminar flames. J Aerosol Sci 2024;181:106429. http://dx.doi.org/10.1016/j.jaerosci.2024.106429, URL: https://www.sciencedirect.com/science/article/pii/S002185022400096X.

**Fengshan Liu**

**Academic Background**

Ph.D: Chemical Engineering, Sheffield University, 1991, UK; B.Eng: Engineering Mechanics, Tsinghua University, 1986, China.

**Professional Background**

1996-Present: Research Officer, National Research Council Canada; 1992-1996: Research Assistant Professor, Queen's University, Canada; 1990-1992: Postdoctoral Fellow, Leeds University, UK.

**Relevant Awards and Commitment**

2014: Adjunct Professor, University of Toronto Institute for Aerospace Studies; 2017: Associate Editor, Journal of Quantitative Spectroscopy and Radiative Transfer; 2013-2025 Board Member, Combustion Institute Canadian Section; 2019: Fellow, Combustion Institute; 2019: Member of the Scientific Council of International Center for Heat and Mass Transfer.

**Selected Research Grants in the Field (last ten years)**

2016-2020: Improved Measurement Methods for Quantification of Black Carbon Emissions from Vehicles; 2012-2016: Black Carbon Measurement.

**Jérôme Yon**

**Academic Background**

Bachelor's and master's degree: Mechanics; Master degree: Energetics and aerothermochemistry option real flow; PhD Thesis: High pressure diesel jet in near and far field : Imaging study; Habilitation to Supervise Research: Contribution to the development of the metrology of nanoparticle aggregates and to the characterization of soot particles.

**Professional Background**

2004-2022: Lecturer at INSA Rouen Normandie; since 2022: Full Professort at INSA Rouen Normandie.

**Relevant Awards and Commitment**

2021: Journal of Aerosol Science Excellence in Research Award https://doi.org/10.1016/j.jaerosci.2021.105948.

**Selected Research Grants in the Field (last ten years)**

2015: Project BioCar funded by Project BioEngine funded by Labex EMC3; Project on Soleil synchrotron (France) << Soot oxidation and thermal stability of nanoparticles in flames, a SAXS approach >> ,

2016 : Project on Soleil synchrotron (France) << SAXS Study of Silicon Oxide Nanoparticles Formed in an Electrical Arc >>; Eureopean project SOPRANO << SOot Processes and Radiation in Aeronautical inNOvative combustors >>; Project Excalibur.

2017 : Surface project ; Pufbio project funded by ANSES.

2018 : Project ASTORIA, << Accounting for soot particle morphology in flame thermal radiation and optical diagnostics in complex systems >> funded by french ANR.

2019 : Project BACON (BlAck Carbon Optical agiNg) funded by LEFE program ; Project GASPROPRES funded by Normandie region.

2020 : Project SONOLINO << SOot nanoparticle structure analysis in aerosol phase by NOn LINear Optics >>, funded by Normandie region ; European Intereg project FireDrone, << Fire/Fast Incident Response Equipment for the DescRiption Of Noxious particle Emissions >>,

2022 : Project ProfilTox ; Project COCPIT funded by Normandie region.

2023 : Project Oxy-soot, << Numerical et experimental investigation of soot oxydation >>, funded by SAFRAN.

2024 : Chair CNRS RADDAERO, funded by Normandie region ; Project RetroDif funded by Normandie region and ONERA ; Project ToxycoMAC funded by ANSES.

2025 : French program ANR Toscana ; FireDrone-Light, << Fire/Fast Incident Response Equipment for the DescRiption Of Noxious particle Emissions — LIGHTweight versio >>

**José Morán**

**Academic Background**

Ph.D: Physics, Normandie Université, France; MSc: Industrial Engineering, Universidad Técnica Federico Santa María, Chile; BSc: Industrial Engineering, Universidad Técnica Federico Santa María, Chile.

**Professional Background**

2024-Present: Assistant Professor, University of Ottawa, Canada; 2022-2024: Postdoctoral Associate, Hogan's Laboratory, University of Minnesota, USA; 2021-2022: Visiting Researcher, Particle Technology Laboratory, Carleton University, Canada; 2018-2021: Research and teaching assistant, CORIA Laboratory, France; 2018-2018: Lecturer, Universidad Adolfo Ibañez, Chile; 2014-2018: Research and teaching assistant, Universidad Técnica Federico Santa María, Chile.

**Relevant Awards and Commitment**

2022: Best Poster award, French Association for Aerosol Research (ASFERA), France; 2021: Best Poster award, 24th ETH Combustion Generated Nanoparticles Conference, Switzerland; 2021: Laureate of the Jean Bricard prize, French Association for Aerosol Research (ASFERA), France.

**Selected Research Grants in the Field (last ten years)**

2025-Present: Synthesis of nanomaterials in reactive flows to reduce indoor air pollutants (NSERC Discovery Grant, Canada)

**Georgios A. Kelesidis**

**Academic Background**

Ph.D.: Mechanical and Process Engineering, ETH Zürich, 2019, Switzerland; M.Sc.: Process Engineering, ETH Zürich, 2015, Switzerland; Dipl.: Chemical Engineering, University of Patras, 2013, Greece.

**Professional Background**

2024-Present: Assistant Professor, Delft University of Technology, The Netherlands; 2023-2024: Assistant Professor, Rutgers University, USA; 2021-2022: Senior Lecturer and Research Associate (Oberassistent), ETH Zürich, Switzerland; 2019-2021: Lecturer and Research Associate, ETH Zürich, Switzerland; 2015-2019: Research and Teaching Assistant, ETH Zürich, Switzerland.

**Relevant Awards and Commitment**

2024-Present: Topic Editor, Aerosol Research; 2024-Presenr: Chair, Aerosol Physics Working Group, American Association for Aerosol Research; 2023-Present: Chair of Aerosol Technology Working Group, European Aerosol Assembly; 2022-Present: Program Leader, Laminar Flames and Chemistry and Particle Formation, International Sooting Flame Workshop; 2022: Best 3-min presentation prize, 6th International Sooting Flame Workshop; 2020: Forbes 30 under 30 Europe List, Science and Healthcare; 2020: Gesellschaft für Aerosolforschung (GAeF) PhD Award, Association for Aerosol Research; 2020: Best Poster Award, European Aerosol Conference 2020; 2020: Fellow of the Global Young Scientists Summit, National Research Foundation; 2019: ETH Medal for Outstanding Doctoral Thesis, ETH Zurich; 2019: Best Poster Award, 2019 Material

Research Society (MRS) Fall Meeting; 2019: First Carbon Nanomaterials Graduate Student Award, 2019 AIChE Annual Meeting; 2019: First Best Poster Award, 2019 ETH Conference on Combustion Generated Nanoparticles; 2017: IBM Research Prize for M.Sc. Thesis on Computer Modelling and Simulations in Chemistry, Biology and Material Science.

**Selected Research Grants in the Field (last ten years)**

2019-2022: Tailor-made Carbonaceous Nanoparticles by Multiscale Combustion Design, Swiss National Science Foundation; 2017-2018: Fire Detection by Light Scattering through Modeling Mature Soot Dynamics during Volatile Condensation, Siemens AG, Building Technologies.

**Felipe Escudero B.**

**Academic Background**

Ph.D: Engineering Sciences, Major in Energy, Université d'Aix Marseille, France; Msc.: Master of Engineering Sciences in Mechanics, Universidad de Chile, Santiago, Chile; Eng.: Mechanical Engineering, Universidad de Chile, Santiago, Chile; Bsc.: Mechanical Engineering, Universidad de Chile, Santiago, Chile.

**Professional Background**

2024-present: Assistant Professor, Departamento de Industrias, Universidad Técnica Federico Santa María; 2019-2023: Postdoctoral fellow, Departamento de Industrias, Universidad Técnica Federico Santa María. ; 2019: Research stay at the Nano Aerosol Computational Engineering (NanoACE) research group, University of Windsor; 2015-2016: Research assistant at the Energy Conversion and Combustion Group (EC2G), Universidad Técnica Federico Santa María; 2009-2012: Teaching assistant at Facultad de Ciencias Físicas y Matemáticas, Universidad de Chile.

**Relevant Awards and Commitment**

2021: Best paper award at the 15th International Conference on Heat Transfer, Fluid Mechanics and Thermodynamics; 2019: Canadian Government fellowship (MITACS research award) for research stay at University of Windsor; 2007 - 2015: Chilean Government scholarships for PhD studies (CONICYT - Becas Chile, 2015) and MSc studies (CONICYT - Becas Chile, 2012), and for Engineering studies (Andrés Bello).

**Research Grants in the Field**

2025-2029: Toxicity of particulate emissions from next-gen fuels: characterization of chemical composition and detailed morphology of flame-generated soot particles, Fondecyt 1252119 (Co-PI, PI: Andrés Fuentes); 2025-2029: Impact of local flaming conditions on the detailed structure of flame-synthesized nanomaterials: from soot to metal-oxides nanoparticles, Fondecyt 1252096 (Co-PI, PI: Rodrigo Demarco); 2024-2027: Improving Numerical and Experimental Characterization of Soot Production using Physics-Informed Machine Learning, Fondecyt 11241102 (PI); 2022-2025: Detailed numerical modeling of liquid-fuels: effect of PAH species on soot nucleation and adsorption mechanisms, Fondecyt 1221532 (CoPI, PI[1] : Rodrigo Demarco); 2021-2024: Capturing features of soot propensity from combustion processes through a machine learning approach, Fondecyt 3210498 (PI).

**Andrés Fuentes C.**

**Academic Background** Ph.D: Fluid Mechanics, major in Energy and Combustion, Université de Poitiers, France; MSc.: Thermal energy and Combustion, Université de Poitiers, France; Eng.: Industrial engineering, Universidad Técnica Federico Santa María (USM), Chile; BSc.: Industrial engineering, Universidad Técnica Federico Santa María (USM), Chile.

**Professional Background**

2022-present: Provost at USM; 2009-present: Full Professor in the Departamento de Industrias (DI) at USM, Valparaíso, Chile; 2007-present: Maître de Conférences (on leave) at the Aix-Marseille Université, Marseille, France; 2006-2007: Research Fellow at University of Edinburgh, Edinburgh, UK; 2002-2006: Graduate Research Assistant in the Pprime institute of CNRS, Poitiers, France.

**Relevant Awards and Commitment**

2018: Silver Combustion Medal, awarded by the Combustion Institute; 2017: Selected distinguished paper of International Symposium on Combustion, Korea; 2016-present: Chair of the Chilean Combustion Section of the Combustion Institute; 2013-2018: Board member of founding council called Fondecyt, Chile; 2005: Bronze medal for CNES and ESA Parabolic Flight Campaigns, France; 2006: Contribution to ESA's Sounding Rocket Programme for Microgravity Research.

**Selected Research Grants in the Field (last ten years)**

2025-2029: Toxicity of particulate emissions from next-gen fuels: characterization of chemical composition and detailed morphology of flame-generated soot particles, Fondecyt 1252119 (PI); 2022-2024: Fostering e-Fuels and Biofuels: Revealing Sooting Propensity and Evolution of Soot Maturity and Morphology in Non-Premixed Flames, Fondecyt 1191758 (PI); 2020-2024: Revealing Soot Chemistry Evolution in the Combustion of Biofuels for Jet Applications, NSFC190009 (PI); 2019-2021: Understanding Soot Evolution and Morphology in Non-Premixed Steady and Forced Flames, Fondecyt 1191758 (PI); 2016-2018: Towards Cleaner Combustion: Characterization of the Sooting Propensity of Biofuels, Fondecyt 1161453 (PI); 2013-2015: Soot Production in an Inverse Diffusion Flame: Application for Non-Conventional Fuels, Fondecyt 1130627 (PI); 2010-2012: Soot Production in a Laminar Diffusion Flame: Application for Non-Conventional Fuels, Fondecyt 1100913 (PI).

[1] Principal Investigator.